Liquid induced long range phononic interaction in solids beyond the wetted hydrophilic interface

Max Warburton

THÈSE DE DOCTORAT

NNT: 2025UPASP151

université PARIS-SACLAY

Liquid induced long range phononic interaction in solids beyond the wetted hydrophilic interface

Interaction phononique longue portée induite par mouillage d'une interface hydrophile modèle

Thèse de doctorat de l'université Paris-Saclay

École doctorale n°564, Physique en Île-de-France (EDPIF)
Spécialité de doctorat : Physique
Graduate School : Physique. Référent : Faculté des Sciences d'Orsay

Thèse préparée dans l'unité de recherche **LLB** (Université Paris-Saclay, CEA, CNRS) (Laboratoire Léon-Brillouin), sous la direction de **Laurence NOIREZ**, Directrice de recherche CNRS, Université Paris-Saclay

Thèse soutenue à Paris-Saclay, le 12 décembre 2025, par

Max WARBURTON

Composition du Jury

Membres du jury avec voix délibérative

Stefan KLOTZ Directeur de recherche, Université Sorbonne	Président
Marie PLAZANET Directrice de recherche, Université Grenoble Alpes	Rapporteure & Examinatrice
Marc DE BOISSIEU Directeur de recherche émérite, Université Grenoble Alpes	Rapporteur & Examinateur
Laurent JOLY Professeur des universités, Université Lyon 1	Examinateur
Livia BOVE Directrice de recherche, Université Sorbonne	Examinatrice

université PARIS-SACLAY

ÉCOLE DOCTORALE
Physique en Île-de-France (PIF)

Titre : Interaction phononique longue portée induite par mouillage d'une interface hydrophile modèle

Mots clés : phonon, interface liquide-solide, hydrophile, mouillage, écoulement

Résumé : La mécanique des fluides, fondée sur l'hypothèse du continuum, a décrit avec succès les écoulements macroscopiques. Des concepts tels que la tension de surface et la loi de Young permettent de distinguer le caractère hydrophile ou hydrophobe de l'interaction d'un liquide avec une surface. Cette interaction est d'une importance capitale lors de la réalisation de mesures rhéologiques. Le comportement des fluides est généralement modélisé en termes de réponses visqueuses et élastiques à une sollicitation mécanique. Le modèle rhéologique dominant est celui de Maxwell qui définit un temps de relaxation viscoélastique. Frenkel a proposé une explication physique moléculaire du temps de relaxation pour les liquides simples. Ce modèle prédit un comportement élastique en cisaillement pour tout liquide sollicité à très hautes fréquences. Cependant, au cours des dernières décennies, différents résultats expérimentaux ont mis en évidence que ce n'est plus vrai lorsque les liquides sont confinés ; un comportement élastique en cisaillement émerge à basses fréquences, de l'échelle nanométrique à l'échelle mésoscopique, démontrant ainsi la capacité des liquides à propager une onde élastique en cisaillement. Pour accéder à cette réponse élastique, une condition nécessaire est que l'interaction solide-liquide soit fortement mouillante, optimisant ainsi le transfert du mouvement de la surface au fluide. Les résultats sur l'élasticité de cisaillement dans les liquides ont conduit à de nouveaux cadres théoriques (par exemple, le modèle k-gap). . Cependant, le rôle du solide a été largement ignoré Puisque les liquides peuvent propager des états vibrationnels à longue portée lorsqu'ils sont contact avec des surfaces à haute énergie, cette thèse examine si ces états vibrationnels à longue portée interagissent avec les phonons du solide et se propagent loin de la surface. En utilisant la diffusion inélastique des rayons X et des neutrons, nous révélons l'existence d'une interaction phononique entre l'eau et l'α-Al_2O_3 (cristal fortement mouillant). Les phonons acoustiques du solide massif (à des centaines de microns de l'interface) sont perturbés par le liquide en écoulement à la surface. Un élargissement des phonons acoustiques et, de manière plus surprenante, un durcissement des phonons acoustiques transversaux et longitudinaux du solide ont été identifiés. Le durcissement et l'élargissement sont tous deux dépendants de l'isotope, l'eau lourde présentant un effet moindre. En utilisant la diffraction à haute énergie et la diffusion Raman des rayons X, aucun changement structurel ou électrochimique n'a été observé, ce qui suggère que nos résultats ont pour origine une interaction essentiellement dynamique anharmonique entre un liquide et un solide. Cette interaction est dépendante de la zone de Brillouin observée. Ainsi, l'interface solide-liquide ne peut pas être traitée comme une simple interaction surfacique. Le couplage mécanique qui s'étend profondément dans le matériau massif, résultant d'un état hors-équilibre induit par un écoulement liquide, appelle à de nouveaux cadres théoriques, intégrant les nouvelles propriétés des liquides telles que l'élasticité de cisaillement mésoscopique.

université PARIS-SACLAY

ÉCOLE DOCTORALE
Physique en Île-de-France (PIF)

Title : Liquid induced long range phononic interaction in solids beyond the wetted hydrophilic interface

Keywords : phonon, solid-liquid interaction, hydrophilic, wetting, flow

Abstract : Fluid mechanics, based on the continuum hypothesis, accurately encapsulated macroscopic flows. Concepts such as surface tension and Young's law allow us to distinguish between the hydrophilic or hydrophobic character of the solid-liquid interaction with a given surface. This interaction is key for rheological measurements. General fluid behaviour is modeled through the viscous and elastic responses to a mechanical solicitation. The dominant rheological model is that of Maxwell. It identifies a relaxation viscoelastic timescale. Frenkel later proposed a molecular physical explanation for simple liquids. This model predicts shear elastic liquid behaviour at very high frequencies. Nonetheless, in the last few decades, experimental results have highlighted that this model breaks down when liquids are confined. A shear elastic behaviour is then observed at low-frequency, from the nanoscale to the mesoscopic scale, proving the ability of the liquid to transmit a shear elastic wave. To observe this shear elastic behaviour, a necessary condition is that the solid-liquid interaction is highly wetting, therefore optimising the mechanical transfer from the surface to the liquid. These results on liquid shear-elasticity have led to new theoretical frameworks (e.g. k-gap model). Nonetheless, the role of the solid has been until now overlooked.
Since liquids can propagate vibrational states over long ranges when in contact with high energy surfaces, this thesis studies whether these vibrational states interact with the solid's bulk phonons, and propagate far from the surface. Using X-ray and neutron diffraction techniques, we highlight a phononic interaction between water and α-Al_2O_3 (highly wetting monocrystal). The bulk acoustic phonons (hundreds of microns from the interface), are perturbed by the flowing liquid. A broadening of acoustic phonons, and curiously, a hardening of transverse and longitudinal acoustic phonons are observed. Hardening and broadening are isotope dependent, with heavy water showing a lesser interaction. Furthermore, using Raman-X and high resolution diffraction techniques, no chemical or structural changes were observed, suggesting our results correspond to a purely vibrational anharmonic dynamic interaction between a liquid and a solid. This interaction depends on observed Brillouin zones, and cannot be considered as a surface interaction only. The mechanical coupling that extends deep into the bulk results from a non-equilibrium state induced by a flowing liquid, calling for new theoretical frameworks to describe this coupled phononic state, integrating new liquid properties such as mesoscopic shear elasticity.

Acknowledgements

It is no easy matter to thank all the people with whom one has crossed paths in life and work that may have contributed to a three-year work like a PhD thesis. This is my attempt, though I know that many people will be left out, not out of intent but sheer forgetfulness. To these people, I am sorry.

It seems customary to start with the professional side — though over the course of the thesis this became more and more blurred.

First, I want to thank from the bottom of my heart Laurence Noirez, the supervisor of this thesis. Without her, nothing. Literally: no one would have even thought to study the phonon dynamics of bulk solids when wetted if not for her. But outwith the science, I want to thank Laurence Noirez for being extremely supportive, for being there to push me beyond my limits when needed, and for giving me time to breathe (when needed) in order to develop my own personal understanding of the work. For all of this, I am incredibly grateful. Thank you.

Second, the other two people who helped and guided me the most scientifically. Luigi, I could not have spent so much time at the ESRF without the energy that you brought, and I could not have begun understanding the physics without your guidance. I had a lovely time in Grenoble, and it was in no small part your presence (and the Korner Pub) that made that possible. Thank you and good luck with the violins, though I don't think you need it. The other person who guided me later in the project, but with enormous impact: Philippe. You made me love 3-axis neutron experiments and the tinkering; it felt like a puzzle that you showed me how to solve. Beyond that, our conversations about music, politics and general life were a pleasure to have.

It now seems appropriate to thank the members of the Jury: Marie Plazanet and Marc de Boissieu for reviewing the work, and Laurent Joly, Livia Bove, and Stefan Klotz for examining the work and the defence. Thank you for having taken time out of your busy schedules to come to the Plateau, and for asking insightful questions; those I could not answer will no doubt be the subject of further study.

Then, the Laboratoire Léon Brillouin and all its members. An incredible place to work, very friendly and welcoming. It was an immense pleasure to call it my lab for the last three years, and I want to thank the director and deputy director, Arnaud Desmedt and Sylvain Petit. Here the full list of names to thank is long, but in no particular order: Antoine, William, Olivier, Olivier Sineau, Sarah, Aurore, Dalila, Quentin, Daniel, Arsène, Marion, Nicolas, Paul, Richard, Grégory, Kyriakos, Xavier, Xiang, Gaston, Rémy, Thomas, Alain, Frédéric, Marie-

Claire, Isabelle, Françoise, Yvan, Arnaud, etc... I would like to add a few people to the list, despite not being part of the lab: Victor, Yassine and Ursula. I had a blast and learnt so much; what more could I ask for ?

Beyond the people that I met at the LLB, I want to thank Dan, Johnny, and Alexei from ID28 at the ESRF; you were of precious help during my time in Grenoble. Similarly, Sacha, thank you for being very pedagogical during my stay at IN8, and Alessandro and Christoph for helping me at ID20. James and Jean-Pascal are to thank for the first experiment taking place at ESRF, as without them, especially James, I would have been lost. I very much enjoyed our time there, and I wanted to thank you for having come back for the next sets of experiments: it made them run smoothly, allowing for more time for drinks... Another person I would like to add is Mark, it was a pleasure meeting you in Cargèse and seeing you regularly afterwards.

On a more sombre note, I also want to thank two people who passed away during the thesis, but whose scientific work was crucial: Patrick Baroni and Kostya Trachenko. Their contributions to science live on.

Finally, on a personal note, I would like to thank my friends and family. The list is too long to mention everyone but the members of the Generalgruppen stand out, my parents, and most importantly, Rachel.

Contents

General Introduction

Fluid mechanics, built on the continuum hypothesis [1] and encapsulated by the Navier-Stokes equation [2, 3], has successfully described a vast range of macroscopic flows [4, 5]. Within this framework, the boundary between a solid and a liquid is understood through concepts like surface tension and wettability [6], mathematically formalised by Young's Law [7], which allows for a clear distinction between hydrophilic and hydrophobic interactions mostly dependent on the surface free energy [8, 9]. This solid-liquid interaction is of crucial importance, as it dictates the boundary conditions for rheological measurements [10]. For the study of flowing matter, the dominant rheological paradigm is Maxwell's viscoelastic model [11, 12], which considers a no-slip boundary condition at the solid-liquid interface [13]. It introduces a critical relaxation time, τ_m, which separates the liquid-like and solid-like responses of a material to mechanical stress. A molecular-level explanation for this timescale in simple liquids was proposed by Frenkel [14], who identified it as the characteristic time for a molecule to hop between temporary equilibrium positions—a timescale on the order of picoseconds for water [15]. This established model therefore predicts that liquids are predominantly viscous, and any shear elastic behaviour is confined to the very high-frequency (THz) regime, far beyond typical mechanical solicitations.

However, in recent decades, a growing body of experimental results has directly challenged this classical view [16, 17]. Evidence has accrued demonstrating that a wide range of liquids, from polymer melts [18, 19] to simple molecules like water [20], can exhibit a finite, low-frequency shear elastic behaviour, from the nanoscale up to the mesoscopic scale of hundreds of micrometres [21]. These findings reveal a brittle, solid-like response in a frequency domain where liquids were expected to be purely viscous. Two experimental conditions have been identified as requisite for this novel behaviour to be observed: the confined liquid must be subjected to a low shear strain [22], and, when in contact with a highly wetting, high-energy surface [23]. This strong solid-liquid interaction appears to be a necessary condition to enable the liquid to sustain a collective elastic response, indicative of large-scale vibrational patterns. Furthermore, beyond a purely mechanical response, related unexpected thermal bands have been identified [24]. The observation of thermal bands within multiple liquids under shear points towards the existence of highly correlated, long-range vibrational patterns that are incompatible with classical fluid dynamics [25, 26, 27]. These multiple novel observations converged with the independent development of novel theoretical undertakings [28], such as the k-gap theory and Non-Affine Lattice Dynamics [29, 30, 31, 32], which have begun to provide frameworks capable of predicting some of these experimental results [33].

Although the solid-liquid interface has been highlighted as crucial for observing these

phenomena, one of the missing perspectives in the current literature is the detailed coupling between the solid and the liquid in the THz regime (corresponding to IR wavelengths of the thermal bands observed [34]). The impact on the bulk of the solid has been ignored, with the solid treated as a passive boundary that enables the shear collective dynamics within the liquid [21, 20, 35]. Is the solid itself dynamically affected by this interaction? Since liquids demonstrably exhibit large-scale, phonon-like collective dynamics when tightly bound to a hydrophilic surface, one can wonder how these interactions influence the dynamics of the solid itself. This is the central subject of study of this thesis. The present work investigates whether these long-range vibrational states within the liquid can interact with and modify the intrinsic phonon modes of the solid, far from the immediate interfacial layer. To address this question, we investigate a model system composed of liquid water (H_2O) or heavy water (D_2O) in contact with the highly wetting (0001) surface of a monocrystalline α-Al_2O_3 (sapphire) substrate. The choice of α-Al_2O_3 is motivated by its status as a well-characterised, high-energy surface [36], a chemically inert material favouring the H-bond anchoring and thus more efficiently transmitting the mechanical stress to the sample [37, 38], while the use of isotopic substitution (H_2O vs. D_2O) allows for a direct probe of how the liquid's molecular mass and specific vibrational modes mediate the interaction. The goal is to use multiple bulk-sensitive tools to see if a trace of the complex vibrational patterns of water [39, 40, 41] is observable within the solid's phononic dynamics and structure.

To conduct this investigation, this work will employ Inelastic X-ray Scattering (IXS), Inelastic Neutron Scattering (INS), high-resolution X-ray diffraction, and X-ray Raman Spectroscopy (XRS). All of these tools will allow us to scan the phononic dynamics, structural parameters, and core electron excitations within the solid, distinguishing purely dynamic effects from any potential structural or chemical changes. The thesis is structured as follows:

- Chapter 1 reviews the classical framework of fluid mechanics and rheology, presents recent experimental findings for various types of liquids at low frequency and mesoscopic scale, establishing the central motivation of our study.
- Chapter 2 discusses the particular natures of the studied liquids, H_2O and D_2O, and the studied solid, α-Al_2O_3, providing an overview of the water and α-Al_2O_3 interface.
- Chapter 3 introduces the fundamental mechanisms of the X-ray and Neutron scattering methods used to scan the solid's structure and dynamics.
- Chapter 4 presents the first experimental observation of the solid-liquid phonon interaction, detailing results from IXS that reveal a previously hidden, time-dependent hardening and broadening anharmonic effect of bulk acoustic phonons.
- Chapter 5 utilises Inelastic Neutron Scattering and transmission IXS to further probe the interaction, confirming a phonon broadening and proving the absence of a simple depth-dependency. A strong isotopic effect is highlighted.
- Chapter 6 investigates whether this hardening is due to underlying structural or chemical changes in the bulk solid, using diffraction and X-ray Raman experiments to search for such effects.
- Chapter 7 provides a final discussion that synthesises the results from all experiments, and proposes new theoretical and experimental considerations.

Chapter 1

Liquids down to the interface

In this chapter, after a brief historical overview of fluid mechanics, we will introduce the general approach of continuous hydrodynamics through the Navier-Stokes equation, taking a careful look at the solid-liquid interface and rheology through the Frenkel-Maxwell model. Relevant experimental results show its limits in the low-frequency range when the liquid is confined and/or solicited at low shear-rate at the hydrophilic interface. This highlights the necessity for a novel theoretical understanding, and we shall discuss three models that have yielded accurate predictions.

1 General Hydrodynamics

1.1 A bit of history

The first foray into fluid mechanics was through the lens of engineering, notably in the Indus Valley civilisation and Mesopotamian Kingdoms some $7\,\mathrm{millennia}$ to $8\,\mathrm{millennia}$ ago with the birth of agriculture, and later around the Nile. Fluid mechanics then, if it can be called as such, was about developing intricate irrigation and drainage systems (see Fig.1.1) through an intuitive understanding of the flow of water. In those ages, water was also used to measure time, through water clocks (or clepsydra), present in ancient Persia, Greece and Rome. While not accurate by modern standards, they functioned by transferring water from one container to a marked other, such that the water level would indicate the passage of time, see 1.1. They were used in courts and legal proceedings throughout the ancient world [42].

Figure 1.1: Left: An ancient Indus valley draining system from [43]; Right: Reconstruction of a clay original clepsydra of the late 5th cent. B.C from the Ancient Agora museum

This approach was ultimately practical, and, lacking the mathematical tools, no known conceptualisation from any of these civilisations was made to understand the liquid flow.

The first *physical* attempt —as in trying to derive laws to predict the behaviour of liquids— came from the Greeks of the classical period with Archimedes of Syracuse ($\sim$ 250 BCE) being the first to formalise the principle of buoyancy. The principle simply states that the upward force experienced by a body immersed in water is equal to the weight of displaced water. This principle is still in use today in hydrostatics and is the first physical understanding of liquids through their weight (proportional to their volume), i.e. as a continuous field.

While improvements on the understanding of flows were made throughout late antiquity and the middle ages (e.g. the aqueducts in Rome and Leonardo da Vinci's drawings of flowing water), the next big breakthroughs came by way of Newton. First, he established the mathematical framework of differential equations (calculus) that would be central for physics as a whole. Second, he was the first to introduce the notion of *viscosity* and proposed a linear relationship between shear stress and shear rate for certain fluids [44]. Viscosity is simply a macroscopic quantity that represents how resistant a liquid is to flow, by way of internal friction within itself. Following this, Bernoulli, succeeded by Euler, used these mathematical frameworks to describe inviscid, incompressible flows, relating pressure, fluid flows and

height. In these approaches the fluid is modelled again as a continuous field.

It was in the 19th century that Navier [2] and Stokes [3], independently of one another, managed to incorporate Newton's viscosity in the frameworks of Euler and Bernoulli. This led to the titular Navier-Stokes equation.

1.2 The Navier-Stokes equation: cornerstone of fluid mechanics

1.2.1 On the continuum hypothesis

In the framework of fluid mechanics, the object studied is continuous matter, and its properties and laws governing said properties are expressed in terms of continuous fields that can vary in position and time. "The validity of the simpler aspects of this continuum hypothesis under the conditions of everyday experience is evident" says Batchelor in [1]. To arrive at equations in the continuum hypothesis, a sensitive volume small enough relative to the flow and general volume of fluid, but big enough to contain a large number of molecules —such that fluctuations arising from the nature of the constituent particles have no effect on the observed average— is chosen as an infinitesimal volume. Consequently, the nature of the particle structure or its existence is independent of the observed flow; liquids and gases are treated as one and the same. Similar hypotheses are made in the field of continuum mechanics of solids. In this framework, two laws are needed to encapsulate the dynamics of fluids: conservation of mass and conservation of momentum.

1.2.2 Conservation of mass

The principle of mass conservation states that mass can neither be created nor destroyed within a closed system. For a fluid, this means that the rate of change of mass within a control volume must be equal to the net rate of mass flowing into that volume. Mathematically, this is expressed as:

$$\frac{\partial \rho}{\partial t} + \nabla \cdot (\rho \mathbf{v}) = 0 \tag{1.1}$$

with t the time, ρ the fluid density, $\mathbf{v}$ the velocity field, and ∇ is the divergence operator (that measures the outward flux of a vector field from the infinitesimal volume described above).

In the case of an incompressible fluid, the spatial and temporal variation of density are null ($\frac{\partial \rho}{\partial t} = 0$). Thus (1.1) becomes $\nabla \cdot \mathbf{v} = 0$.

1.2.3 Conservation of momentum

This law is a restatement of Newton's second law of motion in the continuum hypothesis. Simply put, the rate of change of momentum for a fluid infinitesimal volume is equal to the forces acting upon it. This translates, mathematically, to:

$$\rho \left(\frac{\partial \mathbf{v}}{\partial t} + (\mathbf{v} \cdot \nabla)\mathbf{v} \right) = \nabla \cdot \sigma + \rho \mathbf{f} \tag{1.2}$$

with :

- σ the Cauchy stress tensor: within it are contained all the infinitesimal surfaces forces that are applied to the fluid.
- f contains all the body forces per unit volume that are applied to the fluid. Generally, it is gravity.

It is important to note that in equation (1.2) the liquid can be compressible. It is easy to see how this equation relates to Newton's second law: $\frac{\partial \mathbf{v}}{\partial t}$ is the local acceleration and $(\mathbf{v}\cdot\nabla)\mathbf{v}$ is the convective acceleration, and both are equal to the sum of the forces (either per volume or surface originated).

For the case of Newtonian fluids (where shear stress is linearly proportional by way of the dynamic viscosity μ to the shear rate), the Cauchy stress tensor can be divided in two parts as such

$$\sigma = -P\mathbf{I} + \tau \tag{1.3}$$

$P\mathbf{I}$ represents the isotropic pressure and the viscous stress tensor τ the stresses due to fluid deformation. If we further consider the fluid of μ dynamic viscosity to be incompressible, then

$$\tau = \mu(\nabla\mathbf{v} + (\nabla\mathbf{v})^T) \tag{1.4}$$

We thus obtain the full Navier-Stokes equation:

$$\rho\left(\frac{\partial \mathbf{v}}{\partial t} + (\mathbf{v}\cdot\nabla)\mathbf{v}\right) = -\nabla P + \mu\nabla^2\mathbf{v} + \rho\mathbf{f} \tag{1.5}$$

Despite many strong hypotheses on the nature of fluids (continuous, Newtonian, incompressible), this equation has not yet been solved analytically (because of the convective term), and is incredibly accurate in its predictions of flows at large ranges of applications and scales. From aeronautics [4], microfluidics [5] and even for understanding granular flows [45] (where the continuum hypothesis is a priori less applicable), the Navier-Stokes equation truly is ubiquitous.

2 The solid-liquid interface

2.1 Surface tension

While a liquid flows following equation (1.5), it nonetheless has stable geometric properties at the small scale at rest. One of which is the fact that below the capillary radius, droplets of a liquid in a surrounding fluid environment (gas, other immiscible liquid) are spherical to the atomic scale. In effect, the surface of a liquid in such conditions behaves like a membrane under stress, this is surface tension γ.

The physical origin of surface tension is the difference in molecular cohesion between the liquid and its surroundings, and a general rule is that it is proportional to the Van der Waals attractive forces between molecules of the liquid [6]. Despite this molecular origin, surface tension is a macroscopic quantity, and in that framework it can be seen as the amount of

energy needed to increase the surface of a liquid. It is expressed in $\mathrm{mN\,m^{-1}}$ and for water it is equal to $72\,\mathrm{mN\,m^{-1}}$, and can vary greatly between liquids. Interfacial tension is the same phenomenon but with a different immiscible medium, like another given liquid, and would be written γ_{AB} with A and B the media in question. In this way, surface tension is de facto the measure of the interfacial tension between air and the liquid in question at room temperature and pressure.

2.2 Wetting a solid surface

Wetting is a central question in a multitude of industrial processes in chemical engineering, for surface treatment of cars, to protect buildings from water etc... but also vital physical process in life sciences like the transport of sap in a tree through capillary forces. The foremost consideration is that of a droplet wetting a horizontal flat surface at equilibrium. In this case, there are two wetting regimes, schematised on Fig.1.2.

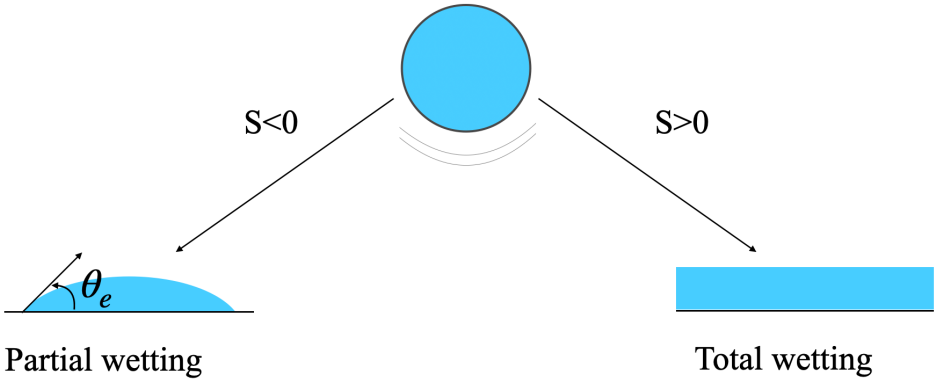

Figure 1.2: The two possibilities of wetting for a droplet deposited on a solid.

Each of these regimes is mathematically characterised by the spreading coefficient S, which is the change of interfacial energy between the dry solid E_{dry}^{solid} and the wetted solid E_{wet}^{solid}

$$S = E_{dry}^{solid} - E_{wet}^{solid} = \gamma_{SA} - (\gamma_{SL} + \gamma) \tag{1.6}$$

the three interfacial tensions are respectively solid-air, solid-liquid and surface tension of the liquid. We note that in the case of partial wetting ($S < 0$), a contact angle θ_e is apparent and in this case (equivalent to $S < 0$), Young's Law, obtained by force balance on the contact line, is applicable [7]:

$$cos(\theta_e) = \frac{\gamma_{SA} - \gamma_{SL}}{\gamma} \tag{1.7}$$

The interface is thus characterised by both the nature of the solid and the liquid. Nonetheless, looking at the orders of magnitude of γ (for most fluids below $75\,\mathrm{mN\,m^{-1}}$) and comparing it to γ_{SA} we can distinguish between high [9] or low energy surfaces [8]. This criteria is simply that if the free surface energy of the solid γ_{SA} is of the same order of magnitude that the liquid, i.e. up to $100\,\mathrm{mN\,m^{-1}}$, the solid is classed as being a low energy surface. On the

contrary, if it is above $\sim 500\,\mathrm{mN\,m^{-1}}$ to $5000\,\mathrm{mN\,m^{-1}}$, it is classed as a high surface energy. High (or low) energy surfaces are more (or less) likely to be totally (or partially) wetted.

3 On the rheology of fluids

Rheology is the study of flowing matter to extract applicable macroscopic properties [10]. In the context of Newtonian liquids, it is most notably concerned with viscosity. Classical rheology, built on the continuum hypothesis, traditionally assumes that a fluid is a homogeneous substance and that its properties are obtained regardless of surface. To measure these properties, one must generate a flow, which necessitates interaction with a solid boundary. The classical assumption in this context is the no-slip boundary condition [46, 13].

3.1 The no-slip boundary condition

Despite debate in the 19th century, the prevalent model is the no-slip boundary condition in which the liquid at the solid surface is bound (e.g. by Van der Waals forces, Hydrogen bonding or roughness). Considering incompressible fluid flowing described by (1.5) above a static solid boundary, the no-slip boundary condition reads:

$$\mathbf{v}(\mathbf{x}, t) = \mathbf{0} \qquad \text{at the interface} \tag{1.8}$$

The no-slip boundary condition is particularly applicable in the case of rough surfaces [46], which are much more common in nature. Modern research has shown that this condition is not a fundamental property of the interface, with hydrodynamic slips reported in the literature [47, 48, 49]. Nonetheless, the no-slip boundary has been widely accepted and proved for Newtonian fluids up to the nanometre scale using Surface Force Apparatus [50], where the atomically smooth mica (traditionally), silica or glass surfaces are used to measure Van der Waals forces of the interface over a wide range of wetting and flow conditions [13]. This has not only been verified for water and aqueous solutions [51], but for many others. This boundary condition is crucial to model how one generates a flow.

3.2 Maxwell's model: general visco-elastic model

Mechanically, solids are differentiated from other states of matter by their shear elastic properties. In this sense they react like springs, and their shear stress σ_s is proportional to the shear displacement ϵ_s, following Hooke's law, with G a shear stiffness:

$$\sigma_s = G\epsilon_s \tag{1.9}$$

Material of this nature stores energy during deformation and returns to its initial state. Newtonian liquids, however, follow Newton's law:

$$\sigma_s = \eta\dot{\epsilon_s} \tag{1.10}$$

In this case, all the deformation is dissipated by way of molecular fluctuations taken into account in the dynamic viscosity $\eta = \frac{\mu}{\rho}$. More complex liquids, named non-Newtonian, can

Figure 1.3: The Maxwell model is a Hookean denoted by k (spring) (we name it G in our case) and a viscous (Newtonian) dashpot in series [52]

deform in a visco-elastic process. The simplest of which is the Maxwell model, the schematic of which is in Fig. 1.3.

This leads to the following differential equation [12]:

$$\dot{\epsilon}_s = \frac{1}{G}\dot{\sigma}_s + \frac{1}{\eta}\sigma_s \tag{1.11}$$

This equation has a simple analytical solution in the case of constant η and G: $\sigma_s(t) = \sigma_0 e^{-t/\tau_m}$ with $\tau_m = \frac{\eta}{G}$ the Maxwell relaxation time. For classical liquids its order of magnitude is $10^{-9}\,\mathrm{s}$ to $10^{-12}\,\mathrm{s}$, making the Newtonian approximation of liquids very much sufficient for most deformations.

It is important to note that other models exist that will not be discussed here, such as Kelvin-Voigt [53], Oldroyd-B [54] for more complex material, and Rouse [55] and de Gennes [56] for dilute polymer solutions.

Nonetheless, this model has lead to the development of rheology and an established protocol: a sinusoidal (of frequency ω) shear strain ϵ_s is applied to a given liquid at a given scale, from which one can extract from the shear stress the frequency dependent *elastic modulus* G' and the *viscous modulus* G'' as a function of shear strain and frequency.

$$\sigma_s(t) = \epsilon_s[G' sin(\omega t) + G'' cos(\omega t)] \tag{1.12}$$

with

$$G' = G\frac{\omega^2\tau_m^2}{1+\omega^2\tau_m^2} \quad ; \quad G'' = G\frac{\omega\tau_m}{1+\omega^2\tau_m^2} \tag{1.13}$$

From equation (1.12) we can see that the in-phase (sin) response to a sinusoidal shear strain is a solid-like behaviour and a $\frac{\pi}{2}$ out of phase response (cos) is a liquid-like dissipative response. Alternatively, looking at the relative intensities of G' and G'' would also help distinguish the two regimes. When $G' >> G''$, the behaviour is solid-like, when $G' << G''$ the behaviour is that of a liquid. Both of these interpretations can be seen in figure 1.4.

Most rheological experiments consider a large sample of liquid, such that the continuum hypothesis is valid, and in those conditions the solid-liquid substrate wettability is not considered.

A crucial point of Maxwell's theory is that it introduces the Maxwell relaxation time. This simple framework highlights that the behaviour of a visco-elastic medium is inherently dependent on the frequency of the excitation, as per equation (1.13). As such, at higher and higher frequencies beyond τ_m^{-1}, an elastic behaviour is expected for all media. Conversely, at lower frequencies a viscous behaviour is expected. But what is the physical origin of this relaxation time? The first explanation comes by Frenkel in his kinetic theory of liquids [14].

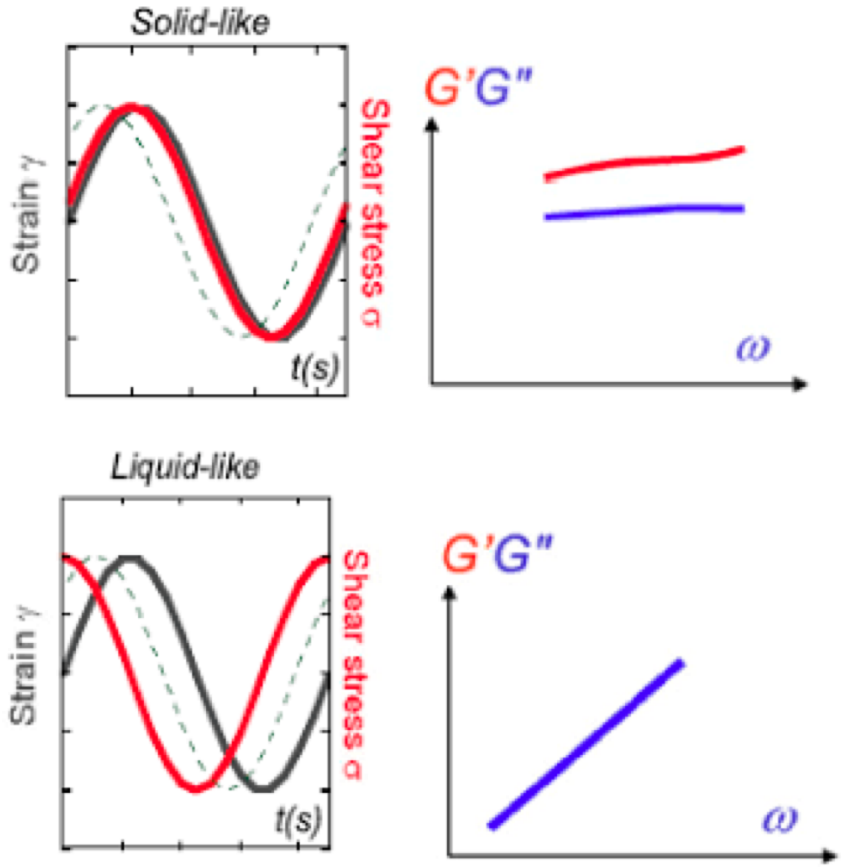

Figure 1.4: The general behaviour of a solid-like and therefore in phase (top) liquid-like and therefore with a $\frac{\pi}{2}$ out of phase wave response to a sinusoidal shear, from [20]

4 Molecular liquids

"*It has been said that there exists no general theory of liquids*" wrote Born and Green in 1946 [57], in one of their first paper on the Kinetic theory of liquids.

4.1 On the specific problem of liquids

Gases, solids and liquids are treated differently due to the varying nature of the intermolecular attractions in each state. The kinetic theory of gases, established by Maxwell [11] and later by Boltzmann [58], is based on the infrequent interactions between molecules. From there, a 'small parameter,' such as the ratio of molecular volume to total volume, allows for the use of perturbation theory to derive thermodynamic properties from statistical mechanics.

In solid crystals, constituent atoms are arranged in a fixed crystal lattice and undergo small oscillations around their equilibrium positions, defining a small repetitive parameter. The theoretical description of these systems and their thermodynamic quantities notably relies on the concept of phonons, the quantised vibrational modes of the crystal lattice [59, 60].

The liquid state presents a significant challenge to theoretical physics because it lacks

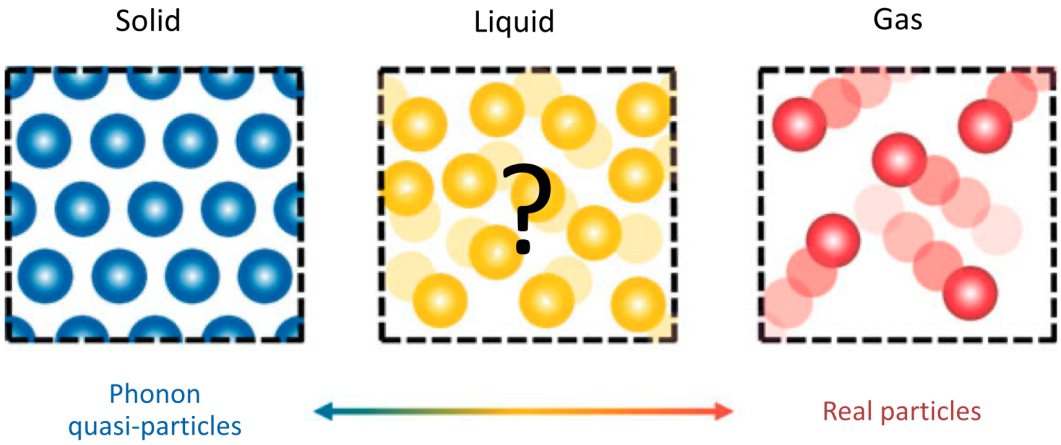

Figure 1.5: The solid state of matter where phonon vibrations carry heat (left), the gaseous state where heat is transferred through real particle collisions (right). Where do liquids (centre) fit ?, from [61]

a readily identifiable 'small parameter' that would simplify its treatment. The strong intermolecular forces, characteristic of solids, and the continuous, disordered motion of molecules, typical of gases, coexist in liquids [62]. Consequently, each liquid is often treated as a unique system. The distinct molecular arrangements of these three states of matter are schematically illustrated in Fig. 1.5

Throughout the first half of the 20th century, multiple attempts were made to establish a similar kinetic theory of liquids, Sommerfeld and later Brillouin tried by linking liquid vibrations to phonons, but to no avail [32].

4.2 Frenkel's theory

While solid crystals are clearly different in arrangement from liquids, solid glasses, however, are structurally very similar. The main macroscopic difference is that one can sustain shear stress (glass), while liquids cannot. Frenkel proposed this to be false, or rather a question of timescales: liquids can sustain shear waves only if they are on a sufficiently small time scale τ_F, that he physically explained to be the time needed for liquid particles or molecules to go from one equilibrium position to another. It is thus a structural relaxation time of a molecule in a given temporary equilibrium position. Its dependency on the temperature is expressed by the equation:

$$\tau_F = \tau_{0,F} e^{-W/kT} \tag{1.14}$$

with W the activation energy of the jump, k Boltzmann's constant and T temperature. By considering the flowing particle to be subject to a resistance akin to a Stokes flow, he managed to obtain the following relationship for the Maxwell relaxation time [14]:

$$\tau_M = \tau_F \frac{kT}{G\delta^3} \sim \tau_F \tag{1.15}$$

with G the shear modulus and δ the average distance between particles in a liquid. This

ratio represents the relative importance of thermal energy (kT) versus the elastic energy ($G\delta^3$) stored in a small volume. For simple liquids, this ratio is of order unity, hence $\tau_M \sim \tau_F$.

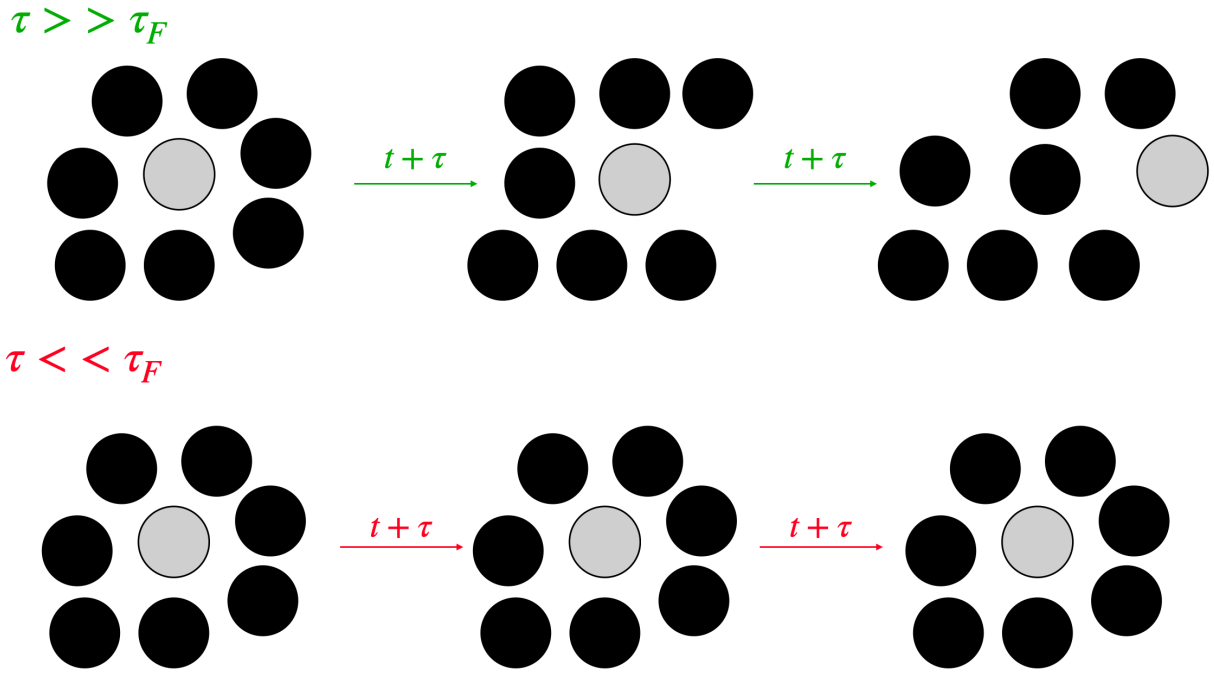

Figure 1.6: Illustration of the liquid state at different times. The grey particles are followed at each time jump τ, and can only jump from temporary equilibrium positions if $\tau >> \tau_F$ (upper part). If $\tau << \tau_F$ (lower part) , particles do not have time to jump and the state is fixed, thus able to carry shear elastic waves

This approach provides a molecular physical explanation to the Maxwell relaxation time, as well as a strong theoretical prediction: the existence of shear waves in liquids at high frequency, experimentally observed in glycerol [63] and other liquids [64, 65, 66].

5 Beyond Frenkel: low frequency shear elasticity

In both Frenkel's and Maxwell's understanding of liquids, they cannot exhibit low frequency shear elasticity as the solicitation is on a larger timescale than the relaxation time. However, a growing number of experimental results from polymer melts to defined simple liquids like liquid water exhibit a shear elastic behaviour, from the nanometre scale up to hundreds of micrometres.

5.1 At the nanometre scale

Mentioned in section 3.1, a common way to observe the response of liquids at smaller scales, up to the nanometre, is the surface force apparatus, in which a studied liquid is placed between two mica plates [13, 50]. It was later modified to carry dynamic measurements such as oscillatory shear at the nanoscale [51]. It was quickly observed that "Ultrathin films

of simple nonpolar molecular fluids (3–8 segmental dimensions thick) show a strikingly long relaxation time in response to oscillatory shear when confined between mica plates at $27\,^{\circ}\mathrm{C}$" [67]. This response was scale dependent and the transition from the solid-like behaviour to the viscous behaviour was continuous, indicating a glass-like transition [68]. By looking at the Density Of States (DOS) $g(\omega)$ scaling laws at small energy transfer ($\hbar\omega$), we see a continuous transition from the solid-liquid Debye scaling $g(\omega) \propto \omega^2$ to the liquid-like $g(\omega) \propto \omega$, seen in Fig. 1.7. The solid-like properties of liquid when confined at the nanoscale are therefore

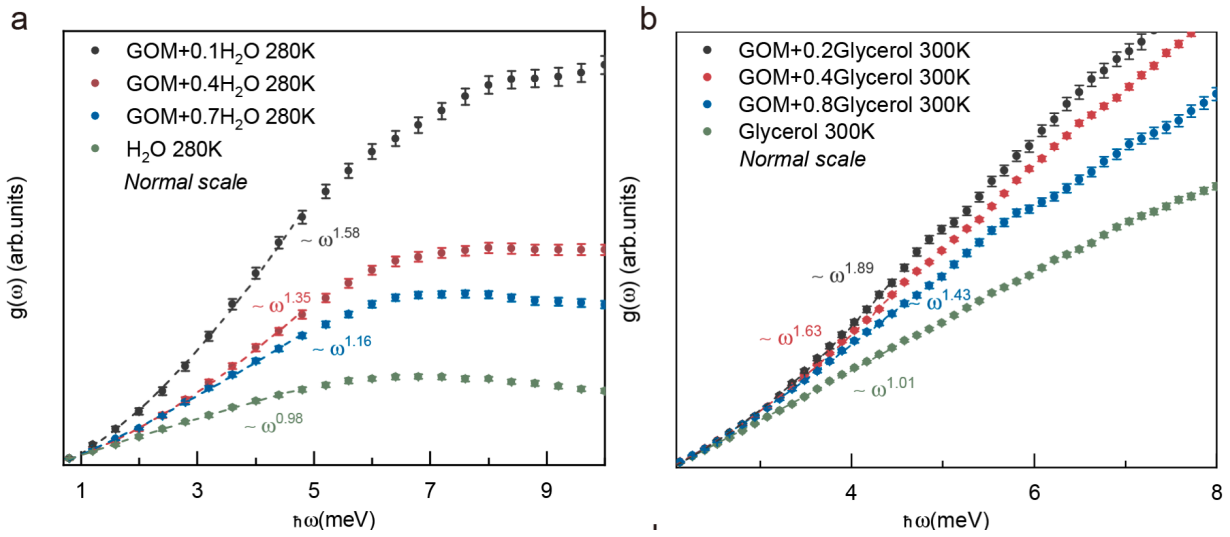

Figure 1.7: Experimental DOS by means of Neutron Scattering of: a) water at different hydration levels (gram of water/gram of GOM and b) glycerol analogous to water from [69]

The measured elastic shear response is proposed to be due to the slowing down of the dynamics of the liquid molecules because of the solid-liquid interactions at the walls [67, 68]. In the context of nanofluidics, molecular simulations have shown that the specific nature of the interface governs the hydrodynamic boundary condition [48, 49]. When either the scale is larger or the shear stress higher, confined liquids can go back to exhibiting their conventional viscous flow, depending on the nature of the interface.

5.2 At the micrometre scale

In parallel with experiments at the nanoscale, Derjaguin and his group performed resonant rheological measurements using a piezo-quartz at $73\,\mathrm{kHz}$ (thus far from the Frenkel timescale [16, 17], the experimental setup is visible in Fig. 1.8 a). Doing so, they used a highly wetting high energy quartz surface that needed proper cleaning (high temperature annealing). They performed experiments at the $1\,\mu\mathrm{m}$ to $5\,\mu\mathrm{m}$ scale on low-viscosity polymers [16] and small molecule liquids [17, 70]. In the case of diethylene glycol visible in Fig. 1.8 b), the decrease of liquid layer thickness entails an increase in identified shear elastic moduli. These experiments were performed in the kHz region, thus liquids can exhibit shear elastic behaviour far from the Frenkel/Maxwell relaxation time cut-off ($10^{-9}\,\mathrm{s}$ to $10^{-12}\,\mathrm{s}$), indicating a collective shear dynamic response of the liquid. While this response could be due to

long-chain entanglement in polymers, creating a rigid-type lattice, the case of small molecule liquids such as water, cannot be treated in the same way.

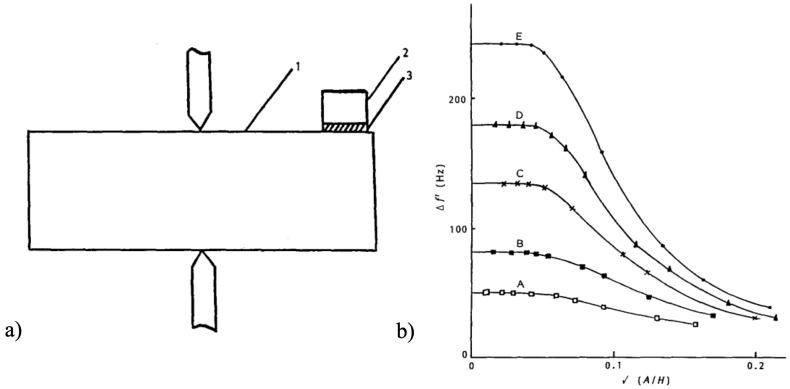

Figure 1.8: a) Experimental setup of resonant quartz measurements. 1) Piezo-quartz at $73\,\mathrm{kHz}$ 2) Plate 3) Studied liquid layer. b) Evolution of piezo-quartz frequency phase shift of the shear wave of diethylene glycol film at different thicknesses ($1\,\mu\mathrm{m}$ to $4\,\mu\mathrm{m}$ from top to down), from [16]

Following Derjaguin, Martinoty & al. found, at much lower frequencies, an elastic behaviour in the isotropic phase of liquid crystal polymers contained between glass surfaces [18]. The range of shear amplitudes was within $1\,$Å to $500\,$Å, and the range of liquid thickness was between $15\,\mu\mathrm{m}$ to $120\,\mu\mathrm{m}$. The results followed the same trend highlighted before: a gradual transition from viscous to elastic behaviour as the thickness is lowered from $120\,\mu\mathrm{m}$ to $15\,\mu\mathrm{m}$.

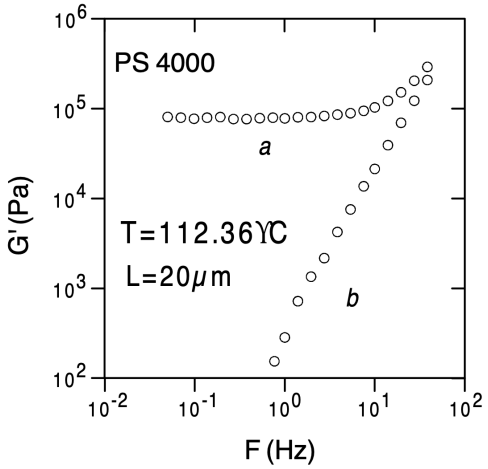

Figure 1.9: Shear elastic modulus G' of the molten polymer (PS) measured at $20\,\mu\mathrm{m}$ confinement versus frequency, depending on if the solid -liquid interaction is strong (a) or weak (b). from [23]

Perhaps of equal importance, they only observed this elastic behaviour when the glass surface on which the liquid lies has grooves perpendicular to the solicitations, i.e. the interaction with the solid surface is highly attractive, which they generalised between strong and

weak interaction [23], as visible in Fig. 1.9. Furthermore, Badmaev & al "obtain a monotonic correlation between the measured shear modulus of elasticity of the liquid and the magnitude of static friction surface" [71], confirming the importance of solid-liquid interaction to access liquid shear elasticity.

5.3 At larger scales

Using a conventional plate-plate rheometer but changing the surface to α-alumina in order to increase solid-liquid interaction by optimising the stress chain transmission system, L. Noirez and her team consistently observed shear elasticity at large scale ($\sim 100\,\mu\mathrm{m}$ to $1000\,\mu\mathrm{m}$). Liquids studied range from high viscosity polymer melts [21, 72] and liquid crystal polymer melts [19, 73] to glycerol [22], water [20] and others [37], visible in Fig. 1.10.

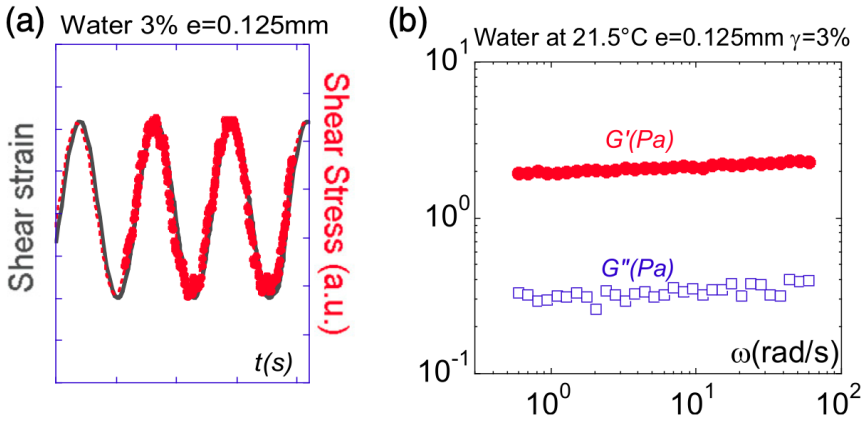

Figure 1.10: Imposed shear deformation (grey squares) and shear stress (red circles) measured on liquid water at low strain ($\epsilon_s = 3\,\%$) and at $\omega = 1\,\mathrm{rad\,s^{-1}}$. The continuous and dashed lines correspond to a sinus modelling of the input (-) and the output waves (- - - (red)). (b) Low strain frequency viscoelastic moduli of liquid water measured at room temperature ($21.5\,^{\circ}\mathrm{C}$), at $0.125\,\mathrm{mm}$ gap thickness and $\epsilon_s = 3\,\%$. The shear modulus G' (red circles) and viscous modulus G" (blue squares) from [20]

They showed that the elastic response of liquids is brittle and requires both small imposed shear strain rate and high solid-liquid interaction. It is of interest to note that the small shear strain condition was met by results discussed in the previous subsection 5.2. A shear elastic response is therefore only possible for liquids in the low frequency range, shown in Fig. 1.10 b), but at larger frequencies for a given strain, the classical viscoelastic response is observed. The transition between solid-like and liquid-like regimes is continuous. As such, the longest relaxation time of the liquid is not the Frenkel/Maxwell time scale corresponding to particle hopping from temporary equilibrium position to temporary equilibrium position, but a large scale elastic collective excitation throughout the liquid medium.

A further consideration is the solid-liquid interaction and its consequences on the liquid. The Maxwell model of viscoelasticity theoretically considers a no-slip boundary condition, but in cited experiments, as we draw closer to this ideal state by means of Van der Waals interaction or roughness, the liquid behaves elastically. It becomes then increasingly complicated

to distinguish between an intrinsic physical property and one indicative of a complex out of equilibrium thermodynamic state. Since recent experimental results of a laser-driven free surface flow on liquid glycerol have shown irregular elastic behaviour at timescales "much longer than the structural relaxation time" [74] without the presence of a highly wetting surface, it is the opinion of the author that shear elasticity is an intrinsic property of liquids, while it may be enhanced by solid-liquid interaction. Regardless, the Maxwell viscoelastic model and its associated Frenkel kinetic model cannot account for the large timescale elastic behaviour of liquids, far beyond the nanoscale.

5.4 Thermal response

At a thermal equilibrium, a liquid would have a macroscopically homogeneous temperature down to thermal fluctuations: a change of this temperature would be due to external fields only. As shear elasticity, present at large range of time and spatial scales, was not predicted by the classical viscoelastic model, one might ask whether the liquid also has a thermal response when shear strained, as would a solid [75]. This was the question that E. Kume investigated in his thesis [25]. Using multiple liquids, from PPG-40000 to glycerol, various shear strains ($0\,\%$ to $4000\,\%$), oscillatory frequency ($\omega = 0.5\,\mathrm{rad\,s^{-1}}$ to $5\,\mathrm{rad\,s^{-1}}$), and thicknesses ($100\,\mu\mathrm{m}$ to $500\,\mu\mathrm{m}$) were probed and the liquid temperature field was observed with an infrared camera using 2D thermal mapping [26, 34, 76, 27].

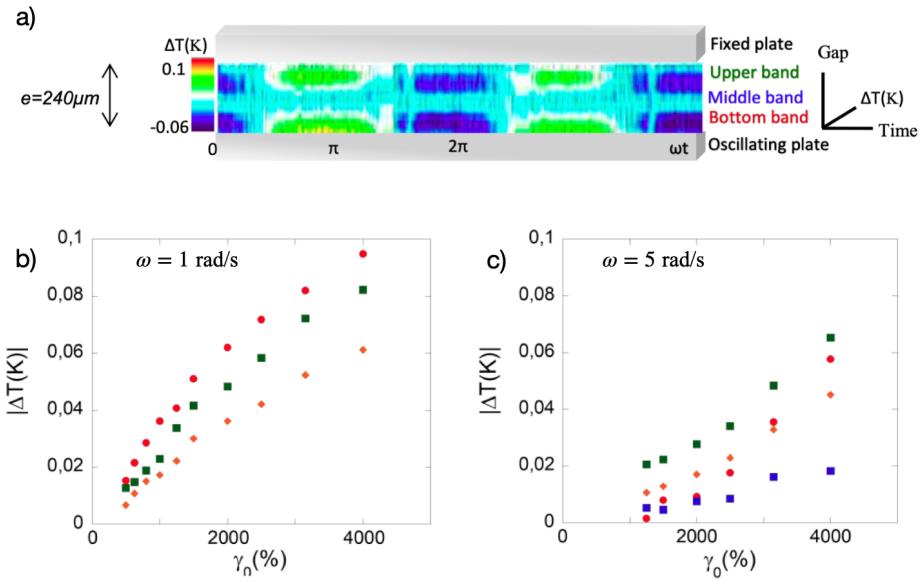

Figure 1.11: a) Micro-thermal mapping polypropylene glycol (PPG-4000) under $\omega = 0.5\,\mathrm{rad\,s^{-1}}$ oscillatory shear strain $\epsilon_s = 4000\,\%$ (room temperature measurements) at $0.240\,\mathrm{mm}$ gap thickness as function of time (679 frames) b) Strain dependence of the maximum of the temperature variation amplitude (from maximum to minimum temperature) $|\Delta T|$ as function of shear strain at $\omega = 1\,\mathrm{rad\,s^{-1}}$ for the bottom (red circle), middle (blue square), upper (green square) and total liquid volume (yellow diamond) c) same for $\omega = 5\,\mathrm{rad\,s^{-1}}$, from [25]

The results for PPG-4000 in Fig.1.11 show a couple key results:

- The presence of thermal bands in the liquid on a $\sim 10\,\mu\mathrm{m}$ scale. As infrared cameras observe the THz vibrational heat-carrying regime of matter, the observed changes in temperature are due to long range correlated interactions in the liquid matter. A further result of note from [25] is that the liquid thickness between two plates needs to be sufficiently small to observe the thermal bands, but once observable these are not scale dependent. This is indicative of a vibrational range of heat transfer from collective dynamics within the liquid.

- Shear rates where such thermal bands were visible were far beyond the elastic response of liquids discussed in the previous subsection, a regime where one would have assumed prior to carrying out these measurements that the classical thermal viscoelastic response would be visible. This indicates that even in the range of classical viscoelastics of the Frenkel-Maxwell type, highly correlated vibrational patterns can be observed in liquids by their thermal response.

Another interaction highlighting this complex thermodynamic state at the solid-liquid interface of wetting materials is at the quiescent state, where L. Noirez and her team observed a local cooling in the $\sim 10\,\mathrm{mm}$ range in a deionized liquid water bath with a solid plate at room temperature, itself placed in a box isolated from external thermal fluctuation, in darkness, to replicate conditions as close as possible to the equilibrium state [24]. The bath was left for several hours. Several solid surfaces were probed.

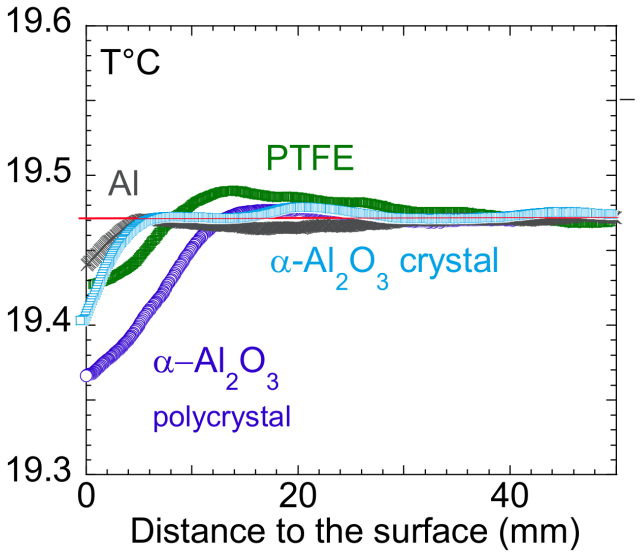

Figure 1.12: Average temperature profile from 10 measurements recorded at $\sim 15\,\mathrm{mm}$ from the air/liquid surface measured in liquid water as a function of the distance from the solid surface (temperature accuracy $\pm 5 \times 10^{-3}\,\mathrm{K}$). The red line is an eye guide of the asymptotic value of a classical Fourier exchange in such a setup, from [24]

While negligible in most cases, the surface dependent temperature effect visible in Fig. 1.12 is not present in general thermodynamic models of the interface and is another indication of liquid ability to convey, at large time and spatial scale, a complex state through collective vibrational dynamics.

From the nanoscale [67, 68] to large mm scale [24], as well as at the μm scale [17, 20, 34], experimental evidence with a wide range of techniques of complex momentum transport in classical liquids has accrued over the last 4 decades. This highlights the need for a novel theoretical understanding of momentum transport in liquids at the molecular scale, as well as new viscoelastic models to encapsulate and shed light on this growing literature on shear-elasticity and thermal effects.

6 Novel theoretical undertakings on liquids

6.1 The k-gap theory: beyond Frenkel

A continuation of the Frenkel theory was done independently of the growing literature on low-frequency elastic responses in liquid by Trachenko and his colleagues [29]. Two approaches they took were to either update the shear modulus in the equation of solids to allow for flow or by introducing the Frenkel timescale in the general Navier-Stokes equation (1.5). We will focus on the latter. Considering no external forces and a flowing liquid in a single direction by changing the viscosity to Maxwell-type viscoelastic term, they showed that the internal dynamics of liquids is governed by the "telegraph equation" [29, 32]. This differential equation, which is second-order in time and therefore permits wave-like solutions, gives us the following dispersion relation with c the shear wave velocity, k the wavevector in the reciprocal space and τ_F the Frenkel relaxation time:

$$\omega^2 + \omega\frac{i}{\tau_F} - c^2k^2 = 0 \tag{1.16}$$

Considering a complex ω and real k, corresponding to the decay in time, they obtained

$$\omega = -\frac{i}{2\tau_F} \pm \sqrt{c^2k^2 - \frac{1}{4\tau_F^2}} \tag{1.17}$$

We thus obtain a transverse wave that decays in a manner proportional to $e^{-\frac{t}{2\tau_F}}e^{i(kx-\omega_r t)}$ with

$$\omega_r = \sqrt{c^2k^2 - \frac{1}{4\tau_F^2}} \tag{1.18}$$

ω_r can only be real if the wavevector is above a critical value of $k_g = \frac{1}{2c\tau_F}$. This is a gapped momentum state. This gap in k-space is indicative of a finite propagation length in liquids, such that the propagation length of a shear wave d_{el} is

$$d_{el} = c\tau_F \tag{1.19}$$

This is not in opposition to Frenkel and does not explain the low frequency dynamics, but in this framework “a propagating wave does not require all particles it encounters during its propagation to be solid-like” [31].

6.2 k-gap and non-affine-lattice dynamics

Combining the insight of the k-gap theory with Non-Affine Lattice Dynamics (NALD), A. Zaccone and K. Trachenko proposed a theory to explain the puzzling low-frequency shear elasticity in confined system [77]. NALD is primarily used to study amorphous materials like melts or glasses [78, 79], but the studied object at the microscopic level can be extended to atoms so that simple liquids can be included.

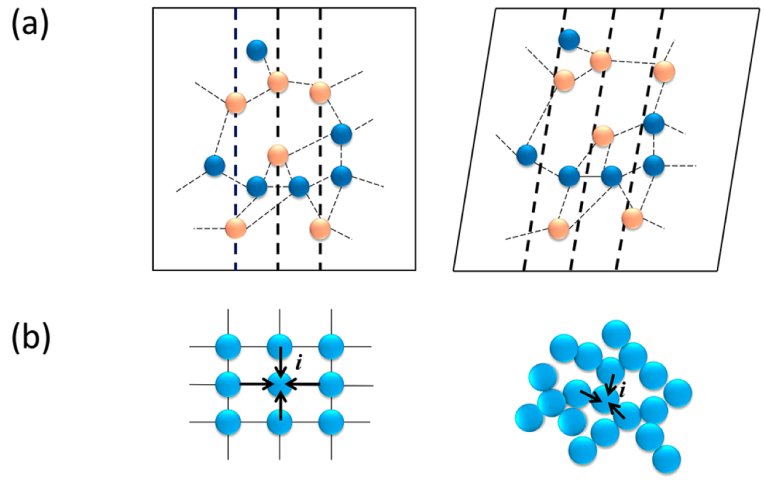

Figure 1.13: Non-affine displacement in amorphous materials, a) rearrangement of atoms on account of applied shear strain, b) Physical illustration contrasting an ordered crystal (left) where displacements are purely affine with an amorphous material (right) where the disordered structure gives rise to local, non-affine relaxations, from [33]

Each object is surrounded by neighbours at varying distances, as seen in Fig.1.13a), generating a non-affine force field on the object due to the lack of overt symmetry. The lattice relaxes to a new-temporary equilibrium (echoing Frenkel), resulting in a non-affine deformation in the material. The equation of motion of an object in such a medium is then derived, and taking into account the insights of the k-gap theory as well as making the assumption of transverse plane waves —a thorough theoretical framework can be found in [77]—, a confinement (L) dependent law for the shear elastic modulus is obtained

$$G'(L) = G_\infty - \frac{\alpha}{3}k_D^3 + \frac{\beta}{3}L^{-3} \tag{1.20}$$

with G_∞ the shear elastic modulus at high frequency, k_D the Debye wavevector, a concept borrowed from solid-state physics where it represents the maximum wavevector in a solid's vibrational spectrum, and L the size of confinement. α and β are numerical constants. $-\frac{\alpha}{3}k_D^3$ captures short-range solid-like properties and is negative, it is the non-affine contribution of the bulk material while $\frac{\beta}{3}L^{-3}$ is the solidifying effect due to confinement. If zero elasticity is observed at large scales ($L \to \infty$), then the first two terms cancel each other out and we obtain the final scale law

$$G' \propto L^{-3} \tag{1.21}$$

This simple final universal scaling law has been incredibly accurate at explaining the confinement-dependent behaviour of the shear elasticity of liquids, and an example of its accuracy can be observed in Fig. 1.14

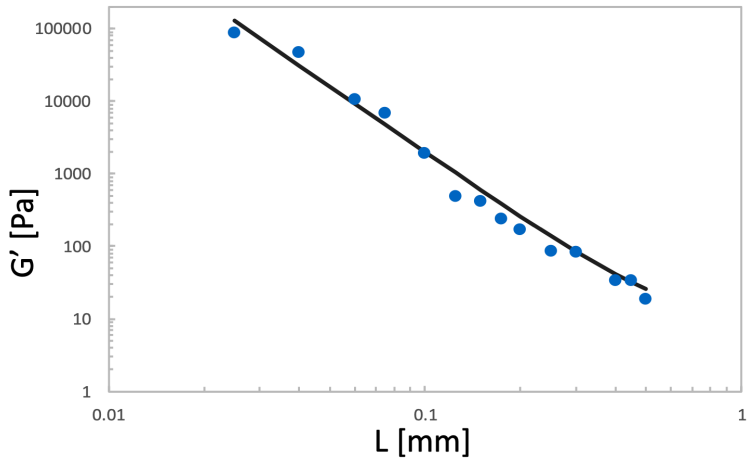

Figure 1.14: Universal $G' \propto L^{-3}$ law in black for experimental results in blue dots of a polymer melt from [37], picture from [77]

While very accurate, this is a phenomenological model, and as it is presented here, it does not provide a fundamental explanation for the observed elastic behaviour. This first-principles understanding is precisely what Baggioli & al proposed with their unified theory based on Goldstone modes [80]. Goldstone modes are bosons that appear when symmetries are broken, and acoustic phonons are such by nature [81]. The authors provide a first-principle derivation of the k-gap phenomenon by means of symmetry breaking analysis and phase relaxations. In essence, they propose that the Goldstone bosons have a finite propagation length (thus in accordance with k-gap theory) by means of a phase relaxation rate Ω such that the decay will be $\sim e^{-\Omega t}$. Non-zero in liquids, this phase relaxation is null in solids and the authors suggest that the crystal to glass to liquid transitions are continuous by means of increase of the phase relaxation rate of the bosons. When this relaxation rate becomes critical, one recovers the behaviour of gases.

6.3 Other models

We briefly outline two other models that have yielded accurate predictions and explanations of different experimental results.

6.3.1 The dual-model

The Dual-Model is a dynamic approach to liquid modelling proposed by F. Peluso [82, 83, 84, 85]. Similarly to the k-gap discussed above, it considers liquids as being a superposition of two states, but in this model, these are "liquid particles" and "lattice particles". "Liquid particles" are mesoscopic-scale, short-lived, quasi-solid structures that disperse throughout the fluid. "Lattice particles" are a population of elastic waves that propagate through the medium and carry both elastic and thermal energy, akin to phonons in solids. This model has given two strong interpretations:

- The interaction between the "liquid particles" and the "lattice particles" is modelled as an inelastic process, allowing for exchange of both energy and momentum between systems.
- Propagation of energy in the Dual Model is therefore not a purely diffusive process but instead operates through wave-packets. This results in a finite propagation velocity for both heat and elastic waves.

This model has been able to predict the finite length and intensity of the thermal shear bands observed by E.Kume [25] discussed in section 5.4 [86].

Finally, the Dual-Model also predicts a k-gap in momentum space [83]. This independent prediction reinforces the idea that the existence of a gapped momentum state is a fundamental and universal property of the liquid state.

6.3.2 General viscoelastic model on elastic modes

In contrast to Trachenko and others, F. Volino & al propose a completely different modelling of the liquid that does not start from the Navier-Stokes equation [87, 88, 89, 90, 91]. Instead of using the conservation laws of continuum mechanics (mass and momentum), this model begins from a microscopic, energy-based approach by considering a collection of N molecules that vibrate and rotate around their equilibrium positions. When put out of equilibrium by external actions, these actions have a direct impact on the thermal fluctuations of the objects, increasing their internal energy which can lead to a dynamic phase transition. eThe key concept here is that liquids at rest intrinsically possess a shear elasticity and lose it as external action (mechanical or thermal) induce a dynamic phase transition towards a viscous state. As such, experiments where the liquid is either confined [17] or excited by low-strain, such as [20, 21, 72] necessarily exhibit shear elasticity.

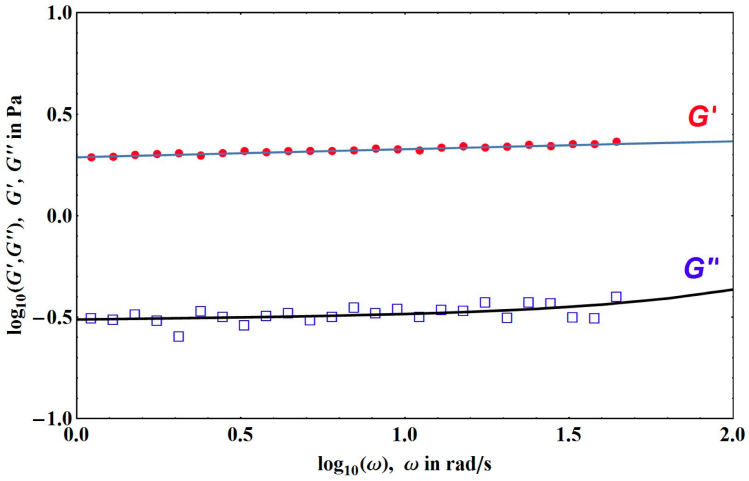

Figure 1.15: Logarithmic plot of G' and G''. Experimental data (red points and open blue squares) of a water layer of $\sim 100\,\mu\mathrm{m}$ thickness, are from [20], the black and blue lines are the theoretical predictions of the elastic-mode theory, picture from [28]

This model has yielded very accurate predictions for the value of shear elasticity in water,

as observed in Fig.1.15, but also relative to dynamic viscosity and self-diffusion coefficient for all fluid phases of water [91].

7 A Synthesis of observations and motivations

Historically, fluid mechanics, built on the continuum hypothesis and encapsulated by the Navier-Stokes equation (1.5), successfully described macroscopic flows. Concepts like surface tension and Young's Law allow us to distinguish between hydrophilic and hydrophobic solid-liquid interactions. Maxwell's viscoelastic model and its associated critical relaxation time from (1.11) is ubiquitous in rheological measurements, and Frenkel [14] proposed a molecular physical explanation for this relaxation time for simple liquids. This dominant model predicts liquids as predominantly viscous, with accepted shear elastic behaviour at very high frequencies only.

However, in recent decades, experimental results have shown that all types of confined liquids exhibit low-frequency shear elastic behaviour, from the nanoscale to the $\sim 100\,\mu\mathrm{m}$ scale. Beyond the mechanical response, thermal bands have been identified [25, 86]. This has led to multiple new theoretical frameworks, some building upon Frenkel and his understanding, such as the k-gap model by Trachenko & al [31, 32], and others like the Dual model by F. Peluso & al [82] or the novel viscoelastic model by F. Volino & al [91] from a different point of view. Each has been able to predict some of the aforementioned experimental results [33, 86, 28].

Although the solid-liquid interface has been highlighted as crucial for observing low-frequency elasticity and associated thermal bands in liquids [18, 71, 22], one of the missing perspectives in the current literature is the detailed coupling between the solid and liquid in the THz regime. As previously discussed, experimental and subsequent theoretical results show large-scale collective phonon-like dynamics within liquids at such interfaces. Since at these interfaces, the liquid atoms/ions are bound to the solid, with a liquid able to exhibit shear elasticity, one can wonder how these interactions influence the dynamics of the solid itself. This is the central subject of study of this thesis.

Chapter 2

H_2O, D_2O and α-Al_2O_3

In this chapter, we will first discuss the particular natures of the studied liquids, H_2O and D_2O, followed by the studied solid α-Al_2O_3 at ambient temperature and pressure. The chapter ends with an overview of the relevant literature on the interface with α-Al_2O_3 surfaces and water.

Contents

1 Liquid Water

In chapter 1 we showed that a wide range of liquids exhibit mesoscopic low-frequency shear elasticity when confined, and localised thermal waves were observed [26]. One of those liquids is water [20, 25]. Water is present at all scales of the life cycle on earth [92] and maybe beyond, being a key object of study for astronomical purposes due to its ever-more complex phase-diagram [93, 94]. The present section will only deal with the structural and dynamic properties of water at room temperature and pressure. More thorough works can be found in [95, 96, 39].

1.1 Structural properties at room temperature and pressure

Water, H_2O, is a polar molecule composed of a central oxygen atom with two covalently bonded hydrogen atoms. The complexity of water arises due to its hydrogen bond (H-bond) network, a direct consequence of its polar intramolecular geometry, seen in Fig. 2.1a). This allows its molecules to act as hydrogen donors or hydrogen receptors via the lone pair of electrons associated with the O atom. At room temperature, each water molecule, thus, interacts with up to 4 H-bonds with its neighbours, creating a 3D transient local nanometre structure [97], breaking and creating H-bonds at a timescale of $\sim 10^{-12}\,\mathrm{s}$ [15] (similar to the Frenkel timescale for water). This constant state of flux is often described as a "flickering cluster" model, where small, "ice-like" regions (where each water molecule has 4 H-bonds) form, rearrange, and dissolve, only to reassemble elsewhere [98]. It was later found that water at wide ranges of its phase diagram exhibits a bimodal structural distribution corresponding to distinct phases. As such, the dual nature of water has been a subject of intense discussion for the past three decades [99, 100, 96, 101].

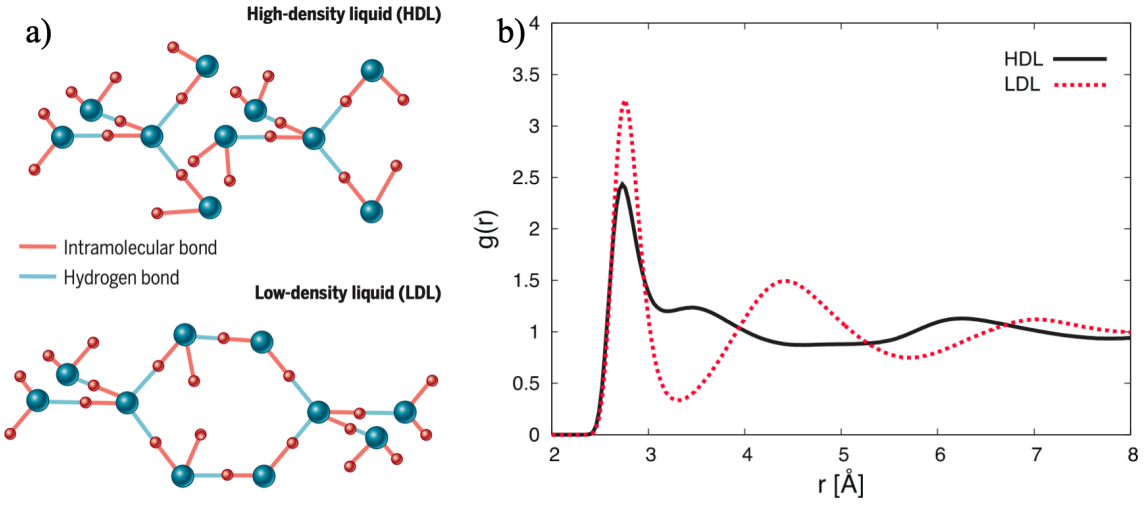

Figure 2.1: a) representation of High-Density Liquid (HDL) and Low-Density Liquid (LDL) water structure from [102], b) O-O radial distribution function for HDL and LDL, from [103] and data from [104]

Using neutron and X-ray scattering of water over a wide range of pressures [104, 95] the

two structural states of ambient liquid water were identified as Low-Density Liquid (LDL) and High-Density Liquid (HDL). LDL is a tetrahedrally bonded open structure, closer to the arrangement of molecules in ice. HDL, on the other hand, is a more disordered, non-tetrahedral, and compact structure where molecules are more closely packed. It has a higher density due to the breakdown of the hydrogen-bond network, allowing molecules to move into the gaps. Both are visible in Fig.2.1 a). At other positions in its phase diagram, water is known to exhibit a bimodal structural distribution in the form of HDA and LDA (A stands for Amorphous ice) [105, 106], allowing a parallel to be drawn [107]. HDL and LDL have distinct O-O radial distribution functions —which quantifies the probability of finding an atom at a specific distance, r, from a reference atom—, as per Fig.2.1 b). Nilsson & al identified through molecular dynamics force-field simulations that water at ambient conditions exhibits this bimodal behaviour, with $\sim 25\,\%$ of water being LDL and the rest HDL [108, 103]. Various anomalous phenomena of water are argued to be a consequence of the interplay between HDL and LDL [109].

1.2 Dynamic properties

Starting from a single molecule, water *intramolecular* dynamics —dynamics of internal bond lengths— consist of three main modes: a bending mode, a symmetric and an asymmetric stretch. In the gaseous state, they are clear and well defined, but in the liquid state the surrounding molecules widen and 'red-shift' the peaks associated with each mode, such that both stretching modes are hard to separate [110]. Nonetheless, the bending and stretching modes are visible at $\sim 200\,\mathrm{meV}$ and $\sim 400\,\mathrm{meV}$ respectively for water in ambient conditions [111].

In its liquid phase, the constant "flickering" between HDL and LDL states at the picosecond discussed in the previous subsection leads to complex vibrational dynamics through what is called the Hydrogen-bond (H-bond) network. These are the *intermolecular* dynamics, and they are coupled with the intramolecular dynamics [112]. The H-bond bending mode is visible at $6\,\mathrm{meV}$ with a broad peak [113], and further, between $20\,\mathrm{meV}$ to $35\,\mathrm{meV}$, a broad band corresponding to H-bond stretching arises [114, 95, 115]. For completeness, another intermolecular mode, librational modes (rotation of molecules around themselves without changes in bond lengths) at around $60\,\mathrm{meV}$ is also present [111].

As each peak is observed, corresponding to intra or inter molecular dynamics, one may wonder how they propagate throughout the water. These are the 'phonon-like' *collective* dynamics. For example, Elton & al have observed a longitudinal-transverse optic phonon splitting, and by analogy to Ice XI "believe both modes likely consist of coupled wagging and rocking librations" [116].

Anomalous collective phenomena are also present in water. For example, 'fast-sound' is the phenomenon observed by which the speed of sound of water goes from the accepted value of $\sim 1500\,\mathrm{m\,s^{-1}}$ at large distances ($Q < 0.003\,\mathrm{\AA}^{-1}$) to, in an intermediary distance ($0.4\,\mathrm{\AA}^{-1} < Q < 1.4\,\mathrm{\AA}^{-1}$) where it is of $\sim 3300\,\mathrm{m\,s^{-1}}$ [117], equivalent to the speed of sound in ice Ih [95].

Furthermore, it is of interest to note that "it is possible to derive a characteristic time scale where the density fluctuations change from the macroscopic to a solid-like elastic behaviour" [118], i.e a Frenkel timescale. Beyond the study of bulk water, the intermolecular dynamics due to the H-bond network vary due to confinement and close to surfaces [119, 120].

1.3 Replacing light water with heavy water: an isotopic effect

When hydrogen atoms (^1H) are replaced with their heavier isotope, deuterium (^2H or D) we obtain heavy water (D_2O), see Fig 2.2a). While very similar to water by its chemical formula and structure, there are subtle differences between H_2O and D_2O: an isotopic effect. The reason to replace H with D is also practical and intimately linked to neutron spectroscopy: H and D have significantly different incoherent scattering [121], making neutron experiments of aqueous solutions significantly easier with D_2O, and the differences between the two have often been wrongly ignored [122].

The isotopic effect, and its associated quantum effects, are a direct consequence of the doubling of the mass between H and D, by way of changing the reduced mass —the inertial centre of the H_2O or D_2O molecule. With a lower reduced mass, D_2O has a more stable structure by way of a stronger H-bond (despite competing effects between O-O distance and bond angle) [122, 123]. This leads to a sharper and slightly different O-O radial distribution function, seen in Fig.2.2b), indicating an increase in hydrogen-bonds per water molecule [124], i.e., a more pronounced "ice-like" structure in D_2O [124, 123, 39].

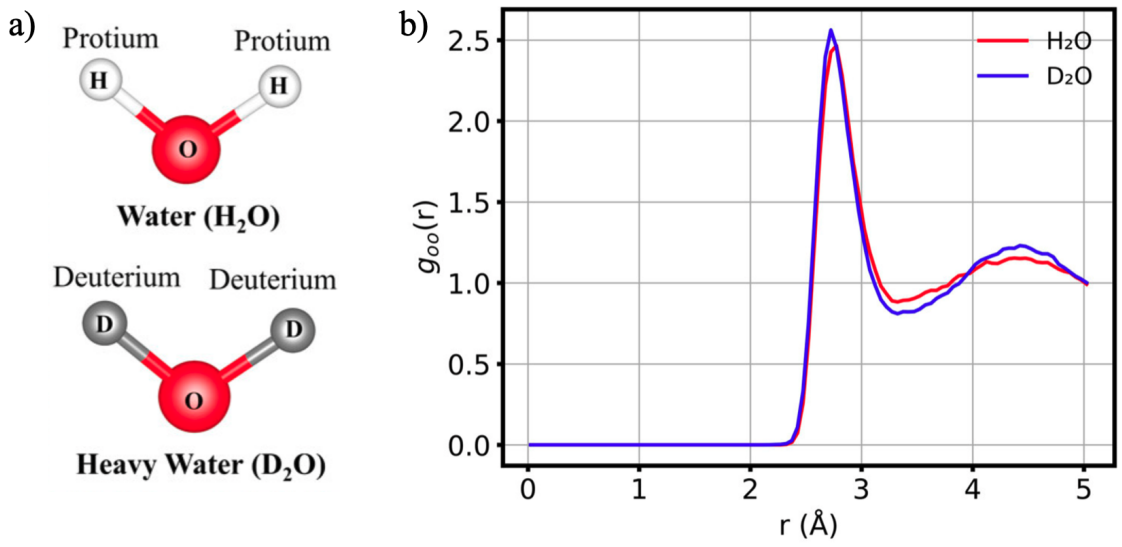

Figure 2.2: a) representation of H_2O and D_2O b) O-O radial distribution function for H_2O and D_2O using ab initio PIMD simulations, both from [125]

This isotopic effect extends beyond static structure to the dynamic properties of D_2O, including both individual vibrations and collective excitations. Indeed, the intramolecular dynamics of heavy water are 'red-shifted' (reduced frequency/energy) as a consequence of the reduced mass, leading to bending and stretching modes of $\sim 150\,\mathrm{meV}$ and $\sim 290\,\mathrm{meV}$

respectively, compared to the $\sim 200\,\mathrm{meV}$ and $\sim 400\,\mathrm{meV}$ for H_2O. This ratio is a direct consequence of the $\sqrt{\frac{m_H}{m_D}} = 0.707$ ratio, suggesting these effects mostly arise from pure ballistic motion of the H and D molecules [123], but more subtle and complex behaviour is observed [126].

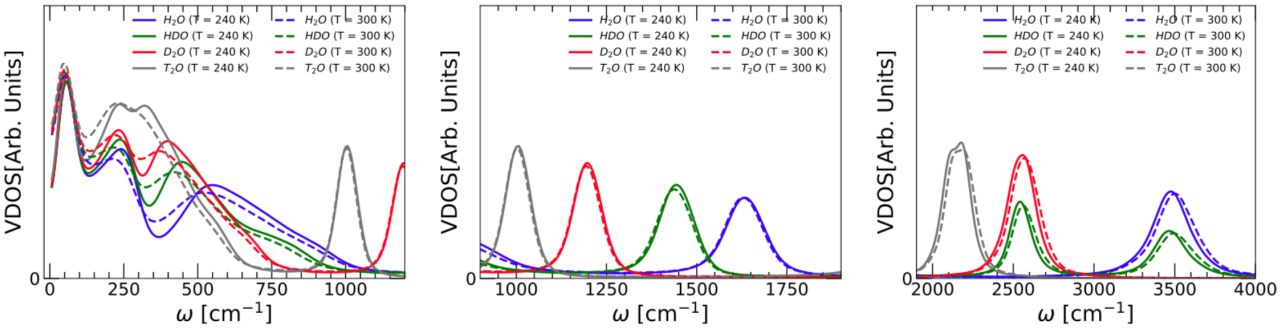

Figure 2.3: VDOS for H_2O (blue), HDO (green) , D_2O (red) , and T_2O (grey) from RPMD simulations at $T = 240\,\mathrm{K}$ (solid lines) and $T = 300\,\mathrm{K}$ (dashed lines). $1\,\mathrm{meV} \approx 8.1\,\mathrm{cm}^{-1}$. The left is the translational/librational intermolecular modes. The intramolecular bending modes and stretching are shown on the left and right figure respectively. Figures from [39]

Furthermore, we see a direct pathway of red-shifting by increasing molecular H-bond strength — from $H_2O \rightarrow HDO \rightarrow D_2O \rightarrow T_2O$— on all intra and intermolecular modes, as seen in Fig.2.3 left.

This change at the molecular vibrational level also has consequences for large scale transport and collective dynamics [127]. Indeed, the speed of sound in heavy water is lower than its regular counterpart ($\sim 1400\,\mathrm{m\,s^{-1}}$ against $\sim 1500\,\mathrm{m\,s^{-1}}$) [128]. This is in accordance with sound being a density fluctuation wave, therefore the movement of the whole molecule, and the ballistic correction because of increased inertia is due to whole molecule ratio $\sqrt{\frac{m_{H_2O}}{m_{D_2O}}} = 0.95$. Similar results are visible for the 'fast-sound' of heavy water, first observed in [41], such that "it is then possible to conclude that this excitation involves the centre of mass of the whole molecule, and it is not limited predominantly to the motion of the lighter hydrogen atoms" [40].

To conclude, while structure and dynamics are altered when changing from water to heavy water, they exhibit the same behaviour ("flickering" type clusters, fast-sound etc...), but with slight changes, owing to molecular mass changes and nuclear quantum effects [123].

Finally, our study on surface wetted bulk α-Al_2O_3 will be up to $\sim 35\,\mathrm{meV}$, such that direct interaction between the solid vibrations and the intramolecular vibrations are unlikely.

2 α-Al_2O_3: a well-known crystal

As highlighted in the previous chapter 1, highly wetting surfaces were needed to observe mesoscopic low-frequency shear elasticity in confined liquids. One of these surfaces identi-

fied by L. Noirez and her group was α-Al_2O_3 polycrystal in the form of ceramics [26, 20, 24]. Figure 1.12 shows that both the polycrystal and monocrystal α-Al_2O_3 induce a complex thermodynamic state in a quiescent bath. Our study beyond the wetted interface into the solid bulk at its THz vibrational states was performed using monocrystalline α-Al_2O_3 due to its single, well-defined lattice structure. Al_2O_3 is historically known as sapphire and is a key material in watchmaking, notably for its water resistance [129], engineering for growing crystals [130] and even medicine for implants [131]. There are multiple phases of Al_2O_3, but the one of interest in this thesis is the corundum phase α-Al_2O_3, most common in nature. α-Al_2O_3 is the hardest of all oxide crystals, and highly resistant to chemical attack [129].

2.1 α-Al_2O_3 Crystal growth: a primer

The crystals used for this study were purchased from Neyco manufacturer [132]. They were grown using the Kyropoulos method, which was proposed in 1926 by Spyro Kyropoulos [133] to grow larger crystals compared to the previously developed Verneuil and Czochralski methods [134, 135].

The raw high-purity ($99.999\,\%$) alumina powder is heated to a temperature above its $2054\,^{\circ}\mathrm{C}$ melting point in a crucible. A small oriented "seed crystal" (a template of sorts) from which the growth will take place is lowered and dipped into the top of the molten material. The furnace temperature is then precisely reduced, such that the melt begins to solidify onto the seed. The crystal grows downwards and radially from the seed. The growth interface remains submerged in the molten liquid, minimising internal stress. Once the entire crucible's contents have crystallised, the large single-crystal is slowly cooled to room temperature to minimise thermal stress and prevent cracking. The resulting crystal is then cut following crystallographic planes using diamond saws, polished, and then annealed at $1800\,^{\circ}\mathrm{C}$ for 24 hours to reduce internal stress. It is then cooled down to room temperature [136].

2.2 Structure

The α-Al_2O_3 structure is based on a hexagonal close-packed arrangement of oxygen ions O^{2-}. Within this arrangement, the aluminium ions Al^{3+} occupy two-thirds of the octahedral interstitial sites. The Al ions are thus octahedrally coordinated by six O ions. α-Al_2O_3 belongs to the space group $R\bar{3}c$ [137], which can be expressed in both hexagonal and rhombohedral structure coordinates [138], a common feature of rhombohedral lattices. The primitive rhombohedral cell is the smallest repeating unit that generates the entire lattice [139]. It contains two formula units, or 10 atoms (4 Al and 6 O) per cell. This is the unit cell used to define the first Brillouin Zone [140]. The larger hexagonal cell (three times the volume of the primitive cell) is used for convenience as its axes are orthogonal to the a and b directions (see Fig. 2.4a)). It contains 30 atoms (12 Al and 18 O).

The previously mentioned AlO_6 octahedral structures are connected by sharing edges and are stacked along the c-axis by sharing a face with another. This is typical of corundum structures and is a key reason behind their highly sought mechanical properties.

With a high dielectric constant and a large electronic band gap, α-Al_2O_3 is an exceptional electrical insulator, a property complemented by its high thermal conductivity which allows it to efficiently dissipate heat without conducting electricity. All relevant information for

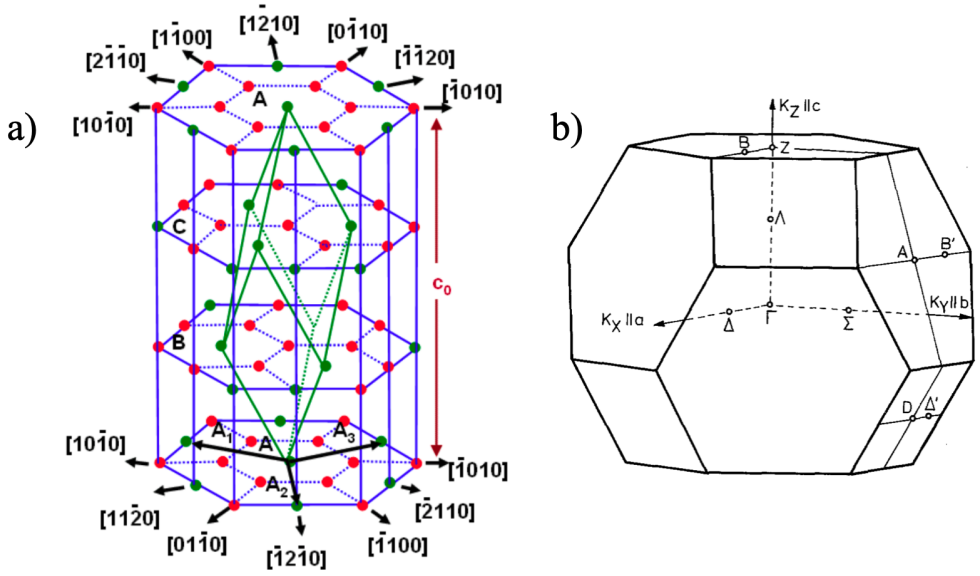

Figure 2.4: a) α-Al_2O_3 crystal structure in hexagonal coordinates, green points represent the aluminium atoms, while red points the oxygen ones, from [141], note that the structure has twice the length in the c-axis, b) α-Al_2O_3 first Brillouin Zone from [142]

our study on the structural, mechanical and chemical properties of α-Al_2O_3 can be found in Tab.2.1 and Tab.2.2.

Parameter	**Value**
Lattice (Conventional)	
Lengths (a, b, c)	4.77 Å, 4.77 Å and 13.04 Å
Angles (α, β, γ)	90.00°, 90.00° and 120.00°
Volume	262.26 $Å^3$
Symmetry	
Crystal System	Trigonal
Lattice System	
Hall Number	-R 3 2"c
International Number	167
Symbol	$R\bar{3}c$
Point Group	$\bar{3}m$

Table 2.1: Crystal Structure for α-Al_2O_3, data from [137, 132]

The primitive cell is a rhombohedral structure, and the resulting first Brillouin Zone of this space group can be seen in Fig.2.5. Its reflection conditions —rules that predict which crystallographic planes, identified by their Miller indices (hkl) (see Appendix **??**), will produce a detectable diffraction Bragg peak— are the following [138]:

- General condition of rhombohedral lattice: $-h + k + l = 3n$ with n an integer.

Parameter	Value
Chemical Properties	
Melting Point	$2054\,^{\circ}\mathrm{C}$
Solubility	Insoluble in water and most organic solvents
Chemical Resistance	Highly resistant to chemical attack (amphoteric)
Mechanical Properties	
Mohs Hardness	9
Density	$3.987\,\mathrm{g\,cm^{-3}}$
Young's Modulus	$393\,\mathrm{GPa}$
Compressive Strength	$2100\,\mathrm{MPa}$ to $2600\,\mathrm{MPa}$
Physical Properties	
Dielectric Constant	9.0 to 10.1
Thermal Conductivity	$30\,\mathrm{W\,m^{-1}\,K^{-1}}$
Coefficient of Thermal Expansion	$8.1 \times 10^{-6}\,^{\circ}\mathrm{C}^{-1}$

Table 2.2: Chemical and mechanical parameters for α-Al_2O_3, data from [137, 132]

- Symmetry conditions. In the $(00l)$, $(h0l)$ and $(0kl)$ planes l must be even.

Both conditions need to be satisfied for a reflection to be valid.

2.3 Phonon dispersion

As α-Al_2O_3 exhibits a well defined periodic structure, as discussed previously and seen in Fig.2.4 a). The atoms are stable in their positions, but oscillate around them, and in doing so the vibrational modes are transferred from neighbour to neighbour. The quantized collective vibrations are called phonons (of energy $E = \hbar\omega$), and can be treated as propagating waves, sound or otherwise, in the material [143].

The relationship between the phonon frequency (ω) or energy ($E = \hbar\omega$) and the wave vector (k) is known as the phonon dispersion curve. This curve provides a complete picture of the crystal's vibrational properties. Since the primitive rhombohedral cell of α-Al_2O_3 contains $N = 10$ atoms, there are a total of $3N = 30$ vibrational modes. These modes are divided into three acoustic branches and 27 optical branches.

Acoustic branches are long-wavelength, in-phase vibrations of the unit cell, which propagate as sound waves through the crystal. Their frequency approaches zero as the wave vector approaches the Brillouin zone centre (Γ) as acoustic phonons are Goldstone modes [81, 80]. These are the branches studied in this thesis. The optical branches correspond to out-of-phase vibrations of the atoms within the unit cell. They have finite frequencies at the Γ point, and can be excited by light ("optical") [144]. All these branches for α-Al_2O_3 at room temperature and pressure are seen in Fig. 2.5.

The first Brillouin Zone of α-Al_2O_3 is a truncated octahedron, see Fig.2.4. For the calculation of (as seen in Fig. 2.5), or for the observation of, the phonon dispersion curves and lattice dynamics [145, 146], it is essential to consider the high-symmetry points and lines within this zone.

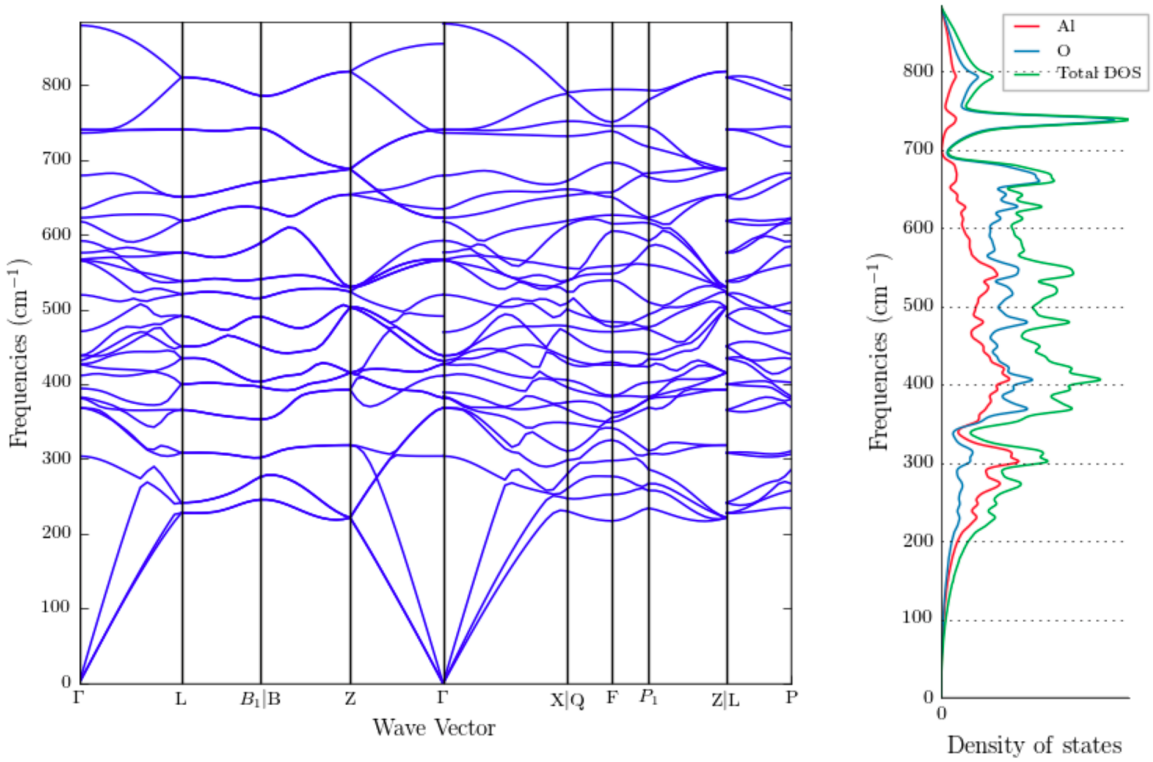

Figure 2.5: Phonon dispersion within the first Brillouin Zone, $8.1\,\mathrm{cm}^{-1} = 1\,\mathrm{meV}$ (left) and density of state (right) of α-Al_2O_3, from [137] and method from [147]

The symmetries of the crystal give rise to degeneracies in the phonon branches at high-symmetry points such as Γ and others, shown in Fig.2.4b) and Fig. 2.5. In practice, our study will focus on the Γ-Z direction, the main crystallographic c-axis of the hexagonal cell, allowing us to investigate vibrational modes propagating along a specific major crystal direction.

3 α-$Al_2O_3(0001)$ surfaces and water

As a result of the growth process described in section 2.1 and the (0001) orientation of the α-Al_2O_3 seed crystal, the surface termination that will arise after the annealing is α-$Al_2O_3(0001)$ [132].

3.1 A wetting interface: macroscopic point of view

α-$Al_2O_3(0001)$ is a highly wetting surface with a contact angle lower than $5°$ [36] (visible in Fig.2.6), classifying it in the super hydrophilic category [148]. It therefore satisfies the adherence conditions so that a confined liquid between two of its plates would exhibit low-frequency shear elasticity [37, 71], as discussed in section 5.2.

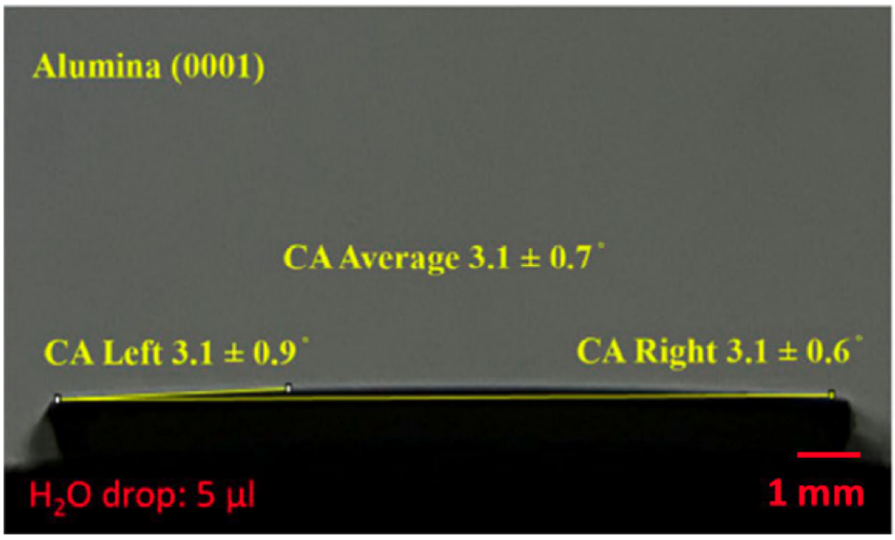

Figure 2.6: Contact angle of a $5\,\mu$L deionised droplet deposited on a $Al_2O_3(0001)$ surface, from [36]

The wetting of the surface is very quick, indeed nanometre scale droplets were simulated to spread in less than $3\,\mathrm{ns}$ [36], resulting in a $0°$ contact angle at that scale, whereas the macroscopic contact angle visible in Fig.2.6 is at the edge of the crystal.

3.2 The interface at the molecular scale

Multiple terminations of the α-$Al_2O_3(0001)$ are possible, ending with a single Al layer (Al-I termination), Oxygen layer (O or OH termination), or a double Al layer (Al-II termination). The latter is not present at room temperature or pressure [149]. In a vacuum Al-I termination is most probable [150], but the high energy of the free Al-I surface means that in the presence of oxygen from the air, a binding will take place, such that certain reports indicate a 2:1 ratio of Al-I to OH-terminated surfaces [151]. Finally, in ambient conditions (where water is present in the air), the hydroxylated OH-terminated is most likely [149].

Another consideration crucial for the understanding of the structure and subsequently dynamics of the surface is the preparation of the α-Al_2O_3 sample. Indeed, different surface preparation yields different results on the IEP (Isoelectric Point, the specific pH value at which a surface has a net electrical charge of zero) of the surface, and some methods, such as acid etching, even produce a nominally hydrophobic interface as the surface bonded water molecules do not interact with above layers of water [154]. This does not appear with mild temperature annealing, and the surface treatment chosen for our studies is to heat the crystal to about $750\,\mathrm{K}$, such that, as visible in Fig.2.7, a coexistence of Al-I and Al-OH termination is present [153].

When completely wetted, α-$Al_2O_3(0001)$ surfaces form a Gibbsite-like $Al(OH)_3$ layer at the surface [153, 154] (see Fig.2.8a)). This layer, only stable under $400\,\mathrm{K}$, as per Fig.2.7, presents different vibrational properties, visible in Fig.2.8d).

When confined between α-$Al_2O_3(0001)$ surfaces at the nanometre scale, molecular dynamics simulations have outlines that the surface induces a more ordered structure in the water, and a highly connected H-bond network [155].

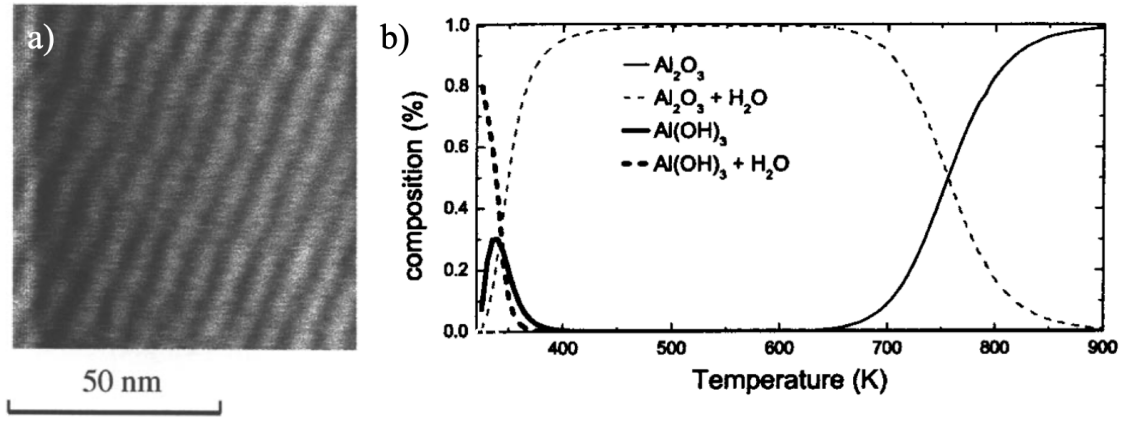

Figure 2.7: a) Atomic Force Measurements (AFM) showing the surface of dry regular α-$Al_2O_3(0001)$ surface at ambient conditions, from [152]. b) Cross section of the equilibrium (OH) coverage of the α-$Al_2O_3(0001)$ at room pressure as a function of temperature, from[153]

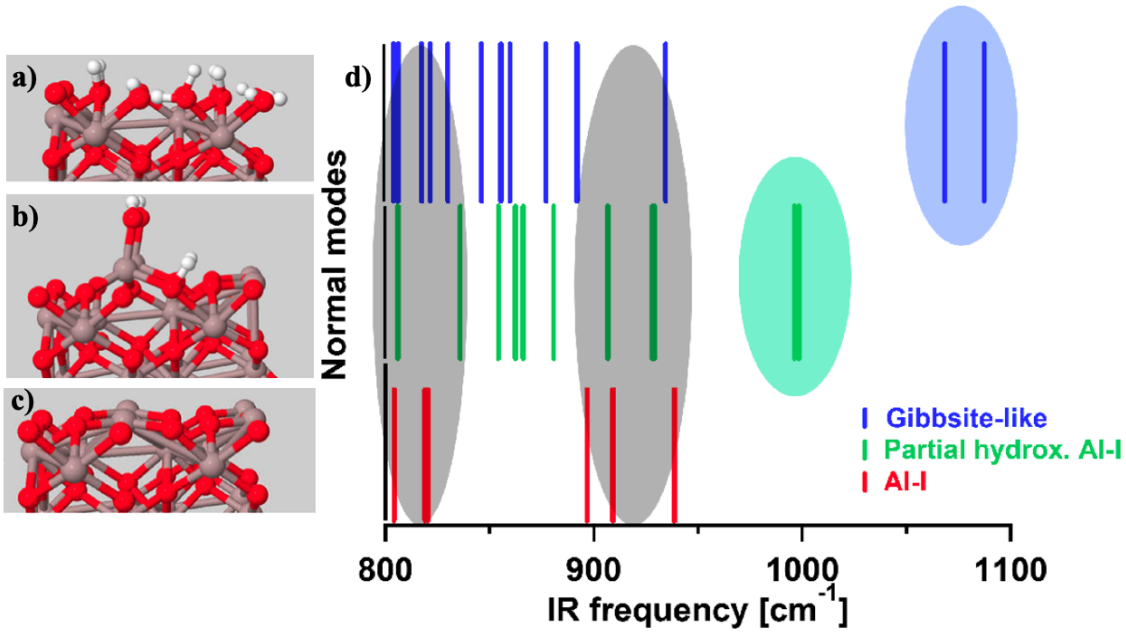

Figure 2.8: Oxygen atoms in red, Al atoms in grey and O atoms white visible on the a) Gibbsite-like termination b) partially OH-terminated (hydroxylated) c) Al-I terminated. d) Calculated normal-mode frequencies of the phonon vibrations for each termination. $1\,\mathrm{meV} = 8.1\,\mathrm{cm}^{-1}$. All images from [154]

In general, the above framing is fundamentally similar for heavy water, and similar behaviour of the surface is to be expected. The main difference appears in the vibrational spectra, where the associated modes are constantly red-shifted [156].

3.3 Separating the surface from the bulk

While the structural and vibrational aspects discussed above are crucial to understand the mechanisms of wetting and hydroxylation on α-$Al_2O_3(0001)$, they only deal with the exact first layer.

On mica, a common hydrophilic surface notably used for surface force apparatus (see the subsection of the previous chapter), interfacial order in water was simulated up to $0.3\,\mathrm{nm}$ [157]. In that region water dynamics will be slowed down, resembling more an LDL "ice-like" structure, as well as surface $Al(OH)_3$ "donating and receiving bonds from water molecules, causing a weak lateral and surface normal water reordering" [158].

In the solid, the bulk region is generally defined as a few atomic layers, which in the case of α-Al_2O_3 would be up to $8\,\mathrm{nm}$, and some studies go as high as $\sim 100\,\mathrm{nm}$ [159].

4 Conclusions

Liquid water is a treasure trove of anomalous effects, from the complex structural interplay between LDL and HDL [103], argued to be leading to vibrational [109] and collective motion throughout the liquid [117]. All of these effects are still present in its isotopic counterpart D_2O, but the slight tightening of the H-bond leads to a general red-shift of its vibrational and collective dynamics [39].

Despite all these anomalous effects, the low-frequency shear elasticity of water at small scales [20] is a common feature of liquids, see previous chapter. The only necessary conditions to observe it are low-shear strain and a highly wetting surface [71], L. Noirez and her group identified α-Al_2O_3 ceramic as a prime candidate [21, 72, 37]. To understand the THz range dynamic interplay between solid and liquid by looking into the solid bulk, the studied solid is thus α-Al_2O_3 monocrystal, to see if structural or vibrational properties by the way of phonons would be altered.

When water is brought into contact with α-Al_2O_3 via its highly wetting (0001) surface layer, tight binding of water molecules takes place through adsorption [36, 153]. This is called hydroxylation [149]. In the case of an abundance of water, Gibbsite-like $Al(OH)_3$ structures are formed at the interface, with distinct vibrational spectra [153, 154, 155].

The central subject of study of this thesis is the bulk acoustic phonon dispersion of α-Al_2O_3 monocrystal in the $\Gamma - Z$ direction when wetted by water and heavy water. This is to see if a trace of the interaction of the complex vibrational patterns of water, exhibited by shear elasticity or thermal bands [25], is observable. In order to do so, we shall use X-ray and neutron scattering techniques, detailed in the following chapter.

Chapter 3

Experimental methods used

In this chapter, we introduce fundamental mechanisms of X-ray and Neutron scattering, followed by the scattering methods used to scan the crystalline solid structure and probe its dynamics.

Contents

1 X-ray and Neutron scattering

It would take a full book to explain the many ways in which both X-rays and neutrons can be –and are— scattered. This section only serves as a very brief introduction on the subject, limiting ourselves to scattering in monocrystals, both inelastic and elastic.

1.1 On X-rays

X-rays are electromagnetic waves in the $1\,\mathrm{keV}$ to $100\,\mathrm{keV}$ energy range. They are transverse, polarised waves, such that their electric and magnetic fields are orthogonal to one another. The direction of the electric field is given by the polarisation vector ϵ.

In the quantum description, they can be quantized as photon of a given energy and momentum $E_p = \hbar\omega$ and $\hbar\mathbf{k}$. As the photon is a massless particle, its wavelength is $\lambda_p = hc/E_p$ with h the Planck constant, c the speed of light. In the X-ray range, we thus have a photon wavelength $\lambda_p \sim$ Å, of the same order of magnitude as the interatomic distance.

An X-ray photon interacts with matter in two ways: it can either be absorbed or scattered. The X-ray beam can also, at the interface, be refracted and reflected. Furthermore, the X-rays interact with the electronic cloud present in the crystals and not with the nuclei themselves.

1.2 On neutrons

Neutrons are neutral subatomic particles, a fundamental part of the atomic nucleus together with the proton. Discovered in 1932 when James Chadwick theorised that the mysterious γ-ray emitted by the interaction between high energy α particles and Beryllium was that of a massive particle capable of ejecting protons from hydrogenated materials [160]. This discovery was rewarded by the 1935 Nobel Prize for Physics. The neutron mass M_n is similar in weight to the proton mass, but has no electrical charge (and a $s = 1/2$ spin).

It is precisely the absence of electrical charge that makes the neutron-matter interaction weak and a neutron flux can be approximated as a plane wave, resulting in neutrons being a pertinent probe for large-volume samples.

Neutrons can interact with matter by two ways: directly with atoms themselves via the strong interaction and through its magnetic properties by magnetic dipolar interaction, beyond the scope of this thesis.

Being a massive particle, the thermal de Broglie wavelength of neutrons is $\lambda_n = \sqrt{\frac{2\pi\hbar^2}{M_n k_B T}}$. At ambient temperature, this is equal to about $\lambda_n \sim 3\,$Å, about the interatomic distance of a typical crystal. Neutrons can therefore be diffracted by a monocrystal, first demonstrated in 1936 [161].

We can distinguish three types of neutrons, depending on their energy or speed : cold, thermal and hot neutrons. Having a different energy, and therefore de Broglie wavelength,

they can scan for different physical phenomena at different scales. In our case, our experiments were performed with thermal neutrons. They offer a good compromise between resolution and flux, allowing us to observe the phonons in monocrystals.

Before we introduce the theory of neutron and X-ray scattering, here is a small table to distinguish X-rays and neutrons from each other and from electrons 3.1.

Quantity	neutron	photon	electron
Mass	$M_n = 1.675 \times 10^{-27}\,\mathrm{kg}$	0	$M_e = 9.109 \times 10^{-31}\,\mathrm{kg}$
Charge	0	0	$e = 1.602 \times 10^{-19}\,\mathrm{C}$

Table 3.1: Relevant basic properties of neutrons, photons and electrons

1.3 Scattering cross-sections

We develop a formalism which will be used throughout the rest of the thesis. In this subsection, we will introduce the notion of a *scattering cross-section* and *dynamic structure factor*. This is a fundamental part of any neutron or X-ray experiment, whether in the case of an elastic or inelastic process. While we will mostly discuss the latter in this thesis, both will be introduced in the following sections.

The general principle of scattering is shown in Fig. 3.1.

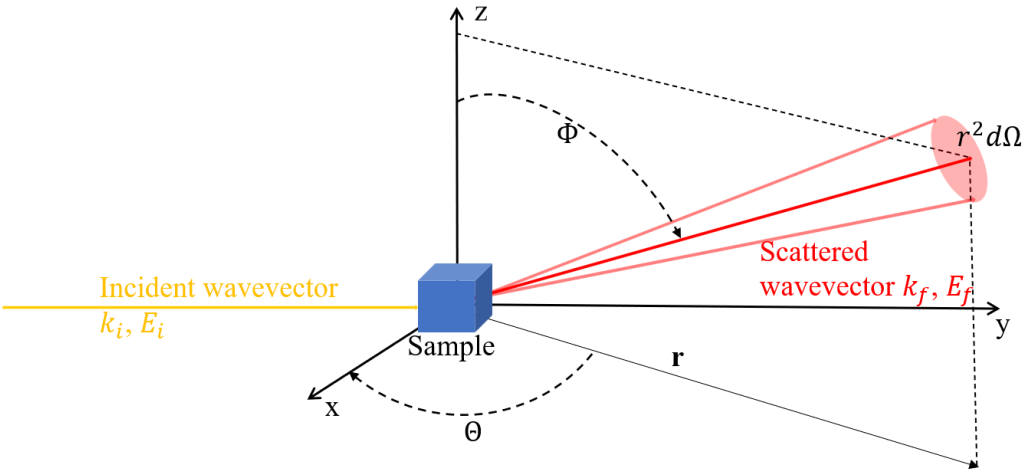

Figure 3.1: General principle of scattering

An incident flux of wave vector $\mathbf{k_i}$ and energy E_i arrives on a sample in a state λ. It is scattered by said sample in a solid angle $d\Omega$. By scattering, the wave vector changes to $\mathbf{k_f}$ and the energy to E_f. In doing so, the sample goes from the λ state to a new state, λ'. We then define the momentum transfer (scattering vector) as $\mathbf{Q} = \mathbf{k_i} - \mathbf{k_f}$ (the difference between incident and final vectors) and the energy transfer $\Delta E = E_i - E_f = -(E_\lambda - E_{\lambda'}) = \hbar\omega$ follows from the energy conservation.

Here it is time to introduce Fermi's Golden rule (first formalised by Dirac in [162]), from which all analysis of both neutron and X-ray scattering flows:

> *The transition rate from an initial to final state in quantum mechanics is the matrix element squared of the density of states times the Hamiltonian.*

A complete derivation from this golden rule can be found for neutrons in [163], and for X-rays in [164]. The main quantity obtained after analysis of either Inelastic X-ray Scattering (IXS) or Inelastic Neutron Scattering (INS) is the dynamic structure factor $S(\mathbf{Q},\omega)$. It is the space-time Fourier transform of the density-density correlation function. In crystals, it gives us the crucial information about the crystal structure and vibrational states, for a given momentum and energy transfer.

$$\frac{d^2\sigma}{d\Omega dE_f} \propto S(\mathbf{Q},\omega) \tag{3.1}$$

The proportionality factor varies fundamentally on the scattering method. In the case of Inelastic X-rays, assuming both the validity of the adiabatic approximation and that the differences between the initial and final state are only due to atomic density fluctuations [165]:

$$\frac{d^2\sigma}{d\Omega dE_f} = \frac{k_f}{k_i} r_0^2 |\epsilon_\mathbf{f}{}^* \cdot \epsilon_\mathbf{i}|^2 |f(\mathbf{Q})|^2 S(\mathbf{Q},\omega) \tag{3.2}$$

Here r_0 corresponds to the electronic radius $e^2/4\pi M_e c^2 \epsilon_0$ (M_e is the mass of the electron and ϵ_0 vacuum permittivity), and $\epsilon_\mathbf{f}$ and $\epsilon_\mathbf{i}$ to the final and incident polarisation vectors, mentioned in section 1.1. M_e is the mass of the electron. $|f_j(\mathbf{Q})|^2$ is the squared atomic form factor, a measure of the interaction of the X-ray beam with the electronic cloud of a given atom j. The prefactor detailed in equation (3.3) is the scattering of polarised light, named after Thomson [166].

$$\left(\frac{d^2\sigma}{d\Omega}\right)_{Th} = r_0^2 |\epsilon_\mathbf{f}{}^* \cdot \epsilon_\mathbf{i}|^2 \tag{3.3}$$

Neutrons, as said in previous section 1.2, interact with matter via the strong force interaction —a direct interaction between neutron and atomic nucleus, not with the electronic cloud. It is quantified by the scattering length b, which is *highly* dependent on atoms and even isotopes, as shown in Fig. 3.2, but independent of $\mathbf{Q}$. Van Hove [167] derives the double-differential cross-section, with N the number of nuclei, as:

$$\frac{d^2\sigma}{d\Omega dE_f} = N\frac{k_f}{k_i} b^2 S(\mathbf{Q},\omega) \tag{3.4}$$

The previous equations (3.2) and (3.4) make the assumption of a single atomic species but can be generalised by summing over the different atoms of the cell.

For completeness, it may be added that neutrons interact with matter also due to their 1/2 spin. Magnetic form factors, not detailed here, have a similar dependency to X-rays, but with the magnetic component instead of electronic density.

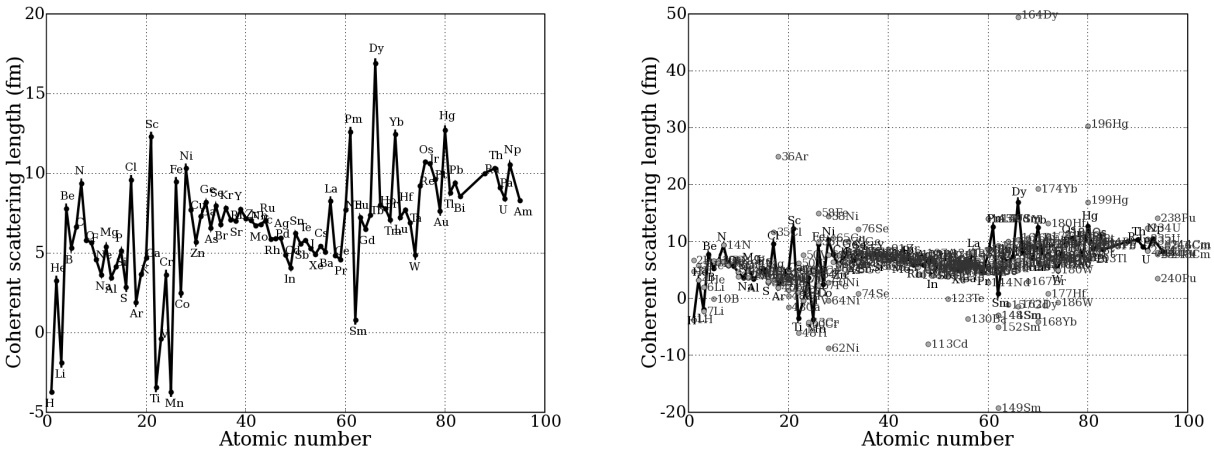

Figure 3.2: Left: Neutron coherent scattering lengths by atomic number ; Right : Neutron coherent scattering length taking into account isotopes. Both figures are from the ILL Neutron Data Booklet [121]

Fig. 3.2 also only shows the coherent scattering lengths. The difference between coherent and incoherent scattering will be explained in the next subsection.

1.4 Incoherent & coherent scattering

The double-differential cross section (3.1) can be separated into two terms, the coherent and incoherent part :

$$\frac{d^2\sigma}{d\Omega dE_f} = \left(\frac{d^2\sigma}{d\Omega dE_f}\right)_{coh} + \left(\frac{d^2\sigma}{d\Omega dE_f}\right)_{inc} \tag{3.5}$$

Coherent scattering provides information on crystal structure and dynamic correlation between atoms. The incoherent part of this decomposition is a measure of self-diffusion and single particle dynamics due to isotopic differences in the material.

The neutron coherent scattering length $\bar{b}$ in (3.6) is the weighted (by the isotope frequency c_r) average over the different incoherent lengths b_r of each isotope or nuclear spin state of the rth distinct isotope. In contrast, the neutron incoherent double differential cross-section is proportional to the squared variance of scattering lengths within a sample, by inserting b_{inc} from (3.6) into (3.4). Since incoherent scattering is a measure independent of microscopic atomic arrangements and movements (the physical quantities of interest), in practice these differences change the background noise. We will encounter them in the following chapters, on the notable case of water and heavy water.

$$\begin{cases} \bar{b} = \sum_r c_r b_r \\ b_{inc} = \sqrt{\overline{b^2} - \bar{b}^2} \end{cases} \tag{3.6}$$

As isotopes have a very similar amount of electrons, it follows that X-ray scattering is less sensitive to incoherence, thus barely changing the atomic form factor $f(\mathbf{Q})$ from (3.2). In fact, in (3.2), we have already made the assumption of coherence to extract our form factor from the structure factor. In our study, these isotopic effects in X-ray scattering are of no importance and will therefore not be detailed, but a detailed explanation can be seen in [168].

The advantage of the previous simplified formalism is that, for the following sections, we can treat the structure factor of both neutrons and X-rays in exactly the same way. At the end of each section, the case of a multi-atomic cell will be detailed for each probe.

Let us first introduce the atomic density operator $\rho_{\mathbf{Q}}(t)$.

$$\rho_{\mathbf{Q}}(t) = \sum_l e^{i\mathbf{Q}\cdot\mathbf{r}_l(t)} \tag{3.7}$$

With $\mathbf{r}_l(t)$ the coordinates of the scattering centres. Therefore the dynamic structure factor can be written as :

$$S(\mathbf{Q},\omega) = \frac{1}{2\pi\hbar}\int_{-\infty}^{+\infty} dt e^{-i\omega t}\langle\rho_{\mathbf{Q}}(0)\rho_{-\mathbf{Q}}(t)\rangle \tag{3.8}$$

1.5 Coherent elastic scattering & Bragg's Law

For coherent elastic scattering, we just consider the time averaged dynamic structure factor (3.8) for a rigid lattice $\mathbf{r}_l(t) = \mathbf{r}_l$, leading to:

$$S(\mathbf{Q},\omega) = \delta(\hbar\omega)\Big\langle\sum_{ll'} e^{i\mathbf{Q}\cdot(\mathbf{r}_l-\mathbf{r}_{l'})}\Big\rangle \tag{3.9}$$

Which becomes in our monoatomic cell:

$$S(\mathbf{Q},\omega) = \delta(\hbar\omega)\frac{(2\pi)^3}{v_0}\sum_{\mathbf{G}}\delta(\mathbf{Q}-\mathbf{G}) \tag{3.10}$$

where v_0 is the unit cell volume and $\mathbf{G}$ is the scattering vectors of the reciprocal lattice.

Here let us focus on the condition $\delta(\mathbf{Q}-\mathbf{G})$. Physically, it means that elastic scattering is only possible when the scattering vector is equal to a reciprocal lattice vector $\mathbf{G}$. This is known as the Laue condition and is equivalent to the more commonly known Bragg's Law [169], which states that waves incident on a crystalline material can only constructively interfere when the path difference between waves scattered from successive atomic planes is an integer multiple of the wavelength. Mathematically, this is expressed as

$$n\lambda = 2d_{hkl}sin\theta \tag{3.11}$$

with n an integer, λ the incident wavelength, d_{hkl} the distance between planes and θ half the scattering angle. This can be directly recovered from $\mathbf{Q} = \mathbf{G}$, imposing that $Q = 2k_i sin\theta$.

If we further consider that the centres $\mathbf{r}_l(t) = \mathbf{r}_l + \mathbf{u}_l(t)$ to take into account fluctuations, the averaging of the phase $e^{-i\mathbf{Q}\cdot\mathbf{r}_l}$ results in an extra factor e^{-2W} with W the Debye-Waller factor such that:

$$W = \frac{1}{2}\langle(\mathbf{Q}\cdot\mathbf{u}_l)^2\rangle \tag{3.12}$$

Let us return to a more general case, beyond that of the Bravais lattice. We here suppose that the cell is composed of more than one atom. The j-th atom within the cell sits at position $\mathbf{d}_j$. We can therefore derive the coherent elastic differential cross section as:

$$\frac{d\sigma}{d\Omega}|_{coh}^{el} = N\frac{(2\pi)^3}{v_0}\sum_{\mathbf{G}}\delta(\mathbf{Q}-\mathbf{G})|F_N(\mathbf{G})|^2 \tag{3.13}$$

with:

$$F_N(\mathbf{G}) = \sum_j \overline{b}_j e^{\mathbf{G}\cdot\mathbf{d}_j}e^{-W_j} \tag{3.14}$$

In the case of X-rays, one only needs to add the prefactor of Thomson scattering (3.3) as well as change $F_N(\mathbf{G})$ to $F_X(\mathbf{G})$:

$$F_X(\mathbf{G}) = \sum_j f_j(\mathbf{G})e^{\mathbf{G}\cdot\mathbf{d}_j}e^{-W_j} \tag{3.15}$$

The factor $f_j(\mathbf{G})$ is the electronic form factor for X-ray interaction from (3.2) for the j-th atom and W_j is the Debye-Waller factor (3.12) for the j-th atom.

1.6 Coherent inelastic scattering : the study of phonons in the harmonic approximation

When subtracting the elastic contributions ($E_i \neq E_f$), the dynamic structure factor corresponds to the fluctuations in the sample, as a function of both momentum and frequency. The dynamic structure factor follows the principle of detailed balance:

$$S(-\mathbf{Q},-\omega) = e^{-\hbar\omega/k_BT}S(\mathbf{Q},\omega) \tag{3.16}$$

This property is due to the fact that the probability of transitions in the sample is weighted by the nature of the initial state of transition —either an excitation annihilation or excitation creation (Stokes, anti-Stokes).
This formalism is correct for any inelastic excitations within the sample, but from now on we shall be discussing only the phonons: the vibrational modes of the lattice. Considering a lattice with n atoms per unit cell, it will have $3n$ distinct phonon branches of frequencies $\omega_{\mathbf{q}s}$ with s the different modes and $\mathbf{q}$ is a vector from the nearest reciprocal lattice vector $\mathbf{G}$ in the following way:

$$\mathbf{Q} = \mathbf{G} + \mathbf{q} \tag{3.17}$$

For a mode s, ξ_{js} is the polarisation vector for the jth atom of the unit cell. Considering the case of a single phonon being created or destroyed, scattered by either X-rays or neutrons, one has

$$S(\mathbf{Q},\omega) = \frac{(2\pi)^3}{2v_0(1-e^{-\hbar\omega/k_BT})}\sum_{\mathbf{G},\mathbf{q}}\delta(\mathbf{Q}-\mathbf{q}-\mathbf{G})\sum_s \frac{1}{\omega_{\mathbf{q}s}}|\mathcal{F}(\mathbf{Q})|^2\times[\delta(\omega-\omega_{\mathbf{q}s})-\delta(\omega+\omega_{\mathbf{q}s})] \quad (3.18)$$

with the dynamic form factor $\mathcal{F}(\mathbf{Q})$, depending on the scattering method, is equal to:

$$\mathcal{F}(\mathbf{Q}) = \begin{cases} \mathcal{F}_N(\mathbf{Q}) = \sum_j \frac{\bar{b}_j}{\sqrt{m_j}}(\mathbf{Q}\cdot\xi_{js})e^{i\mathbf{Q}\cdot\mathbf{d}_j}e^{-W_j} & \text{for neutrons} \\ \mathcal{F}_X(\mathbf{Q}) = \sum_j \frac{f_j(\mathbf{Q})}{\sqrt{m_j}}(\mathbf{Q}\cdot\xi_{js})e^{i\mathbf{Q}\cdot\mathbf{d}_j}e^{-W_j} & \text{for X-rays} \end{cases} \quad (3.19)$$

with m_j the mass of the jth atom. For completeness, in the case of X-rays, one needs to add the Thomson scattering (3.3) as a prefactor to equation (3.18).

Throughout this section, we can see that the destruction (anti-Stokes) or creation (Stokes) of a phonon is modelled by a Dirac δ function. This is called the harmonic approximation, where physically the vibrations are seen as being able to propagate throughout the crystal without being damped. In the next subsection we shall discuss a more realistic model: the Damped Harmonic Oscillator (DHO).

1.7 Coherent inelastic scattering : the damped harmonic oscillator

In real systems, electron-phonon and phonon-phonon interactions tend to give phonons a finite lifetime. Not being able to propagate infinitely, they have to be damped, and therefore this dissipation is accounted for in the damped harmonic-oscillator (DHO) model. In this model the Dirac delta functions from equation (3.18) are replaced by Lorentzian functions and renormalising the phonon frequencies as such:

$$\frac{1}{\omega_{\mathbf{q}s}}\delta(\omega\pm\omega_{\mathbf{q}s}) \rightarrow \frac{1}{\pi\omega'_{\mathbf{q}s}}\frac{\gamma_{\mathbf{q}s}/2}{[\omega\pm\omega'_{\mathbf{q}s}]^2+(\gamma_{\mathbf{q}s}/2)^2} \quad (3.20)$$

with

$$\omega'^2_{\mathbf{q}s} = \omega^2_{\mathbf{q}s} - \left(\frac{\gamma_{\mathbf{q}s}}{2}\right)^2 \quad (3.21)$$

This simple substitution allows for a plethora of phenomena to be described and studied [170].

2 X-ray scattering synchrotron techniques

In this section, we shall only explain the few techniques that we had the pleasure to use at the ESRF (European Synchrotron Radiation Facility) lines ID28 and ID20.

2.1 On synchrotron radiation sources

X-rays, unlike neutrons, can be generated in standard laboratory settings, but some experiments require more brilliance. Synchrotron sources are the main way used to generate high intensity X-rays from soft ($100\,\mathrm{eV}$ to $2000\,\mathrm{eV}$) to hard X-rays (high energy, generally superior to $2\,\mathrm{keV}$).

A synchrotron operates by accelerating electrons generated by an electron gun to relativistic speeds (close to the speed of light) using a linear particle accelerator and guiding them around a circular path using magnetic fields, called the storage ring. These high-energy electrons are deflected by magnetic fields, and when deflected they emit electromagnetic radiation tangential to their circular trajectory (X-rays), known as synchrotron radiation [171]. The X-rays emitted have high brilliance, intensity, and coherence. Beyond the scope of this thesis, they are also polarised and pulsed, allowing insights into anisotropic and short time-dependent phenomena respectively.

Furthermore, X-rays are generated within a very large range of photon energy and can be filtered to obtain very precise incident energies, depending on the machines and experiments.

2.2 Inelastic X-ray scattering at ID28 to observe phonon dynamics

High-energy inelastic X-ray scattering such as present at the line ID28 of the ESRF was precisely created for the dynamic study of phonons in small samples (X-ray offers a $\mu\mathrm{m}$ size beam compared to cm for neutrons), in either crystalline or amorphous materials, even liquids [172]. The incident and final (diffracted and with change of energy) beam follow the conservation laws

$$\begin{cases} \hbar\mathbf{k_i} - \hbar\mathbf{k_f} = \hbar\mathbf{Q} \\ E_i - E_f = \hbar\omega \end{cases} \tag{3.22}$$

Its general characteristics are visible in Tab. 3.2. What immediately jumps to the eye is the range of energy probed relative to the incident energy, often reaching a $\frac{\Delta E}{E} \simeq 10^{-7}$ ratio. This is of key importance, as in earlier textbooks, it was precisely this ratio that was seen as a limiting factor to be able to observe phonons with low resolution [143].

Reflection (S_i)	(8, 8 and 8)	(9, 9 and 9)	(11, 11 and 11)	(12, 12 and 12)
Wavelength (Å)	0.7839	0.6968	0.5701	0.5226
Energy (eV)	15 816	17 793	21 747	23 725
$Q_{max}(\mathrm{nm}^{-1})$	67.7	76.2	93.2	100
Resolution (meV)	6.0	3.0	1.5 to 1.7	1.3 to 1.4

Table 3.2: Characteristics of the ID28 spectrometer based on incident energy, from [173]

We therefore have a very coherent collimated source with very little energy spread and divergence, making the energy resolution independent of the position in reciprocal space, which is not the case for neutrons as will be discussed in the next section 3.

In Fig. 3.3 we can see in the IXS spectrometer part (top rectangle), that the beam passes through a backscattering monochromator. Let us use Bragg's law (3.11) to explain the interest

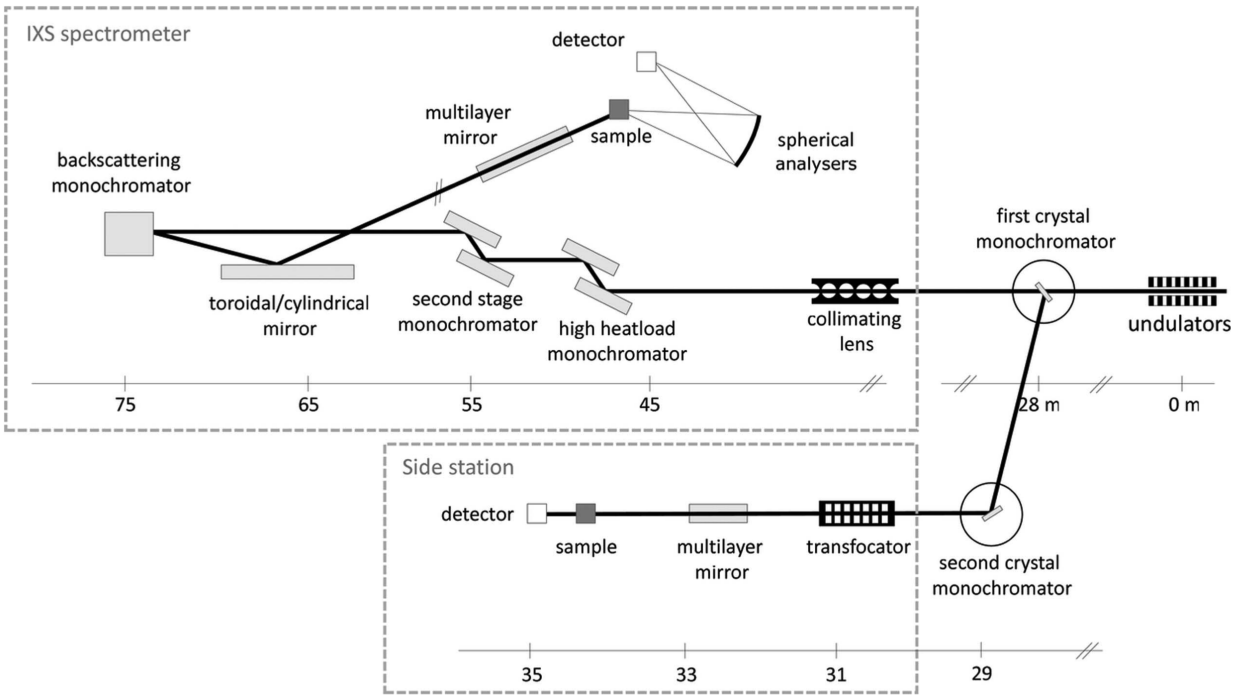

Figure 3.3: Beamline layout of ID28 from [174]

of backscattering. Since $E = \frac{hc}{\lambda}$, we therefore have $E = \frac{nhc}{2d_{hkl}sin\theta}$. Considering a small variation in angle $d\theta$ inducing the small variation in energy dE

$$dE = -\frac{nhccos\theta}{2d_{hkl}sin^2\theta} = -Ecot\theta \tag{3.23}$$

therefore, in backscattering geometry where $\theta \simeq 90°$ we have

$$\frac{dE}{E} \simeq cot\theta \simeq 0 \tag{3.24}$$

this makes the instrument highly insensitive to small angular variations, and solely sensitive on the spacing of the backscattering monochromator (d_{hkl}). Therefore for a given Bragg condition, the scanning in energy is performed by, in a controlled manner, changing the temperature of the backscattering monochromator. This slight (generally less than $0.5\,\mathrm{K}$ for a scanning range of $30\,\mathrm{meV}$) change in temperature induces slight changes in the crystal spacing, and therefore scanning for very small energy transfer. Another practical consequence of this scanning technique is the ability to easily scan in both annihilation and creation of a phonon (negative and positive energy transfers), allowing us to observe both the Stokes and anti-Stokes of a given phonon. A paragraph to compare the IXS resolution functions and INS will be in the next section 3.

2.3 X-ray diffraction at ID28

The "side station," highlighted in the bottom rectangle of Fig 3.3, is a state-of-the-art high-resolution diffractometer. While its capabilities extend to observing subtle phenomena like Thermal Diffuse Scattering (TDS) —a general introduction of which can be found in [171]

and [174]—, for our specific practical purposes, it was utilised exclusively for elastic scattering experiments, focusing on structural characterisation.

Despite its theoretical ability to scan with a different incident energy than the main IXS station, it is in practice coupled to the main beamline as the undulators are typically tuned and optimised to provide maximum flux for a specific energy required by the main IXS spectrometer. Therefore the side station diffractometer operates in practice with the same incident energy of the main station.

In a general experimental setup, the sample is mounted precisely on a goniometer. This goniometer allows the sample to be rotated through known angles. The diffracted signal is then collected by a 2D pixel-detector. This detector's distance from the sample is adjustable, typically ranging from $150\,\mathrm{mm}$ to $400\,\mathrm{mm}$. This offers variability in capturing diffraction patterns with varying angular resolutions or larger portions of reciprocal space. With the incident beam position fixed, the sample rotating through known angles, and the 2D detector capturing the elastic scattering signal in mapped-out directions, one can effectively reconstruct the reciprocal space. This process yields the elastic, structural, and other fundamental parameters commonly obtained in classical diffractometer experiments, providing crucial complementary information to the inelastic scattering data from the main ID28 station.

2.4 Inelastic X-ray scattering at ID20: X-ray Raman

X-ray Raman Spectroscopy (XRS) performed at ID20 is a complementary inelastic method to IXS and diffraction. While IXS probes low energies ($\sim \mathrm{meV}$) and diffraction probes the structure of the material, XRS will probe the electronic excitations, see Fig. 3.4. It has a range of energy transfer of $\sim 50\,\mathrm{eV}$ to $1000\,\mathrm{eV}$, ideal for probing the electronic excitations in the soft X-ray domain, namely K-edges of low number atoms, or $L_{2,3}$-edges of metallic compounds [175]. The spectrometer has an overall energy resolution in the $\sim 0.2\,\mathrm{eV}$ to $\sim 2\,\mathrm{eV}$ range [176].

XRS functions with the same fundamental principles highlighted in equations (3.22), but the energy $\hbar\omega$ is tuned to match a core electron excitation energy. The incident energy E_i is in the hard X-ray range ($\sim 10\,\mathrm{keV}$), and it is therefore by changing E_f that $\hbar\omega$ is tuned. On Fig. 3.5 you can see 5 detector modules (there is one more), both in and out of the plane of the incident beam. Each of the modules is composed of 12 analyser crystals $Si(660)$ (the reflection can be changed) are situated on a precise angular position relative to the sample and to the scattered beam, each individually equipped on a goniometer. Again, by using Bragg's Law (3.11), each of these $Si(660)$ crystals have their angular position θ slightly change to scan in the appropriate energy range.

Having an incident beam in the hard X-ray regime, this method has, depending on the incident angle on the sample, the ability to scan bulk electronic excitations of soft X-rays energy range. Furthermore, XRS can be performed at ambient conditions, unlike other known methods that scan the same quantities, such as X-ray Absorption Near Edge Structure (XANES) [178].

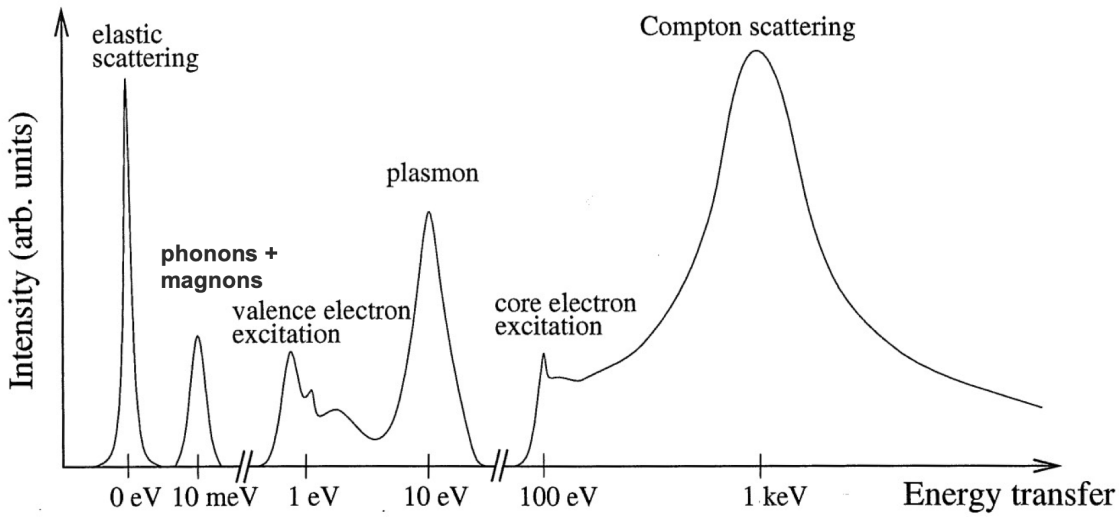

Figure 3.4: Inelastic X-ray Scattering range and observable physical phenomena, from [177]

Moreover, XRS at ID20 allows for change of the momentum transfer $\mathbf{q}$. By varying the scattering angle and/or the position of multiple detector modules (6) seen in Fig. 3.5, one can go beyond the dipole approximation [179, 178], probing both dipole-allowed and non-dipole transitions, which can provide more comprehensive information about the symmetry of unoccupied electronic states.

In practice, more data treatment must take place, notably in the definition of ROIs (Regions Of Interest), before we can obtain a simple $I(\hbar\omega)$ graph. More details on the process of definition of ROIs can be found in [179].

3 3-axis Neutron Spectrometer

3.1 Basis of 3-axis neutron spectrometry

3.1.1 Generalities

Neutron 3-axis spectrometry measures the neutron intensity diffracted by a sample as a function of the angle of scattering and transferred energy. It is named after the three principal mobile elements of the instrument:

- The **monochromator** (first axis): a monocrystal selects a neutron wavelength λ_i from the polychromatic beam generated by the nuclear reactor or spallation source using Bragg's law (3.11).
- The **sample** (second axis): receives the monochromatic beam, which is diffracted with or without energy change —inelastic or elastic scattering, see (3.25).
- The **analyser** (third axis): Another monocrystal that can select the incoming wavelength λ_f of the diffracted beam, again following Bragg's law.

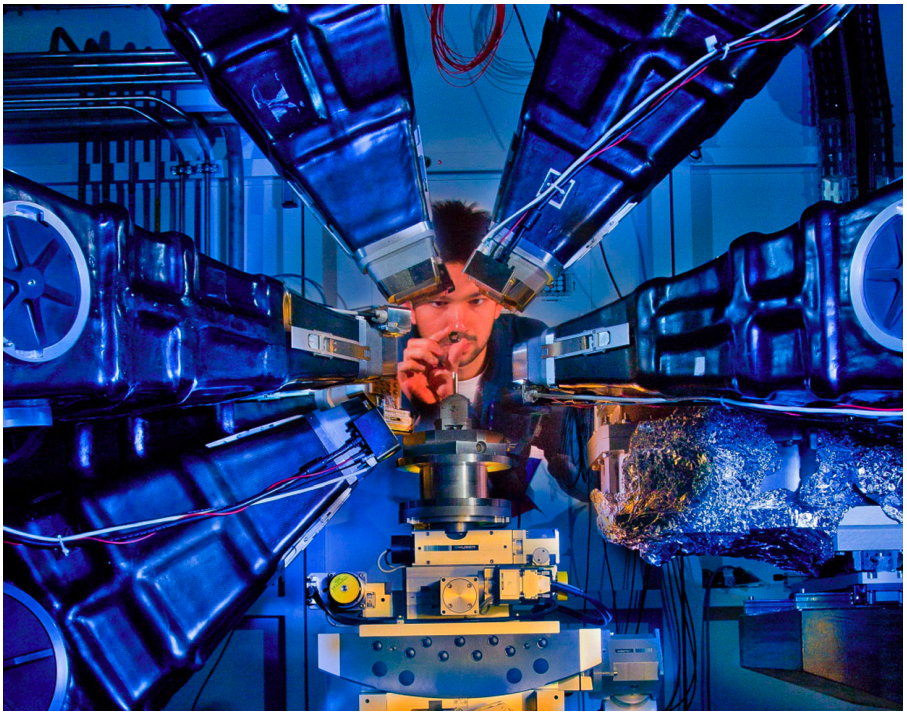

Figure 3.5: Raman X-ray Scattering picture from ID20, showing 5 detector modules, from[180]

- To finish, a **detector** is on the beam path after the analyser to measure the intensity of the given diffracted beam.

Measurements in 3-axis spectroscopy are defined in the reciprocal space associated with the scanned crystal. When neutrons interact with a sample, they are scattered according to the elastic and inelastic scattering cross-sections. The incident and final wavelengths are generally spoken of in terms of wavevectors $k_i = 2\pi/\lambda_i$ and $k_f = 2\pi/\lambda_f$. This whole process — a schematic view can be seen in Fig. 3.6— ensures the scattered neutrons obtained will have exchanged both momentum and energy with the sample, following the conservation laws of momentum and energy (3.25)

$$\begin{cases} \hbar\mathbf{k_i} - \hbar\mathbf{k_f} = \hbar\mathbf{Q} \\ \dfrac{\hbar^2 k_i^2}{2M_n} - \dfrac{\hbar^2 k_f^2}{2M_n} = \hbar\omega \end{cases} \tag{3.25}$$

$\mathbf{Q}$ is the scanned position in reciprocal space (associated with the sample), ω is the change in neutron frequency (or energy) due to the inelastic scattering processes and M_n is the neutron mass. The scans are done at constant neutron count. The intensity of the conservation laws (3.25) are a function of the dynamic structure factor $S(\mathbf{Q}, \omega)$. If the Bloch theorem is applicable to the sample [143], the momentum transfer is separated into two quantities $\mathbf{Q} = \mathbf{G} + \mathbf{q}$ with $\mathbf{q}$ a part of the First Brillouin Zone centred on $\mathbf{G}$.

The key element of the 3-axis spectrometer is the following: a given position of the spectrometer, for a given sample, corresponds to a position in reciprocal space $\mathbf{Q}$ and a vibrational frequency/energy ω.

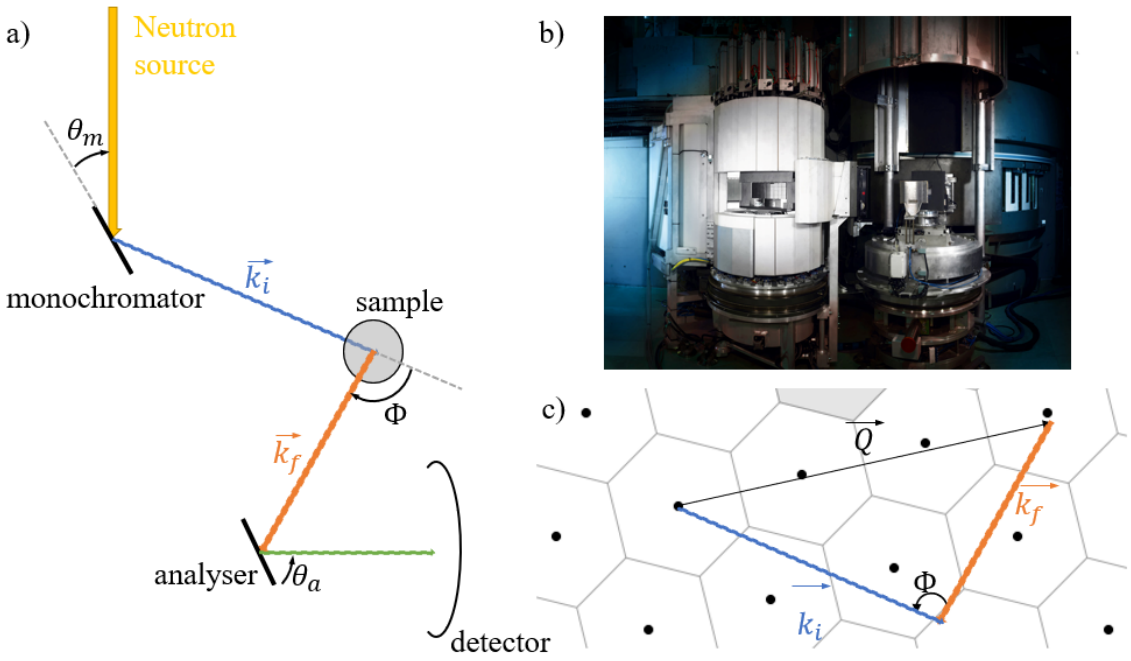

Figure 3.6: a) Schematic operation of a 3-axis spectrometer. b) picture of IN8 3-axis neutron spectrometer from [181]. c) Reciprocal space visualisation of the momentum law of conservation.

3.1.2 Modes of measurement

There two main mode of measuring data on a 3-axis spectrometer, either at constant Q scan or at constant ω scan.

Constant Q scans This is the standard method to measure phonon dispersion. This can be done in multiple ways, but the main way and the one used during the neutron experiment described in chapter 5 is by fixing a constant k_f, and varying sample angle, as well as the analyser angles to maintain the desired position in reciprocal space, and changing the monochromator crystal angle to vary the energy ω. In practice this is all done simultaneously.

Constant ω scans A complementary method, less commonly used, but mostly for "flat" modes. In this case the energy transfer is fixed and the monochromator, analyser and sample angles are rotated to vary the position in reciprocal space.

3.2 Resolution function

3.2.1 Sources and monochromator

The choice of the spectrometer influences what can or cannot be observed in a given sample. 3-axis spectrometers are installed on neutron sources whose energy and flux distribution is dependent on the moderator temperature. We can then define three different sources:

- thermal source: this is the basic neutron source where neutrons are emitted by the reactor core and slowed down by collisions with heavy water. The incident vector roughly $k_i \sim 4.1\,\text{Å}^{-1}$, allowing us to observe energy transfers in the $1\,\text{meV}$ to $120\,\text{meV}$ range. IN8, the ILL spectrometer used in our study, is of this kind.

- cold source: neutrons are slowed down with either low temperature hydrogen or heavy water to limit the flux to around $k_i \sim 2\,\text{Å}^{-1}$, to observe energy transfers from $0.05\,\text{meV}$ to $12\,\text{meV}$.

- hot source : where neutrons are heated with γ radiation through the insertion of a high temperature graphite block. This extends the observable transfers to $\sim 200\,\text{meV}$.

As previously stated IN8 is a thermal source, with an incident k_i varying on the reflection chosen for the monochromator. There are multiple monochromator choices ($PG(002)$, $Si(111)$ etc..), but the one chosen in our case is $Cu(200)$ with a $k_i = 2.662\,\text{Å}^{-1}$.
The analyser generally is $PG(002)$ for its large range of k_f.

In essence, the choice of source, monochromator and analyser dictates the *energy* resolution and *energy* range of the experiment.

3.2.2 Resolution function: a primer

In practice, no measure is perfect. The monochromator, as well as collimators before and after the sample, select a bundle of neutrons with a distribution centred on k_i and k_f. Therefore, when measuring at a given point $\mathbf{Q_0}, \omega_0$, one is in fact measuring an integration of points around this value, centred on it. The function that takes all these parameters into account is called *the resolution function* $R(\mathbf{Q} - \mathbf{Q_0}, \omega - \omega_0)$ in equation (3.26).

$$I(\mathbf{Q_0}, \omega_0) = \int S(\mathbf{Q}, \omega) R(\mathbf{Q} - \mathbf{Q_0}, \omega - \omega_0) d^3\mathbf{Q} d\omega \tag{3.26}$$

$S(\mathbf{Q}, \omega)$ is the aforementioned dynamic structure factor, and the physical quantities studied are contained within. It is therefore the experimentalist's goal to extract the physical data by deconvoluting the intensity measured $I(\mathbf{Q_0}, \omega_0)$ using the resolution function. But what makes up the resolution function ?

We have just mentioned the monochromator, the analyser, collimation before and after the crystal as being contained in the resolution function. The classical approximation, originally derived in [182], is to consider a Gaussian approximation of each of the distributions, such that the resolution function takes the following form:

$$R(\mathbf{Q} - \mathbf{Q_0}, \omega - \omega_0) = R_0 e^{-\frac{1}{2}\Delta\mathcal{L} M \Delta\mathcal{L}} \tag{3.27}$$

where :

- $\Delta\mathcal{L} = \left(\frac{M_n}{\hbar Q_0}(\omega - \omega_0), \mathbf{Q} - \mathbf{Q_0}\right)$ is a four-dimensional vector in which all variations of energy and momentum transfer are incorporated with the same dimension of inverse length.

- M is the resolution matrix.
- R_0 is scalar prefactor.

Complete derivation of the resolution matrix M and resolution prefactor R_0 can be found in appendix 4 of [183], but we shall explain the basics of it. Before doing so, one last parameter to take into account is the sample mosaicity. Indeed, it is not always possible to have sufficient volume of a given single crystal to be able to scan it —therefore needing to align them and stick them to a sample holder. In either cases, the resolution function takes into account the sample mosaicity as supplementary parameter, modelled like the monochromator and analyser. This does not change the previous approximations' physical understanding but does change the resolution matrix and the scalar prefactor.

To give us a physical understanding of the resolution function, let us look at a more detailed path of the neutron, from the source to the detector 3.7.

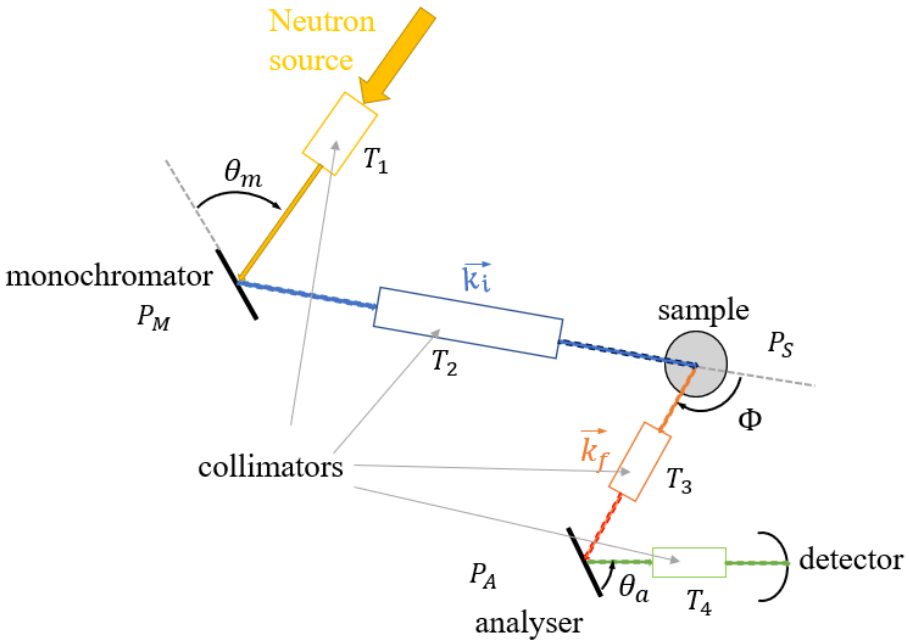

Figure 3.7: Detailed path of the neutron beam

The beam goes from source to monochromator, and is naturally collimated by the geometry of the spectrometer. There is therefore already a transmission function T_1 associated to said part of the path. A similar transmission function can be used to detail the path between monochromator and sample, from sample to analyser, and finally from analyser to detector, numerated from 2 to 4. At each interaction with a crystal (monochromator, sample, analyser), a different probability function to account for crystal inaccuracies is introduced —P_M, P_S and P_A. In the analyser and monochromator, there are large differences between horizontal and vertical orientation probabilities, but for the sample these are considered equal. Once all these steps are defined, one multiplies the transmission function of collimator one and two with the monochromator, then integrate it over all incident wave-vector, and does the same with collimator three and four with the analyser function. A weighting factor due

to the reflectivity of the given crystal is also introduced.

This gives us two distributions: that of the incident beam and final beam. To obtain the full resolution function one integrates the product of both distributions over all the pairs of incident and final wavevectors. This finally gives us the resolution function $R(\mathbf{Q}-\mathbf{Q_0}, \omega-\omega_0)$.

But neither of these distributions consider the sample itself. While the resolution itself is technically independent of the sample, said sample has finite mosaic width, and therefore one never measures the *true* structure factor $S(\mathbf{Q}, \omega)$ but an effective structure factor $S'(\mathbf{Q}, \omega)$, a normalised integration on the variation of $\mathbf{Q}$ weighted by the distribution of the sample P_S. This is then used to define a *effective* resolution function $R'(\mathbf{Q} - \mathbf{Q_0}, \omega - \omega_0)$, where sample mosaicity is integrated in the resolution.

Essentially, spectrometer geometry, collimation, monochromator, analyser and sample mosaicity are all taken into account to model the resolution function as a 4D-ellipsoid. In our case, this is all done in an in-house program by Bernard Hennion, the outlines of which can be found in [184].

3.2.3 Qualitative comparison between INS and IXS resolution functions

IXS and INS work with fundamentally the same principles and the equation (3.26) is perfectly valid for both. However, when taking into account the discussion about the backscattering monochromator in IXS from 2.2, we see that there is both no need for moving one of the axes to observe inelastic phenomena, and the high insensitivity in angular variations described means in practice that the 4D (momentum space and energy) ellipsoid that is the resolution function becomes a 1D line, independent of the scattering vector in reciprocal space. A schematic view of the resolution differences can be found in Fig. 3.8.

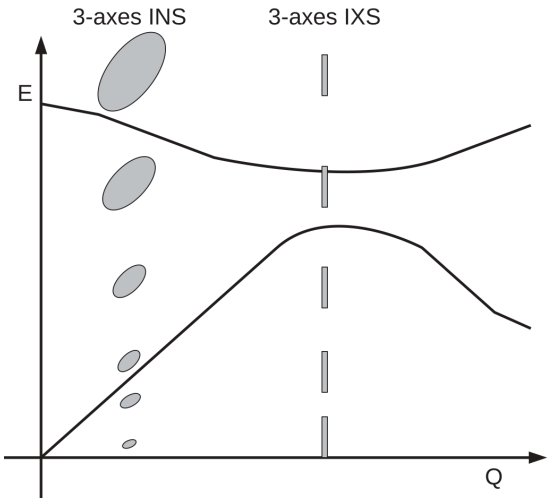

Figure 3.8: Comparison of the resolution function in INS and IXS, from [185]. grey ellipses indicate the energy evolution of the resolution function with INS for a given $\mathbf{Q}$, which are thin rectangles unchanged for IXS

Note that in this case the the 4D ellipsoid is represented in 2D for clarity. In practice, it means that deconvolution from the resolution function for IXS is more straightforward, as it does not depend on $\mathbf{Q}$, but only is a function of energy.

Having now defined the experimental methods used from the theory of scattering, either inelastic and elastic, we will be using each of the four experimental methods discussed in the work of the following chapters. All of these bulk tools will allow us :

- Scan the phonon dynamics of the bulk of the system: using IXS at ID28 of the ESRF synchrotron and INS at IN8 of the ILL source.
- Scan the structural parameters of the system: using the high-resolution diffractometer at ID28 of the ESRF.
- Scan the core electron excitations in the bulk of the material, using XRS at ID20 of the ESRF.

The goal of the present work is to see how the vibrational properties of α-Al_2O_3 changes in the presence of water or heavy water on the α-$Al_2O_3(0001)$ surface.

Chapter 4

First observation of solid-liquid phonon interaction

This chapter is, to our knowledge, the first foray into the hydrophilic solid-liquid interaction between liquid water and α-$Al_2O_3(0001)$ and its consequences for bulk acoustic phonons of the solid. We highlight, using inelastic scattering, a plethora of new effects, of varying importance and complexity —such as hardening and broadening of acoustic phonons— using reflectometry measurements at the ESRF ID28 beamline.

Contents

As highlighted regularly in the previous chapter, our goal is to investigate *bulk* effects in the solid due to the presence of liquid at the surface. We have highlighted that liquids themselves have shown states indicative of a complex vibrational behaviour in Chapter 1 through mesoscopic low frequency shear elasticity present in a wide range of liquids. The specific liquids studied, H_2O and D_2O, also show complex vibrational patterns through the H-bond, discussed in Chapter 2. Combining these novel perspectives highlighting a non-equilibrium state at the interface, we will first investigate the bulk acoustic phonon of the highly wetting solid α-Al_2O_3 through Inelastic X-ray Scattering (IXS) at the ESRF ID28 beamline.

1 Experimental setup

The α-Al_2O_3 crystals scanned, manufactured as detailed in 2.1 by the company Neyco [132], are of $22\,\mathrm{mm}$ diameter and $2\,\mathrm{mm}$ thickness. The X-ray beam penetrates the α-$Al_2O_3(0001)$ surface which will be wetted, the process of which is detailed in 3. The experiments are performed in reflectometry conditions, in which the beam penetration is equivalent to the attenuation length.

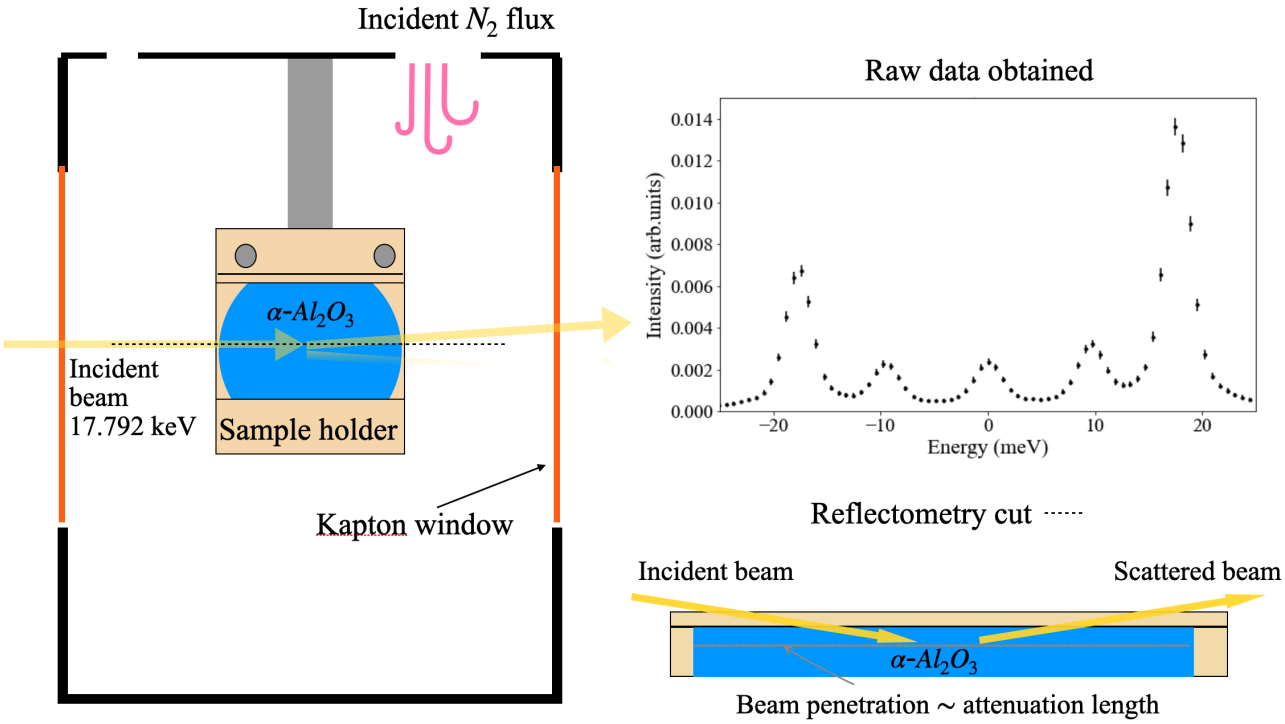

Figure 4.1: Reflectometry experimental setup. The sample holder is 3D printed and made out of ... . The crystal is contained within a metal and Kapton film (for the beam to pass through), and is isolated from the room by a continuous nitrogen flux of $6\,\mathrm{L\,min^{-1}}$. An example of raw data obtained is shown, and the (- - -) cut is shown to highlight the reflectometry process. All experiments are performed at room temperature and pressure, with an incident beam energy of $17.792\,\mathrm{keV}$.

The reason for the use of reflectometry conditions (besides the crystal size) was that by scanning the same point in a given BZ associated with a given incident angle, we would be

able to identify a depth dependent effect if one were to take place. However, in practice, due to a combination of structure factor and geometric conditions, mainly 3 BZs were available to study: the $(\bar{1}014)$, the (006) and (0012). Our goal here was to observe the phonons — especially acoustic phonons as they are carriers of vibrational patterns at the longest range— in the crystal at these different BZs.

The (006) showed a low signal relative to the other two. Indeed, the obtained intensity of the scattering process is directly proportional to the double differential cross-section (3.2), and in the case of phonons (more precisely one-phonon scattering), this dependence is proportional to $|\mathbf{Q}|^2$ [168]. Therefore, while some scans in the (006) BZ will be shown, the main study will revolve around $(\bar{1}014)$ and (0012). $(\bar{1}014)$ is the BZ of main importance in this study, as the phonon polarisation vector ξ_{js} from (3.15) allows us to observe both transverse and longitudinal acoustic phonons, unlike in the (0012) in which only the longitudinal acoustic phonons are observed. The incident angles associated with the $(\bar{1}014)$ and (0012) BZ are $\sim 10°$ and $\sim 20°$ respectively, as shown in Fig. 4.2. However, due to the $(\bar{1}014)$ being in a non-symmetric reflectometry condition, and (0012) a symmetric one, the penetration depth is the same ($\sim 150\,\mu\mathrm{m}$).

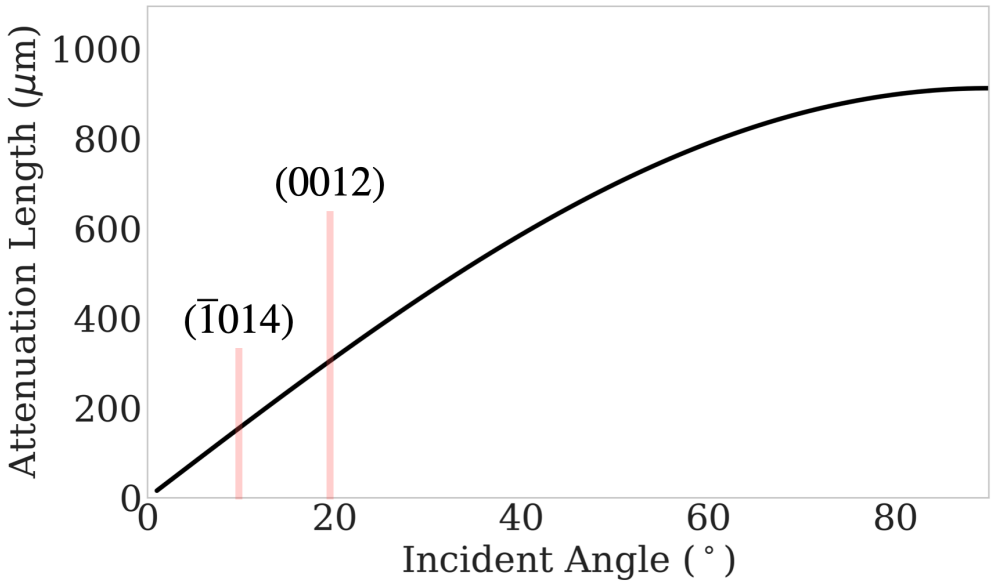

Figure 4.2: Attenuation length in $\mu\mathrm{m}$ as a function of incident beam angle in $^\circ$ for an incident beam energy of $17.792\,\mathrm{keV}$. Data for $90°$ attenuation length taken from [186].

The general experimental protocol, a schematic view of which can be seen in Fig.4.1, was as follows:

- The crystals were heated to $460\,^\circ\mathrm{C}$, corresponding to a mixed surface state of $Al+H_2O$ hydroxylated surface and Al-I terminated surface, as per Fig. 2.7b). Heating to such a temperature ensures the Gibbsite-like formation will disappear and maintains a highly wetting surface unlike if it had been treated by acid etching [154]. Once maintained at this temperature for more than $2\,\mathrm{h}$, the crystals were gradually maintained at $120\,^\circ\mathrm{C}$ until they were taken out of the oven FB1300 and put in the sample holder.

- The sample holder (with the α-Al_2O_3 crystal) was then quickly put in the sealed environment at room temperature and pressure, and a constant nitrogen flux was pumped in said environment. With these steps, we ensured that the surface had minimal interaction with the ambient environment.

- The crystal was then aligned. This requires finding two Bragg peaks first using a custom CCD (Charge-Coupled Device) camera by scanning the angular position of the sample, and tilting the sample to ensure that it is reflected in the arm. The pixel indexation on the camera corresponds to angular positions of the arm on which the spherical analysers are mounted (see Fig. 3.3). After removing the camera, we can then finely tune the angular position of the arm to have a high precision position of the Bragg peaks. The two Bragg peaks must not be collinear to recover the reciprocal space, and in practice these were (0012) and (300), to obtain the orientation (UB) matrix. From here we entered them in the in-house MathCAD program to obtain the (HKL) positions of the analysers (i.e the angular positions of the sample, tilt of the sample and angular position of the arm), and we verified that the reciprocal space was properly mapped out by finding the $(\bar{1}014)$ Bragg peak. From this point onwards we can perform our inelastic scans.

- We then started by scanning the crystal dry in regions of interest.

- To wet the crystal with high purity H_2O or D_2O (both water and heavy water were provided by the ESRF), we briefly took off the containment. The wetting was simply performed by spraying the liquid on the surface until completely wet, generally this takes around $\sim 50\,\mu\mathrm{L}$ of water. The majority of this water will be quickly drained away by gravity, leaving only a thin film on the crystal surface. Once done, we sealed the containment again. The operation was performed with continuous nitrogen flux throughout, in order to limit the interaction of the surface with the ambient atmosphere, even without containment.

- We then checked that the orientation (UB) matrix was still correct by positioning ourselves at known Bragg peaks, before performing our 'wetted' inelastic scans.

Each inelastic scan required an hour or more to complete, and it was then not always feasible within our limited allotted beamtime to re-measure the dry state for every scanned position. In these cases, we compared the data from wetted crystals to a baseline established from a separate but nominally identical dry crystal of the same batch purchased at Neyco [132]. We validated this approach by performing comparative measurements on multiple dry samples and confirmed that any crystal-to-crystal variation was negligible. Therefore, using a reference dry scan from a different crystal does not compromise the comparison and our analysis.

A natural question follows: does the X-ray beam interact with the water or heavy water at the crystal's surface? To answer this, let us first consider what type of interaction could put in jeopardy our goal of observing potential acoustic phonon changes in the bulk of the solid due to liquid wetting at ambient temperature and pressure. Two interactions are immediately apparent: does the high energy X-ray beam evaporate the water? Can we be sure not to pick

up on an inelastic signal from the water?

For both of these, an order of magnitude of the thickness of the film at the surface needs to be estimated. We shall therefore just consider two counteractive forces on the liquid: gravity and the adherence to the surface. In this simple estimate evaporation is neglected. We consider the wetting to occur on a surface that is orders of magnitude larger than the thickness, such that a one dimensional equilibrium taking into account film thickness h only can occur. The adherence to the surface is estimated using the disjoining pressure $\Pi(h) = \frac{A}{6\pi h^3}$ with A the Hamaker constant. This concept was introduced by Derjaguin in 1936 [187], who also investigated the low-frequency shear elasticity of thin liquid films [17]. It describes the pressure generated by van der Waals interactions acting between the solid-liquid and liquid-vapour interfaces, mediated through the thin liquid film. The surface therefore acts as a confinement of the liquid. For α-Al_2O_3, the Hamaker constant is in the literature in the range of 2×10^{-20} J to 5×10^{-20} J, and we shall here take the largest value of 5.3×10^{-20} J from [188] (which is measured between two surfaces of α-Al_2O_3) as this would yield the largest volume of water at the surface. Considering an equilibrium condition, we therefore have:

$$\rho g h = \frac{A}{6\pi h^3} \tag{4.1}$$

leading to

$$h = \left(\frac{A}{6\pi\rho g}\right)^{1/4} \tag{4.2}$$

Using the known values for gravity and the density of water, we obtain from equations (4.1) and (4.2) $h \sim 232\,\mathrm{nm}$. Let us now consider both of the potential X-ray beam interactions.

First, considering the lowest incident angle of $\sim 10°$, and therefore the longest beam path in the liquid, we shall calculate the absorbed proportion of the beam by the liquid layer using the Beer-Lambert law $\frac{I}{I_0} = e^{-L/L_{att}}$ where L is the path of the beam in the given material (in our case for $\sim 10°$, $L = 1.34\,\mu\mathrm{m}$) and L_{att} the attenuation length in that material. For water, $L_{att} = 10\,617\,\mu\mathrm{m}$ from [186], therefore we have $1 - \frac{I}{I_0} = 0.0126\,\%$ of the X-ray beam absorbed. Furthermore, due to the high specific heat of water, evaporation due to the X-ray beam is even less likely.

Second, the proportion of the inelastic signal recovered to be that of water instead of α-Al_2O_3 is entirely negligible for two reasons. The total signal from each material depends on the beam's interaction length, the number density of scattering units (molecules or formula units), and their intrinsic scattering power (proportional to ΣZ^2, with Z the atomic number). By combining these factors for the water film ($0.232\,\mu\mathrm{m}$ path) and the crystal ($150\,\mu\mathrm{m}$ interaction length), the calculated signal from the water is only $0.02\,\%$ of the signal from the crystal. Finally, the inelastic process studied is of a different nature than those of water. Phonon signals are sharp, localised features in energy-momentum space that arise from a periodic lattice. No such signal exists in an amorphous liquid like water.

In summary, high-resolution inelastic X-ray scattering scans were performed on α-Al_2O_3 crystals under both dry and (0001) surface wetted conditions, focusing on the $(\bar{1}014)$ and

(0012) BZs. We established that the thin ($\sim 100\,\mathrm{nm}$) water film's contribution to the signal is negligible, ensuring the collected spectra are a direct probe of the crystal's phonons. The raw data from these scans, seen in Fig.4.1, are of scattered intensity as a function of energy transfer. They must be analysed to extract the physical parameters of these phonons: energy, width etc. The following section details the procedure for this data treatment.

2 Data treatment

The raw signal from the IXS experiment is a measure of scattered intensity as a function of energy transfer, as shown for the $(\bar{1}013.5)$ position in Fig.4.3. The spectrum displays five distinct peaks corresponding to three physical phenomena. The one centred on $E = \hbar\omega = 0$ is the quasi-elastic peak, indicative of static defects and other slow diffusive dynamics of the solid. The other four inelastic peaks corresponding to two phonons are the transverse and longitudinal acoustic phonon signals, with their Stokes (positive energy) and anti-Stokes (negative energy) components respectively, as discussed in Chapter 3 section 1.6.

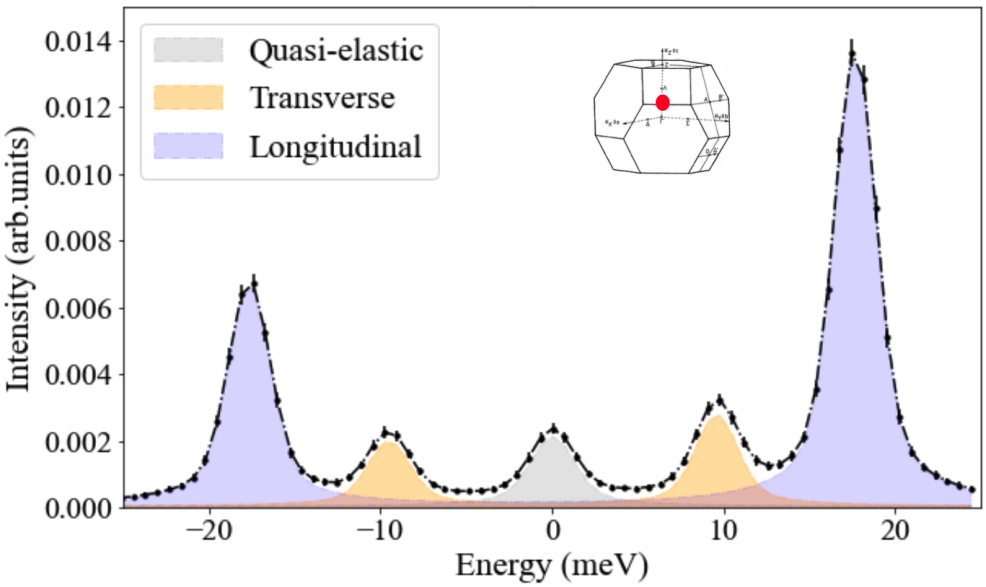

Figure 4.3: Illustration of data obtained at $\mathbf{Q} = (\bar{1}013.5)$ of a dry α-Al_2O_3 sample from ID28. Scan data is the points and the dashed black is the fitted data. The Transverse Acoustic (TA), Longitudinal Acoustic (LA), and quasi-elastic peaks are highlighted in orange, purple and grey respectively. Insert of the first BZ of α-Al_2O_3 from [142]

As explained in 3, the perceived signal is the convolution between the resolution function and the dynamic structure factor $S(\mathbf{Q}, \omega)$ (see (3.26)), and our goal is to deconvolute the dynamic structure from the resolution function to extract the physical phenomena. Thankfully, as discussed in 3.2.3, the resolution function for IXS can be considered independent of $\mathbf{Q}$, and therefore is a 1D function dependent on energy only. In practice, to deconvolute, we use Fit28, an in-house built program from the ID28 beamline.

Each of the contributions to the signal are fitted as such:

- The quasi-elastic peak (in grey in Fig.4.3) is fitted using a Lorentzian function

$$S_{qep}(\mathbf{Q},\omega) = \frac{A_{qep}(\mathbf{Q})}{\pi}\frac{\Gamma_{qep}/2}{\omega^2 + (\Gamma_{qep}/2)^2} \tag{4.3}$$

  where $A_{qep}(\mathbf{Q})$ is the amplitude of the quasi-elastic peak and Γ_{qep} the Full-Width-Half-Maximum of said peak.

- Each of the phonons are modelled as a Damped Harmonic Oscillator (DHO)

$$S_{DHO}(\mathbf{Q},\omega) = A_s(\mathbf{Q})\left[(\eta(\omega'_{\mathbf{q}s})+1)\frac{1}{\pi}\frac{\gamma_s/2}{(\omega-\omega'_{\mathbf{q}s})^2+(\gamma_s/2)^2} + \eta(\omega'_{\mathbf{q}s})\frac{1}{\pi}\frac{\gamma_s/2}{(\omega+\omega'_{\mathbf{q}s})^2+(\gamma_s/2)^2}\right] \tag{4.4}$$

  as defined in section 1.7. $\eta(\omega_{\mathbf{q}s}) = 1/(e^{\hbar\omega_{\mathbf{q}s}/k_bT}-1)$ is the Bose factor, and the Stokes and anti-Stokes have different intensity factors, respectively $\eta+1$ and η. Finally, $A_s(\mathbf{Q})$ is the intensity of the given phonon peak. The transverse acoustic phonon is visible in orange and the longitudinal acoustic phonon in purple in Fig.4.3.

A small note on Fig.4.3. The filled areas under the curve represent the individual contributions of each component (e.g., the LA phonon, the quasi-elastic peak) to the total fitted model, and not the component itself.

Combining all of these, the full dynamic structure factor is:

$$S(\mathbf{Q},\omega) = \underbrace{\frac{A_{qep}(\mathbf{Q})}{\pi}\frac{(\Gamma_{qep}/2)}{\omega^2+(\Gamma_{qep}/2)^2}}_{\text{Quasi-Elastic Peak}} + \sum_{s=1}^{2} A_s(\mathbf{Q})\underbrace{\left[(\eta(\omega'_{\mathbf{q}s})+1)\frac{1}{\pi}\frac{\gamma_s/2}{(\omega-\omega'_{\mathbf{q}s})^2+(\gamma_s/2)^2} + \eta(\omega'_{\mathbf{q}s})\frac{1}{\pi}\frac{\gamma_s/2}{(\omega+\omega'_{\mathbf{q}s})^2+(\gamma_s/2)^2}\right]}_{\text{Phonon Mode (DHO)}} \tag{4.5}$$

Having detailed the experimental setup and the data treatment protocol to obtain the full dynamic structure factor (4.5), we are now positioned to analyse the first results.

3 First identification of solid-liquid phononic interaction at a given point

3.1 Hardening of acoustic phonons

As previously stated, mainly two Brillouin Zones were scanned in the Γ-Z direction (see Fig.2.4), $(\bar{1}014)$ and (0012), each corresponding to a given penetration depth of $\sim 150\,\mu\text{m}$ and $\sim 300\,\mu\text{m}$ respectively. The first results were published in [189], but the results shown here are a mix of that set of experiments and those of a subsequent set, all performed at the ID28 ESRF. The reason for the second set being shown is that the scans were performed with a better incident flux leading to better statistics and confirming the replicability of the

experiment. We shall first discuss results obtained in the $(\bar{1}013.5)$ position, a specific position in reciprocal space, before expanding our analysis and presenting results in the full Γ-Z direction and in different BZs.

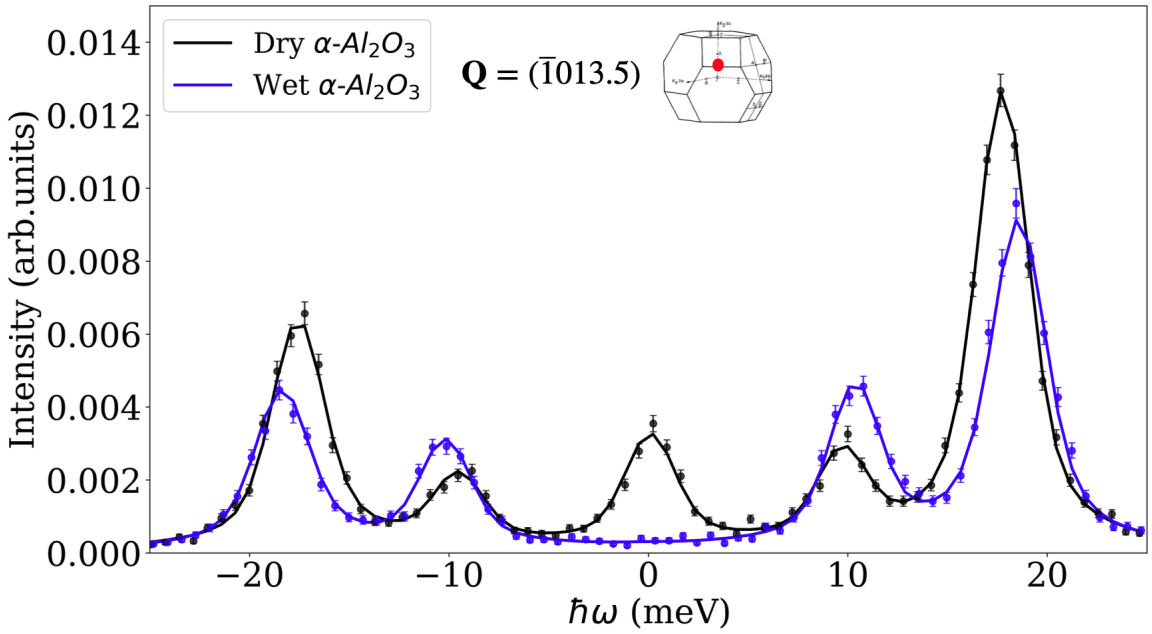

Figure 4.4: Inelastic X-ray scattering $(\bar{1}013.5)$ scans and fits of dry (black) and wetted (blue) results at $\mathbf{Q} = (\bar{1}013.5)$ of the same α-Al_2O_3 crystal performed at ID28 with $3\,\mathrm{meV}$ resolution, corresponding to a beam penetration of $\sim 150\,\mu\mathrm{m}$. The wet scan was performed roughly $6\,\mathrm{h}$ after the wetting. Experiments performed under $6\,\mathrm{L\,min^{-1}}$ nitrogen flux, at room temperature and pressure. Insert of the first BZ of α-Al_2O_3 from [142]

As can be seen in Fig.4.4, a multitude of effects are visible due to wetting:

- Collapse of the quasi-elastic peak at the $(\bar{1}013.5)$ position. Indeed, at $\omega = 0\,\mathrm{meV}$, the signal is completely gone, indicating as a first interpretation a suppression of a slow diffuse process or inducing a more ordered state within the crystal.
- A change of phonon energy of both transverse acoustic and longitudinal acoustic phonons at the $(\bar{1}013.5)$ position. More precisely, both the LA and TA phonons increase in energy. In the literature, this process is named hardening. A first interpretation is an increased rigidity of the crystal due to wetting. We will see in this chapter that the wetting is not sufficient and that an induced non-equilibrium state must be established.

We shall discuss the collapse of the quasi-elastic peak in the further section 6 and will, in this section, concentrate on the hardening process at this given position of $(\bar{1}013.5)$.

The hardening process shown in Fig.4.4 shows a $0.83\,\mathrm{meV}$ and $0.73\,\mathrm{meV}$ increase of the LA and TA branches respectively. This is a clear indication that the liquid has an effect on phonon vibrations far from the interface. A more thorough discussion of hardening will take place in section 5.

It is noteworthy to highlight that this scan was performed six hours after wetting, and therefore it is highly improbable that the hypothesis of negligible evaporation used in section 1 to determine a reasonable liquid thickness at the surface is still valid. It was therefore our idea to continuously scan the same point in reciprocal space to determine whether this effect is time dependent, as within those timescales it is reasonable to assume that evaporation takes place. This will be the main subject of the rest of this section.

3.2 Kinetic effects of hardening and observation of broadening

Scanning the $(\bar{1}013.5)$ continuously was done in the following way: each scan took $50\,\mathrm{min}$ and between scans we waited $5\,\mathrm{min}$ to leave time for the monochromator to be stabilised in temperature. As such, the average time of the experiment is written, as seen in Fig. 4.5.

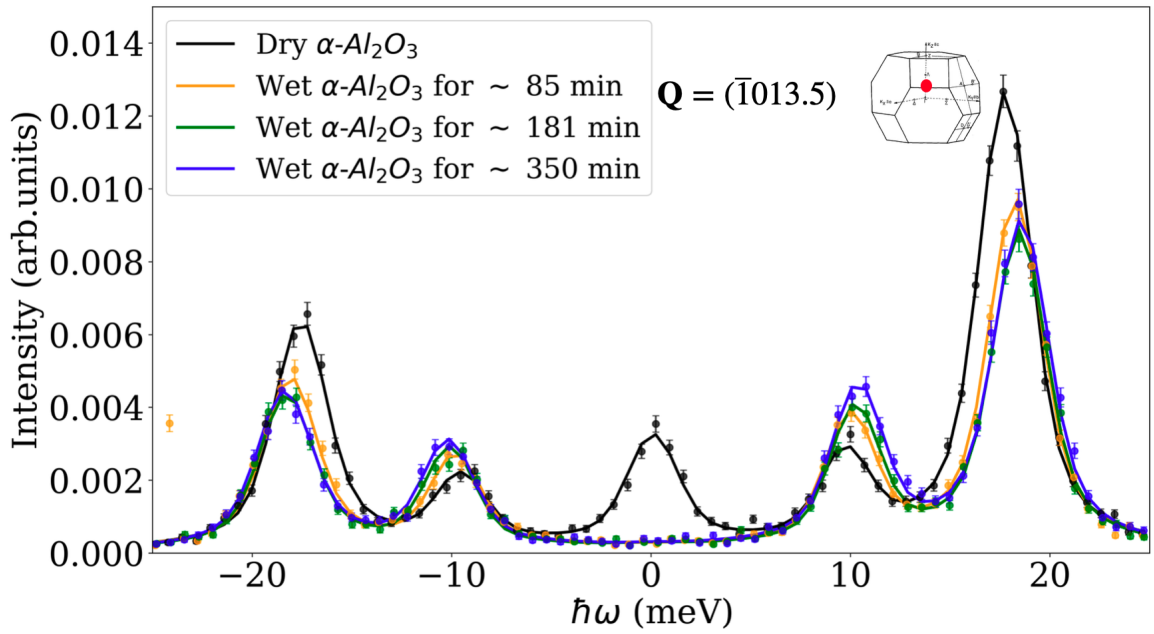

Figure 4.5: Inelastic X-ray scattering $(\bar{1}013.5)$ scans and fits of dry (black) and wetted at $\sim 85\,\mathrm{min}$ (orange), $\sim 181\,\mathrm{min}$ (green) and $\sim 350\,\mathrm{min}$ (blue) results at $\mathbf{Q} = (\bar{1}013.5)$ of the same α-Al_2O_3 crystal performed at ID28 with $3\,\mathrm{meV}$ resolution, corresponding to a beam penetration of $\sim 150\,\mu\mathrm{m}$. Experiments performed under $6\,\mathrm{L\,min^{-1}}$ nitrogen flux, at room temperature and pressure. Insert of the first BZ of α-Al_2O_3 from [142]

Fig.4.5 shows a clear temporal dependence of the hardening, where the LA energy continuously increases from $17.7\,\mathrm{meV}$ seemingly stabilising around $18.5\,\mathrm{meV}$, and the TA branch goes from $9.6\,\mathrm{meV}$ to $10.3\,\mathrm{meV}$ with a similar kinetic profile. But what is at the source of the kinetic effect? As we do not see such effects without wetting (we verified by rescanning the same dry point twice, without any change), it must be due to the presence of water at the surface. Our first intuition relative to this phenomenon is that it may be due to evaporation, and, as the liquid evaporates, the quantity of liquid at the surface lowers, until only a few layers remain many hours later. However, this would not explain why a hardening would increase with a decreasing volume of liquid?

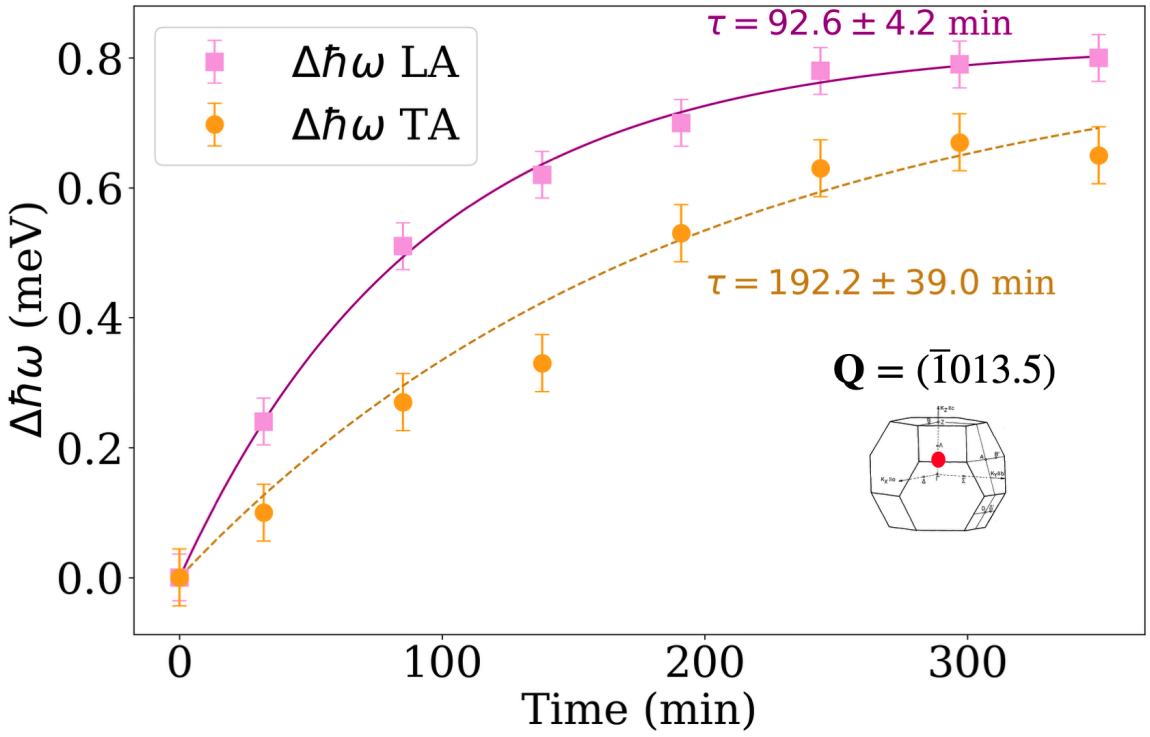

Figure 4.6: Time evolution of TA (orange circles) and LA (purple squares) hardening fitted with a relaxation $\Delta\hbar\omega = A(1 - e^{-t/\tau})$ law at $\mathbf{Q} = (\bar{1}013.5)$ of the same α-Al_2O_3 crystal after H_2O wetting. Scans performed under continuous $6\,\mathrm{L\,min^{-1}}$ nitrogen flux. Error bars are of $\pm 0.036\,\mathrm{meV}$ for the LA branch and $\pm 0.044\,\mathrm{meV}$ for the TA branch. Data obtained by Inelastic X-ray scattering at room temperature and pressure. Insert of the first BZ of α-Al_2O_3 from [142]

Fig.4.6 reveals that the hardening takes a long period of time for TA and LA branches, about $\sim 4\,\mathrm{h}$ to $5\,\mathrm{h}$ for both, to reach a stationary state. We have purposely chosen a simple relaxation model to have an idea of the behaviour of hardening, but not impose a form of physics onto the data. This leads to very good agreement for the LA branch and a poor agreement for the TA branch. Indeed both the branches saturate and reach an overt maximum, well captured for the LA branch but not the TA. To obtain the physical error bars, one would have to scan multiple times the same dry crystal, at the same position, to obtain a large amount of LA and TA phonon energy data, and associate a standard deviation on that set. This, however useful, is not generally feasible with the time constraints associated with performing experiments in large facilities such as the ESRF. However, one set of experiments at $(\bar{1}013.5)$ that we will discuss in a following subsection showed no significant effects, and we have used this as the experimental error bar. The numerical error bar, in comparison, was more than an order of magnitude lower, so is completely neglected.

This stationary state itself is both puzzling and reassuring. Indeed it is puzzling, as if the kinetic aspect is a consequence of evaporation, it should continue and not saturate as the evaporation continues until only a few layers of liquid are present at the surface. On the other hand, as the free water molecules completely evaporate, one would intuit that there are no effects on the bulk of the solid, as we postulate that the hardening effects here discussed

must be a consequence of the novel long-range dynamics within liquids observed by means of their low-frequency shear elasticity. We do not have an answer to this question but will come back to the kinetics of the phononic interaction in Chapter 5.

Furthermore, we show, from another set of experiments, visible in Fig.4.7, that the hardening remains stable for at least $12\,\mathrm{h}$ after wetting (the blue curve corresponding to $12\,\mathrm{h}$ post wetting is overlapping with the green and purple curves corresponding to $6\,\mathrm{h}$ and $9\,\mathrm{h}$ in Fig.4.7). This therefore gives us a window of at least $6\,\mathrm{h}$ where the hardening phenomena has stabilised.

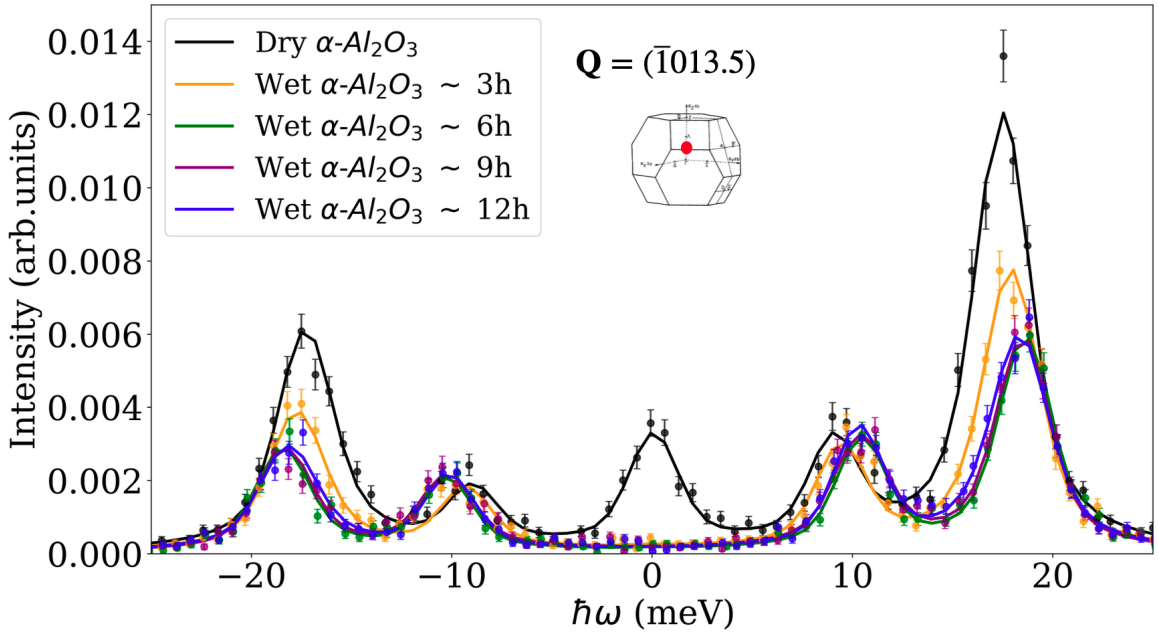

Figure 4.7: Inelastic X-ray scattering $(\bar{1}013.5)$ scans and fits of dry (black), H_20 wet $3\,\mathrm{h}$ (orange), $6\,\mathrm{h}$ (green), $9\,\mathrm{h}$ (purple) and $12\,\mathrm{h}$ (blue) of the same α-Al_2O_3 crystal performed at ID28 with $3\,\mathrm{meV}$ resolution, corresponding to a beam penetration of $\sim 150\,\mu\mathrm{m}$. The blue ($\sim 12\,\mathrm{h}$ after wetting) overlaps with the green and purple curves corresponding to $\sim 6\,\mathrm{h}$ and $\sim 9\,\mathrm{h}$ after wetting. Experiments performed under $6\,\mathrm{L\,min^{-1}}$ nitrogen flux, at room temperature and pressure. Insert of the first BZ of α-Al_2O_3 from [142]

Observation of broadening While we have treated mostly the energies of the phonon branches, other quantities may be of interest, namely the phonon width (FWHM), and the key question here would be: do they follow the same kinetic behaviour? This is shown in Fig. 4.8. For the TA branch, while there are changes in phonon width, it neither follows a trend nor can it be concluded that it is a wetting induced effect. Indeed, the dashed line in Fig.4.8 is the upper limit of the resolution, in the sense that the resolution at the ESRF for the Si(999) reflection is of $3.0(2)\,\mathrm{meV}$, and as such we have disregarded any increase if the phonon width observed was not above the $0.2\,\mathrm{meV}$ threshold. The LA branch, on the other hand, shows a sustained broadening after $200\,\mathrm{min}$, but a kinetic evolution similar to hardening is not clear. Our current results shown in Fig.4.8 suggest this does not follow the same

kinetic trend, while it does seem to settle on a stationary state. Nonetheless, a broadening of phonon peaks is observed for the LA branch, passing from $0.45\,\mathrm{meV}$ to $0.63\,\mathrm{meV}$ after $4\,\mathrm{h}$. The broadening kinetics do not match the hardening kinetics, which could be due to TA and LA peaks being close to one another in energy (see Fig.4.5). It may be harder to dissociate these two peaks' width, and we would suggest scanning a BZ where the Γ-Z branch is orthogonal to the polarisation vector (of either TA or LA) to elucidate this. Another consideration would be to change the energy resolution is of $1.5\,\mathrm{meV}$ (changing reflection to Si(121212), but greatly reducing incident photon flux) or perform experiments with inelastic neutron scattering.

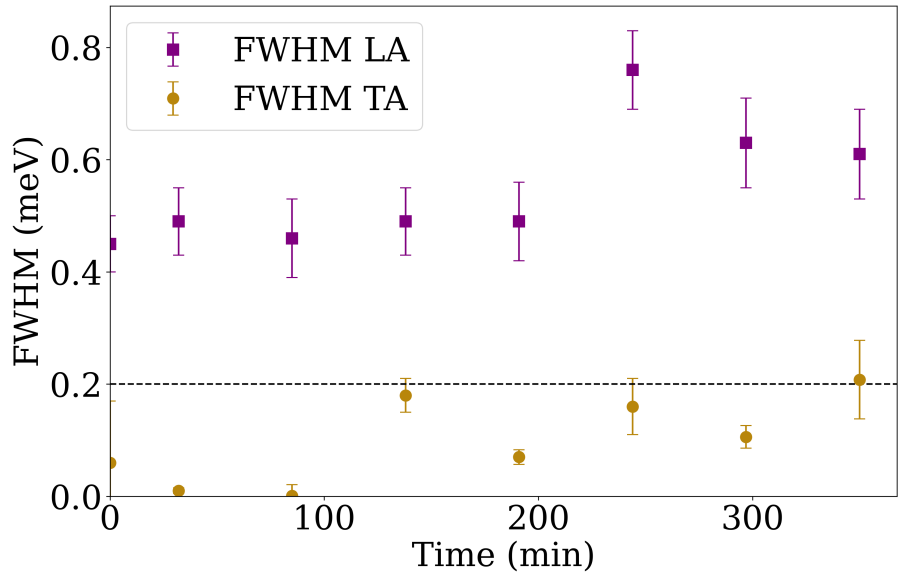

Figure 4.8: Time evolution of FWHM of TA (orange circles) and FWHM of LA (purple squares) of the same α-Al_2O_3 crystal at $\mathbf{Q} = (\bar{1}013.5)$. Dashed black line is the upper limit of the resolution of ID28. Data obtained by Inelastic X-ray scattering at room temperature and pressure. Scans performed under continuous $6\,\mathrm{L\,min^{-1}}$ nitrogen flux. The error bars are numerical error bars.

We have therefore identified an unexpected wetting induced hardening of both TA and LA peaks at the $(\bar{1}013.5)$, following a long-timescale kinetic evolution. This is accompanied by a broadening of LA peaks at long time, but not clearly following the same kinetics as hardening. Wetting the surface is interfering with solid phonon dynamics at $\sim 150\,\mu\mathrm{m}$ from the surface.

3.3 Reversibility of hardening and broadening

When the free molecules of water are fully evaporated and few molecular layers of water remain, are the "normal" (i.e., dry) alumina characteristics recovered? This became apparent when we scanned crystals (in practice we had ten) without tracking them individually. In that sense, throughout our experiments, we often rescanned a previously wetted crystal, but as long as it underwent the heating process described in section 1, rescanning it would yield back single crystal 'normal' behaviour. Furthermore this highlights that wetted crystals were in no way damaged, changed or underwent irreversible transformations. The liquid at the

surface is therefore key to initiate this new form of solid-liquid phonon interaction.

3.3.1 Reversibility of hardening

When crystals were aligned, as discussed in the experimental protocol 1, we would perform scans at different positions in reciprocal space. After having discovered the kinetics of wetting induced hardening discussed in the previous subsection, we would systematically wait $6\,\mathrm{h}$ prior to scanning at multiple points, as we found out that between $6\,\mathrm{h}$ to $12\,\mathrm{h}$ at least the hardening effects were stable, see Fig.4.7. Once these scans were performed, we came back, $\sim 15\,\mathrm{h}$ after wetting, to the $(\bar{1}013.5)$ position, to see whether the hardening had in any way changed. This is shown in Fig. 4.9.

The Fig.4.9 result is a very strong indicator of a reversible effect of wetting induced hardening over time. Indeed, the $\sim 890\,\mathrm{min}$ (i.e $15\,\mathrm{h}$ after wetting) scan is regressing towards lower energies compared to the scan $\sim 350\,\mathrm{min}$ (i.e $6\,\mathrm{h}$ after wetting). The energies of the LA branch go from $18.49\,\mathrm{meV}$ at $6\,\mathrm{h}$ after wetting to $18.17\,\mathrm{meV}$ $15\,\mathrm{h}$ after wetting. Similarly, the TA branch goes from $10.28\,\mathrm{meV}$ to $9.99\,\mathrm{meV}$ between the scans.

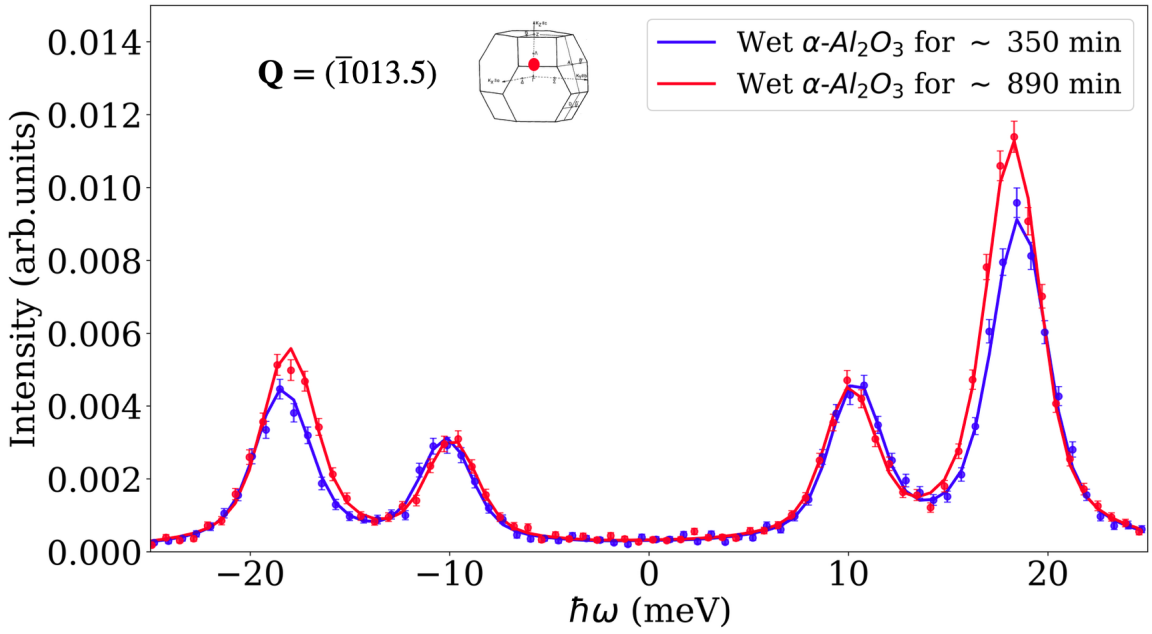

Figure 4.9: Inelastic X-ray scattering $(\bar{1}013.5)$ scans and fits of wetted at $\sim 350\,\mathrm{min}$ (dashed blue) and at $\sim 891\,\mathrm{min}$ (dashed red) results at $\mathbf{Q} = (\bar{1}013.5)$ of the same α-Al_2O_3 crystal performed at ID28 with $3\,\mathrm{meV}$ resolution, corresponding to a beam penetration of $\sim 150\,\mu\mathrm{m}$. Experiments performed under $6\,\mathrm{L\,min^{-1}}$ nitrogen flux, at room temperature and pressure. Insert of the first BZ of α-Al_2O_3 from [142]

As previously stated, it wasn't feasible for us to scan the crystal under constant nitrogen flux continuously until the effects had reversed due to time constraints inherent to experiments in large scale facilities. However, in one of our experiments, there was a technical

problem with the storage ring of the ESRF meaning that the beam flux was null for a period of $74\,\mathrm{h}$. This happened as we were scanning, for $4\,\mathrm{h}$ continuous hours, a position in reciprocal space. We therefore decided to leave the crystal in the previously established experimental setup 1. $78\,\mathrm{h}$ after wetting, we rescanned said crystal, the results are visible in Fig.4.10. During this set of experiments the orientation (UB) matrix was slightly off, meaning that the scanned point was off-plane in the $a*$ direction and it is not directly, in terms of energy, comparable to the previous scans at $(\bar{1}013.5)$. The scanned point is nonetheless in the $(\bar{1}014)$ BZ.

Fig.4.10 highlights that after $78\,\mathrm{h}$, wetting induced hardening is gone back closer to dry conditions. Four hours after wetting the 'TA' and 'LA' phonons peaks have shifted from their dry values of $10.85\,\mathrm{meV}$ and $18.9\,\mathrm{meV}$ towards $12.55\,\mathrm{meV}$ and $20.47\,\mathrm{meV}$ respectively. We note that these are not exactly the same energies as those at the $(\bar{1}013.5)$ position (see Fig. 4.9 and 4.4) for the reason that the scanned position was off-plane discussed above. Nonetheless, the kinetic hardening is visible. After $\sim 78\,\mathrm{h}$, the 'TA' and 'LA' peaks have nearly reverted towards the dry state, with respective energies of $11.14\,\mathrm{meV}$ and $19.1\,\mathrm{meV}$ (here we use the apostrophe as it is not exactly either a TA or LA branch, due to being slightly off-plane). Unlike the 'TA' peaks due to off-plane scans, the 'LA' peaks are well encapsulated by the fit, and more subtle results can be extracted from them.

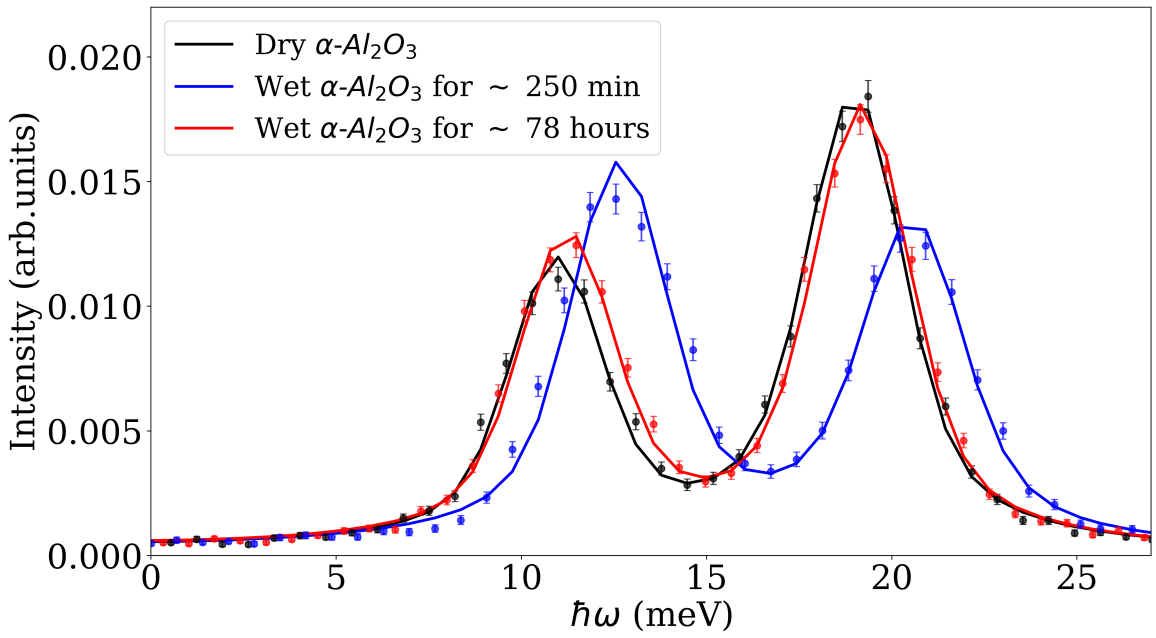

Figure 4.10: Inelastic X-ray scattering scans at the same off-plane position of the same α-Al_2O_3 crystal. Dry α-Al_2O_3 crystal data is in black, wet after $\sim 250\,\mathrm{min}$ in blue and wet after $\sim 78\,\mathrm{h}$ in red. Scans performed at ID28 with $3\,\mathrm{meV}$ resolution, corresponding to a beam penetration of $\sim 150\,\mu\mathrm{m}$. Experiments performed under $6\,\mathrm{L\,min^{-1}}$ nitrogen flux, at room temperature and pressure.

The result from Fig. 4.10 underlines that the hardening observed is not a consequence of the $Al(OH)_3$ Gibbsite layer formation formed during the wetting process. Indeed, the $Al(OH)_3$ Gibbsite-like surface does not disappear by evaporation itself, it is tightly bound to

the surface, and said surface must be annealed at least $170\,^{\circ}\mathrm{C}$ for it to evaporate at room pressure, as shown in Fig. 2.7b) from [153]. Furthermore, at room temperature and pressure, a molecular amount of water at the surface will remain, and this is also shown in Fig.2.7b) from [153], where $Al(OH)_3 + H_2O$ curve is about $80\,\%$ of the wetted surface. This may be the reason for the remaining, even after $78\,\mathrm{h}$, ever so slight hardening state observed on Fig.4.10.

What would happen if we were to re-wet the same crystal? Would the kinetics restart? The results at $\sim 250\,\mathrm{min}$ after initial wetting and at the same time after rewetting are shown in Fig.4.11. The 'TA' and 'LA' branches are not exactly equal, but similarly show a hardened state from the dry crystal. Here, the 'LA' peaks have $0.26\,\mathrm{meV}$ difference, and the 'TA' peaks $0.3\,\mathrm{meV}$, compared with respect to the initial dry crystal energy differences of $1.75\,\mathrm{meV}$ for the 'TA' peaks and 1.57 for the 'LA' peaks.

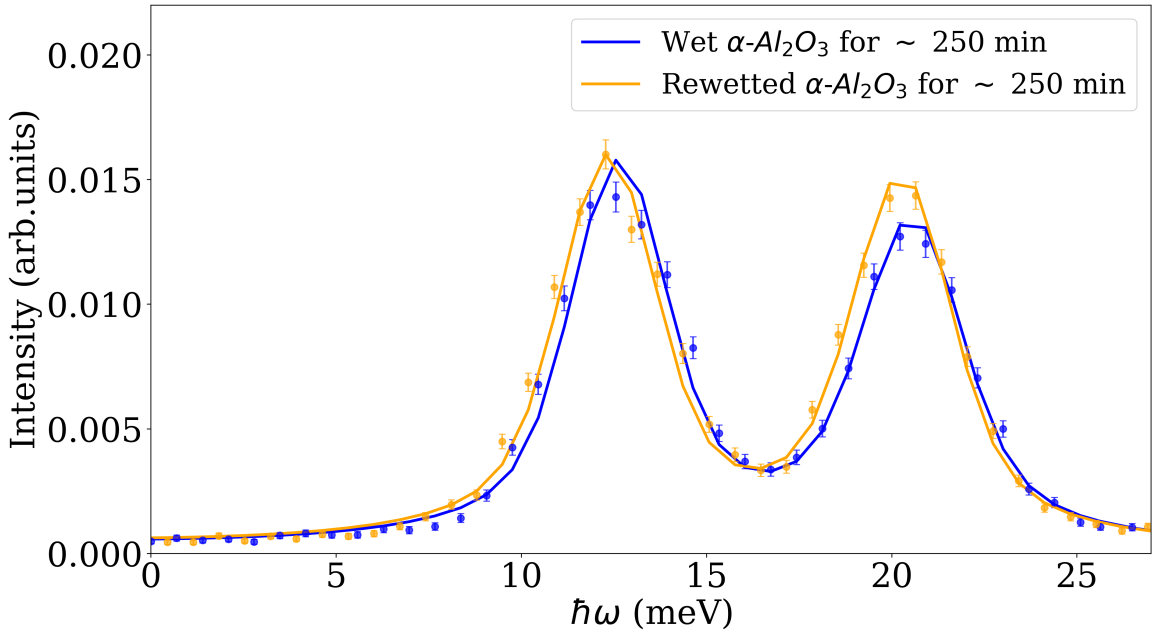

Figure 4.11: Inelastic X-ray scattering scans and fits at the same off-plane position of the same α-Al_2O_3 crystal comparing the hardening obtained by wetting and rewetting. H_20 wetted scan after $\sim 250\,\mathrm{min}$ data in blue and $H_2 0$ rewetted after $\sim 250\,\mathrm{min}$ data in orange. Scans performed at ID28 with $3\,\mathrm{meV}$ resolution, corresponding to a beam penetration of $\sim 150\,\mu\mathrm{m}$. Experiments performed under $6\,\mathrm{L\,min^{-1}}$ nitrogen flux, at room temperature and pressure.

3.3.2 Identification of a broadening effect

Furthermore, Tab.4.1 shows the FWHM of the 'LA' peaks of the scans, and $\sim 250\,\mathrm{min}$ after wetting a broadening of the 'LA' peak is clear, whether wetted or rewetted. This is a clear indicator that the hardening effects are linked to a broadening of the peak, and will be a crucial part of our attempt to explain these results as anharmonic effects in section 5 and chapter 5.

	Dry scan	H_20 wet $\sim 250\,\mathrm{min}$	H_20 wet $\sim 78\,\mathrm{h}$	H_20 rewet $\sim 250\,\mathrm{min}$
FWHM (meV)	0.44(6)	0.66(9)	0.41(6)	0.57(7)

Table 4.1: Broadening of the 'LA' branch of the scan shown in Fig.4.10 and Fig.4.11 at $\mathbf{Q} = (\bar{1}013.5)$ under continuous $6\,\mathrm{L\,min^{-1}}$ nitrogen flux. Data obtained by Inelastic X-ray scattering at room temperature and pressure.

To conclude, the long term kinetics in Fig.4.9 indicated a return towards an unwetted state after a long period of time, and Fig.4.10 clearly confirms this indication on an off-plane series of scans. Furthermore, rewetting said crystal that was maintained in the experimental conditions shown in Fig.4.1 restarts the kinetic process, and leads to both a hardening of peaks and a broadening of the 'LA' peak. This highlights very clearly that wetting induced hardening and broadening are kinetic processes, not only reversible by heating, but that can be retriggered by re-adding water at the surface.

3.4 Dependence of hardening and broadening on nitrogen flux

The long-term kinetics discussed in subsection 3.2 are likely related to evaporation of the free water molecules at first, followed by a slow kinetic 'relaxation' towards the dry state discussed in the previous subsection.

Therefore, in an effort to increase the stable window of $6\,\mathrm{h}$ to $12\,\mathrm{h}$, we decided that we would lower the incident nitrogen flux to $3\,\mathrm{L\,min^{-1}}$ to see if this were to slow down the evaporation by potentially slightly increasing the relative humidity in the atmosphere. However, as shown in Fig.4.12, the main impact that this had was to lower the hardening value for both TA and LA peaks after roughly $6\,\mathrm{h}$, i.e the time scale at which hardening stabilises for a few hours. Indeed the hardening of the TA wave was $0.21\,\mathrm{meV}$ and the LA wave was $0.31\,\mathrm{meV}$, in contrast with the $0.65\,\mathrm{meV}$ and $0.82\,\mathrm{meV}$ respectively observed at the same position in reciprocal space when the scans were under $6\,\mathrm{L\,min^{-1}}$ nitrogen flux.

This was in opposition to our intuition where we thought that this would not have an impact on the hardening, but maybe on the kinetic. It therefore is of interest to see how the kinetics are changed by this change of incident nitrogen flux. Fig.4.13 shows these results. While there is a difference of roughly $30\,\mathrm{min}$ on the relaxation time τ, the kinetics observed are of the same order of time magnitude to reach a stationary state for the LA branch with an incident nitrogen flux of $6\,\mathrm{L\,min^{-1}}$ (see Fig.4.5) and the simple relaxation function is sufficient to encapsulate the hardening kinetics.

The TA branch at $3\,\mathrm{L\,min^{-1}}$ nitrogen flux kinetic behaviour is also correctly encapsulated by the exponential relaxation fit, contrary to the $6\,\mathrm{L\,min^{-1}}$ nitrogen flux kinetics in Fig.4.6. It yields a similar relaxation time to the LA branch of roughly $78(19)\,\mathrm{min}$. This is a reassuring result, as while we could not fit it with the simple relaxation of the TA for $6\,\mathrm{L\,min^{-1}}$ nitrogen, we clearly observed a saturation. Therefore, Fig.4.13 confirms that the TA hardening is saturated, and of the same time order of magnitude as the LA branch. A noteworthy similarity between the $6\,\mathrm{L\,min^{-1}}$ and $3\,\mathrm{L\,min^{-1}}$ nitrogen flux hardening kinetics is the ratios of asymptotic hardening, which are shown in equations (4.7) and (4.6).

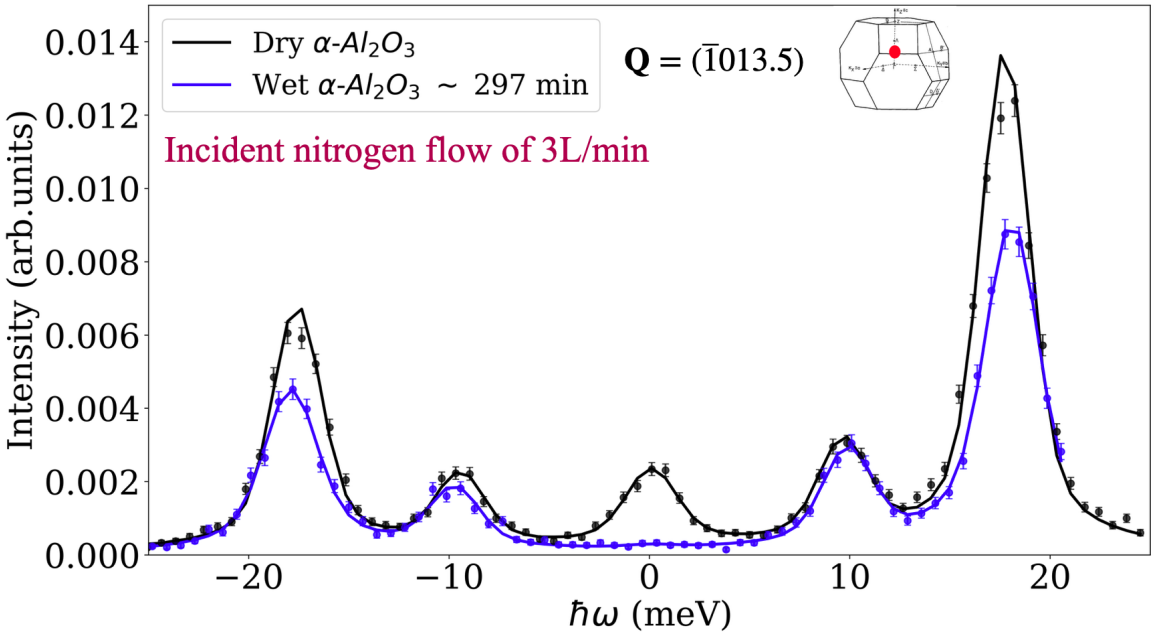

Figure 4.12: Inelastic X-ray scans and fits of dry α-Al_2O_3 data (black) and wetted at $\sim$ 297 min data (blue) results at $\mathbf{Q} = (\bar{1}013.5)$ of the same crystal performed at ID28 with 3 meV resolution, corresponding to a beam penetration of $\sim 150\,\mu$m. Experiments performed under 3 L min^{-1} nitrogen flux, at room temperature and pressure. Insert of the first BZ of α-Al_2O_3 from [142]

$$\frac{\Delta\hbar\omega_{TA}(3L.min^{-1})}{\Delta\hbar\omega_{LA}(3L.min^{-1})} = \frac{0.21 \pm 0.044}{0.31 \pm 0.036} = 0.68 \pm 0.16 \tag{4.6}$$

$$\frac{\Delta\hbar\omega_{TA}(6L.min^{-1})}{\Delta\hbar\omega_{LA}(6L.min^{-1})} = \frac{0.61 \pm 0.044}{0.82 \pm 0.036} = 0.74 \pm 0.06 \tag{4.7}$$

As a small note, the hardening $\Delta\hbar\omega$ of the branches was taken to be the asymptotic value from the relaxation fit. The $\Delta\hbar\omega_{TA}(6L.min^{-1})$ is the value of the last point on Fig.4.6, as the relaxation fit did not properly encapsulate the kinetic behaviour. While this similarity seems to be a general indication of both TA and LA hardening behaviour, we do not know how to interpret it.

To further this understanding we decided to scan a dry crystal under the conditions outlined prior in 1, with a continuous nitrogen flux to limit contamination. We then wetted with H_2O said crystal, put it back in the container, and stopped the nitrogen flux. The time evolution and a direct scan comparison are shown in Fig.4.14a) and b). The results are clear: nitrogen flux is needed to observe this hardening effect.

Furthermore, the insert b) in Fig. 4.14 clearly shows no broadening whatsoever due to wetting, confirming that with the hardening of the LA and TA branches comes a measurable broadening of the LA peak (as the TA one is within the resolution of the measurements).

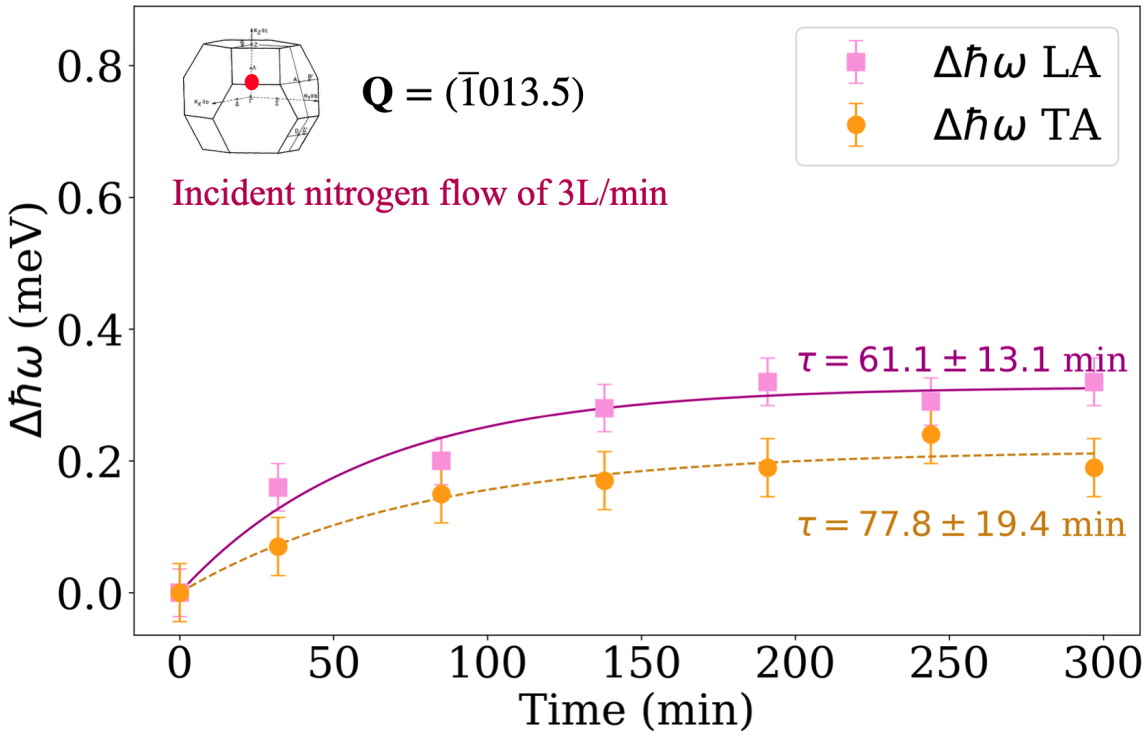

Figure 4.13: Time evolution of TA (orange circles) and LA (purple squares) hardening fitted with a relaxation $\Delta\hbar\omega = A(1 - e^{-t/\tau})$ law at $\mathbf{Q} = (\bar{1}013.5)$ of the same α-Al_2O_3 crystal. Scans performed under continuous $3\,\mathrm{L\,min^{-1}}$ nitrogen flux. Error bars are of $\pm 0.036\,\mathrm{meV}$ for the LA branch and $\pm 0.044\,\mathrm{meV}$ for the TA branch. Data obtained by Inelastic X-ray scattering at room temperature and pressure. Insert of the first BZ of α-Al_2O_3 from [142]

On a side note, the results showing no change whatsoever, the experimental error bars on the LA and TA branches used in Fig.4.6, 4.13 and 4.14 are calculated with this data set.

The necessity for nitrogen flux rules out the evaporation as being necessary and sufficient to induced hardening and broadening. This is highly particular and the only physical explanation that we could find, was that the nitrogen flux, when turned on, would create a recirculating bubble of air that will result in air flow at the interface.

We therefore decided to use an anemometer Anemometer TA300 (Trotec) with an accuracy of $\pm 5\,\%$ m/s and minimum measurement of $0.1\,\mathrm{m\,s^{-1}}$, taking off the kapton window and measuring close to the surface the speed of air due to the incident nitrogen flux. The results are shown in Tab.4.2. The nitrogen flux does in fact create an air recirculation that results in an air flow at the liquid surface.

Nitrogen flux	$0\,\mathrm{L\,min^{-1}}$	$3\,\mathrm{L\,min^{-1}}$	$6\,\mathrm{L\,min^{-1}}$	$9\,\mathrm{L\,min^{-1}}$
Speed (m/s)	0	0.08	0.12	0.16

Table 4.2: Speed of air due to the nitrogen flux measured with anemometer Anemometer TA300 (Trotec)

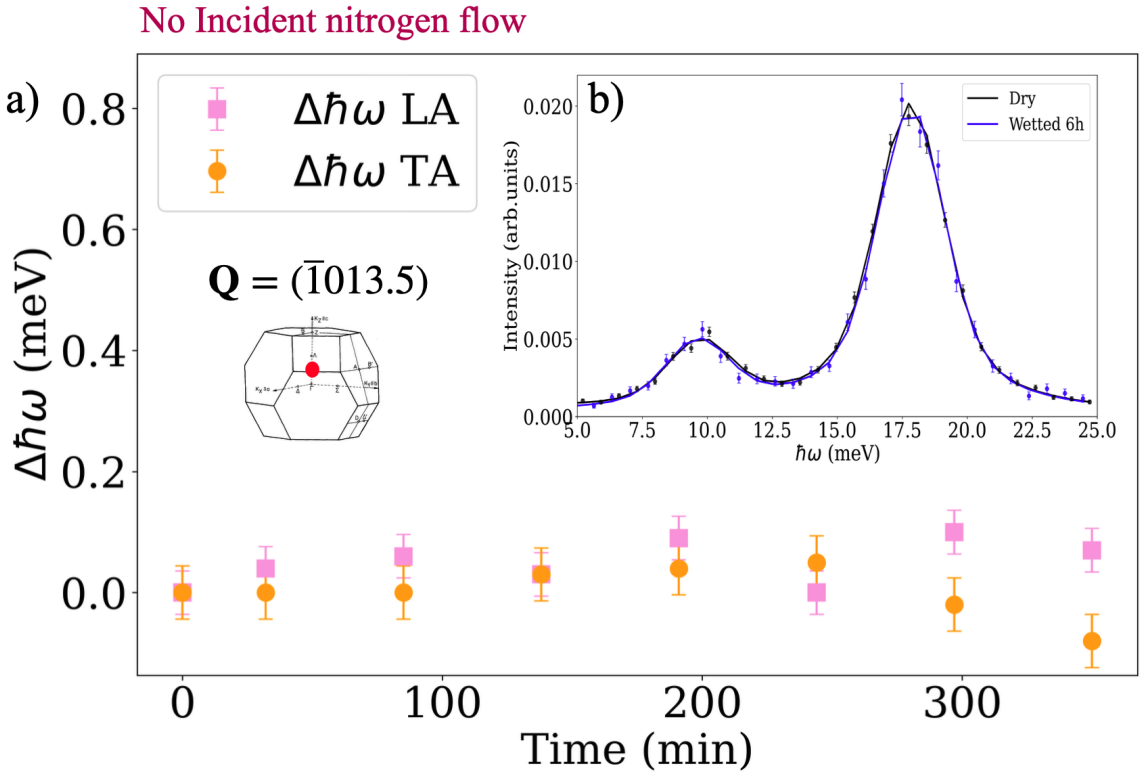

Figure 4.14: a) Time evolution of TA (orange circles) and LA (purple squares) energy shifts at $\mathbf{Q} = (\bar{1}013.5)$ of the same α-Al_2O_3 crystal. b) Comparison of a dry and wetted scans at $\sim 6\,\mathrm{h}$ after H_2O wetting. Wetted scans performed no nitrogen flux. Error bars are of $\pm 0.036\,\mathrm{meV}$ for the LA branch and $\pm 0.044\,\mathrm{meV}$ for the TA branch. Data obtained by Inelastic X-ray scattering at room temperature and pressure. Insert of the first BZ of α-Al_2O_3 from [142]

This air flow maintains the liquid in a non-equilibrium stressed state, and given the assumed nanometre scale of the liquid thickness, with the high solid energy acting as a de facto confinement, our interpretation is the remaining liquid, exhibiting shear elastic-like behaviour, is solicited and interacts beyond the hydrophilic interface. Furthermore, this is not the first case in literature where liquid flows induce a non-equilibrium thermodynamic state that leads to anharmonic effects. We shall discuss this in further detail in section 7, before discussing isotopic results by substituting water for heavy water in the next subsection.

To conclude, we have observed a nitrogen flux dependence on the values of hardening and broadening of inelastic peaks in the solid bulk. When there is no flux, there is no hardening and/or broadening of either LA or TA peaks at $(\bar{1}013.5)$. We have linked this flux dependence to air recirculation stressing the liquid wetting the crystal, maintaining it in a non-equilibrium thermodynamic state. Furthermore, the results shown in Fig.4.14 clearly indicate that evaporation is not the driving parameter for hardening. We shall confirm this in the following chapter.

4 Isotopic effects: the case of heavy water

4.1 Results

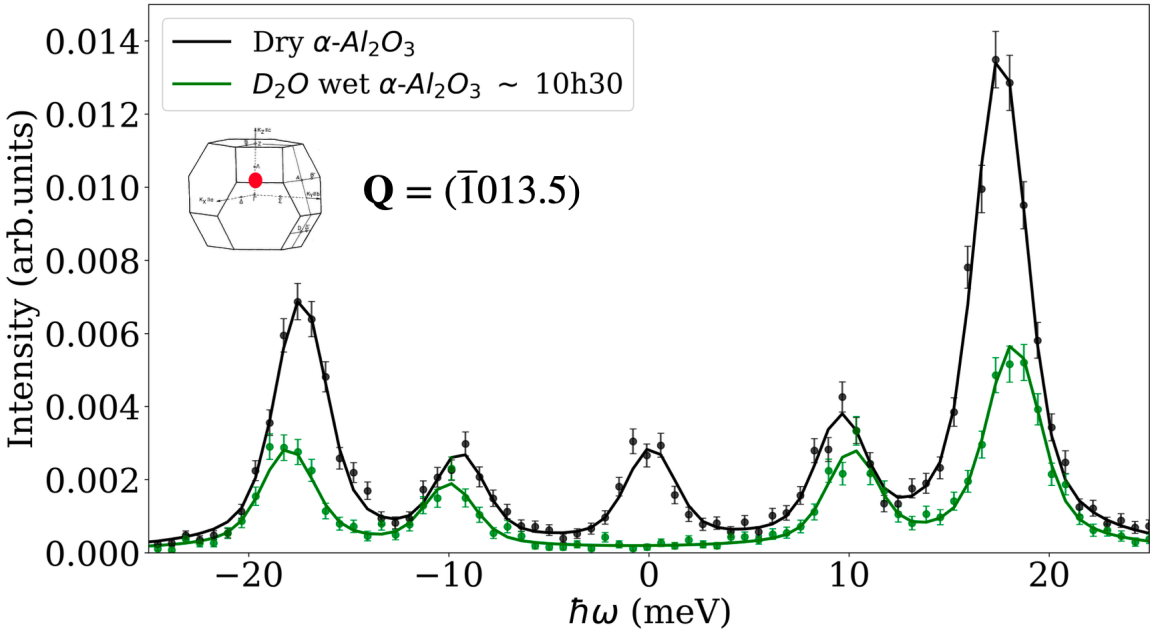

Figure 4.15: Inelastic X-ray scattering scans and fits of dry (black) and D_2O wetted at $\sim 10.5\,\mathrm{h}$ (green) results at $\mathbf{Q} = (\bar{1}013.5)$ of the same α-Al_2O_3 crystal performed at ID28 with $3\,\mathrm{meV}$ resolution, corresponding to a beam penetration of $\sim 150\,\mu\mathrm{m}$. Experiments performed under $6\,\mathrm{L\,min^{-1}}$ nitrogen flux, at room temperature and pressure. Insert of the first BZ of α-Al_2O_3 from [142]

In this subsection we will discuss results of an experiment where we followed all the steps of section 1 but simply replaced the liquid from light water to heavy water. This experiment was performed under $6\,\mathrm{L\,min^{-1}}$ nitrogen flux. Fig.4.15 shows two fitted scans of the same crystal dry and in the wetted state after $10.5\,\mathrm{h}$ with D_2O. Similarly to light water, heavy water induces a TA and LA hardening of the α-Al_2O_3. However, while hard to simply see with scans, with D_2O, the hardening is less than with light water, with the LA branch seeing a hardening of $\sim 0.6\,\mathrm{meV}$ and the TA branch of $\sim 0.45\,\mathrm{meV}$ compared to the $\sim 0.8\,\mathrm{meV}$ and $\sim 0.6\,\mathrm{meV}$ of light water shown in Fig.4.5. The FWHM of the LA also broadens from $0.3\,\mathrm{meV}$ to $0.42\,\mathrm{meV}$, continuing to link the hardening to an anharmonic effect resulting in broadening. Finally, similarly to previously, a kinetic aspect to this hardening is observed.

Fig.4.16 shows the kinetics of hardening due to D_2O wetting under $6\,\mathrm{L\,min^{-1}}$ nitrogen flux. Similarly to light water in the same conditions, the relaxation fits for the LA branch captures the behaviour of the hardening kinetics with a very strong agreement, and the TA branch is not encapsulated by the fit, similarly to the TA branch in Fig.4.6. Nonetheless, the orders of magnitude in time to reach a stable position for both branches is roughly $4\,\mathrm{h}$ to $5\,\mathrm{h}$, much like light water wetting induced hardening. The time to reach a stable heavy water induced hardening position for the LA branch is slightly faster ($61\,\mathrm{min}$ for heavy water compared to $92.6\,\mathrm{min}$ for light water). It is not clear if this is significant enough to indicate a

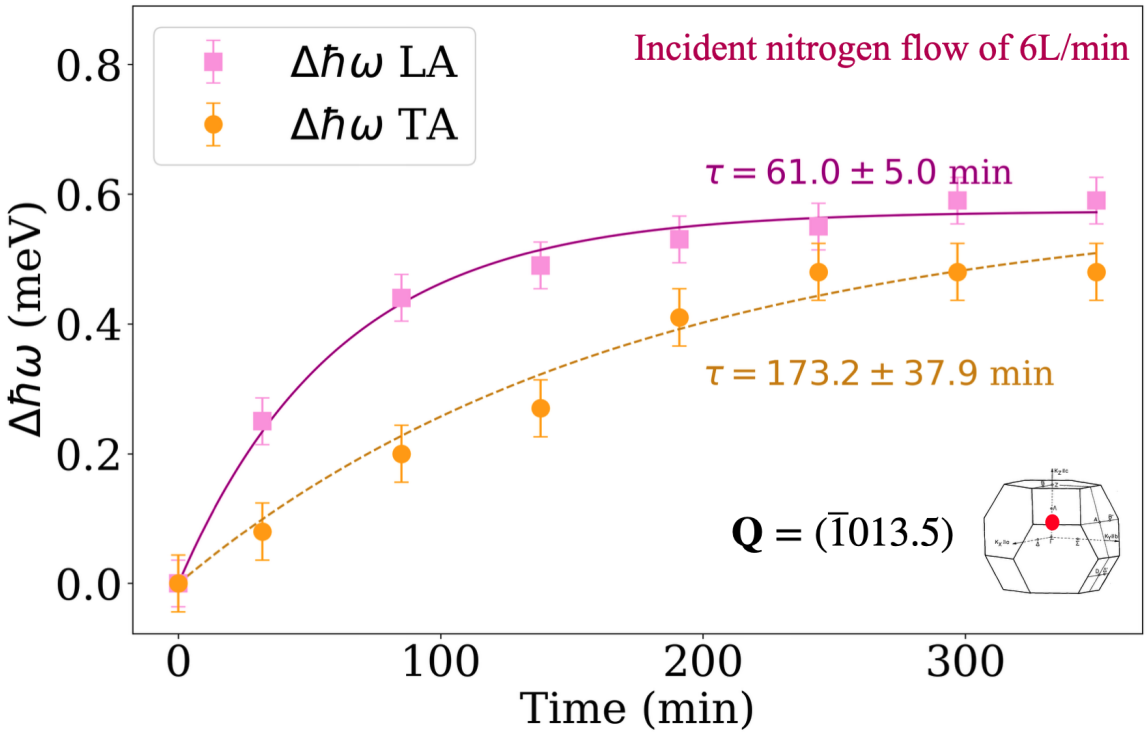

Figure 4.16: Time evolution of TA (orange circles) and LA (purple squares) hardening at $\mathbf{Q} = (\bar{1}013.5)$ of the same α-Al_2O_3 after D_2O wetting, obtained by Inelastic X-ray scattering at room temperature and pressure. Wetted scans performed under $6\,\mathrm{L\,min^{-1}}$ nitrogen flux. Error bars are of $\pm 0.036\,\mathrm{meV}$ for the LA branch and $\pm 0.044\,\mathrm{meV}$ for the TA branch. Insert of the first BZ of α-Al_2O_3 from [142]

different behaviour as such. Finally, throughout the kinetic process, we observe that hardening is smaller with heavy water wetting than light water.

The ratio of heavy water induced hardening to light water induced hardening throughout the kinetic process is shown in Fig.4.17. The ratio of both the TA and LA branches converges towards a value around 0.7. The black line at 0.707 is the ballistic ratio of the isotopic masses of H and D. The hardening ratios converges towards said ratio, and it is always present within the error bars of each point. This is a fundamental insight into what might be at an origin of the hardening.

4.2 Discussion

Considering that a necessary condition for hardening to happen is the nitrogen recirculation bubble resulting in a stress of the remaining liquid at the solid surface, the resulting hardening is therefore interpreted as the complex interaction of a non-equilibrium thermodynamic state composed of both the flow-solicited liquid and the solid, linked together by the high energy surface. However, the elastic behaviour of liquids close to such interfaces, and in our case water, is by its long-range nature something that we would think to be a result of longer range vibrational patterns, and therefore lower energies. In light water and heavy water, as we discussed in chapter 2, the collective excitations of lower energies are

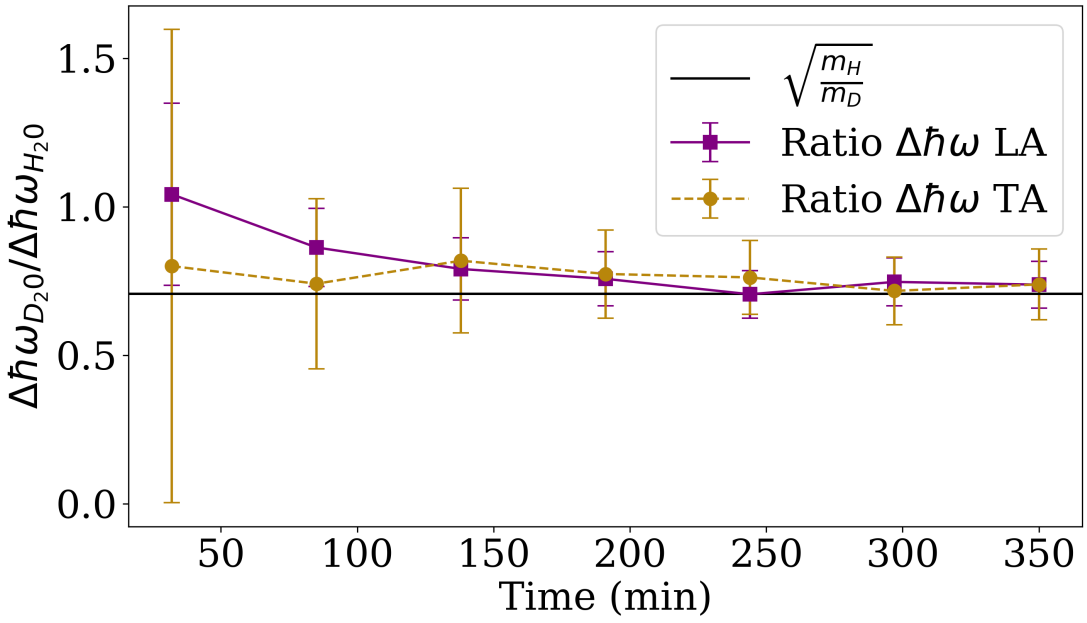

Figure 4.17: Time evolution of TA energy changes ratio (orange circles) and LA energy changes ratio ($\Delta\hbar\omega_{D_2O}/\Delta\hbar\omega_{H_2O}$) (purple squares) hardening between D_2O wetted α-Al_2O_3 crystal and H_2O wetted crystal at $\mathbf{Q} = (\bar{1}013.5)$ under continuous $6\,\mathrm{L\,min^{-1}}$ nitrogen flux, obtained by Inelastic X-ray scattering at room temperature and pressure. The black line is the ballistic mass ratio of the D and H isotopes ($\sqrt{m_H/m_D} \approx 0.707$).

those of sound transport and fast sound [41]. Both of these are results of the whole molecule vibrating [117, 40], not just the lighter hydrogen or deuterium atoms. However, the ballistic ratio of hardening observed in the same experimental setup shown in 4.17 suggests that the hardening process is somewhat linked to vibrational patterns of hydrogen or deuterium themselves and not the molecule. It seems unlikely that the hardening is a result of *intra* molecular vibrations, as these are at much higher energies ($\sim 150\,\mathrm{meV}$ to $\sim 400\,\mathrm{meV}$ for bending and stretching modes) [39].

The H-bond network intermolecular vibrations arising from the "flickering" from LDL to HDL, however, shows a very broad energy peak in bulk water at $\sim 6\,\mathrm{meV}$ [113]. Vibrational modes are generally 'red-shifted' by a factor of $1/\sqrt{2}$ when comparing D_2O and H_2O [190, 39], and the H-bond collective vibrations are better transferred in H_2O [126] and behave like optical phonon-like modes [116]. Adding to this fact that the water is coupled at the highly wetting α-$Al_2O_3(0001)$ surface, leading to hydroxylation and molecular binding altering the H-bond itself, creating a more stable H-bond with a longer relaxation time for D_2O than H_2O, as per the more structured nature of D_2O, see chapter 2. The lower frequency of the D_2O modes coupled with its more structured nature limits its transfer of vibrational energy to the surface, demonstrated by the convergence towards a hardening ratio corresponding to the ballistic mass ratio, may be the reason for this hardening discrepancy between light water and heavy water.

5 Hardening as a localised interaction

For the past subsection, we have discussed hardening and its kinetics 3.2, nitrogen flux dependence 3.4 and isotopic dependence 4 at a single point in reciprocal space, $(\bar{1}013.5)$, except for some of the off-plane results shown for the reversibility of wetting induced hardening in 3.3, but still within the same BZ of $(\bar{1}014)$. As said in 1, we have scanned other points, notably the (0012) BZ and along the Γ-Z direction in the $(\bar{1}014)$ BZ. We shall first discuss the (0012) BZ.

5.1 Absence of hardening in the (0012) Brillouin Zone

As throughout the set of highlighted experiments we have been scanning in reflectometry conditions, a change of BZ is accompanied with a change of beam penetration length. The (0012) BZ in this configuration corresponds roughly to a $150\,\mu\mathrm{m}$ beam penetration due to an incident angle of $\sim 20°$ in a symmetric reflection geometry, as shown in Fig.4.2. Looking at the same point $q = [000.5]$ or $q = [00\overline{0.5}]$ within any first BZ for α-Al_2O_3 should yield the same results in energy for a bulk solid, barring the polarisation of the phonon. As such, in BZ (0012), we will only be able to observe the longitudinal phonons as the transverse phonons are orthogonal to the scattering vector $\mathbf{Q}$. Nonetheless, LA phonons can be directly compared.

Results shown in Fig.4.18 were obtained during our first set of experiments, where we alternated between the $(\bar{1}013.5)$ position and the (0012.5) position shown. The results shown in previously discussed Fig.4.7 are from the same set of experiments. As such, by alternately looking at what should show the same behaviour of the LA branch due to wetting, the goal was to determine if the effect could be depth dependent. The results shown in Fig.4.18 show no hardening compared to any of the $(\bar{1}013.5)$ scans discussed in the previous section. There is an ever so slight hardening of roughly $0.08\,\mathrm{meV}$ of the LA branch at (0012.5). While the error bars obtained for the energy of LA and TA phonons used in the previous section correspond to error bars of 0.036 and $0.044\,\mathrm{meV}$ respectively. They are not applicable in this set of experiments. Indeed, the results shown in Fig.4.7 were obtained under a photon flux of the synchrotron a third of that for all the previous results discussed bar those shown in Fig.4.7. Before wetting, we scanned the (0012.5) position twice and observed a $0.06\,\mathrm{meV}$ difference, making the $0.08\,\mathrm{meV}$ difference observed in Fig.4.18 negligible.

Fig.4.18 therefore highlights either two points: the hardening is likely BZ dependent, not depth dependent. In a more general way, the effects of wetting must be depth dependent as it seems highly unlikely that if the distance to the surface is larger than the mesoscopic scale, one would still observe such effects. Nonetheless, while the hardening is not significant at (0012.5), there is a widening of the LA branch from 0.41 to $0.59\,\mathrm{meV}$, indicative of the anharmonic interaction still being present, reported in Tab.4.3. This broadening is very similar to that reported in the $(\bar{1}013.5)$ position, see Fig.4.8. This indicates that the liquid wetting at the surface still has some impact on the phonon dynamics.

To conclude, since no significant hardening is observed at $\mathbf{Q} = (0012.5)$, the hardening previously discussed is indicative of a more complex interaction between the liquid vibrational patterns and the solid acoustic phonons, which may be a result of a depth dependence

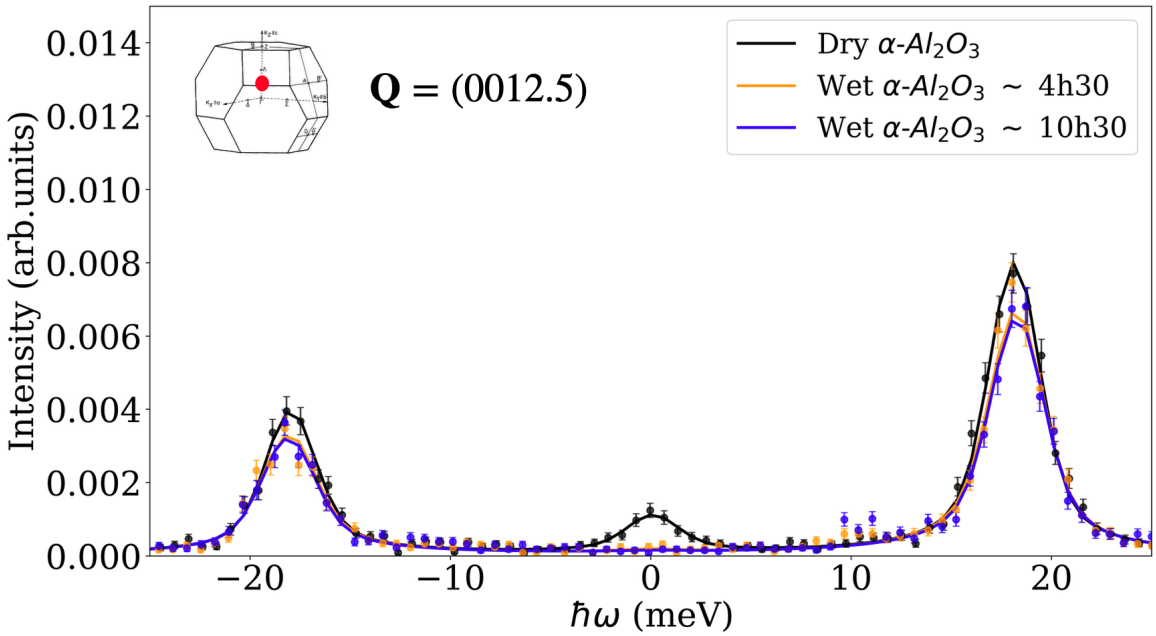

Figure 4.18: Inelastic X-ray scattering scans and fits of dry (black) and H_2O wetted at $\sim$ $4.5\,\mathrm{h}$ (orange), $\sim 10.5\,\mathrm{h}$ (blue) results at $\mathbf{Q} = (0012.5)$ of the same α-Al_2O_3 crystal performed at ID28 with $3\,\mathrm{meV}$ resolution, corresponding to a beam penetration of $\sim 300\,\mu\mathrm{m}$. Experiments performed under $6\,\mathrm{L\,min^{-1}}$ nitrogen flux, at room temperature and pressure. Insert of the first BZ of α-Al_2O_3 from [142]

	Dry scan	H_20 wet $\sim 4.5\,\mathrm{h}$	H_20 wet $\sim 10.5\,\mathrm{h}$
FWHM (meV)	0.41(10)	0.63(11)	0.59(11)

Table 4.3: Broadening of the 'LA' branch of the scan shown in Fig.4.18 at $\mathbf{Q} = (0012.5)$ under continuous $6\,\mathrm{L\,min^{-1}}$ nitrogen flux

which will be rediscussed in following chapters with new experimental data.

5.2 Results in the full Γ-Z direction: towards a gapped mode

We have also scanned the α-Al_2O_3 crystal throughout the Γ-Z direction (or $q = [00\xi]$). These scans were performed in the $(\bar{1}014)$ BZ for two reasons: in this BZ one can observe both TA and LA branches, and the hardening was observed in this BZ.

Fig.4.19 shows the dry and H_2O wetted scans and respective fits under $6\,\mathrm{L\,min^{-1}}$ nitrogen flux for multiple position in reciprocal space along the $q = [00\xi]$ direction. The scans shown were performed between 6 and 12 hours after wetting, what we identified in section 3.2 as a reasonable window where the effects have stabilised and are no longer time dependent. Through this data it is clear that hardening happens throughout the Γ-Z direction. We shall also point out that the quasi-elastic peak collapses at each position. Furthermore, it visually seems that the closer to the Γ point, the more the hardening, which is why Fig.4.20 shows the dispersion curve in the Γ-Z direction.

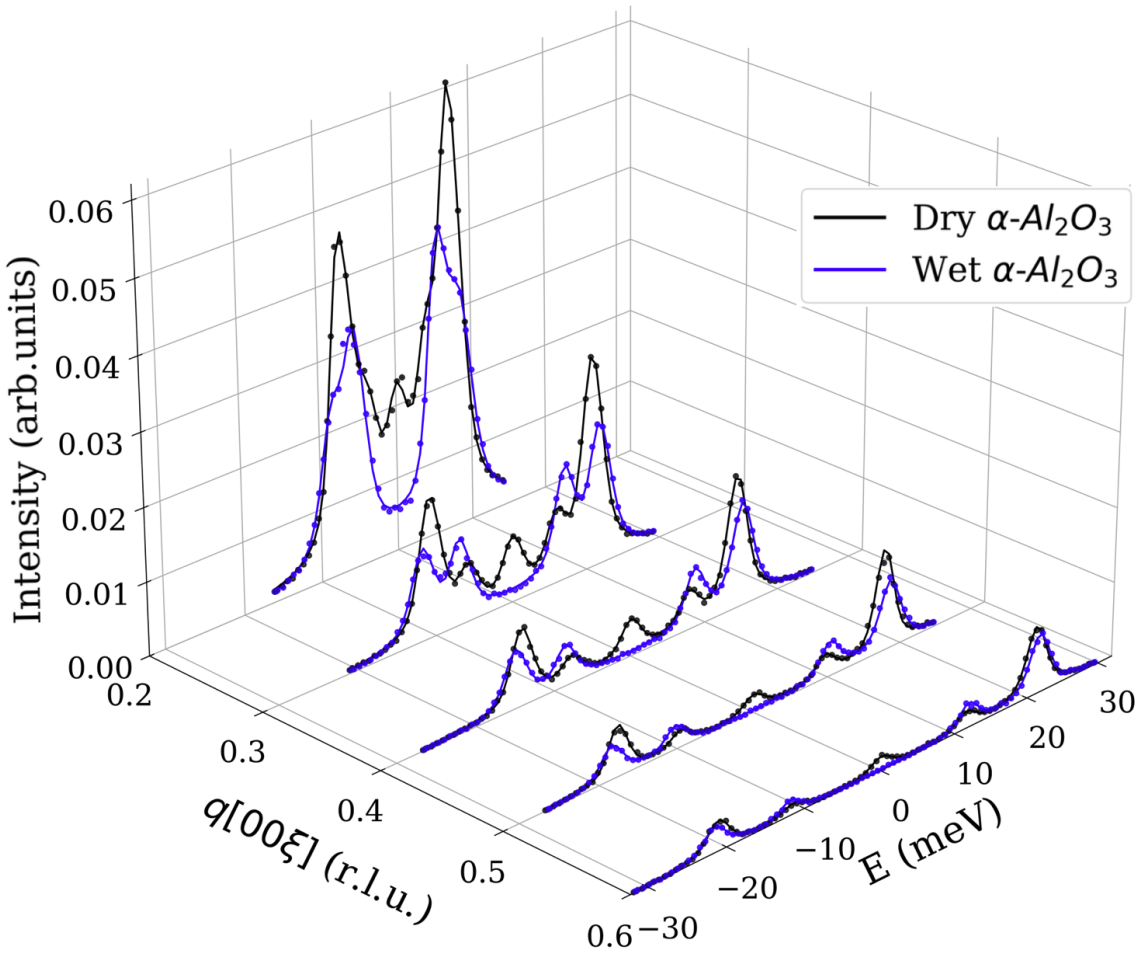

Figure 4.19: Inelastic X-ray scattering scans and fits of dry (black) and H_2O wetted between $6\,\mathrm{h}$ and $12\,\mathrm{h}$ (blue) in the $(\bar{1}014)$ BZ, in stable conditions in reciprocal space in the $[00\xi]$ direction of the same α-Al_2O_3 crystal performed at ID28 with $3\,\mathrm{meV}$ resolution, corresponding to a beam penetration of $\sim 150\,\mu\mathrm{m}$. Experiments performed under $6\,\mathrm{L\,min^{-1}}$ nitrogen flux, at room temperature and pressure.

Fig.4.20 confirms the visible $q[00\xi]$ dependent hardening observed in Fig.4.19. We note the excellent agreement of the theoretical prediction of the dispersion curve using data from [191] and the dry results. This highlights that the crystal was well aligned. Furthermore, the hardening is present throughout the Γ-Z direction, but is much stronger the closer to the Γ position, thus suggesting that the LA and TA modes become gapped. This is highly unusual, and will be discussed further in section 7. Once the scans were performed, the $(\bar{1}014)$ Bragg peak was at the same position, confirming that the crystal had not moved due to wetting. This would have been highly unlikely, as when the same experimental protocol was followed but alternating scanning between the (0012) BZ and the $(\bar{1}014)$ BZ, the hardening was only visible in the $(\bar{1}014)$ BZ. Furthermore, the hardening is not only $q[00\xi]$ dependent, but the relative hardening, shown in Fig.4.21 is much more pronounced the closer to the Γ point.

The relative hardening shown in Fig.4.21 is expressed in the following formula $(E_{L,T}^{wet} -$

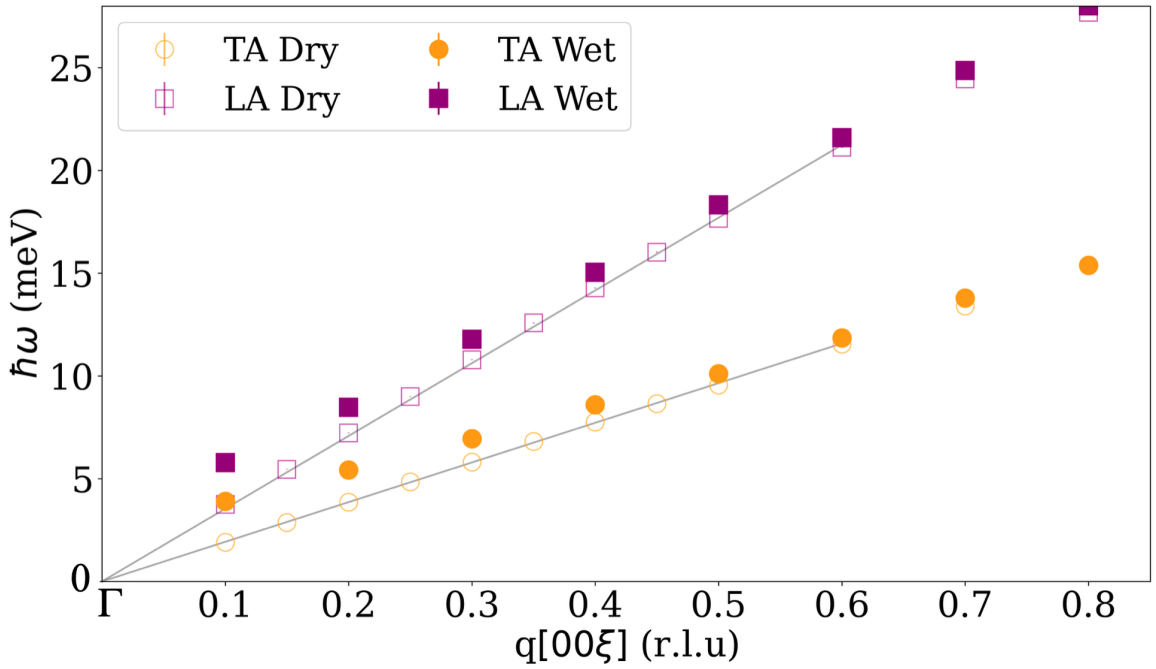

Figure 4.20: Dispersion curve obtained by Inelastic X-ray scattering in $[00\xi]$ (Γ-Z) direction of dry α-Al_2O_3 TA (empty circle orange) and LA (empty square purple). The alumina disk is H_2O wetted in the stable window of 6 to 12 hours after wetting results in the wetted dispersion curve of TA (filled circle orange) and LA (filled square purple). The grey lines correspond to acoustic dispersion slopes obtained from C_{33} and C_{44} moduli from [191]. The same α-Al_2O_3 crystal is shown. Scans performed at ID28 with $3\,\mathrm{meV}$ resolution, corresponding to a beam penetration of $\sim 150\,\mu\mathrm{m}$. Experiments performed under $6\,\mathrm{L\,min^{-1}}$ nitrogen flux, at room temperature and pressure.

$E^{dry}_{L,T})/E^{dry}_{L,T}$ for each LA and TA branch. It highlights that relative to the initial energy of the acoustic branch in question, the TA branch hardens much more consequently, with a doubling of energy at $q = [000.1]$, i.e. $\mathbf{Q} = (\bar{1}013.9)$. The ratio of hardening converges towards a null ratio when getting towards the BZ boundary.

As we highlighted throughout the chapter, hardening at the $(\bar{1}013.5)$ position is accompanied by a broadening of the LA peak, i.e. an increase of the FWHM. Fig.4.22 shows the FWHM of both LA and TA branch throughout the Γ-Z direction. Similarly to results discussed in section 3.2, the TA branch does not show a broadening, as the FWHM is within the resolution function. The LA branch, however, shows hardening at every scanned point until $q = [000.7]$, where hardening is also present, see Fig.4.20. The LA FWHM shows a clear peak at $q = [000.2]$, and decreases further closer to the Γ point.

As such, we can clearly associate, at least in the $(\bar{1}014)$ zone, hardening of acoustic phonons and broadening of LA branch, suggesting an anharmonic effect due to flowing liquid at the surface to be the cause of this phononic interaction. This will be discussed in further detail in section 7.

To summarise, we have highlighted a q-dependent hardening that tends towards a gapped

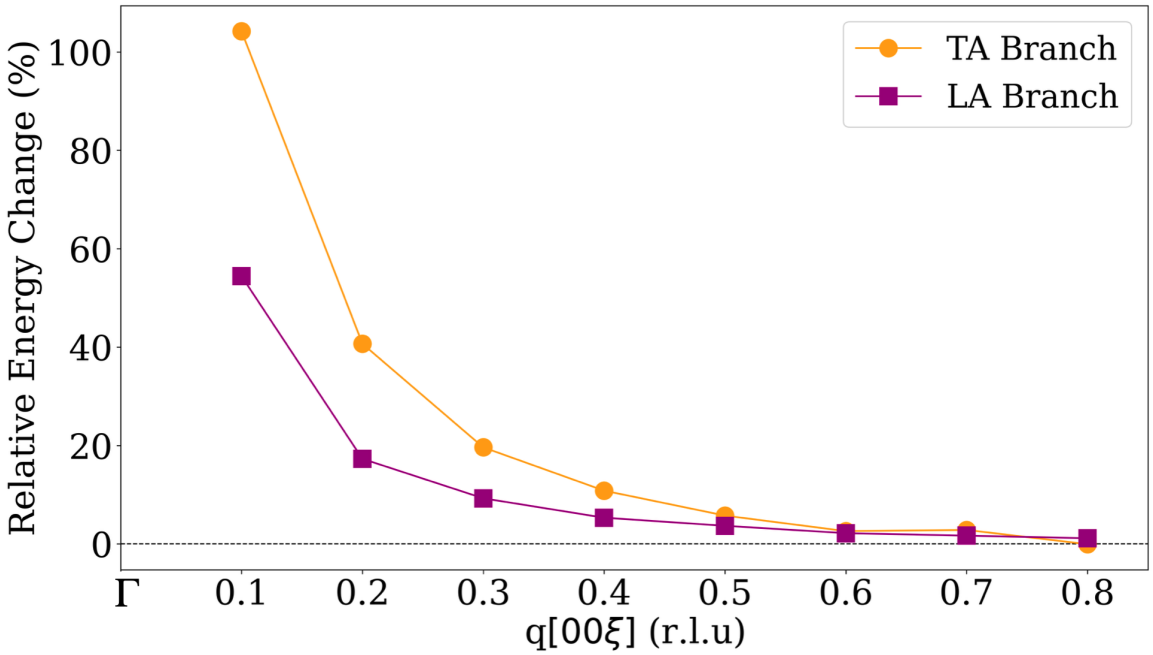

Figure 4.21: Percentage relative hardening $(E^{wet}_{L,T} - E^{dry}_{L,T})/E^{dry}_{L,T}$, each obtained by Inelastic X-ray scattering, in the $[00\xi]$ (Γ-Z) direction. TA branch is shown in orange circles and LA branch in purple squares. The same α-Al_2O_3 crystal is scanned in dry and H_2O wetted conditions. Scans performed at ID28 with $3\,\mathrm{meV}$ resolution, corresponding to a beam penetration of $\sim 150\,\mu\mathrm{m}$. Experiments performed under $6\,\mathrm{L\,min^{-1}}$ nitrogen flux, at room temperature and pressure.

mode at the Γ point, accompanied by a q-dependent broadening where a clear maximum is identified at the $q = [000.2]$ point.

6 Collapse of the quasi-elastic peak

6.1 Results

At zero energy, an effect that is common to both BZs scanned, and therefore irrespective of penetration depth, is the collapse of the quasi-elastic peak along the Γ-Z direction. Indeed, the scans shown in 4.18 and 4.4, both at identical points within their respective BZ ((0012) and $(\bar{1}014)$), and both show, in a timescale of one scan, i.e., between one and three hours, a collapse of the quasi-elastic peak.

Fig.4.23 shows the quasi-elastic peak at $\mathbf{Q} = (\bar{1}013.5)$ of a dry and H_2O wetted α-Al_2O_3 crystal without nitrogen flux. As such, we see the collapse of the quasi-elastic peak, therefore confirming that this effect is independent from the non-equilibrium flow dependent hardening. Such a collapse is visible at any point along the Γ-Z direction, as seen in Fig.4.19. In the results for reversibility (Fig.4.10) where the scans were slightly off the c-axis, no such elastic peak is visible for either a dry or wet crystal, as seen in Fig.4.10 and Fig.4.11. This therefore suggests the phenomenon to be linked to that specific crystallographic direction.

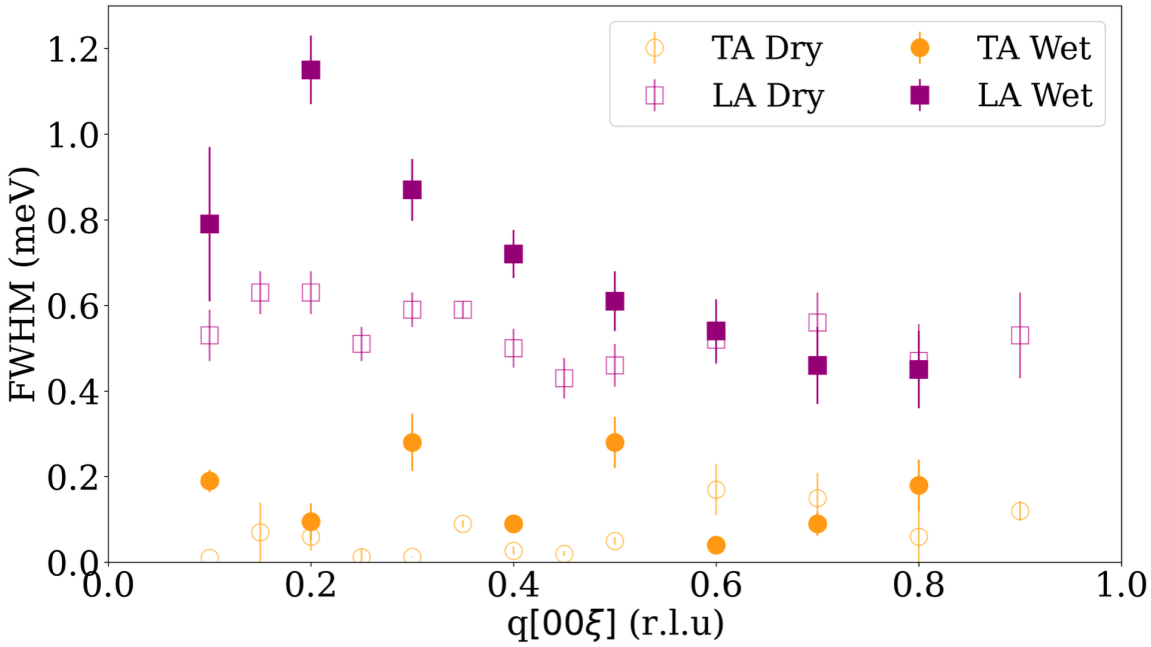

Figure 4.22: FWHM(meV) obtained by Inelastic X-ray scattering in $[00\xi]$ (Γ-Z) direction of dry α-Al_2O_3 TA (empty circle orange) and LA (empty square purple). The sample is H_2O wetted in the stable window of 6 to 12 hours after wetting results in the wetted dispersion curve of TA (filled circle orange) and LA (filled square purple). The same α-Al_2O_3 crystal is shown. Scans performed at ID28 with $3\,\mathrm{meV}$ resolution, corresponding to a beam penetration of $\sim 150\,\mu\mathrm{m}$. The error bars are the numerical error bars. Experiments performed under $6\,\mathrm{L\,min^{-1}}$ nitrogen flux, at room temperature and pressure.

6.2 Discussion

Generally, a collapse of the quasi-elastic peak is indicative of a relaxation process within the material, resulting in reduced internal constraints that have remained during the growth and treatment process of the crystal discussed in chapter 2 section 2.1. The first observation is that it seems highly unlikely that a relaxation process to reduce stress within the bulk of the material would be possible only with liquid wetting, nonetheless this was our first intuition outlined in [189].

The Γ-Z direction is a highly symmetrical direction, but most importantly, is perpendicular to the crystal surface. Our understanding of this phenomenon involves physics of Crystal Truncation Rods (CTRs) [192], rods of elastically scattered X-rays along the perpendicular direction of the surface that arise due to the breakage of symmetry by the crystal surface. As such, these rods are indicative of the crystal surface structure, arrangement, and a powerful tool in surface science [171]. Their general intensity profile is

$$I_{el} \propto q_z^{-2} \tag{4.8}$$

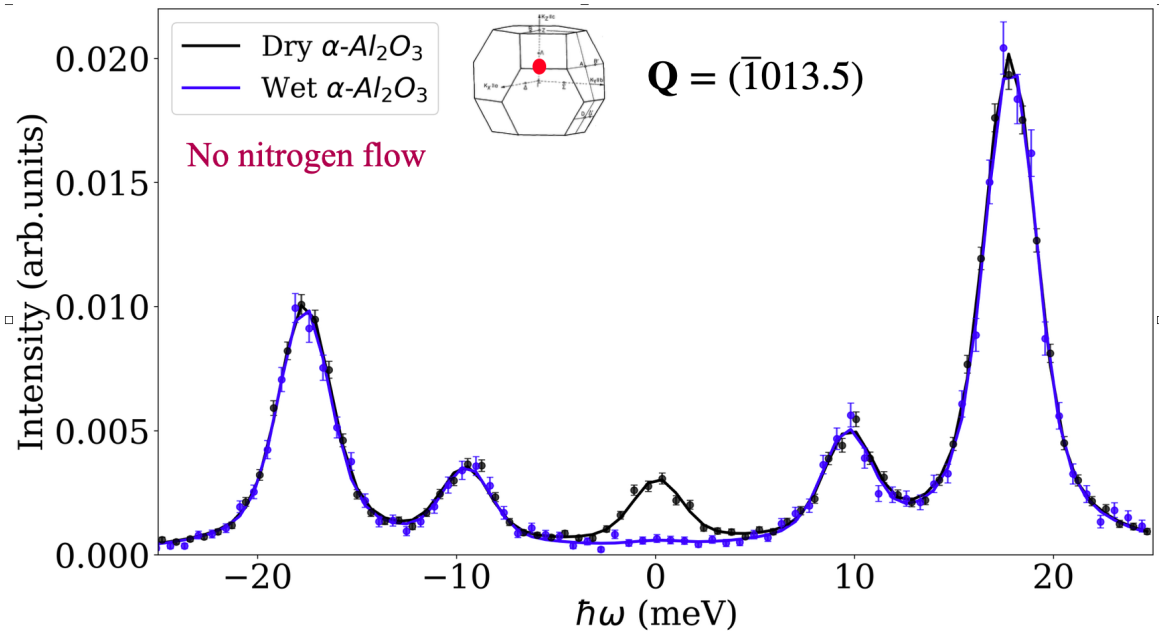

Figure 4.23: Inelastic X-ray scattering scans and fit of dry (black) and H_2O wetted (blue) at $\mathbf{Q} = (\bar{1}013.5)$ of the same α-Al_2O_3 crystal performed at ID28 with $3\,\mathrm{meV}$ resolution, corresponding to a beam penetration of $\sim 150\,\mu\mathrm{m}$. Experiments performed under no nitrogen flux, at room temperature and pressure. Insert of the first BZ of α-Al_2O_3 from [142]

with q_z the momentum transfer in the direction perpendicular to the surface in reduced lattice units. Fig.4.24 displays the quasi-elastic peak intensity along the Γ-Z direction for a dry and wetted crystal. We note the agreement with the simple scaling law (4.8) of the dry scan and the complete disappearance of the quasi-elastic peaks along the direction. This suggests the high-energy surface of the dry α-Al_2O_3 surface is relaxed, altering the interaction with X-rays by no longer having an abrupt change in electron density at the α-$Al_2O_3(0001)$-air interface.

Furthermore, CTRs of α-$Al_2O_3(0001)$ H_20 wetted surfaces have been studied, highlighting that wetting induces a "significant relaxation" at the surface, as per [149]. Our experimental results strongly echo this behaviour. Furthermore, these relaxation effects have a characteristic timescale different from the anharmonic effects of hardening and broadening discussed prior, require a maintained out-of-equilibrium state, see Fig.4.23. We can therefore conclude with high certainty that the effects of wetting on the quasi-elastic peaks are due to CTRs, given that the quasi-elastic peaks are absent out of the Γ-Z direction (shown in Fig.4.10 and Fig.4.11). In Chapter 5, experiments with neutron scattering (which do not exhibit statistically relevant CTRs due to low particle flux compared to X-rays) will further test this conclusion.

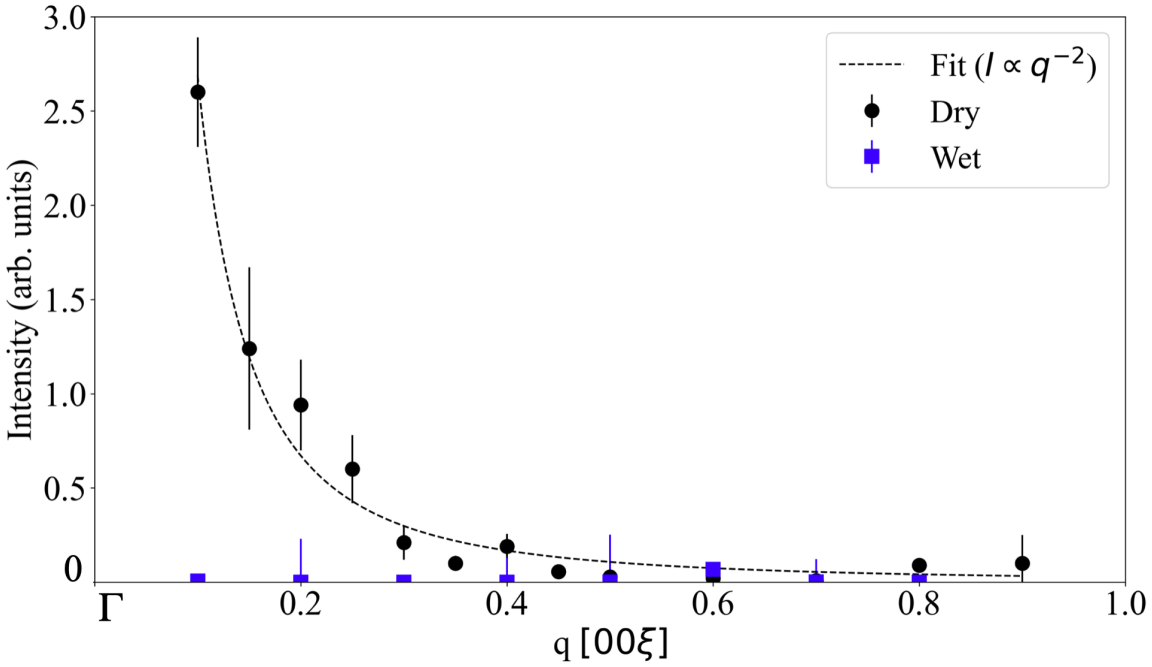

Figure 4.24: Intensity of q-dependent the quasi-elastic peak in $[00\xi]$ (Γ-Z) direction of dry α-Al_2O_3 (black circles) obtained Inelastic X-ray scattering . The sample is H_2O wetted in the stable window of 6 to 12 hours after wetting results in the wetted quasi-elastic intensity (blue squares). The dashed black line corresponds to at $I_{el} \propto q[00\xi]^{-2}$ is the general behaviour of crystal truncation rods [171, 192]. The same α-Al_2O_3 crystal is shown. Scans performed at ID28 with $3\,\mathrm{meV}$ resolution, corresponding to a beam penetration of $\sim 150\,\mu\mathrm{m}$. Experiments performed under $6\,\mathrm{L\,min^{-1}}$ nitrogen flux, at room temperature and pressure.

7 Discussion & Conclusions

7.1 Key results

Using inelastic x-ray scattering, we have performed the first experimental investigation of α-Al_2O_3 crystal and water phononic interplay through the α-$Al_2O_3(0001)$ surface. Upon wetting the surface, we identified a series of new phenomena:

- **Hardening of acoustic phonons.** A significant hardening of both longitudinal (LA) and transverse (TA) acoustic phonons was observed, as seen in Fig.4.4 and throughout the chapter. This hardening observed in the $(\bar{1}014)$ Brillouin Zone (BZ) was accompanied by a broadening of the LA peak, as seen notably in Fig.4.8 and Tab.4.1. The hardening is clearly anisotropic, with negligible hardening observed in the (0012) BZ, as seen in Fig.4.18. However, broadening was still observed in (0012) BZ on the LA peak.

- **The hardening exhibits a slow-kinetic evolution.** Hardening took place over a long timescale of multiple hours, as seen in Fig.4.5 and Fig.4.6. This kinetic hardening was found to be fully reversible, as discussed in 3.3, showing a near complete return to dry conditions after $\sim 78\,\mathrm{h}$. It was retriggered by wetting the surface anew with similar hardening kinetics, as seen in Fig.4.11. Furthermore, this hardening was systematically

associated with a broadening of the LA branch, as shown in Tab.4.1, which was itself also reversible.

- **A dependence on nitrogen flux.** A strong dependence on nitrogen flux was highlighted in section 3.4, where a non-zero flux was necessary to induce the hardening effect. The nitrogen flux was measured at the surface of the crystal, and showed an increased air flow at the surface with nitrogen flux, as seen in Tab.4.2. This demonstrated that the bulk hardening in the solid is not driven by static wetting, but by inducing a non-equilibrium dynamic process in the liquid.

- **Towards a gapped mode.** The hardening observed in the $(\bar{1}014)$ BZ was shown to increase as q decreased towards the Γ point, tending towards a gapped mode, as shown in Fig.4.20. Throughout this direction, broadening of the LA peak was observed with a strong q-dependence with a maximum at $q = [000.2]$. This highlights a possible anharmonic interaction set in motion by the mechanically stressed liquid at the surface.

The present experiments highlight that the static wetting is not the driving parameter in either hardening or broadening. Evaporation alone is not sufficient for either hardening or broadening to take place and, therefore, is not the driving parameter behind the anharmonic effects. Mechanical solicitations of the liquid by way of the nitrogen flow was necessary, leading us to interpret the anharmonic results as phenomena that are dynamically "fed".

7.2 Discussion: hardening as a structural phenomena

Hardening in a thermodynamic equilibrium is a known and observed phenomenon in solids, but generally requires very high energy input by means of either hydrostatic pressure generally within the GPa range (without inducing a phase transition) [191]. Indeed, by hydrostatically compressing the lattice, the atoms within it will almost always get closer to one another, increasing the repulsive forces and therefore the rigidity of their interactions, leading to an increase in frequency [193]. At a macroscopic scale, this is translated by an increase in the speeds of sound in the material, and all its derivative properties such as stiffness tensor.

Limiting our study to α-Al_2O_3, we shall perform a small calculation to compare what would be needed for an $0.8\,\mathrm{meV}$ increase of longitudinal branch as seen in Fig.4.4 at the $q = (000.5)$(r.l.u) position ($(\bar{1}013.5)$ corresponds to such a position). Cr^{3+} doped α-Al_2O_3 (ruby) is central to the ruby fluorescence scale used to measure pressure in high-pressure experiments, and its properties are therefore highly tabulated. We will compare with the calculated data from [191]. The speed of sound of the longitudinal acoustic branch is directly linked to the stiffness parameter C_{33} by

$$C_{33} = (\rho v_L)^2 \tag{4.9}$$

Using this relation we obtain a LA phonon energy $\hbar\omega = \hbar q v_L = 17.8\,\mathrm{meV}$, with almost perfect agreement with the dry LA branch of Fig.4.4 for a crystal at room temperature ($C_{33} = 500\,\mathrm{GPa}$). To increase by $0.8\,\mathrm{meV}$, one would need to increase C_{33} to $545\,\mathrm{GPa}$ as per [191], which corresponds to a $\sim 10\,\mathrm{GPa}$ hydrostatic pressure. This is a tremendous amount of energy compared to the simple act of wetting a crystal surface.

Logically, this high pressure environment would also change the volume V of the crystal, and the changes in frequency of a given branch can therefore be understood through Grüneisen parameter of the ω_s frequency of a specific phonon mode s (4.10) [194].

$$\gamma_{G,s} = -\left(\frac{\partial ln\omega_s}{\partial lnV}\right)_T \tag{4.10}$$

A decrease in temperature has a similar effect on the solid. Reducing the thermal vibrations within the solid leads to contractions and reduces anharmonic effects in phonons, leading to a hardening of most branches in α-Al_2O_3 [195]. Similarly, this is captured by the mode Grüneisen parameter (4.11), with α the volumetric thermal expansion coefficient.

$$\left(\frac{\partial \ln \omega_s}{\partial T}\right)_P = \left(\frac{\partial \ln \omega_s}{\partial T}\right)_V - \gamma_{G,s}\alpha \tag{4.11}$$

At the surface, such hardening effects can also happen through surface reconstruction, though they do not really pertain to our study as we scan deep into the bulk of the solid. Furthermore, in section 6, we concluded that the α-$Al_2O_3(0001)$ surface underwent relaxation, following CTR results from [149]. This phenomenon is more likely to reduce surface phonon energy.

The hardening effect shown in Fig.4.4 also cannot be the result of an analogue temperature dependent mode dependent Grüneisen parameter as defined in (4.11) as there are no significant temperature changes during the experiment that can explain such a hardening (C_{33} variance within the $50\,\mathrm{K}$ to $500\,\mathrm{K}$ range is negligible [196]). Furthermore, the order of magnitude comparison for pressure dependence of a previous paragraph highlights that this effect can neither be understood as an analogue to a pressure dependent effect.

Therefore we can conclude that, at room temperature and pressure, hardening and the anharmonic effects observed are highly unlikely to be due to structural changes and must be due to a complex non-equilibrium coupling between the solid and the liquid.

7.3 Conclusion

Throughout this chapter, we showed by IXS the first experimental evidence of a novel, long-range phononic interaction induced at a solid-liquid interface, defined by a bulk hardening of acoustic phonons at the $(\bar{1}014)$ BZ of the α-Al_2O_3 crystal, shown in sections 5. This hardening is accompanied by a broadening of the LA branch. This hardening cannot be generalised throughout the reciprocal space, as it is not visible at the (0012) BZ. The broadening of the LA branch is maintained, suggesting a strong coupled anharmonic effect.

For this anharmonic effect to take place, the evaporating liquid must be solicited by a nitrogen air flux that mechanically stresses the liquid surface, maintaining it in a non-equilibrium state. This hardening effect is reversible, depends on the strength of the nitrogen flow stress on the liquid, and shows complex kinetics over hours, which we attribute to a form of complex interplay between flowing nitrogen stressing the liquid and evaporation.

Evaporation is not the driving force behind this mechanism, as shown in Fig.4.14.

Crucially, the hardening at the $(\bar{1}014)$ BZ is strongly q-dependent, increasing near the Γ point. This seems to culminate in the opening of a finite energy gap at the centre of the BZ for both transverse and longitudinal acoustic modes.

Furthermore, a clear isotopic effect, where hardening is substantially weaker with D_2O than with H_2O following the ratio of the isotopes ballistic weights, strongly suggests that the interaction is mediated by the liquid's hydrogen-bond network.

In summary, these experiments reveal that static wetting is not the driving parameter for the observed effects. Instead, the phononic interactions are dynamically "fed" by the externally-driven motion of the liquid. To further investigate and quantify this non-equilibrium state, we designed controlled flow cells to impose a liquid shear flow, eliminating evaporation as a physical parameter. The results from these new setups, using inelastic neutron and X-ray scattering as a probe, are presented in the following chapter 5.

Chapter 5

Inelastic Neutron Scattering & Transmission Inelastic X-ray Scattering

Contents

1 Anharmonic phononic interaction using inelastic neutron scattering

To demonstrate that the mechanically stress-induced effects on the solid dynamics (hardening and broadening) are independent of the scattering method, we performed neutron experiments on the IN8 3-axis Inelastic scattering spectrometer at the Institut Laue-Langevin (ILL) with the help of local contact and scientist Dr. Alexander Ivanov. Following the previous results of Inelastic X-ray Scattering—a non-equilibrium solid-liquid coupling leading to phonon hardening in a given BZ over hours, coupled with an anharmonic effect observed as broadening of the LA branch—we introduced a continuous flow of liquid (heavy and light water) instead of wetting the surface. We performed the experiments in transmission geometry, thus keeping the beam penetration depth equal, leading to the following experimental setup.

1.1 Experimental setup

As detailed in Chapter 4, hardening was observed in the Brillouin zone $(\bar{1}014)$ and not in the Brillouin zone (0012). As the experiments were carried out using reflectometry conditions detailed in 1 and Fig. 4.2, each Brillouin zone corresponds to a different incident angle and therefore a different penetration depth of the beam. This led to the conclusion that this effect *could* be depth dependent, though this is unlikely as discussed in section 7. However, to satisfy this claim, we would have to observe similar effects in another Brillouin zone at a similar penetration depth. This would be very tricky with the previous experimental setup 4.1 given the complex reflection conditions of α-Al_2O_3 (see 2.2).

To free ourselves from these constraints, we opted for a transmission-based experiment, where the beam would go through a crystal of a given size. Therefore, each Brillouin zone would correspond to the same distance to a wetted surface, regardless of incident angle. These experimental conditions allow us to perform the experiments with neutron scattering at IN8, thus also improving our energy resolution from $3\,\mathrm{meV}$ to $1.5\,\mathrm{meV}$.

Finally, another constraint from which we wanted to free ourselves was that of evaporation. We therefore opted to scan the crystal under continuous flow F of $0.35\,\mathrm{mL\,s^{-1}}$. With continuous flow, as opposed to nitrogen flow mechanically-driven wetting conditions, we ensured that the liquid is continuously renewed and the amount of liquid during the flowing process will remain the same, most crucially maintaining the liquid in an out-of-equilibrium state. Furthermore, with continuous flow, we will confirm, by stopping the flow, that the liquid flow is a necessary condition to observe an anharmonic effect on the phonons of the solid. Ideally, this would be verified with a change of phonon energy, but phonon broadening, a more subtle effect reported throughout the previous chapter, would help confirm the flow-induced anharmonic effect on phonons.

While it would have been a boon to compare the $(\bar{1}014)$ in IXS and INS, one of the complexities of the experiments is that it is impossible to observe the same Brillouin zone in its full energy range with the IN8 spectrometer, as the geometrical limitations of the spectrometer only allow scanning above $25\,\mathrm{meV}$, far from the region of interest seen in Fig.4.20. The first part of our set of experiments was to find a Brillouin zone with an intense enough signal

to be studied. Therefore, before the experiment, we first scanned, in transmission, a dry $2\,\mathrm{mm}$ thick α-Al_2O_3 crystal (one of the crystals used in reflectometry conditions). We performed the same surface treatment detailed in chapter 1. This allowed us to identify a Brillouin zone with a high signal in transmission with neutrons: the (300) BZ.

Once this reference scan was performed, we then scanned $4 \times 250\,\mu\mathrm{m}$ thick crystals, pre-oriented and co-aligned, separated by $750\,\mu\mathrm{m}$, that were placed in a home-made 3D-printed sample holder through which flow could take place. The experimental setup can be seen in Fig.5.1.

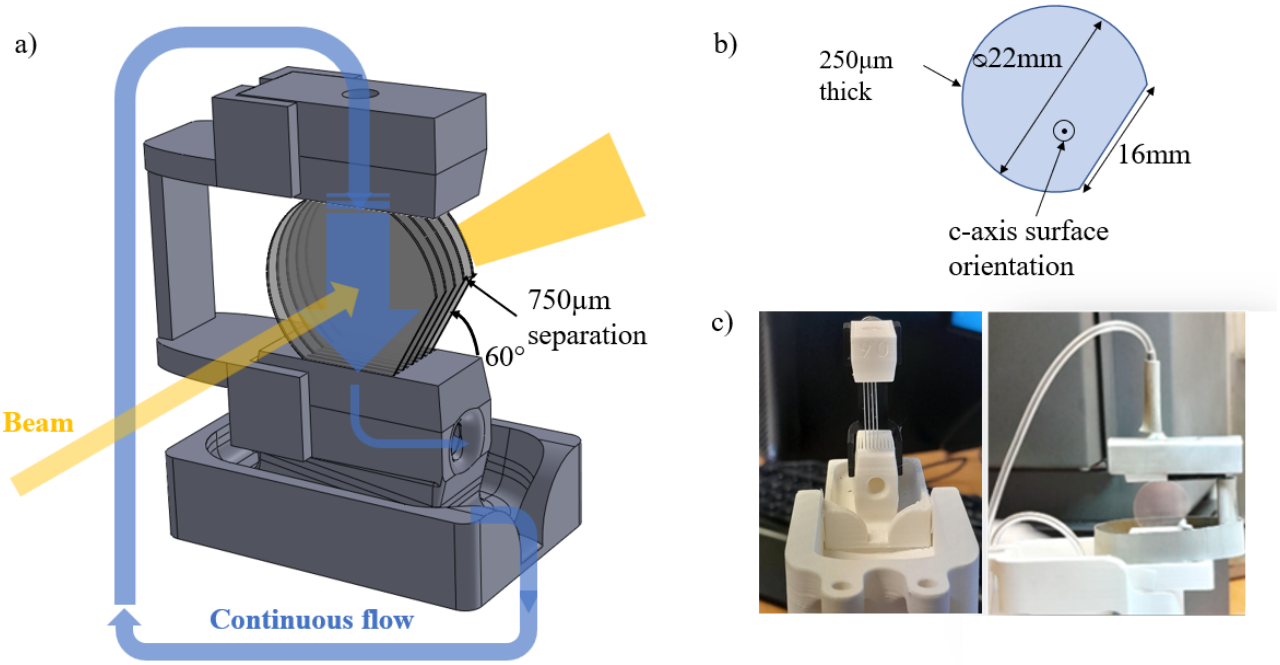

Figure 5.1: a) Schematic view of the setup. 4 α-Al_2O_3 $250\,\mu\mathrm{m}$ thick crystals are mounted with a $60°$ inclination separated by a gap of $750\,\mu\mathrm{m}$. The heavy water or water flow is recycled and repumped. b) Dimensions of each individual α-Al_2O_3 with a c-axis (0001) surface oriented. c) Photographs of the setup sample holder and mounted crystals before and after being mounted (left and right). Notice the added Cadmium to reduce background noise in the right photo.

The sample holder required covering as much as possible of the plastic parts with Cadmium (visible in our picture 5.1c)) so as to minimise incoherent scattering from said plastic sample holder. Nonetheless, a little background noise is observed, and is modelled as a Lorentzian function.

As a summary of this neutron experiment, here we aim to:

- Confirm the mechanically stressed wetting anharmonic effect.
- Investigate the potentially depth-dependent effect of wetting on acoustic phonon dispersion, by scanning a different Brillouin zone with an equivalent crystal penetration depth of $125\,\mu\mathrm{m}$ (half of each crystal width, as both sides of the crystals are wetted).

- Investigate the flow-dependence of the anharmonic effects, to confirm our results from the previous chapter 4.
- Continue our isotopic dependence study.
- See if the hardening kinetics discussed in chapter 4 section 3.2 are linked to a complex form of evaporation and can be minimised.

To do so, we performed the following series of scans around the (300) Brillouin zone:

- Γ-Z direction on a single *dry* $2\,\mathrm{mm}$ thick α-Al_2O_3 monocrystal for reference.
- Γ-Z direction on four *dry* $250\,\mu\mathrm{m}$ thick α-Al_2O_3 crystals co-aligned separated by $750\,\mu\mathrm{m}$.
- Γ-Z direction on four D_2O*-wetted* $250\,\mu\mathrm{m}$ thick α-Al_2O_3 crystals co-aligned separated by $750\,\mu\mathrm{m}$ with a flux F.
- Γ-Z direction on four D_2O*-wetted* $250\,\mu\mathrm{m}$ thick α-Al_2O_3 crystals co-aligned separated by $750\,\mu\mathrm{m}$ when the flux was stopped.
- Γ-Z direction on four H_2O*-wetted* $250\,\mu\mathrm{m}$ thick α-Al_2O_3 crystals co-aligned separated by $750\,\mu\mathrm{m}$ with a flux F.

Due to scanning in the Γ-Z direction (or $q = [00\xi]$ of the (300) zone), only Transverse Acoustic (TA) phonons can be observed due to the polarisation vector of the phonon relative to the scattering vector.

1.2 Data treatment

Data treatment in Neutron experiments is more multifaceted compared to IXS. Let us remember the fact highlighted in chapters 3 and 4, that in IXS, one can make the assumption that the position in reciprocal space is perfect, and therefore our resolution function is only a function of energy. However, with neutron scattering, one needs to extract the structure factor from the complex resolution function detailed in 3. Here we used an in-house code developed by Bernard Hennion [184]; this code allows us to obtain the structure factor deconvoluted from the resolution function. However, we needed to parametrise the resolution function, which we explain in detail in chapter 3.

Spectrometer characteristics: All the experimental parameters from the spectrometer are the following:

- $Cu(200)$ monochromator and $PG(002)$ analyser for constant $\mathbf{Q}$ scans with a fixed $k_f = 2.662\,\text{Å}^{-1}$
- We used the following distances of the IN8 spectrometer in the code to parametrise the effective collimations described in 3: $2280\,\mathrm{mm}$ from virtual source to monochromator; $2480\,\mathrm{mm}$ from monochromator to sample; $1050\,\mathrm{mm}$ from sample to analyser; and $700\,\mathrm{mm}$ from analyser to detector.

Dispersion curve: Let us look at the raw data, like the one in 5.2.a) and how we fit said data to obtain 5.2.b).

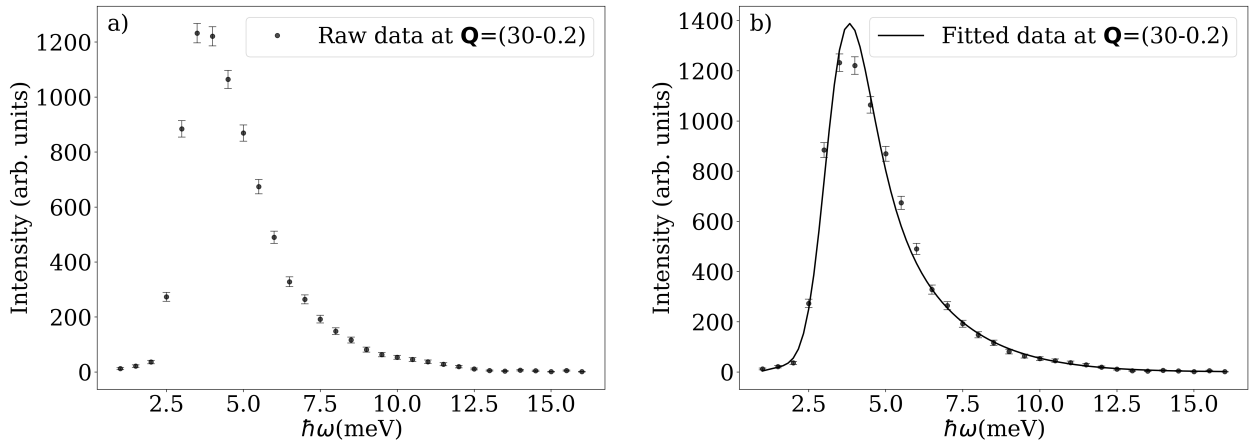

Figure 5.2: a) Raw data scan of the α-Al_2O_3 crystal at **Q**=(30$-$0.2) for the monocrystal obtained by Inelastic neutron scattering at IN8. Resolution of $\sim 1.5\,\mathrm{meV}$ b) Raw data obtained by Inelastic neutron scattering and fitted data scan of the α-Al_2O_3 crystal using the fully parametrised resolution function at **Q**=(30$-$0.2). Experiments performed at room temperature and pressure.

Fig.5.2.a) shows us the raw scan at **Q**=(30$-$0.2). One immediate striking feature is the asymmetry of the phonon as a function of energy, very much opposed to the DHO shape obtained in IXS, as seen in Fig.4.3. The 4D ellipsoid of the resolution function means that there is not a single point but a region in reciprocal space that is scanned. As such, if the speed of sound in the material is high, which it is for α-Al_2O_3, the acoustic phonons are dispersed within the ellipsoid itself. As a consequence, we needed to fit the dispersion curve *at each point in reciprocal space* to obtain the energy of the phonon. We therefore fitted the following parameter a from (5.1) at each point in reciprocal space.

$$(\hbar\omega)^2 = a(b_1^2 q_z^2 + b_2^2 q_x^2 + b_3^2 q_y^2) \tag{5.1}$$

The constants b_1, b_2, in $\mathrm{meV\,\AA}$, are proportional to the speed of sound in a given direction or to $\sqrt{\frac{C_{ii}}{\rho}}$ with C_{ii} the component of elastic modulus tensor associated with directions in the reciprocal space, obtained from [191]. The q_z and q_x direction are in $\mathrm{\AA}^{-1}$ and represent the (001) and (100) direction respectively. The scanned zone being (300), only TA phonons are visible along (001) and LA along (100). They can also be obtained from previous dry results from the last chapter, scaling by the interplanar distance in said direction. The third direction q_y is defined in an orthogonal Euclidean space, is a combination of TA and LA phonons in a direction without symmetry constraints, $(1\bar{2}0)$. As such, we adjust b_3 until we get the best fitting structure factor for each point. Doing so, we obtained the following parameters:

$$(\hbar\omega)^2 = a(1580 q_z^2 + 5600 q_x^2 + 16\,000 q_y^2) \tag{5.2}$$

These parameters were the *same* for all the scans (see Fig.5.2.b)), and we now fit to optimise the closeness of the fitted to the raw data. Information on the phonon energy will be given by the parameter a. Fig. 5.3 shows the dispersion curve obtained thanks to (5.2) for the monocrystal, compared to theoretical results. This process allows us to fit the TA phonon with a Damped-Harmonic Oscillator, as we obtained in previous experiments of IXS and detailed in 1.7.

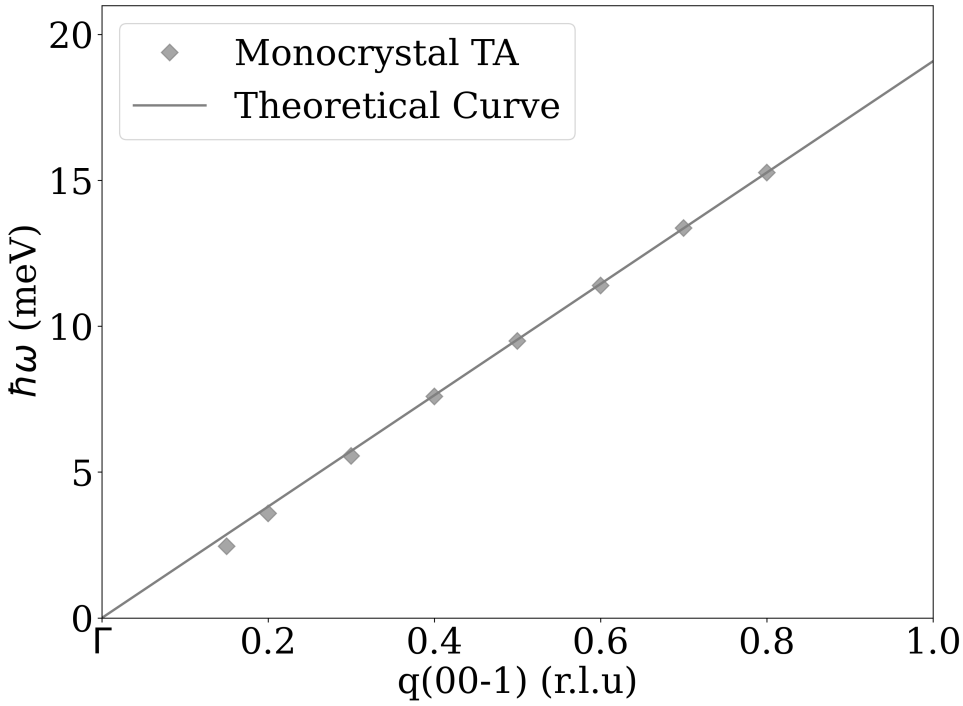

Figure 5.3: Linear dispersion curve used to fit the phonon energy of the α-Al_2O_3 monocrystal in grey line, the fitted monocrystal data obtained by Inelastic neutron scattering at IN8 are shown in grey squares. Numerical error bars from the fitting procedure are negligible. Energy resolution of $\sim 1.5\,\mathrm{meV}$. Experiments performed at room temperature and pressure.

Mosaicity of the crystal Crystal mosaicity is also a key parameter to account for. Here the procedure is the following. The scanned large monocrystal of $2\,\mathrm{mm}$ thickness is used as reference. After finding the dispersion curve detailed in the previous paragraph, we look towards the phonon width. Theoretically, for a perfect monocrystal, acoustic phonon width close to the Brillouin zone centre should be zero. We therefore increased the *crystal* mosaicity in our code until this criterion is satisfied for the $2\,\mathrm{mm}$ thick monocrystal. The measured mosaicity —a (300) Bragg peak scan—, visible for the monocrystal on Fig.5.4a), is itself fitted by a Gaussian curve, allowing us to obtain the crystal-independent parameter $\theta_{resolution} = 9.72'$ from (5.3).

$$\theta^2_{measured} = \theta^2_{resolution} + \theta^2_{crystal} \tag{5.3}$$

Then, as we have multiple crystals that were aligned by hand, we measured the mosaicity

for the subsequent series of scans —visible in Fig.5.4. Using the previously obtained $\theta_{resolution}$, we can then obtain the *crystal* resolution for each scanned series.

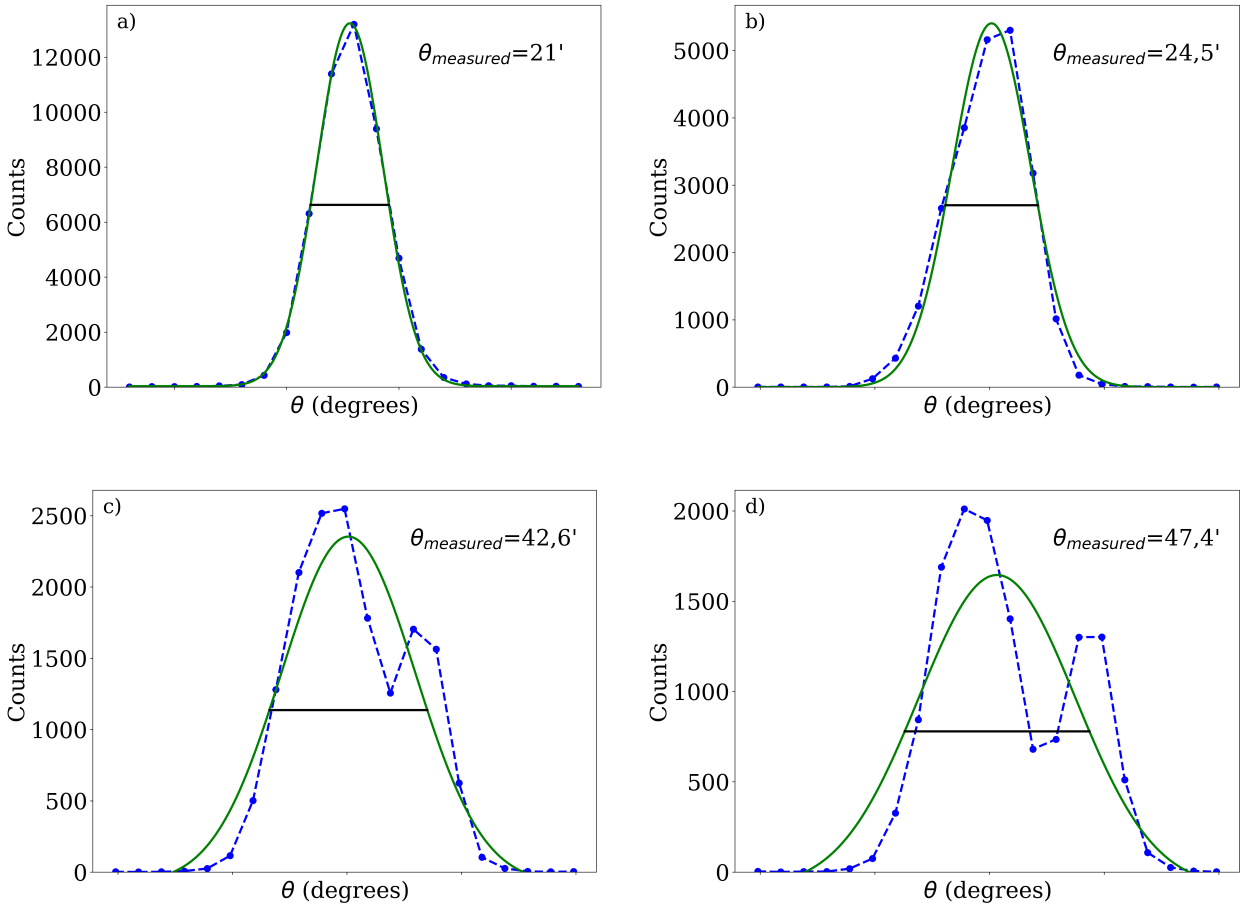

Figure 5.4: Rocking curve raw data (blue points and dashed line) and Gaussian fit (green) obtained at IN8 for the different series a) single $2\,\mathrm{mm}$ thick monocrystal b) multiple co-aligned crystals without wetting c) multiple co-aligned crystals with D_2O wetting (with and without flow F) d) multiple co-aligned crystals with H_2O wetting with flux F

Here, we notice that despite not changing the setup or crystal, there was a significant increase in measured mosaicity between the dry and wet samples. This is because putting the flow slightly modified the crystal positions. To verify that this wasn't time dependent, we regularly measured said Bragg peak width throughout each of the series with multiple crystals. The measured mosaicity can for each series of scans be observed in Fig. 5.4. In the graphs c) and d) we see that the Gaussian approximation is no longer correct, as one of the crystals moved out of alignment due to liquid wetting.

Tab. 5.1 lists all the measured widths, and crystal mosaicities for the different setups used for fitting and to parameterise the resolution function.

Sample holder noise As explained in the previous section, the plastic sample holder (visible in Fig. 5.1) itself is a source of background noise. We modeled this as a Lorentzian centred

on 0 energy (elastic) with a full width half maximum of $3.5\,\mathrm{meV}$, which we obtained by looking at the points closest to the centre zone where the elastic noise is largest, and fixing it throughout, making the assumption that this parameter is independent of positions in reciprocal space.

Background noise The background noise for a given series of scans is taken by taking scans at high $q(r.l.u)$. As the acoustic phonon intensity is lower at such $(r.l.u)$, there we can increase the background noise as needed to obtain the best scan, and reapply the same background noise for a given series on all the scans of said series. When fitting the light water wetted α-Al_2O_3 scans, as opposed to the heavy water, we only increased the fixed background noise, making the assumption that at such incident angle ($\sim 60°$), the incoherent scattering contribution of H_2O is constant. We shall discuss this further in section 1.5.

Scan series	$\theta_{measured}$	$\theta_{crystal}$	Background noise
Monocrystal	$21'$	$18'$	0
Dry crystals	$24'$	$22.46'$	0
D_2O Wetted crystals	$42.6'$	$41.3'$	0 to 15
H_2O Wetted crystals	$47'$	$46.3'$	100 to 130

Table 5.1: Fitting parameters used for each different series of scans

After having done all of this preliminary work to be able to properly deconvolute the structure factor from the resolution function, with the desire to take as much care as possible to obtain the clearest information on said dynamic structure factor, here are our main findings.

1.3 Confirmation of an anharmonic effect with Inelastic Neutron Scattering

Using all the fitting parameters from Tab. 5.1, we then fitted the scans of dry crystals and of wet crystals. As we are observing our data in the (300) Brillouin zone along the Γ-Z direction, only transverse phonons can be observed. Fig.5.5 shows fitted dry and wetted α-Al_2O_3 scans at two positions in the reciprocal space.

The key visual feature of Fig.5.5 is apparent broadening and potential softening of the transverse acoustic phonons. However, we cannot trust a direct comparison in this setup as the change in mosaicity between the dry and wetted samples influences the visual width.

This is why such care in the definition of the resolution function was necessary, as using all the fitted parameters from 5.1, no change in phonon energy took place —see Fig. 5.6, where the dry and wetted points are completely superposed.

This counter-intuitive result arises for two reasons: the mosaicity of samples has changed and phonon anharmonicity of an imperfect phonon propagation. For the latter, this stems from section 1.7 of chapter 3, where considering an imperfect phonon induces a shift on the phonon *maximum* but not on its true energy, following the equation (5.4):

$$(\hbar\omega_{max})^2 = (\hbar\omega_{phonon})^2 - \frac{\gamma^2}{4} \tag{5.4}$$

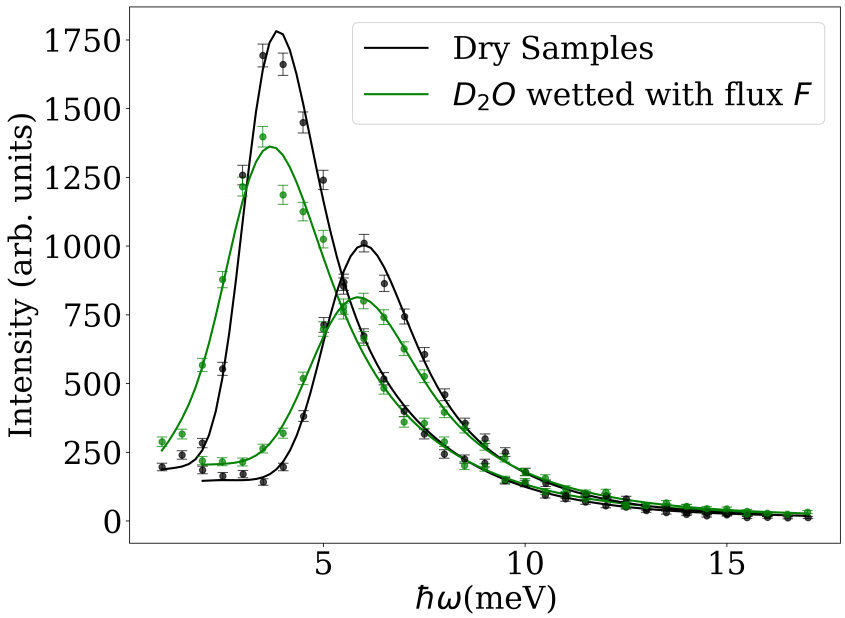

Figure 5.5: Comparison of dry (black) and D_2O continuously wetted samples data and fits with flux F (green) transverse acoustic phonons at $\mathbf{Q} = (300\bar{.}2)$ and $\mathbf{Q} = (300\bar{.}3)$ and maximum energy of $4\,\mathrm{meV}$ and $6\,\mathrm{meV}$ respectively. Data obtained by Inelastic neutron scattering at IN8. Between the dry and D_2O continuously wetted crystals, a change of mosaicity took place as reported in Tab5.1. Experiments performed at room temperature and pressure.

with γ the Full-Width-Half-Maximum (FWHM) of the phonon.

This is why it is necessary to observe the phonon width to try to explain the apparent changes in scanned phonon from Fig. 5.5. This is done in the Fig. 5.7.

Normally, the FWHM is expected to be null throughout the Γ-Z direction and should not exhibit a maximum. The reason for this is unclear, and we can only speculate that certain other parameters in the resolution function could be better taken into account. However, not knowing which, we were forced to continue with the resolution function described in the previous subsection. This 'bump' does not appear for the dry α-Al_2O_3 monocrystal, and our only conclusion is that it may be an artifact of the multi-crystal setup rather than an intrinsic physical phenomenon. Nonetheless, it is present for both dry crystals and D_2O continuously wetted crystals (and later H_2O), such that comparison between experimental sets is possible. Finally, it does not seem to be a result of crystal mosaicity as the rocking curve data for the dry monocrystal and multiple crystals shown in Fig.5.4 a) and b) are remarkably similar.

Broadening (increase of the phonon width) of the transverse phonon is visible throughout the Γ-Z direction, even at low $q(r.l.u)$, closer to the Brillouin zone centre (see Fig.5.7). While some FWHMs are within the numerical error bars, they are systematically above the FWHM of the dry crystals. The results are more subtle than previously shown in Fig.4.22 for the LA branch. However, in inelastic X-ray scattering, only an effect on the LA branch was observed, whilst here the broadening is of the TA branch which were within the IXS resolution in the

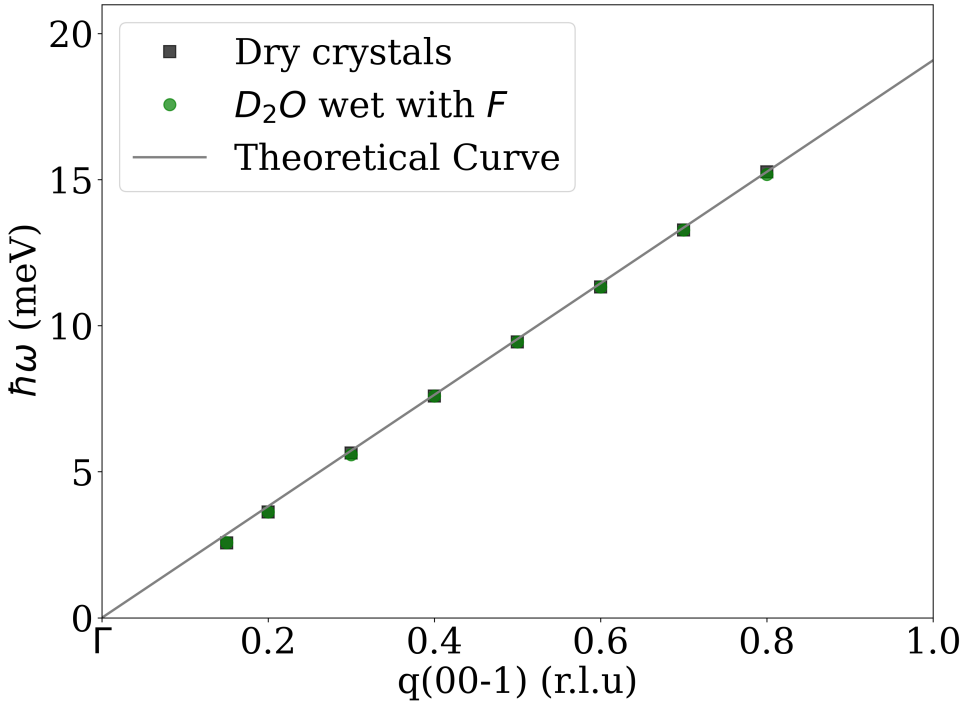

Figure 5.6: Dispersion curve of dry α-Al_2O_3 crystals (grey squares) and D_2O continuously wetted samples with flux F in the (300) Brillouin zone along the Γ-Z direction compared to the theoretical curve from (5.2). Numerical error bars from the fitting procedure are negligible. Data obtained by Inelastic neutron scattering at IN8. Experiments performed at room temperature and pressure.

previous set of experiments. This highlights the usefulness of inelastic neutron scattering in comparison to inelastic X-ray scattering. Furthermore, the liquid which showed the clearest hardening in IXS was light water, and heavy water broadening was more subdued as mentioned in 4. The results between experiments are therefore compatible.

On the point of a depth-dependent hardening, we do not observe, as shown in Fig. 5.6, a hardening through the Γ-Z direction with q dependence. This invalidates the hypothesis made in chapter 4 that the reason why effects were visible with IXS at the $(\bar{1}014)$ Brillouin zone but not the (0012) is a matter of beam penetration depth, as in this INS experiment it is independent. While there must, physically, exist a characteristic length at which the influence of the liquid at the surface has no longer an effect on phonon dynamics, it is *not* at $125\,\mu\mathrm{m}$ depth (or in this case distance to the surface). A way to check this hypothesis would be with INS by scanning the same Brillouin zone, in a similar setup, by changing the thickness of the crystals until no broadening of acoustic phonons is observed, and is recommended as a future study. Furthermore, no visible effects in the (0012) Brillouin zone in IXS does not exclude a broadening of the phonon there, as the resolution of the instrument FWHM is double that of INS ($3\,\mathrm{meV}$ compared to $1.5\,\mathrm{meV}$). It would also be unwise to compare both the zones as only LA can be observed in the Γ-Z direction at (0012), while only TA can be observed in the same direction for (300).

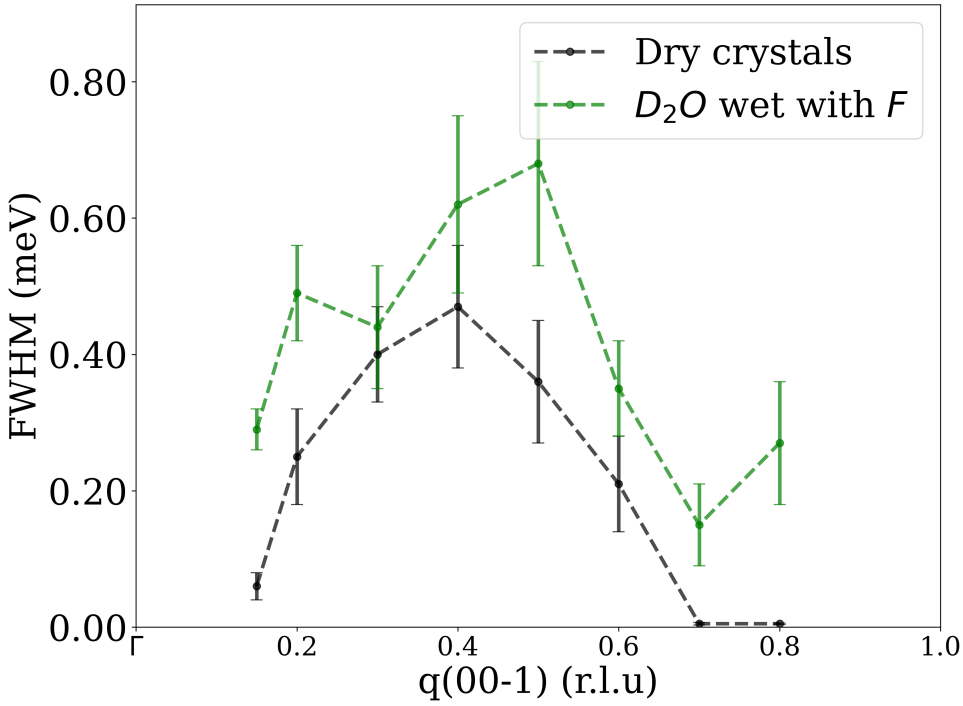

Figure 5.7: Comparison of dry (black) and D_2O wetted with flux F (green) full width half maximum (FWHM) of α-Al_2O_3 TA phonons along the Γ-Z direction. Data obtained by Inelastic neutron scattering at IN8. Experiments performed at room temperature and pressure.

To conclude, broadening of the TA acoustic branch of the α-Al_2O_3 crystal was observed throughout the (300) BZ in the Γ-Z direction when D_2O wetting with a constant flux F. These results point towards the anharmonic nature of the solid-liquid phononic interaction, and are compatible with our previous IXS obtained results. Furthermore, they help rule out the possibility of a depth dependent hardening.

1.4 Investigation on flow dependence down to $125\,\mu$m

As the previous results show, an anharmonic effect due to a flowing liquid at the surface takes place, though of different nature than that observed in the $(\bar{1}014)$ Brillouin zone and discussed widely in chapter 4. As our results suggested in chapter 4, there is a flow-dependent effect on the hardening (and broadening) in the $(\bar{1}014)$ Brillouin zone, and therefore there could be one on the broadening of the TA phonon in the (300) Brillouin zone. We add that, in the previous chapter, broadening of the LA branch was systematic throughout the scanned crystal when it was wetted and maintained in a non-equilibrium state. Therefore we stopped the pump inducing the D_2O liquid flow F, in order to determine whether the anharmonic broadening effects observed in INS are, like their IXS obtained counterparts, flow dependent. Fig. 5.8 shows the phonon width as a result of said stoppage of liquid flow.

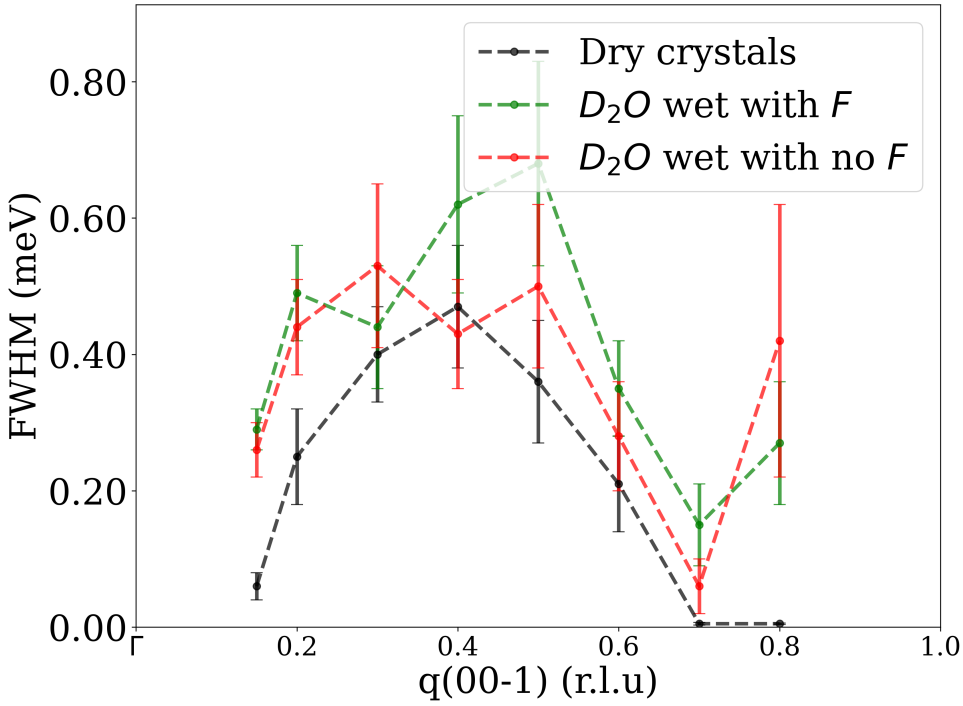

Figure 5.8: Comparison of dry α-Al_2O_3 crystals TA raw data and fit (black), D_2O wetted with flux F (green) and without F (red) FWHM(meV) along the Γ-Z direction. Error bars are numerically obtained from the fitting procedure. Data obtained by Inelastic neutron scattering at IN8. Experiments performed at room temperature and pressure.

Despite the fact that throughout the scanned range there is a slight decrease in width due to flow stoppage, there is not a return to dry crystals phonon width and it would therefore be hard to conclude with these results only, as they are often bordering on or within the numerical error bars. Furthermore, certain points —such as $q(r.l.u) = 0.3$ and $q(r.l.u) = 0.8$— show an increase of broadening, and those at the lower q-range are almost indistinguishable from one another. Examining the raw data may help us establish the veracity of the effect. Fig. 5.9 shows us precisely this at four positions in reciprocal space. It is of importance to note here that direct visual comparison between scans is only possible because the two series of scans have the same mosaicity (see Tab. 5.1).

There is an effect depending on the flow, as each set of raw data when the flow is stopped is contained within the flowing D_2O dataset, even the one at $q(r.l.u) = 0.3$, despite the fitted data being inconclusive on the broadening or not of the TA phonons. Especially important is the phonon picture in Fig.5.9a) at $q(r.l.u) = 0.2$. There not only are all the raw data scans contained within the original phonon scans, but the intensity of the phonons is the same, allowing for the best visual comparison.

To conclude this subsection, while there seems to be a flow dependent broadening effect, it has not been quantified as it was possible for hardening in the previous chapter. Nonetheless, both the FWHM fitted and raw data suggest that the phonon broadening is lesser when

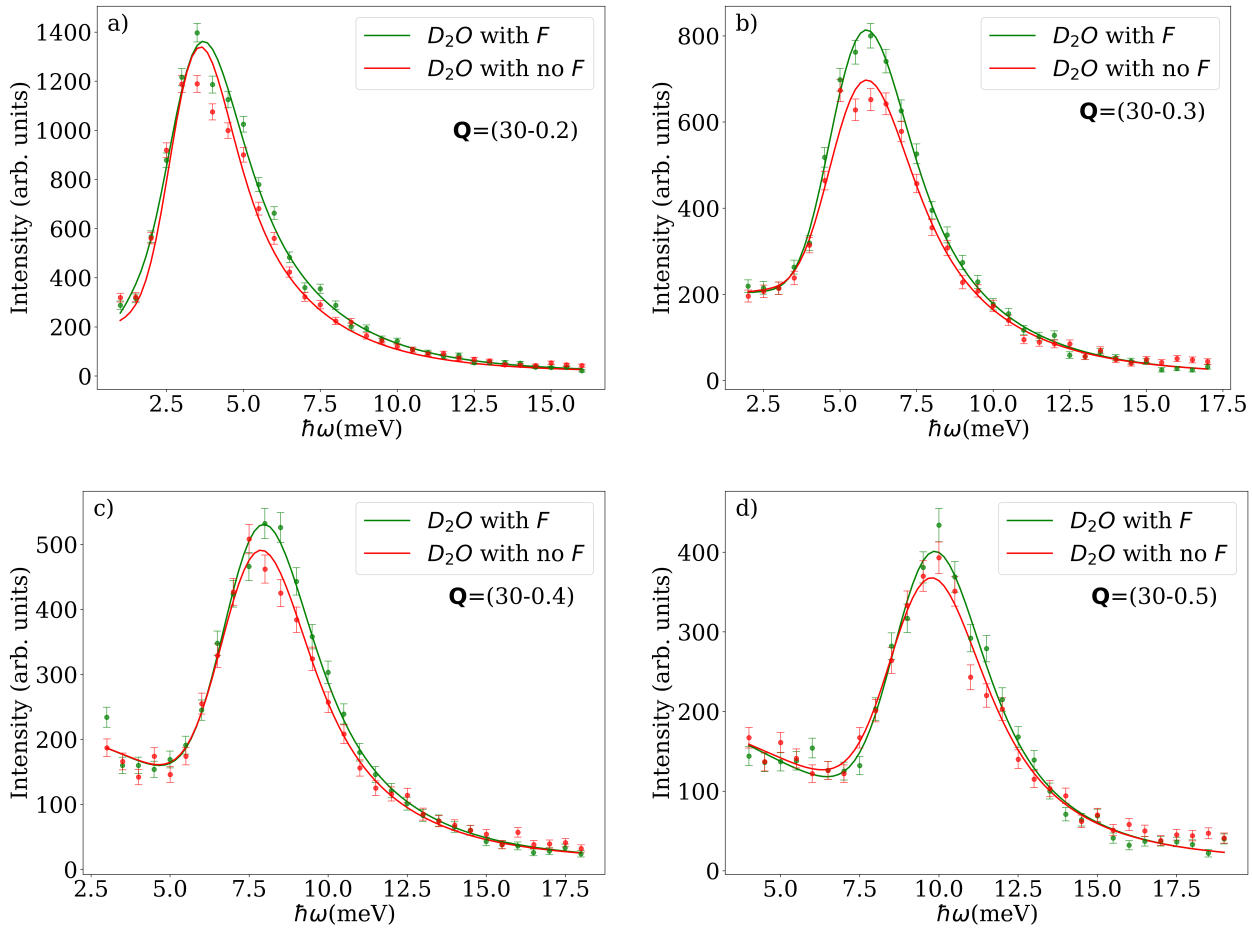

Figure 5.9: Comparison of fitted (line) and raw data (points) of the TA phonon of α-Al_2O_3 crystals for the flowing heavy water in green and the static heavy water after flow in red at a) $\mathbf{Q} = (30 - 0.2)$, b) $\mathbf{Q} = (30 - 0.3)$, c) $\mathbf{Q} = (30 - 0.4)$, d) $\mathbf{Q} = (30 - 0.5)$. Data obtained by Inelastic neutron scattering at IN8. There is no change of mosaicity. Experiments performed at room temperature and pressure.

the flow is stopped, returning towards dry crystals FWHM, supporting our central thesis of a necessary non-equilibrium state characterised by anharmonicity of the acoustic phonons. To be able to conclude with more assurance as to the flow-dependence, the easiest solution would be to change sample holder so that it minimises movement of the crystals, thus reducing the mosaicity, and allowing us to observe effects with better precision.

1.5 The case of water: isotopic effects

The previous chapter highlighted a clear isotopic effect on flow-induced hardening. By changing H to D, the hardening reduced to a ratio of roughly $\sqrt{m_H/m_D} \approx 0.707$. Similarly, our only result on isotopic broadening of the LA branch of α-Al_2O_3 shows a lesser broadening when the flow-induced hardening is by D_2O compared to H_2O. We therefore want to investigate this effect with inelastic neutron scattering.

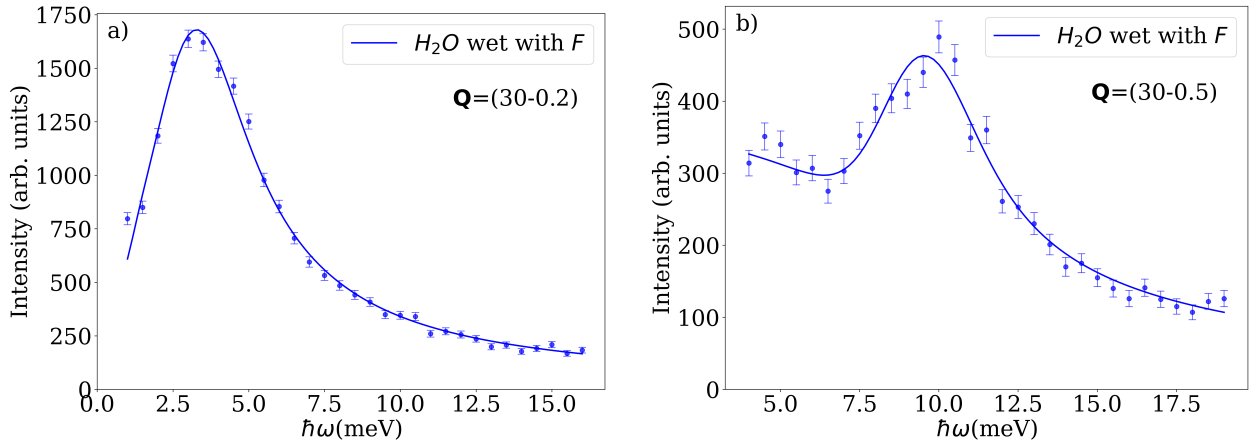

Figure 5.10: a) H_2O continuously wetted with flux F α-Al_2O_3 crystals data and fit of TA phonon at $\mathbf{Q}=(30-0.2)$. b) H_2O continuously wetted with flux F α-Al_2O_3 crystals data and fit of TA phonon at $\mathbf{Q}=(30-0.5)$. Data obtained by Inelastic neutron scattering at IN8. Experiments performed at room temperature and pressure.

The raw data at two points in reciprocal space from Fig.5.10 highlight the drastic effect of changing heavy water to light water, by a general increase of background noise intensity, as the incoherent scattering of water is orders of magnitude higher than that of heavy water ($80\,\mathrm{b}$ vs $2\,\mathrm{b}$). This change also is linked with a large increase in phonon width, as observed in Fig.5.11, especially at low $q(r.l.u)$; with the hardening being clearly much bigger than the numerical error bars and not overlapping. This is similar to the results in IXS 5 in Fig.4.22 for the LA α-Al_2O_3 branch. In Fig.4.22 as in Fig. 5.11, the maximum of the H_2O continuously wetting crystal FWHM (LA for IXS and TA for INS) is obtained at $q = [000.2]$. However, in IXS, we managed to scan at lower q, showing the subsequent decrease of the FWHM, which we were not able to do here. There is clearly a strong increase of broadening in α-Al_2O_3 TA phonon at the (300) BZ.

The fitting of data for the case of water is suboptimal as the incoherent noise from water is not purely constant in energy, though very broad. The constant background noise had to be changed depending on the scans (in the 100 to 130 count range). At lower (< 0.2) $q(r.l.u)$, fitting data becomes near impossible because the approximation of a constant background noise does not encapsulate the quasi-elastic peak of water, which is overlapped with the Bragg peak tails. This crucial point at $q = -0.15$, present in all other scan series, is therefore missing, frustratingly not allowing us to know if the broadening does resolve itself and the general q^2 dependence of the FWHM takes place, as it seems to take place for our results with IXS in Fig.4.22. Furthermore, there is, similarly to D_2O, no effect whatsoever on phonon energy at the (300) scanned zone when changing to H_2O.

In order to have a better understanding of this isotopic effect, an interesting experiment that one could do would be to change the H/D ratio in the water and see if there is a broadening dependence on the ratio and if it is continuous.

To conclude, the isotopic effects, while their quantification could be improved upon, are

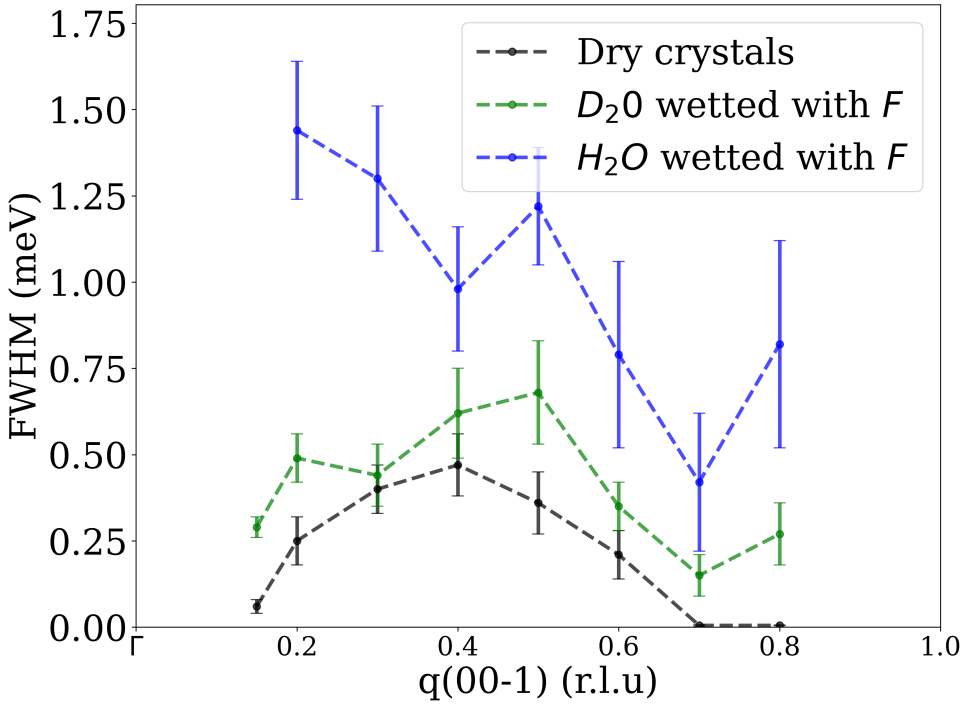

Figure 5.11: Comparison of dry (black), D_2O (green) and H_2O (blue) wetted α-Al_2O_3 crystals with flux F TA phonon FWHM along the Γ-Z direction. Data obtained by Inelastic neutron scattering at IN8. Error bars are numerically obtained from the fitting procedure. Experiments performed at room temperature and pressure.

considerable and echo our results in IXS. Changing D to H has greatly increased the effects on the phonon broadening, and therefore the flow induced anharmonic phononic interaction. This result also echoes the hardening result of IXS in which hardening at $(\bar{1}014)$ was always, in the exact same experimental conditions, higher for light water than heavy water. This continues the trend that water has a stronger anharmonic interaction with the solid.

1.6 On kinetics of flow wetting induced phonon interaction

In chapter 4, we systematically highlighted a kinetic aspect to the mechanically stress-induced hardening at the α-Al_2O_3 crystal by wetting in the $(\bar{1}014)$ BZ, and its reversibility. We were left stuck with our intuitive understanding of it being linked to evaporation, but unclear as to why and especially how. Similarly, in our section on reversibility 3.3, we highlighted in Tab.4.1 that the broadening of the LA peak was itself reversible, even though the kinetic behaviour of broadening was not as clear as for hardening. However, in the previous neutron inelastic scattering experiment, we highlighted a very similar TA broadening behaviour under continuous H_2O liquid wetting than that observed by wetting in 'asymptotic' conditions for the LA peaks by IXS. We therefore strongly suspect that any kinetic aspect would be especially visible in the case of continuous H_2O wetting. Our hypothesis was that this kinetic effect of hardening, being linked to evaporation of the liquid at the crystal surface, would thus disap-

pear were a continuous flow be added. Fig. 5.12 shows the kinetics of wetting for both heavy water and light water. Both highlight no time-dependence on broadening whatsoever.

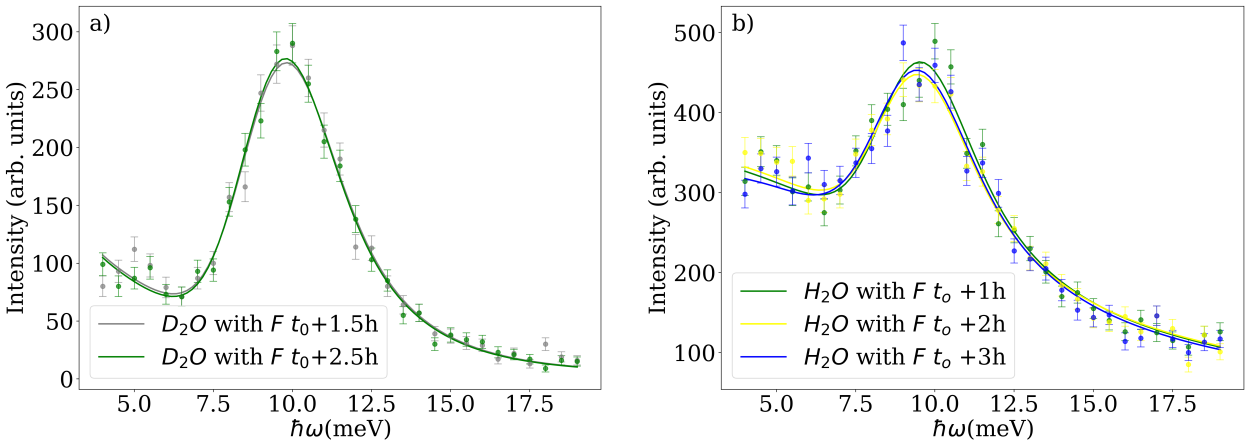

Figure 5.12: a) scans and fits at $\mathbf{Q} = (300.\bar{5})$ 1.5 h (grey) and 2.5 h (green) after D_2O wetting under constant flow F of α-Al_2O_3 crystals TA phonon data (points) and fit (lines). b) scans and fits at $\mathbf{Q} = (300.\bar{5})$ 1 h (green), 2 h (yellow) and 3 h (blue) after H_2O wetting under constant flow F of α-Al_2O_3 crystals TA phonon data (points) and fit (lines). For both scans, t_0 corresponds to the liquid flow being started, and not at the time of wetting. Data obtained by Inelastic neutron scattering at IN8. Experiments performed at room temperature and pressure.

As such, since evaporation is a non-existent factor with our current setup but was clearly one of crucial importance in IXS in reflectometry, this simple set of measurements has solved one of the questions arisen from our previous experiments: the kinetic aspect of the non-equilibrium solid-liquid interaction observed in IXS is the result of a complex interplay between evaporation and surface energy limiting said evaporation. It does not exist in constant flow conditions.

1.7 Discussion and conclusion

These sets of inelastic neutron scattering experiments were designed and were successful to test hypotheses from our previous results from chapter 4. By changing the wetting and mechanical stress of the liquid to a steady flow and changing the scattering geometry from reflectometry to transmission through co-aligned smaller crystals, we managed to decouple the key physical phenomena from evaporation and a variable beam penetration depth.

The key takeaways from this chapter are as follows:

- **Confirmation of anharmonic phononic interaction in a new BZ**. We previously only managed to observe a broadening at one point in the (0012) BZ, and most of our results were obtained in the $(\bar{1}014)$ BZ. Here, we have shown a clear broadening of the TA phonons when continuously wetted throughout the Γ-Z direction, as seen in Fig.5.11, echoing the broadening behaviour of the LA branch in Fig.4.22. Contrary to the $(\bar{1}014)$, the (300) BZ observed in INS showed no hardening or change of phonon energy. This

strongly suggests that there is no depth dependent effect, but rather a selection rule which allows phonons from certain BZs to harden and others to broaden.

- **Confirmation of flow dependence**. Here our data suggests that broadening is more pronounced when the liquid is flowing, a qualitative trend in agreement with previous results from 3.4. While the quantitative analysis is limited by uncertainties, these show a reduced broadening for the less interactive D_2O flow. The general trend follows our central thesis: the liquid must be maintained in a constant non-equilibrium stressed state to induce anharmonic effects such as broadening.

- **A strong isotopic effect in broadening**. Flowing H_2O induced TA broadening is significantly higher than its heavier counterpart. Said light water induced TA broadening also follows the same behaviour as the LA broadening observed with IXS at the $(\bar{1}014)$ BZ. This result reinforces the hypothesis that the solid-liquid phononic interaction is mediated by the H-bond, where the H_2O lighter H atoms allow for more efficient vibrational energy transfer through the liquid, and through the lattice.

- **Kinetics are a consequence of evaporation**. The absence of kinetics in the broadening process due to liquid flow at the surface, when it was shown to be a reversible effect in the previous chapter, highlights that the kinetics were probably due to a complex interplay of evaporation, surface tension, and strong solid-liquid interaction. This would create a time-varying stress at the interface, akin to a time varying flow.

In conclusion, through inelastic neutron scattering, we have confirmed a complex solid-liquid interaction maintained by flowing liquid at the surface, maintaining the linked states of matter in a non-equilibrium thermodynamic state. The observed phenomenon of hardening is mode and BZ-specific, while broadening is observed throughout the reciprocal space if the resolution allows, with a strong isotopic dependence where heavy water shows a subdued effect compared to light water. This strong dependence corroborates our previously discussed understanding that the vibrational patterns in the flowing water are likely mediated by the H-bond, the most isotopically dependent vibrational patterns in this energy range.

2 Transmission Inelastic X-ray Scattering: towards direct neutron/X-ray comparison

2.1 Experimental setup

The goal of this small experimental section is to corroborate the q-dependent hardening in the Γ-Z direction at the $(\bar{1}014)$ BZ of α-Al_2O_3 when there is a constant flowing liquid at the surface rather than the simple wetting stressed by the nitrogen recirculation bubble previously performed in 4. We also directly compared the (300) BZ effects between scans in IXS and INS, in order to verify their compatibility. The experimental setup is shown in Fig.5.13, with a home-made sample holder which imposes a flow with a flux $F = 0.35\,\mathrm{mL\,s^{-1}}$, the same as in the previous section.

The scanned α-Al_2O_3 crystal is $250\,\mu\mathrm{m}$ thick, as shown in Fig.5.1b). In contrast to the neutron experiment, the liquid only flows on one side of the crystal, meaning that the distance

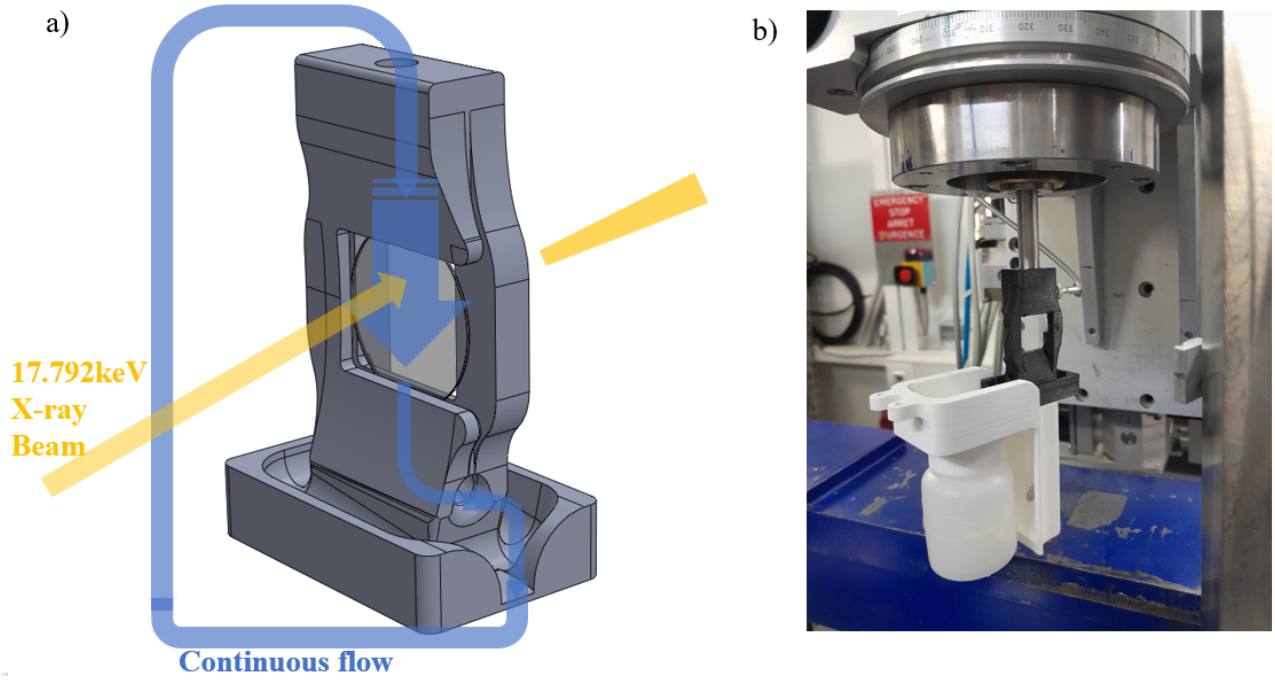

Figure 5.13: a) Schematic view of the setup. An α-Al_2O_3 $250\,\mu$m thick crystal is mounted on the surface of which (α-$Al_2O_3(0001)$) water flows. The water is recycled and repumped at the top of the sample holder. The pump and general setup are the same as for neutron scattering experiments. b) Picture of the setup in the ESRF ID28 experimental hutch.

to wetted surface is $250\,\mu$m instead of $125\,\mu$m.

The full setup with water reservoir and attachment shown in Fig.5.13b) does not fit in any of the containments so that the atmosphere around the crystal cannot be filled with nitrogen to preserve the surface. We have added nitrogen sources close to the setup in the direction of the crystal to minimise the air contamination.

Two series of scans were performed:

- Scan in the Γ-Z direction of the (300) of a $250\,\mu$m thick crystal.
- Scan in the Γ-Z direction of the $(\bar{1}014)$ of a $250\,\mu$m thick crystal, in order to observe both TA and LA phonons and confirm that hardening and the q-dependence of said hardening still take place.

2.2 On data treatment

While the data treatment method is exactly that detailed in chapter 4 section 2, a few caveats must be added. ID28 had a change of monochromator notably in order to theoretically improve upon the resolution. However, this next set of experiments was performed while the new setup was not yet ready for use. The resolution function obtained was unclear leading to a degraded resolution from $3\,$meV to $\sim 3.7\,$meV (FWHM), as reported by beamline scientists. Furthermore, said resolution is asymmetrical and did not allow for clear

deconvolution of the dynamic structure from the resolution function. Nonetheless, even with a subpar fit and by looking at the raw data, we can qualitatively confirm trends observed. This, however, leads to an impossibility to quantitatively discuss more subtle effects, such as phonon broadening.

2.3 Direct comparison with neutron experiments under flow

By using the flow setup shown in Fig.5.13, therefore changing the scattering geometry from reflectometry to transmission, we can observe the (300) BZ that was not within our reach in reflectometry.

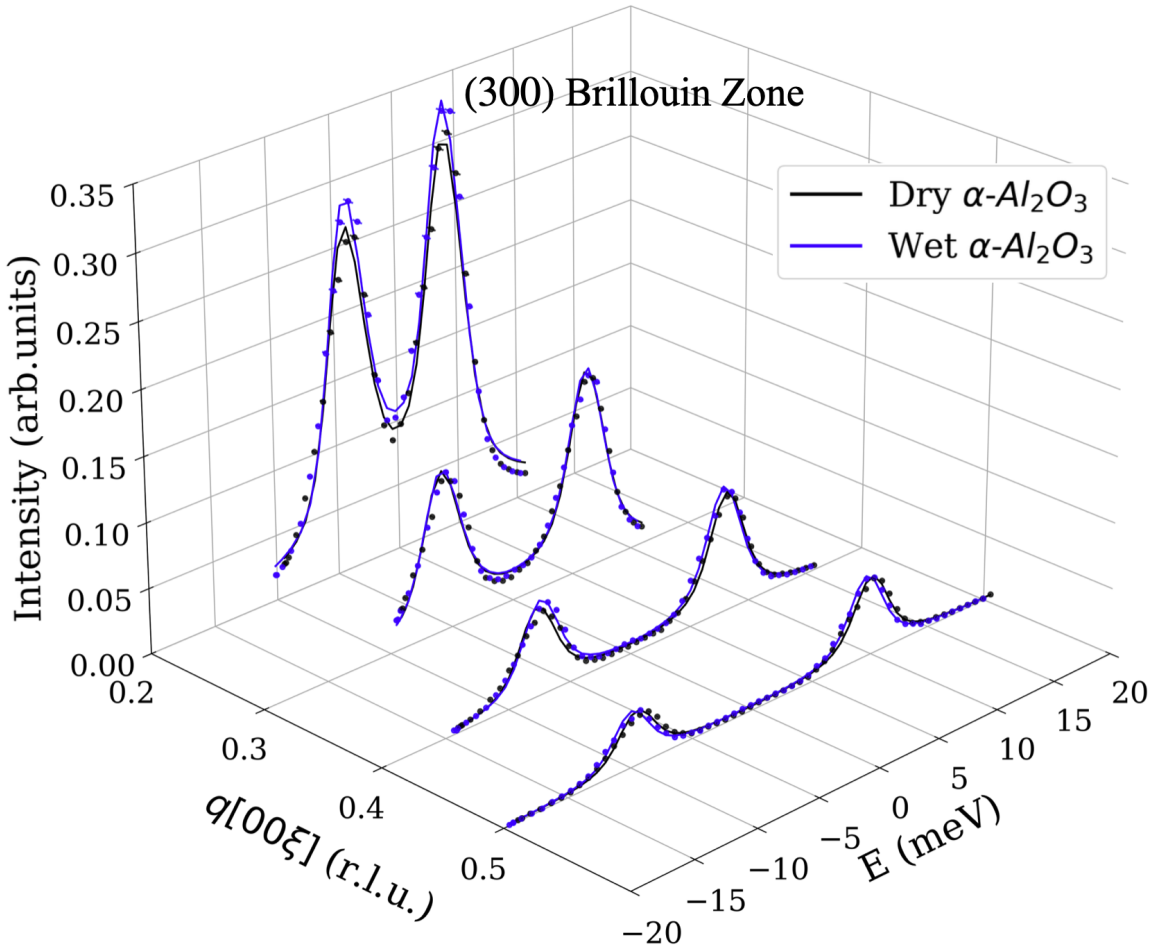

Figure 5.14: Inelastic X-ray scattering scans and fits of dry (black) and H_2O continuously wetted with flow F in the (300) BZ, in stable conditions in reciprocal space in the $[00\xi]$ direction of the same α-Al_2O_3 crystal performed at ID28 with $\sim 3.7\,\mathrm{meV}$ resolution (FWHM) in transmission. Experiments performed at room temperature and pressure.

Fig.5.14 shows the scans in dry and H_20 continuously wetted conditions and respective fits for multiple position in reciprocal space along the $q = [00\xi]$ direction in the (300) BZ. No qualitative effects are visible. As the resolution of the IXS experiments is poorer than that of INS ($\sim 3.7\,\mathrm{meV}$ compared to $\sim 1.5\,\mathrm{meV}$), and the resolution function is not properly defined, it seems likely that the effects of the flowing H_2O on the TA branch shown in Fig.5.11 are just

within the resolution.

To conclude, the results shown in Fig.5.14 of lack of TA broadening in the (300) BZ are compatible with the broadening results from the previous section. This highlights the complementary nature of INS and IXS, with INS being the better technique to observe subtle broadening effects.

2.4 Evidence of q-dependent hardening in IXS transmission geometry

The same crystal was then scanned in the $(\bar{1}014)$ BZ with continuous H_2O flow F (as before).

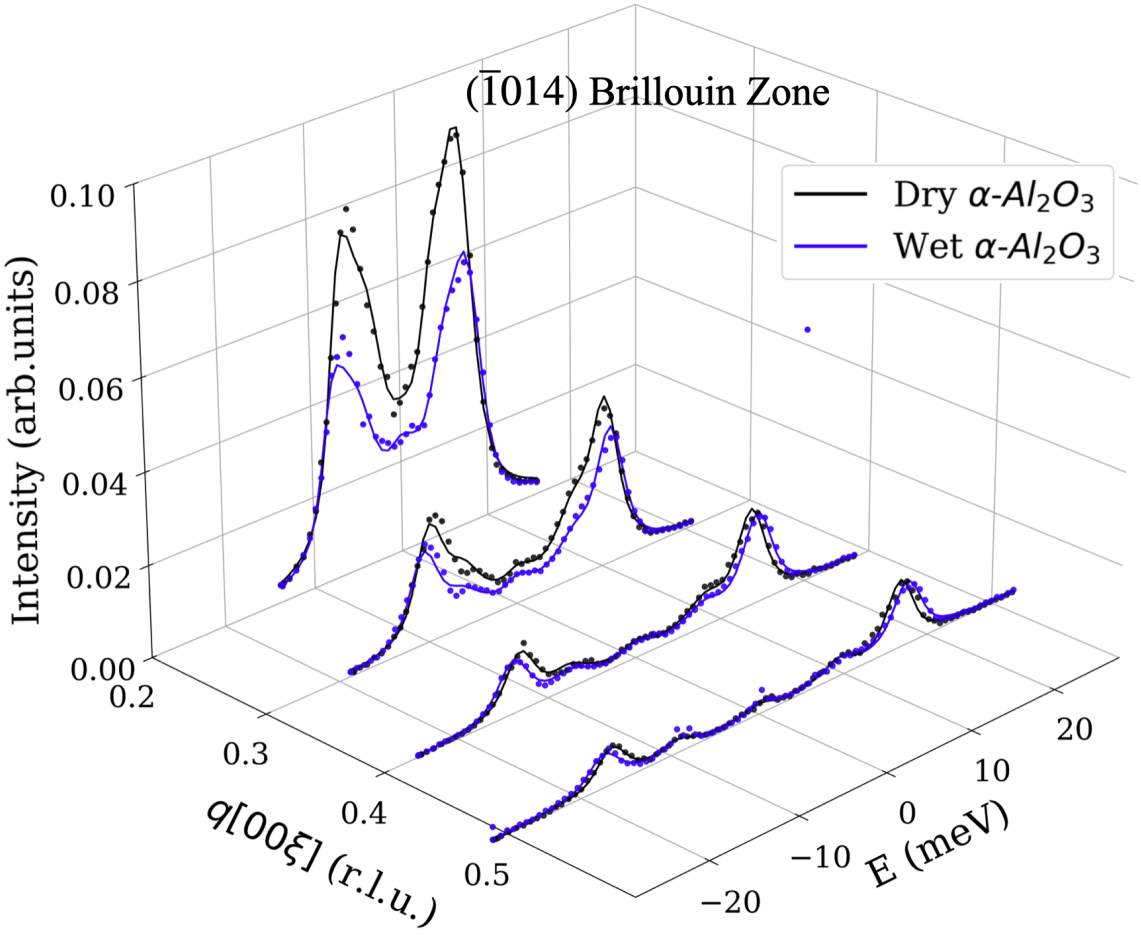

Figure 5.15: Inelastic X-ray scattering scans and fits of dry (black) and H_2O continuously wetted in the $(\bar{1}014)$ BZ, in stable conditions in reciprocal space in the $[00\xi]$ direction of the same α-Al_2O_3 crystal performed at ID28 with $\sim 3.7\,\mathrm{meV}$ resolution in transmission. Experiments performed at room temperature and pressure.

Fig.5.15 shows the scans in dry and H_20 continuously wetted conditions and respective fits for multiple position in reciprocal space along the $q = [00\xi]$ direction in the $(\bar{1}014)$ BZ. Through this data it is clear that hardening of both LA and TA branches happens throughout the Γ-Z direction in transmission, not just in the reflectometry setup of chapter 4. The reso-

lution is too wide, and the TA and LA phonons overlap compared to those shown in Fig.4.19. We have comparative results indicating hardening but cannot extract quantitative data from this series of scans.

One clear result is apparent, confirming the previous results in 5: the hardening of both TA and LA branches is qualitatively larger towards the Γ point. By changing the experimental setup, from mechanically stressed by a nitrogen flow to a continuous flow F of liquid at the α-Al_2O_3 surface, the hardening in the $(\bar{1}014)$ BZ follows the same behaviour.

We shall also point out that, contrary to results shown in Fig.4.19, there is not a complete collapse of the quasi-elastic peak, but one surface is not wetted, such that the CTRs are still present within the crystal.

To conclude, by changing the setup from reflectometry to transmission, the q-dependent hardening in the $(\bar{1}014)$ BZ was maintained, highlighting a fundamental effect of the flow induced out-of-equilibrium solid-liquid couple.

2.5 Summary and discussion

This set of transmission IXS experiments is a critical link between the INS from this chapter and IXS results from the previous chapter. Despite technical challenges with IXS resolution prohibiting us from quantitative analysis, two results emerge:

- The direct comparison between INS and IXS is compatible. The TA broadening observed in INS in the (300) BZ was not visible in IXS due to the resolution being more limited (see Fig.5.14), and is consistent with broadening shown in Fig.5.11. The anharmonic interaction between the flowing liquid and the phonons of the crystal is 'limited' to a broadening in the (300) BZ, pointing towards a selection rule in BZ.
- The $(\bar{1}014)$ BZ scans qualitatively successfully reproduce the results from section 5 under continuous H_2O flow. The hardening effect is therefore a fundamental consequence of the flowing liquid at the surface. Furthermore, the emergence of a gapped mode shown in Fig.4.20 is reproduced, albeit with less certainty due to the resolution function.

3 Conclusion on INS and IXS transmission experiments

These two sets of experiments were designed to test hypotheses resulting from our previous results from chapter 4. By changing the wetting and mechanical stress of the liquid to a steady flow and changing the scattering geometry from reflectometry to transmission through co-aligned smaller crystals, we successfully decoupled the key physical phenomena from evaporation and a variable beam penetration depth.

The key takeaways from this chapter are as follows:

- The anharmonic solid-liquid interaction is driven and "fed" by the external flow. The combination of the IXS results from the previous section 3.4 and the qualitative agreement with INS in section 1.4 highlight that both hardening in the $(\bar{1}014)$ BZ and broadening in the (300) BZ require the liquid to be in a mechanically-stressed, non-equilibrium

state. By eliminating evaporation we confirmed that the kinetics observed in section 3.2 most likely were due to the evolving stress at the interface, not an intrinsic physical phenomenon of the non-equilibrium solid-liquid wetting.

- The nature of the anharmonic interaction depends on the BZ. By performing the experiments in transmission, we have successfully eliminated a potential depth-dependent hardening effect. A selection mechanism suggesting a rule has been identified by these transmission experiments: the flowing liquid generates broadening of the TA phonon in the (300) BZ (and LA phonon in the (0012) BZ previously in section 5), while it induces a q-dependent hardening of both TA and LA phonons in the $(\bar{1}014)$ BZ. We can therefore conclude that the anharmonic effect generated by coupling of the driven liquid dynamics and the solid's lattice vibrations is specific to the phonon mode and its position in reciprocal space.

- A strong isotopic effect. The isotopic dependence of broadening highlighted in section 1.5 shows a much more potent effect of broadening of the TA phonon in the (300) BZ with H_2O than D_2O. Though quantitatively different from those presented in chapter 4 when it came to hardening in the $(\bar{1}014)$ BZ, they point to the same conclusion: H_2O interaction with the α-Al_2O_3 crystal is much stronger than with D_2O. Combining both of these results, we have evidence suggesting that the vibrational energy of the out-of-equilibrium flow is transmitted via the H-bond network, which is known to be more efficient in H_2O than D_2O.

In conclusion, this chapter has confirmed our hypotheses and narrowed down the key mechanism for this novel solid-liquid interaction. The flowing water transmits energy via its H-bond vibrational patterns to the α-Al_2O_3 crystal, inducing a complex long-range anharmonic response interacting with acoustic phonons. The exact nature (hardening and/or broadening) of the anharmonic interaction has been shown to be Brillouin Zone specific, hinting at a selection rule.

Chapter 6

Investigating bulk structural and chemical changes due to the wetting process

In this chapter we will try to answer the questions that arose from our previous results: Do flow induced inelastic effects originate from a bulk modification? Is there an electronic effect due to a mechanically stressed wetting state, indicating an electronic change leading to a potential electron-phonon interaction? We shall answer these with high resolution X-ray diffraction experiments and X-ray Raman scattering experiments.

Contents

1 Investigating bulk structural changes due to wetting

Since hardening was observed in the $(\bar{1}014)$ BZ but not the (0012) BZ, each associated with an approximate penetration depth of $\sim 150\,\mu\mathrm{m}$, the question of a depth dependent effect arose, and it was shown in Chapter 5 with transmission-based geometry in INS and IXS on $250\,\mu\mathrm{m}$ thick samples that the anharmonic effects were BZ dependent, not depth dependent. As the acoustic phonons in the $\Gamma - Z$ direction were changed in the $(\bar{1}014)$ BZ, the question arises whether there is a local change in the structural properties of the crystal that could elucidate the selection rule observed in the previous two chapters. This is what we have investigated using the high-resolution diffractometer of ID28, with the assistance of Alexei Bossak and Daniel Chaney at the ESRF.

1.1 Experimental setup

The crystals scanned with a α-$Al_2O_3(0001)$ surface were of $4\,\mathrm{mm}$ diameter (to accommodate the geometry of the diffractometer) and $150\,\mu\mathrm{m}$ thickness (compared to the $2\,\mathrm{mm}$ thick, $22\,\mathrm{mm}$ diameter crystals used for the experiments discussed in the previous chapter 4) and the $250\,\mu\mathrm{m}$ thick crystals in the previous chapter 5. The crystal was previously heated to $450\,^{\circ}\mathrm{C}$ over $8\,\mathrm{h}$ then relaxed to $150\,^{\circ}\mathrm{C}$ and maintained until the experiment, as explained in 1. For this experiment, we reverted to simply wetting the surface with $\sim 10\,\mu\mathrm{L}$ H_2O. We only tested with light water, as all anharmonic effects were stronger with H_2O than D_2O (see 4 and 1.5).

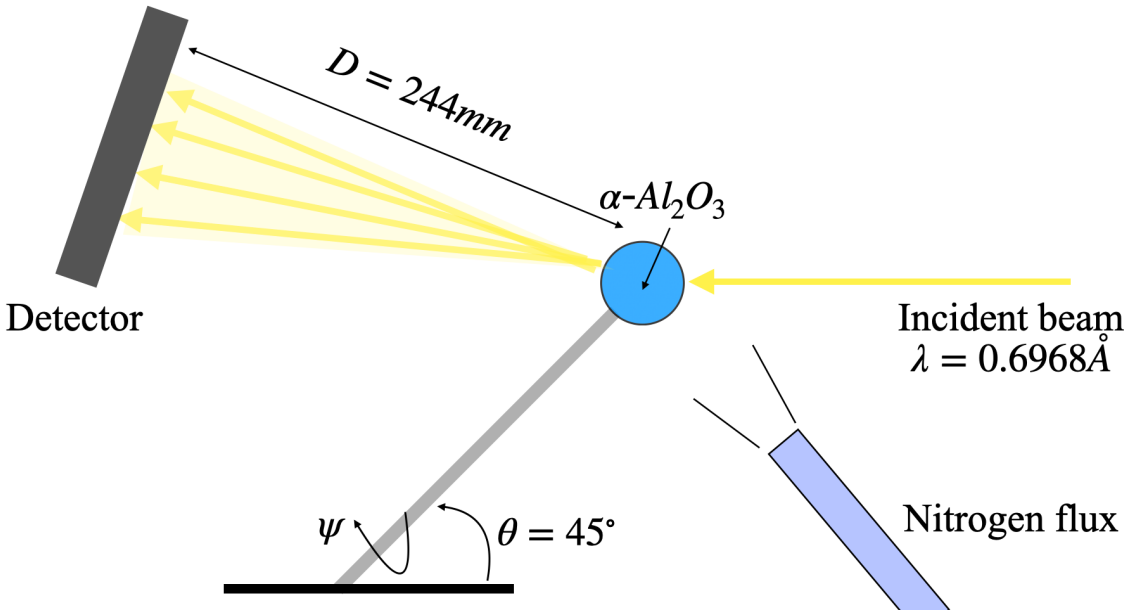

Figure 6.1: Side view of the diffraction experimental setup of a $4\,\mathrm{mm}$ diameter $150\,\mu\mathrm{m}$ thick α-Al_2O_3 schematic view. The pixel size is $174\,\mu\mathrm{m} \times 174\,\mu\mathrm{m}$. Nitrogen flux was chosen after measurement of air flow close to crystal surface of $\sim 0.1\,\mathrm{m\,s^{-1}}$. Scan performed by full 180° rotation of ψ around the 45° rod on which the crystal is glued. All experiments were performed at room temperature and pressure.

The diffractions were performed with a beam energy $17.792\,\mathrm{keV}$ corresponding to the

$Si(999)$ reflection, and therefore an incident wavelength of $0.6968\,\text{Å}$, the same as the previously discussed IXS experiments. The beam size was $20\,\mu\text{m} \times 20\,\mu\text{m}$. A nitrogen air source was added, such that the measured speed of air flux at the position of the crystal was around $0.1\,\text{m}\,\text{s}^{-1}$, in order to maintain the liquid within the same range of mechanical stress as in the experimental setup of chapter 4, as per Tab.4.2. There was no sample holder to separate the environment in which the sample was placed and the air, and the position of the flux relative to the crystal varied during the rotation of the sample necessary for a scan. We performed near complete rotational scans, by rotating the crystal around the axis of the goniometer head ψ by $170°$, itself with a fixed position of $45°$ to horizontal. A beamstop is always present so that the detector remains undamaged. The multi-detector itself is a PILATUS3 X CdTE 1M, with a pixel size of $174\,\mu\text{m} \times 174\,\mu\text{m}$, and a single pixel resolution (FWHM), which for the detector to sample distance $D = 244\,\text{mm}$ with said wavelength is equivalent to $2\theta < 0.05°$ [174].

The crystal was scanned dry, then every hour for twelve hours when wetted. Each individual rotation of $170°$, called from now on a scan, took twelve minutes. In between scans the sample was rotated back to its initial position and left there for the remainder of the hour.

1.2 Data treatment

Specialised software had to be used, and in our case we used CrysAlisPro for peak harvesting and intensity integration [174]. All relevant physical parameters, discussed in the previous subsection, such as incident wavelength, distance between the sample and the detector, scanned range and step etc., were entered. This allowed us to recover the structural parameters of the crystal scanned (which were identical to the one described in chapter 2 2.1). Cuts of the reciprocal space were then chosen (say, for example, $(h0l)$) for 2D representation, and were compared between dry and wet in a given plane.

1.3 Study of diffraction planes

There were no qualitative changes in diffraction data between wet and dry samples, regardless of time from wetting and reciprocal space cut. This is evident (or rather the lack of change is evident), in Fig. 6.2, Fig.6.4 and Fig.6.3.

Keen eyes will see a general decrease of intensity with each following scan. This was simply due to the experiments being performed at a moment where the linear accelerator of the ESRF needed repair and was therefore not filled each hour. The intensity of the photon beam flux was as a consequence steadily linearly decreasing throughout the experiment. Thankfully, this did not affect our results on structure, as our conclusion depends only on Bragg peak positions. Furthermore, the Bragg peaks were of such intensity that they saturated the detector.

While the qualitative visual comparison between scans strongly suggests no change in structure due to wetting, one must still use a quantitative method to prove this. We have first chosen to project the data along one axis, as if one were performing powder diffraction analysis. In order to do so we had to define the centre of the scan as the centre of the reciprocal space. In practice, this centre was determined by the position of the beamstop,

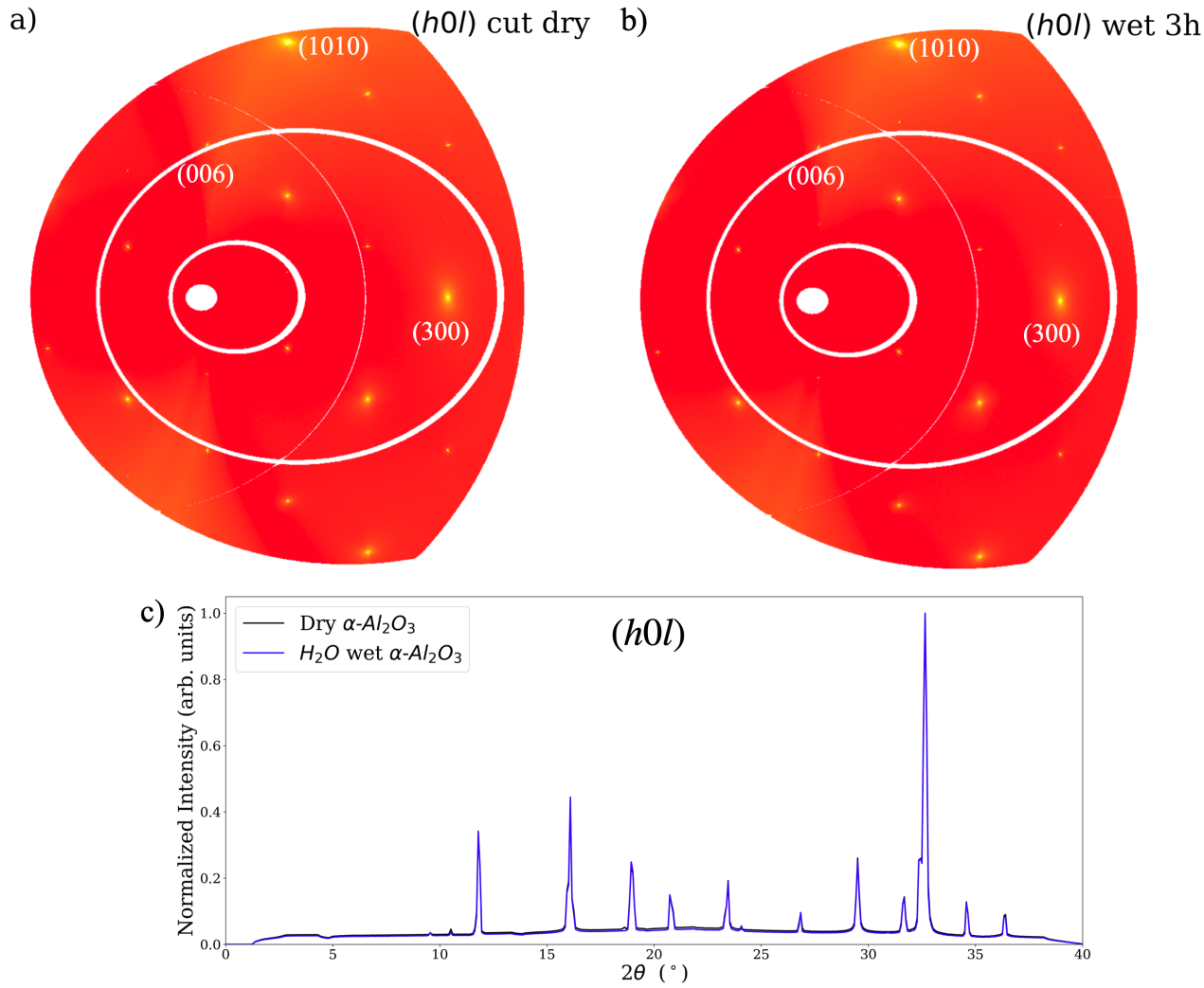

Figure 6.2: $(h0l)$ diffraction scans with some indexed Bragg peak positions for clarity of α-Al_2O_3 from a a) dry crystal, b)H_2O wetted crystal $\sim 3\,\mathrm{h}$ after wetting. Both diffraction patterns are shown in logarithmic scale. c) Azimuthal integration of the diffraction data to compare dry to wet in a non-logarithmic scale normalised by their maximum. Black line is the dry crystal and blue dashed line is the crystal wetted (also $\sim 3\,\mathrm{h}$ after wetting) with H_2O. Experiments performed at room temperature and pressure.

which corresponds to the region of minimum intensity in the diffraction file, and was at the centre of our obtained diffraction file (this is not visible on diffraction figures as they were cropped, so the centre of the scan is visually off-centre in Fig.6.2, Fig.6.4, and Fig.6.3). We then performed an azimuthal integration by calculating the distance to said centre in pixels and averaging the intensities of rings around the centre. The plot is then transformed to an angular scale common with powder diffraction using the relation $2\theta = 2\arctan(\frac{r}{D})$ with r the radial distance from the centre, calculated with a characteristic size of the pixel of $172\,\mu\mathrm{m}$, and D the distance from the sample to the detector, $244\,\mathrm{mm}$. It was impossible to compare Bragg peak intensities due to the saturation of said peaks as discussed in the previous paragraph.

Let us first discuss the results of the $(h0l)$ and $(\bar{h}hl)$ planes in Figures 6.2 and 6.3. Both of these planes are not equivalent by a rotation around the c-axis and therefore the diffraction

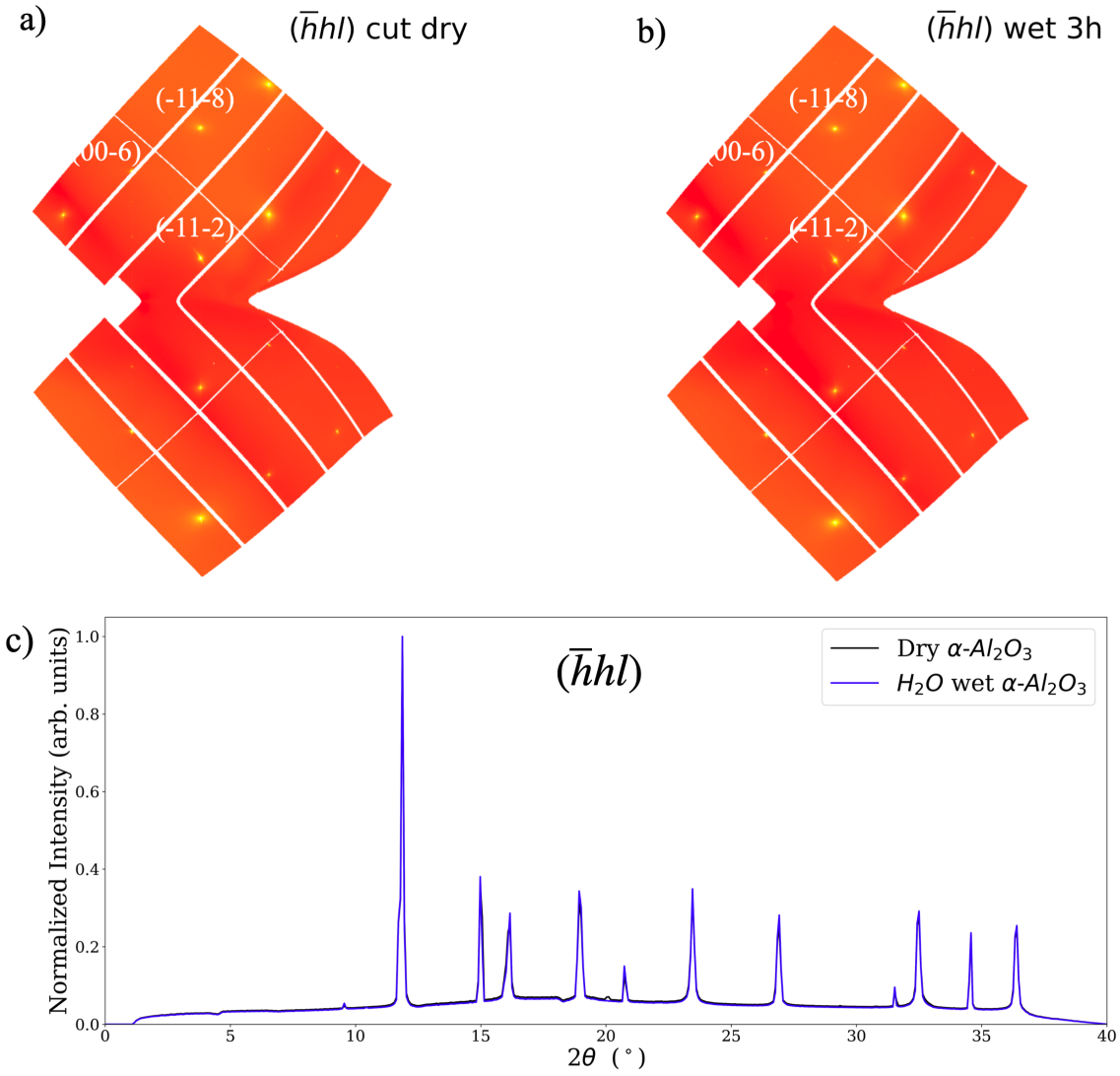

Figure 6.3: $(\bar{h}hl)$ diffraction scans, with some indexed Bragg peak positions for clarity, of α-Al_2O_3 from a a) dry crystal, b)H_2O wetted crystal $\sim 3\,\mathrm{h}$ after wetting. Both diffraction patterns are shown in logarithmic scale. c) Azimuthal integration of the diffraction data to compare dry to wet in a non-logarithmic scale normalised by their maximum. Black line is the dry crystal and blue dashed line is the crystal wetted (also $\sim 3\,\mathrm{h}$ after wetting) with H_2O. Experiments performed at room temperature and pressure.

pattern is different. There are no qualitative and quantitative changes, and this is confirmed by the almost perfectly identical azimuthal projection in Fig.6.2c) and Fig. 6.3c). H_2O wetting under nitrogen flow does not lead to any overt structural changes. This confirms our discussion in section 7 that the anharmonic coupling is not due to a structural change.

For scientific integrity we notice a very small decrease in background intensity throughout the Fig.6.2c) 2θ scan which we do not see in Fig.6.3c), though this is negligible.

The results in the $(0kl)$ plane, shown in Fig.6.4, highlight minor changes, even visible

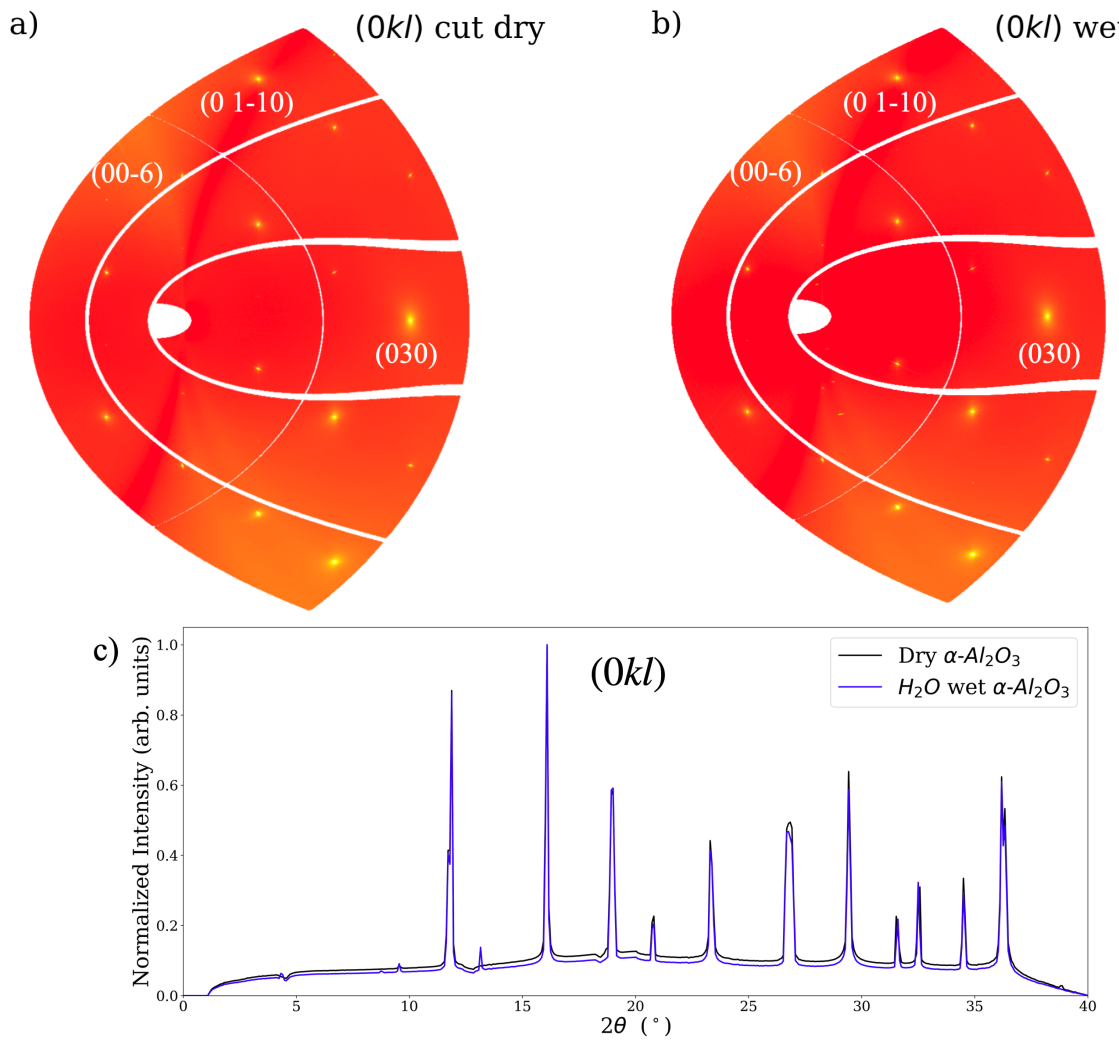

Figure 6.4: $(0kl)$ diffraction scans with some indexed Bragg peak positions for clarity of α-Al_2O_3 from a a) dry crystal, b)H_2O wetted crystal $\sim 3\,\mathrm{h}$ after wetting. Both diffraction patterns are shown in logarithmic scale. c) Azimuthal integration of the diffraction data to compare dry to wet in a non-logarithmic scale normalised by their maximum. Black line is the dry crystal and blue dashed line is the crystal wetted (also $\sim 3\,\mathrm{h}$ after wetting) with H_2O. Experiments performed at room temperature and pressure.

in 2D diffraction patterns. This is made much clearer on the azimuthal projection Fig.6.4c) where two small intensity peaks appear at $2\theta \sim 9°$ and $2\theta \sim 13°$. The peak at $2\theta \sim 9°$ is already present in the dry scan but much less intense, and the peak at $2\theta \sim 13°$ is not present in the dry crystal whatsoever. In the diffraction scans, these formations are rings and this circular pattern is suggestive of non-ordered matter, and so not originating directly from the crystalline structure.

This is coupled with a general decrease of normalised intensity throughout the azimuthal projection. The first piece of context is to consider the angular range in ψ relative to the incident beam which are used to recover the $(0kl)$ plane. It is such that the edge of the crystal passes through the beam and the beam also passes through a larger quantity of water at

the surface. Since a wetted crystal would produce a single layer of Gibbsite-like polycrystal $Al(OH)_3$, the rings could be due to that. However, calculating the angular position using Bragg's law (3.11) and the known interplanar spacings for Gibbsite from [197], no corresponding 2θ angle can be found for the $2\theta \sim 13°$ peak, except one of very low intensity which would be highly unlikely to be visible as the Gibbsite at the surface is a single layer termination. For the $2\theta \sim 9°$ peak, on the other hand, it very well could be due to Gibbsite at the surface, as it seems to correspond to the d_{110} plane of Gibbsite. This d_{110} Gibbsite plane only has a relative intensity of $36\,\%$. It is also already present for the dry scan, but since the crystal is not in a sealed environment, it is likely that $Al(OH)_3$ formation takes place at room temperature but is limited by the constant nitrogen flux, see Fig.2.7b). When wetted however, the proportion of $Al(OH)_3$ terminated surface would increase, making the $2\theta \sim 9°$ peak more intense.

Another explanation would be due to ever-so-slight drift of the beam, which happens throughout an experiment. As mentioned in section 1.1, the beam is $20\,\mu\mathrm{m} \times 20\,\mu\mathrm{m}$. It moves slightly throughout the experiment. Since the $(0kl)$ plane scans were performed in a tight angular range to the beam, we can speculate that a slight movement of the beam would result in passing through the glue used to bind the crystal to the goniometer head. This would absorb part of the signal, leading to a reduced normalised intensity, and since the Bragg peaks are saturated, would not influence their intensity, as seen in Fig.6.4c).

To conclude, by observing and performing an azimuthal projection, no significant effect of mechanically stressed liquid induced structural changes were observed, confirming our understanding discussed in section 7. However, a more robust comparison between given lines in the $(h0l)$ cut was performed, for even more detail, discussed in the next subsection.

1.4 On key diffractions cuts

Another way to compare the scans is to make cuts along given planes, with the indexed Bragg peaks. To do so is relatively straightforward: Bragg peaks (in practice these were defined as points having more than 10^6 counts in a 5 pixel radius) are identified, with a given pixel position. We then cut our scan in a given vertical or horizontal axis using these pixel values, averaging the intensities of ± 5 pixels orthogonal to the given direction. The Bragg peaks themselves were indexed using CrysAlisPro.

Fig.6.5 shows line cuts in $(h0l)$ plane of the reciprocal space in three directions: $(10L)$, $(H00)$ and $(\bar{1}0L)$. The $(h0l)$ plane is of interest because it is in this plane that the previous inelastic scans in chapter 4 and 5 were performed. Sadly, the $(\bar{1}014)$ Bragg peak is not within the range of the diffractometer in the current setup. For each of the cuts, the background noise is lower for the H_2O wetted scans for reasons of the linear accelerator explained above. The known Bragg peaks do not change whatsoever in either of the three line cuts, confirming that the mechanically stressed liquid does not induce structural changes in the solid.

We do, however, see some changes, such as an intermediate peak of roughly $1\,\%$ to $5\,\%$ of the intensity of its neighbours between the (1010) and (104) peaks in Fig.6.5b). We postulate that this is due to multiple scattering, especially since some of these peaks in Fig.6.5d) in the

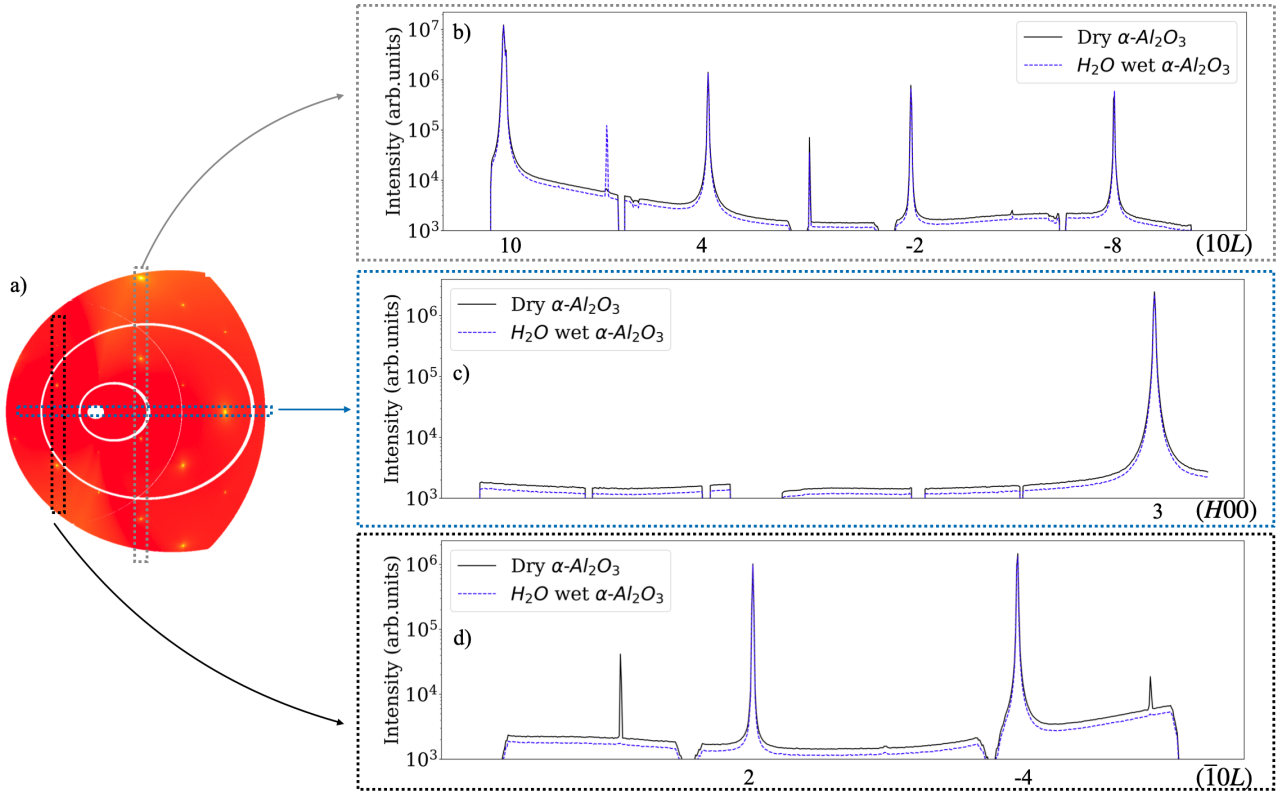

Figure 6.5: a) $(h0l)$ diffraction scans of a dry α-Al_2O_3 crystal in logarithmic scale. b) Cut of the diffraction scan of α-Al_2O_3 in the $(10L)$ direction comparing dry (black) and H_2O wetted under mechanical stress (dashed blue). The Bragg peaks are indexed. c) Cut of the diffraction scan of α-Al_2O_3 in the $(H00)$ direction comparing dry (black) and H_2O wetted under mechanical stress (dashed blue). The Bragg peaks are indexed. d) Cut of the diffraction scan of α-Al_2O_3 in the $(\bar{1}0L)$ direction comparing dry (black) and H_2O wetted under mechanical stress (dashed blue). The Bragg peaks are indexed for each x-axis.

$(\bar{1}0L)$ direction, at the (104) position (not a Bragg peak) disappears with wetting, while still having around the same $\sim 1\,\%$ intensity as neighbouring Bragg peaks.

In summary, there are no visible structural changes to the $150\,\mu\mathrm{m}$ thick α-Al_2O_3 crystal when H_2O wetted and mechanically stressed by a nitrogen flux, as there are no changes in position of Bragg peaks in either the azimuthal projection (see Fig.6.2, Fig.6.3, and Fig.6.4) or line cuts (see Fig.6.5). We can conclude that the change of acoustic phonon dynamics discussed and observed in the previous sections are not due to overt changes in atomic positions. However, the imposed stress on the liquid was not uniform throughout its rotation; therefore, we sought to confirm these results in a more controlled stress environment, which is performed in X-ray Raman scattering.

2 X-ray Raman Investigation of electronic structure and chemical changes

While no structural changes were observed by high-resolution diffraction, there still may be a complex interaction within the electronic structure. This is why we have performed X-ray Raman Scattering (XRS), at ID20 of the ESRF, thanks to the assistance of Alessandro Longo and Philip Sahle.

2.1 Experimental setup

Using a $9.69\,\mathrm{keV}$ X-ray incident beam energy, the $22\,\mathrm{mm}$ diameter wide $2\,\mathrm{mm}$ thick α-Al_2O_3 crystal is contained in an aluminium cap over which a constant nitrogen flux is flowing; the crystals are the same as those used in the previous set of experiments described in chapter 4. There are three detectors corresponding to three positions in reciprocal space, 3.2, 6.2 and 9.2 $\mathrm{Å}^{-1}$ approximately. The crystal is first scanned dry, then the cap is taken off and it is scanned wetted every hour for three hours. The crystal itself is positioned on a $5°$ angle corresponding to a $\sim 15\,\mu\mathrm{m}$ penetration depth according to the Lawrence Berkeley National Laboratory calculator [186]. Using this setup we therefore observed the bulk properties of the material. A schematic view of the setup can be seen in Fig. 6.6.

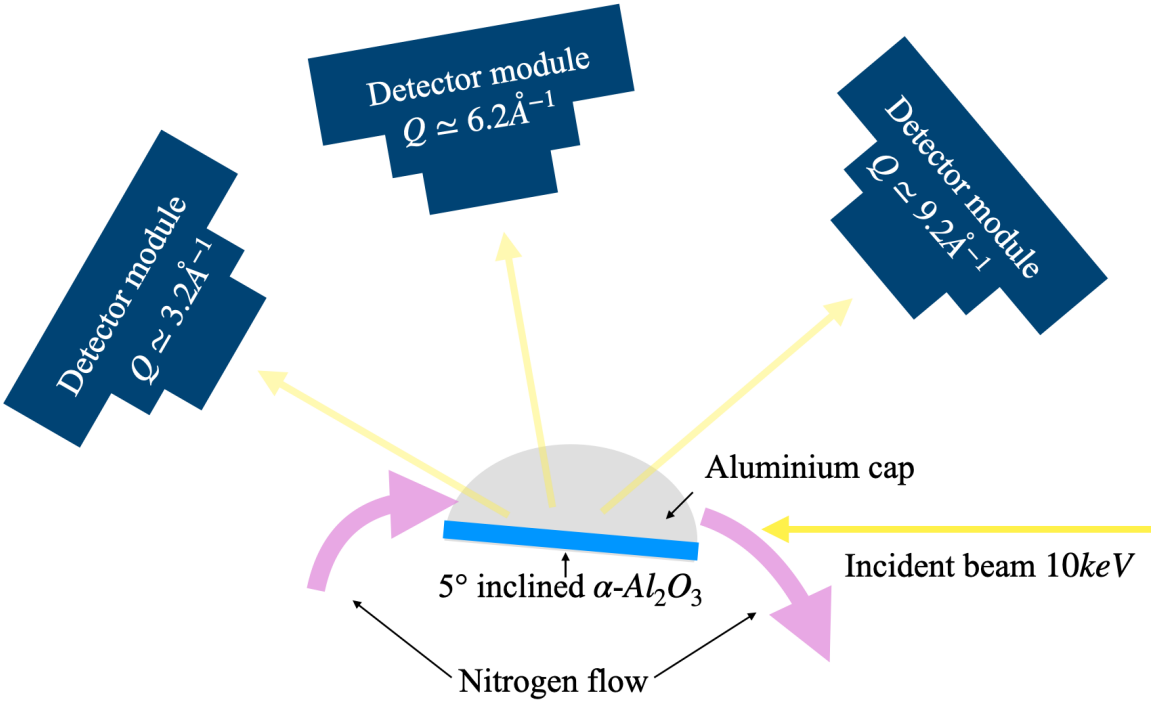

Figure 6.6: XRS experimental setup schematic view, the three detectors and their positions are shown, incident beam energy of $\sim 10\,\mathrm{keV}$ leading to a $\sim 15\,\mu\mathrm{m}$ penetration depth. All experiments are performed at room temperature and pressure with constant nitrogen flux on the sample to minimise interaction between the surface and the environment when scanned dry and mechanically stress the liquid when H_2O wetted.

In this given experimental setup, the energy resolution is around $\Delta E \approx 0.7\,\mathrm{eV}$. The constant nitrogen flux that was added was to replicate as best we could the experimental conditions of the previous inelastic X-ray scattering experiments, and the flux, being very close to the crystal surface, was set as low as $1\,\mathrm{L\,min^{-1}}$, resulting in a flow at the surface around $\sim 0.3\,\mathrm{m\,s^{-1}}$, in the same order of magnitude as previous experiments, see Tab.4.2. Adding this aluminium cap in which the nitrogen flux passed also gave us a clear upgrade from the previous experiments in diffraction, as the crystal was immediately placed from the oven where it was kept at high temperature into the setup, and exposure to the environment was limited, as well as the crystal being fixed, therefore the nitrogen flux relative to the crystal was always kept constant.

We scanned the K-edge of Oxygen and the $L_{2,3}$-edge of Aluminium. Both of these edges are very sensitive to local environment and local electronic structure. From these we can extract local structural changes and chemical changes, and it can give a glimpse into potential changes in the chemical composition within the bulk of the crystal, including oxidation states. A change in either of them (shape or appearance of a peak) is indicative of a broader change within the bulk of the material, or electronic activity.

2.2 Data treatment

The first step before the data treatment is obtaining the data itself. The X-rays from each analyser of each detector are redirected in order to obtain 2D images where Regions of Interests (ROIs) are defined after a processing with an open-source software XRStools [179]. In practice this was performed by ESRF scientists Alessandro Longo and Philip Sahle.

This allows us to obtain a raw spectrum, on which two more operations need to be performed to obtain the final spectrum. The edge (K of Oxygen or $L_{2,3}$ of Aluminium in our case) studied is often lower in energy than valence Compton scattering but also in intensity, it is therefore common to take the first points before the edge and linearly interpolate them before subtracting them from the data, as they are the beginning of the valence Compton scattering profile and the resulting data is normalised by the area under the curve [198].

2.3 Results

Fig.6.7 shows the K-edge of O and the $L_{2,3}$-edge of Al at low and medium **Q**. Let us consider the K-edge of Oxygen at $Q = 6.2\,\mathrm{\AA}^{-1}$, shown in Fig. 6.7.c). At the peak around $540\,\mathrm{eV}$, we see the H_2O wetted crystal K-edge being of ever so slightly higher intensity, and this is not observed elsewhere in reciprocal space. This may suggest some sort of effect, but it seems unlikely that such a small change, the trace of which is not visible in other configurations, would lead to the significant hardening observed.

In Fig.6.8 , where we can see the $L_{2,3}$-edge of aluminium at high **Q**, the second bump at around $82\,\mathrm{eV}$ presents a slight intensity difference. However, all the points are within the error bars, leading to an inconclusive result. Furthermore, the scans performed in XRS are at a penetration depth of $\sim 15\,\mu\mathrm{m}$, much less than the previous sets of experiments, and may be more surface sensitive, potentially explaining this increase within the error bars. Similarly,

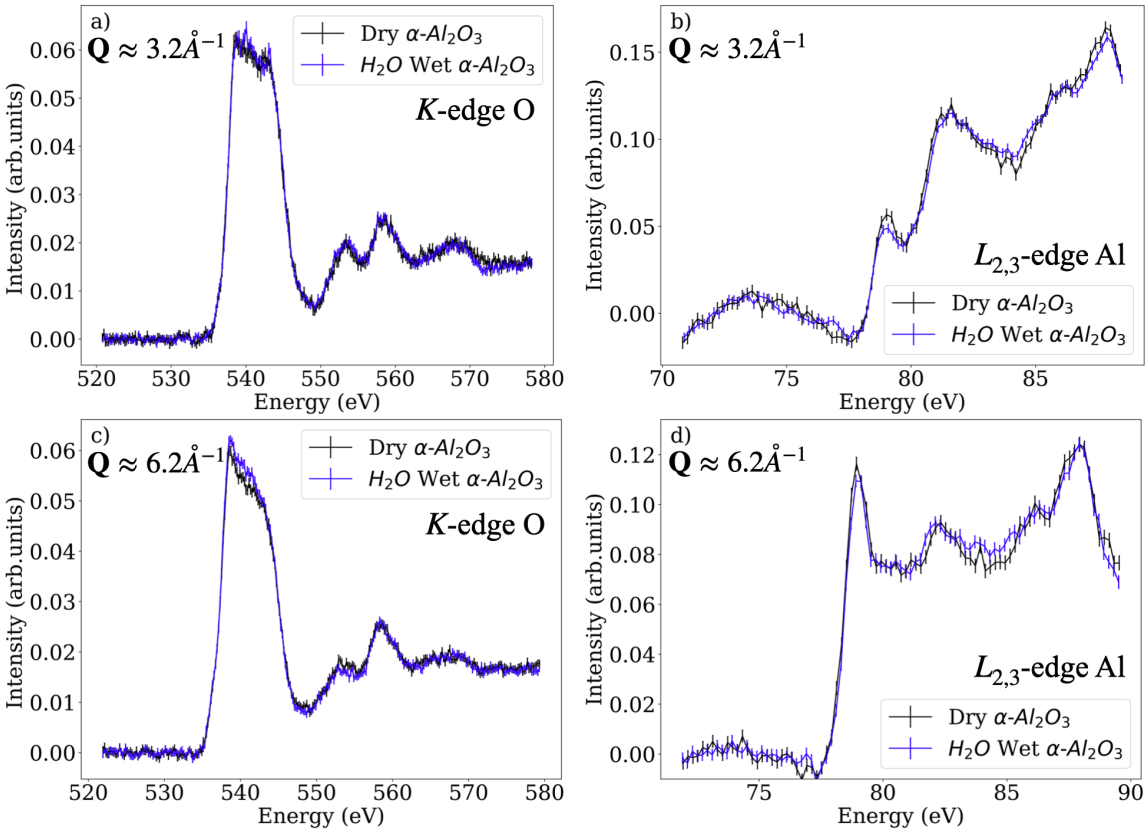

Figure 6.7: a) and c) show the α-Al_2O_3 K-edge of oxygen for each detector, respectively $Q = 3.2\,\text{Å}^{-1}$ and $Q = 6.2\,\text{Å}^{-1}$. b) and d) show the α-Al_2O_3 $L_{2,3}$-edge of aluminium at $Q = 3.2\,\text{Å}^{-1}$ and $Q = 6.2\,\text{Å}^{-1}$ respectively. The dry crystal scans are in black and the H_2O wetted under mechanical stress are shown in blue. All experiments were performed at room temperature and pressure.

no such similar behaviour is observed elsewhere in reciprocal space on the $L_{2,3}$-edge of Al seen in Fig.6.7b) and d).

It is of importance to note that the $L_{2,3}$ of Aluminium is the most sensitive of the two scanned edges, and the high **Q** results shown in Fig.6.8, with the lowest error bars, is the most compelling result showing an absence of electronic and/or chemical interaction between the mechanically stressed liquid and the α-Al_2O_3 crystal.

No quantitative or qualitative changes are visible between the wetted and dry state, indicating no chemical and structural changes in the solid, corroborating our diffraction results from the previous section.

3 Conclusion and limitations

The goal of this chapter was to confirm, with more precise and appropriate methods than inelastic scattering, whether a mechanically stressed water layer on a α-Al_2O_3 crystal induced

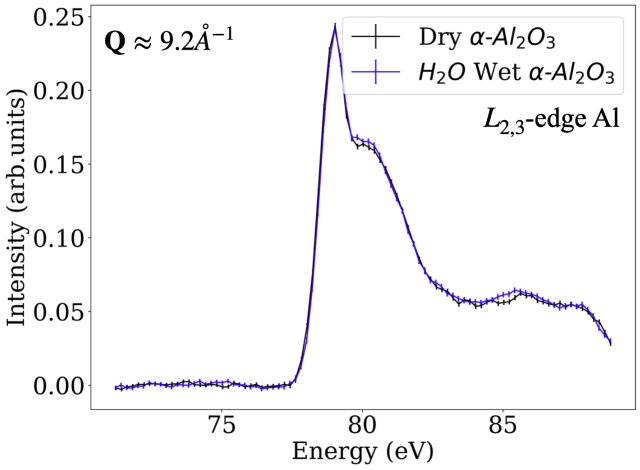

Figure 6.8: α-Al_2O_3 $L_{2,3}$-edge of aluminium at $Q = 9.2\,\text{Å}^{-1}$ obtained by X-ray Raman Scattering. The dry crystal scan is in black and the H_2O wetted under mechanical stress is shown in blue. Experiments were performed at room temperature and pressure.

structural changes which could account for the anharmonic behaviour observed in the previous two chapters.

By scanning a $150\,\mu\text{m}$ thick α-Al_2O_3 crystal in diffraction using the high-resolution ID28 side-station, Bragg peak positions did not discernibly change upon H_2O wetting under mechanical stress, ruling out a measurable structural rearrangement in the solid bulk. The structural symmetry and lattice parameters did not change.

Using X-ray Raman scattering and scanning the K-edge of oxygen and $L_{2,3}$-edge of aluminium show no overt changes in the chemical/electronic environment in the $\sim 10\,\mu\text{m}$ range from the surface (which would change due to oxidation states, coordination environment or local electronic structure change). We can conclude that local structure of the solid during mechanically stressed wetting did not change, confirming our high-resolution diffraction experiments.

We can therefore confidently affirm that the anharmonic phononic interaction between the mechanically stressed water and the α-Al_2O_3 crystal is not a result of structural or electronic changes in the solid.

Chapter 7

Conclusions and future orientations

Contents

1 Summary of key results

In this thesis, we have shown evidence of a novel long-range interaction between a mechanically stressed liquid (light and heavy water) and a hydrophilic surface of a known crystal (α-Al_2O_3), changing the acoustic phonons of the solid in the bulk. The key results are the following:

- **A BZ-selective anharmonic interaction**. Using inelastic X-ray scattering, we observed a phononic interaction in the bulk of the solid leading to hardening in the $(\bar{1}014)$ BZ in the Γ-Z direction (see Fig.7.1d), accompanied by broadening (increase of FWHM) of the LA phonons (see 5), but without a hardening effect on the (0012) LA phonon (see 4.18), though a broadening of this phonon was noted. Using inelastic neutron scattering, we observed a broadening of the TA phonon in the (300) BZ in the Γ-Z direction, seen in Fig.7.1e), but no hardening. These results demonstrate that a form of anharmonic coupling is always present throughout the crystal, but manifests differently depending on the BZ, suggesting a selection rule for such a coupling that remains to be elucidated.

- **A strong impact of liquid isotope on anharmonicity**. The observed anharmonic effect is strongly dependent on the water isotope. It is significantly stronger with H_2O than D_2O. The broadening of the TA phonon in the (300) BZ is strongly isotopically dependent, with a more pronounced broadening with H_2O wetting than D_2O wetting, which can be seen in Fig.7.1e). Similarly, the magnitude of hardening observed in the $(\bar{1}014)$ BZ of both TA and LA branches is stronger for H_2O than D_2O, as seen in Fig.7.1b), with an energy shift ratio $\Delta\hbar\omega_{D_2O}/\Delta\hbar\omega_{H_2O}$ of ~ 0.7, similar to the ballistic mass ratio of the isotopes $\sqrt{m_H/m_D} \approx 0.707$. Combining these results strongly suggests that the anharmonic interaction is driven by the Hydrogen (or Deuterium) bond network within the liquid. The vibrational energy of the liquid is likely transferred more efficiently within the lighter H-bond network than the D-bond network.

- **A dynamically driven phenomenon**. The observed anharmonic effects are not a consequence of wetting as such, but require an external mechanical stress. This was provided by an external nitrogen flux in 3.4 and 6, and an imposed water flow (flow cell) for chapter 5. This is indicative of a non-equilibrium phenomenon driven by the flow, highlighted in Fig.7.1. A relaxation towards the dry state crystal is noticed, observed as the reduced broadening when the flow is stopped, see Fig.5.9. The anharmonic phononic interaction of the solid-liquid is driven and "fed" by an external mechanical stress.

- **Confirmation of no structural changes in the solid**. Finally, we confirmed that the mechanically stressed liquid does not have an effect on the bulk structure by high-resolution X-ray diffraction and chemical/electronic environment by X-ray Raman scattering. There are no changes in oxidation states, coordination, or local chemical environment, see Fig.7.1c). While at the first layer, at the surface, literature informs us of the creation of a Gibbsite-like formation, shown in Fig.7.1a), an equivalent phenomenon does not propagate throughout the solid.

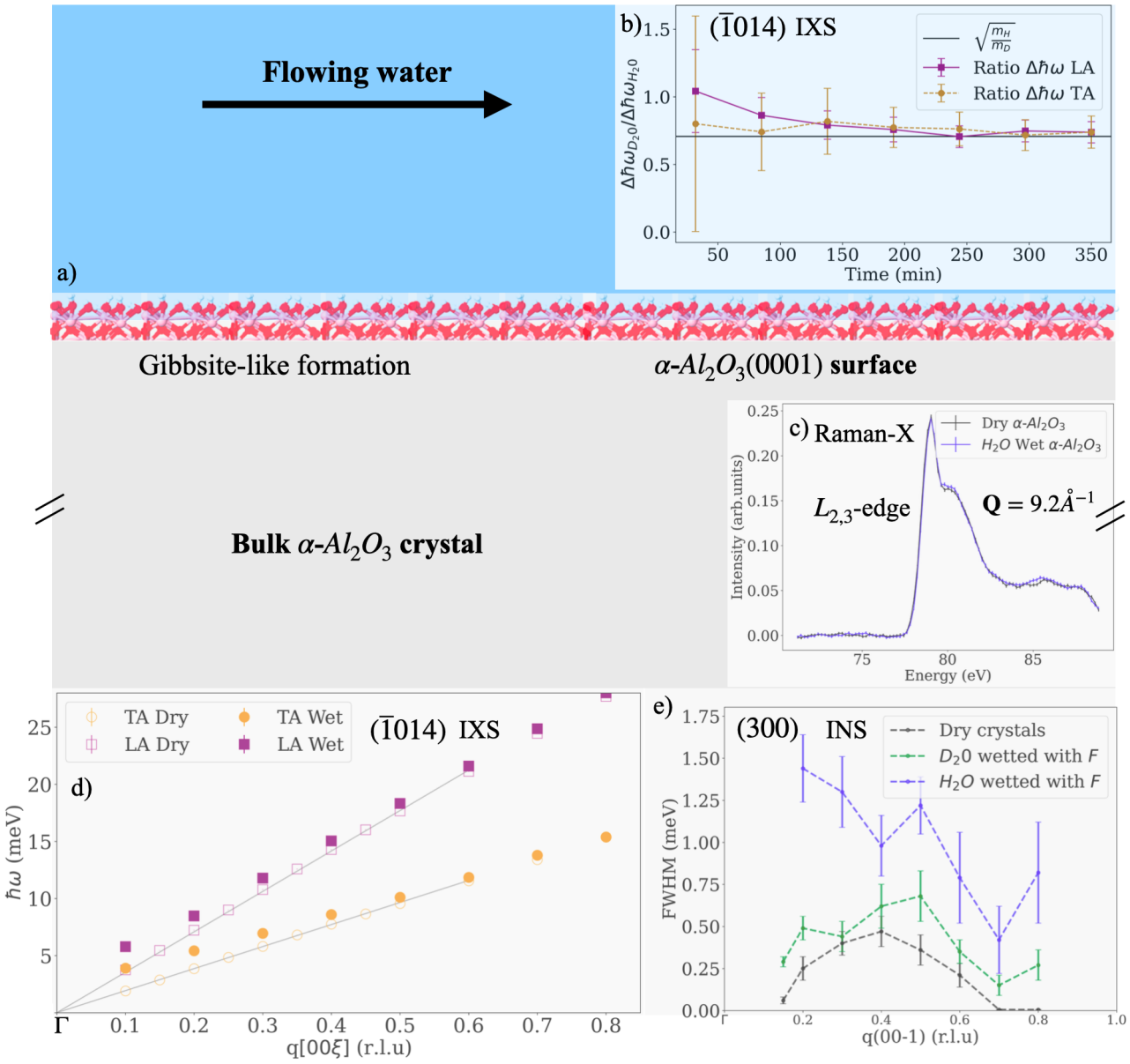

Figure 7.1: This figure gathers the main results obtained during this study on the flow impact on the inelastic dynamics of α-Al_2O_3 a) Gibbsite-like layer formed by wetting the α-Al_2O_3 with water, from [154], with Al atoms in grey and O atoms in red. b) Time evolution of TA energy changes ratio (orange circles) and LA energy changes ratio ($\Delta\hbar\omega_{D_2O}/\Delta\hbar\omega_{H_2O}$) (purple squares) for hardening between D_2O wetted and H_2O wetted α-Al_2O_3 crystal under mechanical stress from $6\,\mathrm{L\,min^{-1}}$ nitrogen flux at $\mathbf{Q} = (\bar{1}013.5)$ by IXS, see Fig.4.17. c) α-Al_2O_3 Al $L_{2,3}$-edge from X-ray Raman of dry (black) and H_2O wet under mechanical stress (blue), see Fig.6.8. d) Dispersion curve from IXS in the $(\bar{1}014)$ BZ with LA branch in purple and TA branch in orange comparing dry (open symbols) to H_2O wetted (full symbols) under mechanical stress from $6\,\mathrm{L\,min^{-1}}$ nitrogen flux, see Fig.4.20. e) FWHM of TA phonon in the (300) BZ measured with INS comparing dry (black), D_2O wetted (green) and H_2O wetted under flow F, from Fig.5.11.

2 A general discussion

2.1 The flowing liquid: a non-equilibrium external field

As we discussed in sections 3.4 and 1.4, the mechanical stress on the water is necessary to induce anharmonic effects in the α-Al_2O_3 single crystal. In Chapter 4 related to IXS experiments, we linked this to the nitrogen-filled air imposing an out-of-equilibrium state on the solid-liquid pair by air flow. In Chapter 5 we directly observed this by imposing a pressure generating a flow.

In other systems, literature indicates that a flowing liquid at a surface can induce complex quantum effects at the interface [199], maintaining the solid-liquid in an out-of-equilibrium state. It has been shown that the flowing liquid can generate an electronic wind blowing under the surface, measured as an electronic current [200], and by phonon-electron interaction through phonon-drag [201], this has anharmonic effects on phonon dynamics. However, these are nanometre-scale effects, not at the $100\,\mu\mathrm{m}$ scale observed throughout the thesis. Furthermore, while the graphene surface (the studied solid in [200]) is a complex multifactorial physical phenomenon [202], current reports indicate that it is clearly not superhydrophilic [203]. Finally, contrary to graphene, α-Al_2O_3 is an electrical insulator, thus making electron-phonon effects highly unlikely. The X-ray Raman results shown in Fig.7.1c) corroborate this point, making an electron-phonon coupling at the source of the anharmonic effect very unlikely.

It has thus been shown that a flowing liquid at a surface can maintain a non-equilibrium thermodynamic state altering phonons at the nanometer scale. In our case, the mechanisms of alteration must be of a different nature in the case of the α-Al_2O_3 and water pair. Our understanding points towards a phonon-"phonon" solid-liquid coupling.

The liquid is mechanically driven out-of-equilibrium, exciting the liquid's own collective vibrational modes. Given the strong isotopic dependence discussed in section 4 and 1.5, it is plausible that the vibrational modes interacting with the solid phonons are primarily channelled through the intermolecular hydrogen-bond network vibrations. These modes in water have been likened to optical phonons [116] in quiescent conditions. Since the hardening takes place at low energy (LA and TA phonons studied are always less than $\sim 28\,\mathrm{meV}$), we naturally look towards intermolecular modes through the H-bond within that energy range. As it happens, through the H-bond, both light and heavy water exhibits a broad peak at room temperature and pressure around $6\,\mathrm{meV}$ to $7\,\mathrm{meV}$ [204] (due to hydrogen-bond bend) and a $\sim 23\,\mathrm{meV}$ collective H-bond stretching [127], though neither of these are strongly isotopically dependent.

This could nonetheless be a source of the collective dynamics of the liquid interacting with the solid vibrations. However, these vibrational patterns are long-range phenomena (like sound and second sound) which involve the full movement of the molecule, and therefore the heavier O atoms [41, 40, 127]. Finally, we will note that a hydrophilic surface such as α-$Al_2O_3(0001)$ tends to 'blue shift', i.e., increase the energy of the H-bond peaks, making identifying a select vibrational mode in quiescent water responsible for the anharmonic effect

even more unlikely.

There must therefore be a vibrational pattern in water responsible for such a mechanical coupling. Our intuitive understanding points towards the long-range vibrational patterns responsible for shear elasticity discussed in Chapter 1, but here also it is not clear why it would reflect such a clear isotopic dependence, and remains an open question.

To conclude, it has been known that a flowing liquid at a surface can lead to strong anharmonic effects via electron-phonon coupling and phonon winds in the water-graphene interface [199, 200]. Graphene is electrically charged and a conductive material. In the case of the insulator α-Al_2O_3-water pair, the coupling is most likely due to an out-of-equilibrium vibrational pattern of the liquid through the H-bond, creating a strong anharmonic effect throughout the solid.

2.2 Anharmonic effects and hybridisation

The effects shown throughout the thesis are clearly indicative of an anharmonic impact of the liquid flow. These can be expressed through the phonon self-energy, the energy a phonon gains or loses by interacting with an external field, in our case, a vibrational long-range pattern seemingly emerging from the stressed H-bond of water.

$$\Sigma(\mathbf{q_s}, \omega_s) = \Delta(\mathbf{q_s}, \omega_s) + i\gamma(\mathbf{q_s}, \omega_s) \tag{7.1}$$

With $\Delta(\mathbf{q_s}, \omega_s)$ the energy renormalisation (in our case hardening) and $\gamma(\mathbf{q_s}, \omega_s)$ the damping rate.

We will note the hardening effects are always accompanied by a broadening of the LA phonon (while the FWHM of the TA phonons is too low in energy to be observed), see Fig.4.22, combining phonon renormalisation and damping from (7.1). Furthermore, the broadening was observed in other BZs: TA in (300) by INS and LA in (0012) by IXS, as per Fig.7.1e) and Fig.4.18 and Tab 4.3. We can therefore conclude that the broadening of the phonon is a necessary but not sufficient condition for hardening to take place, but another condition must be met. The hypothesis of a depth-dependent hardening explaining this discrepancy was thoroughly disproved in Chapter 5 by transmission geometry scattering in both IXS and INS. The more likely explanation is a BZ-dependent (and q-dependent within said BZ, as seen in Fig.7.1d)) effect following a yet-to-be-discovered selection rule.

Last but not least, we will discuss vibrational coupling and hybridisation. Such a phenomenon can occur when two distinct dispersive modes interact, due to close energy and momentum, resulting in hybrid modes [205]. This can happen with edge modes in nanostructures [206], but also with electron-phonon coupling [207]. In our case, it seems evident that vibrations from the stressed liquid interact with the acoustic phonons, but how do these two distant patterns interact? It is straightforward to assume that via hydroxylation of the surface layer of α-$Al_2O_3(0001)$ and the creation of a Gibbsite-like layer, shown in Fig.7.1a), the surface phonons of the crystal interact with the vibrational patterns of the liquid. However, the scanned phonons are bulk acoustic phonons. Here lies the key missing piece: how can these liquid-induced surface vibrations travel through the solid leading to anharmonic

effects capable of mode hybridisation in the bulk?

Another consideration: if hybridised modes in the solid take place, why are we not able to see them in inelastic scattering methods? First, we may not have scanned at a large enough energy range, due to time (IXS) and optimisation. Another explanation would be that the selection rules for IXS do not allow us to observe this behaviour, and since we cannot observe the $(\bar{1}014)$ BZ with INS, we cannot know if this is observable with neutrons. Finally, a hybridisation type mechanism could explain a q dependence and a BZ dependence.

2.3 A discussion on gapped modes

In section 5 we highlighted that the anharmonic interaction results in hardened phonons of the LA and TA branches in the Γ-Z direction tending towards a gapped mode at the Γ point, as visible in Fig.7.1d). This is a highly unusual result. We will discuss similar gapped mode phenomena, to try to find analogue physics at play.

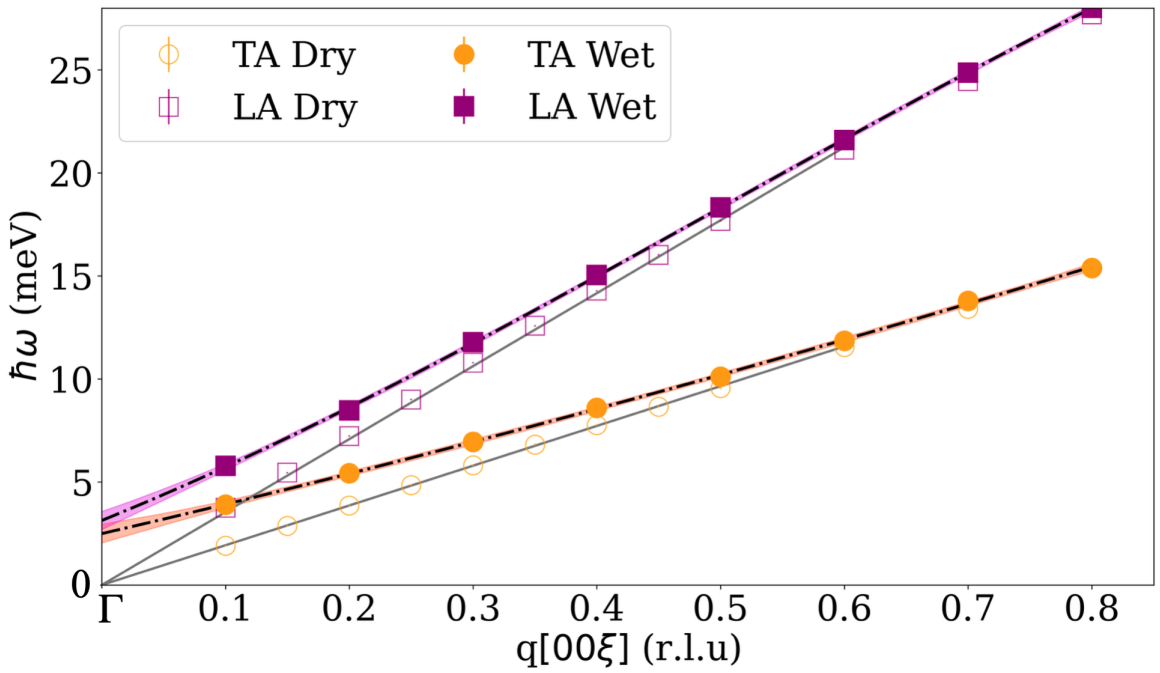

Figure 7.2: Dispersion curve in $[00\xi]$ (Γ-Z) direction of dry α-Al_2O_3 TA (empty circle orange) and LA (empty square purple). The sample is H_2O wetted in the stable window of 6 to 12 hours after wetting results in the wetted dispersion curve of TA (filled circle orange) and LA (filled square purple). The grey lines correspond to linear dispersion curves obtained from C_{33} and C_{44} moduli from [191]. Black dashed lines show a third-degree polynomial fit of the dispersion curves, with error bars in purple and orange for the LA and TA respectively. The same α-Al_2O_3 crystal is shown. Scans performed at ID28 with $3\,\mathrm{meV}$ resolution, corresponding to a beam penetration of $\sim 150\,\mu\mathrm{m}$. Experiments performed under $6\,\mathrm{L\,min^{-1}}$ nitrogen flux, at room temperature and pressure.

As acoustic phonons are Goldstone modes [81], they arise from spontaneous breaking of translational symmetries of the crystals and are a direct consequence of the atomic ordering

of the crystal. A broken symmetry would therefore be necessary for the TA and LA phonons to stop existing at low q, which could result in being gapped in energy, as seen in Fig.4.20. However, a breaking of symmetry as such cannot be a complete structural breakdown of the crystal, as shown by a myriad of results, as early in our thesis as the reversibility of hardening (see 3.3). An alternative explanation would be the creation of a superlattice above the general lattice due to a change of equilibrium position of an atom within the crystal, imposed by the flowing liquid. This would have likely been visible in diffraction, and would almost certainly leave a trace in the $L_{2,3}$-edge of Al, and neither of the experimental verifications performed and discussed in Chapter 6 highlights such an effect.

More generally, vibrational coupling mechanisms can lead to gapped modes in materials by the general mechanism of hybridisation through multiple phenomena [206, 207]. One of these is phonon-phonon interaction [208], which can happen between optical and acoustic phonons [209, 210] to maintain local thermal equilibrium in non-equilibrium conditions. A sheared liquid at the hydrophilic solid-liquid interface results in non-equilibrium thermal shear waves within the liquid [34, 25], discussed in Chapter 1. One can wonder if the observed anharmonic phenomenon in this thesis is the corollary of this effect, but in the solid. Furthermore, a transition from two acoustic to an optical phonon, as in [210], is phenomenologically supported by the fact that both TA and LA wetted curves seem to converge towards a similar gap at $\sim 3\,\mathrm{meV}$ when fitted with a third-degree polynomial, as seen in Fig.7.2.

2.4 An unusual parallel: liquid shear waves and phasons

Phasons, unlike phonons, are not propagative but diffusive modes, which arise from the 'flips' of local arrangements of matter [211]. They have been observed in ferroelectric liquid crystals [212], quasicrystals [213], and in general are a dynamic feature of certain incommensurate systems [214] and at surfaces [215]. Phasons have been extensively studied experimentally using inelastic neutron and X-ray scattering [216, 217].

Phasons are not always gapless at $q \to 0$ as they do not result from an overt symmetry-breaking mechanism, and can be 'pinned' resulting in a gapped energy mode, i.e., an "optical phason" [215]. This 'pinning' corresponds to an energy barrier to be overcome for the 'flip' to occur.

Perhaps more of note to our studies is the work of M. Baggioli et al. [218, 219], who discuss the dispersion relation of phasons from [220]

$$\omega^2 + i\gamma\omega = v^2k^2 \tag{7.2}$$

They conclude "by noticing that the phasons dynamics display striking similarities with that of the shear modes in liquids" [218], both exhibiting a k-gap, as seen when comparing (7.2) with (1.16).

However, Fig.7.2 shows an energy gap, not a k-gap in momentum space, and the analogy between the dispersion of phasons and transverse liquid waves only extends to their k-gap dispersion. However, we may ponder that, as phasons have been known to be 'pinned', perhaps so can transverse waves in liquids. This would provide an alternative vibrational pattern

that would behave like a transverse mode in the liquid, but would be more general than the H-bond, a specific feature of water. In this sense, the imposed shear by the flowing nitrogen flux at the surface would provide sufficient energy for the 'flip' to take place in water, which, if we return to the illustration of liquids in the Frenkel theory 1.6, would correspond to a collective in-phase movement of multiple molecules rather than uncorrelated molecular movements. However, this interpretation has limitations as the hardening ratio highlighted in section 4 strongly suggests an isotopic mass effect. Furthermore, the similarities between phason 'pinning' and shear elasticity in liquids are few, as the phason gap is a result of structure defects, whilst our results arise from a dynamic out-of-equilibrium liquid.

Nonetheless, while this analogy and curious theoretical similarity is intriguing, as we have pointed out, in our set of experiments we have not observed the liquid dynamics as such, but the solid phonon dynamics driven out-of-equilibrium by the flowing liquid, and the coupling mechanism between the collective vibrations of liquids and that of the solid acoustic phonons remains to be discovered.

3 Future works and suggestions

To further our understanding of these novel phenomena at the hydrophilic solid-liquid interface, we shall suggest in this section a few avenues:

- Changing the experimental setup to a controlled microfluidics chamber and flow is the most evident, allowing us to obtain a quantitative understanding of the non-equilibrium conditions. It may help us answer key experimental questions that would point towards the nature of the non-equilibrium conditions, and would help answer questions such as: How is the value of hardening dependent on shear stress? Is there a minimum amount of shear necessary to observe such anharmonic effects?

- Changing the solid-liquid pair. Changing the solid could help observe a larger range in the reciprocal space by INS to elucidate the selection rule on the anharmonic effect. Changing solids to a non-hydrophilic surface seems necessary to check if hydrophilicity is a necessary component, as we believe, to the observed anharmonic phenomena. Changing the liquid would help understand if these phenomena are only due to the anomalous nature of water or a general feature of out-of-equilibrium solid-liquid interactions at the hydrophilic interface.

4 Conclusion

In this thesis, we started from a general perspective on liquids and their mesoscopic shear elastic behaviour in the low-frequency regime at the hydrophilic interface in Chapter 1. We chose an appropriate liquid-solid pair, described in Chapter 2, water and single crystal α-Al_2O_3, to see if the long vibrational patterns characterised by shear elasticity in the mesoscopic liquid could extend beyond the solid-liquid interface deep into the bulk.

To do so, we used large instrument scattering techniques: inelastic X-ray scattering, high-resolution X-ray diffraction and X-ray Raman at the European Synchrotron Radiation Facility, and inelastic neutron scattering at the Institut Laue-Langevin, described in Chapter 3. The inelastic scattering methods were used to access the acoustic phonons in the α-Al_2O_3 bulk. X-ray Raman and high-resolution spectrometry were used to access the electronic and structural components of the single crystal, respectively.

We have demonstrated that, when the liquid is maintained in a non-equilibrium state by mechanical stress, the acoustic phonons in the bulk of the solid are altered by an anharmonic effect. This effect is dependent on the scanned Brillouin zone. Some regions of reciprocal space highlight a strong q-dependent hardening (increase in phonon energy) and broadening (decrease in phonon lifetime), while others only show a broadening. We have highlighted a clear isotopic effect, with flowing H_2O inducing a stronger response in both broadening and hardening. These anharmonic interactions happen without change to the crystal structure or bulk chemical environment. Finally, the observation of an energy gap opening in some acoustic branches points towards a form of hybridisation, the nature of which is an open question.

While the precise mechanism of this non-equilibrium coupling remains to be discovered, our research indicates that the solid-liquid interaction cannot be considered a localised phenomenon, as both media are dynamically coupled at large scales.

Bibliography

[1] G. K. Batchelor. *An Introduction to fluid dynamics*. Cambridge mathematical library. Cambridge Univ. Press, Cambridge, 14. print edition, 2010.

[2] CLMH Navier. Mémoire sur les lois du mouvement des fluides. *Mémoires de l'Académie Royale des Sciences de l'Institut de France*, 6(1823):389–440, 1823.

[3] George Gabriel Stokes. On the theories of the internal friction of fluids in motion, and of the equilibrium and motion of elastic solids. *Transactions of the Cambridge Philosophical Society*, 8:287–319, 1845.

[4] Mori Mani and Andrew J Dorgan. A perspective on the state of aerospace computational fluid dynamics technology. *Annual Review of Fluid Mechanics*, 55(1):431–457, 2023.

[5] Thomas Moragues, Diana Arguijo, Thomas Beneyton, Cyrus Modavi, Karolis Simutis, Adam R Abate, Jean-Christophe Baret, Andrew J deMello, Douglas Densmore, and Andrew D Griffiths. Droplet-based microfluidics. *Nature Reviews Methods Primers*, 3(1):32, 2023.

[6] Pierre-Gilles De Gennes, Françoise Brochard-Wyart, and David Quéré. *Gouttes, bulles, perles et ondes*, volume 159. Belin Paris, 2005.

[7] Thomas Young. Iii. an essay on the cohesion of fluids. *Philosophical transactions of the royal society of London*, (95):65–87, 1805.

[8] HW Fox and WA Zisman. The spreading of liquids on low energy surfaces. i. polytetrafluoroethylene. *Journal of Colloid Science*, 5(6):514–531, 1950.

[9] HW Fox, EF Hare, and WA Zisman. Wetting properties of organic liquids on high-energy surfaces. *The Journal of Physical Chemistry*, 59(10):1097–1106, 1955.

[10] Deepak Doraiswamy. The origins of rheology: a short historical excursion. *Rheology Bulletin*, 71(1):1–9, 2002.

[11] James Clerk Maxwell. Ii. illustrations of the dynamical theory of gases. *The London, Edinburgh, and Dublin Philosophical Magazine and Journal of Science*, 20(130):21–37, 1860.

[12] James Clerk Maxwell. Iv. on the dynamical theory of gases. *Philosophical transactions of the Royal Society of London*, (157):49–88, 1867.

[13] Eric Lauga, Michael Brenner, and Howard Stone. *Microfluidics: The No-Slip Boundary Condition*, pages 1219–1240. Springer Berlin Heidelberg, Berlin, Heidelberg, 2007.

[14] Yakov Ilyich Frenkel. *Kinetic Theory of Liquids*. Dover Publications, New York, 1955.

[15] Ioannis Skarmoutsos, Giancarlo Franzese, and Elvira Guardia. Using car-parrinello simulations and microscopic order descriptors to reveal two locally favored structures with distinct molecular dipole moments and dynamics in ambient liquid water. *Journal of Molecular Liquids*, 364:119936, 2022.

[16] BV Derjaguin, UB Bazaron, KT Zandanova, and OR Budaev. The complex shear modulus of polymeric and small-molecule liquids. *Polymer*, 30(1):97–103, 1989.

[17] BV Derjaguin, UB Bazaron, Kh D Lamazhapova, and BD Tsidypov. Shear elasticity of low-viscosity liquids at low frequencies. *Physical Review A*, 42(4):2255, 1990.

[18] JL Gallani, L Hilliou, Ph Martinoty, and P Keller. Abnormal viscoelastic behavior of side-chain liquid-crystal polymers. *Physical review letters*, 72(13):2109, 1994.

[19] Hakima Mendil-Jakani, Patrick Baroni, and Laurence Noirez. Shear-induced isotropic to nematic transition of liquid-crystal polymers: identification of gap thickness and slipping effects. *Langmuir*, 25(9):5248–5252, 2009.

[20] Laurence Noirez and Patrick Baroni. Identification of a low-frequency elastic behaviour in liquid water. *Journal of Physics: Condensed Matter*, 24(37):372101, September 2012.

[21] H Mendil, P Baroni, and Laurence Noirez. Unexpected giant elasticity in side-chain liquid-crystal polymer melts: A new approach for the understanding of shear-induced phase transitions. *Europhysics Letters*, 72(6):983, 2005.

[22] Laurence Noirez, Patrick Baroni, and Hakima Mendil-Jakani. The missing parameter in rheology: hidden solid-like correlations in viscous liquids, polymer melts and glass formers. *Polymer International*, 58(8):962–968, 2009.

[23] D Collin and Ph Martinoty. Dynamic macroscopic heterogeneities in a flexible linear polymer melt. *Physica A: Statistical Mechanics and its Applications*, 320:235–248, 2003.

[24] L. Noirez, P. Baroni, and J. F. Bardeau. Highlighting non-uniform temperatures close to liquid/solid surfaces. *Applied Physics Letters*, 110(21):213904, May 2017.

[25] Eni Kume. *Highlighting strain-induced thermoelastic effect in mesoscopic liquids*. PhD thesis, 2021. Thèse de doctorat dirigée par Noirez, Laurence Physique université Paris-Saclay 2021.

[26] Eni Kume and Laurence Noirez. Identification of Thermal Response of Mesoscopic Liquids under Mechanical Excitation: From Harmonic to Nonharmonic Thermal Wave. *The Journal of Physical Chemistry B*, 125(30):8652–8658, August 2021.

[27] Eni Kume and Laurence Noirez. Thermal shear waves induced in mesoscopic liquids at low frequency mechanical deformation. *Journal of Non-Equilibrium Thermodynamics*, 47(2):155–163, 2022.

[28] F. Aitken and F. Volino. A novel general modeling of the viscoelastic properties of fluids: Application to mechanical relaxation and low frequency oscillation measurements of liquid water. *Physics of Fluids*, 34(4):043109, April 2022.

[29] K Trachenko and VV Brazhkin. Collective modes and thermodynamics of the liquid state. *Reports on Progress in Physics*, 79(1):016502, 2015.

[30] Alessio Zaccone and Kostya Trachenko. Explaining the low-frequency shear elasticity of confined liquids. *Proceedings of the National Academy of Sciences*, 117(33):19653–19655, August 2020.

[31] Matteo Baggioli, Mikhail Vasin, Vadim Brazhkin, and Kostya Trachenko. Gapped momentum states. *Physics Reports*, 865:1–44, June 2020.

[32] Kostya Trachenko. *Theory of Liquids: From Excitations to Thermodynamics*. Cambridge University Press, 2023.

[33] Alessio Zaccone and Laurence Noirez. Universal g l–3 law for the low-frequency shear modulus of confined liquids. *The Journal of Physical Chemistry Letters*, 12(1):650–657, 2021.

[34] Eni Kume, Alessio Zaccone, and Laurence Noirez. Unexpected thermo-elastic effects in liquid glycerol by mechanical deformation. *Physics of Fluids*, 33(7):072007, July 2021.

[35] Ursula Windberger, Patrick Baroni, and Laurence Noirez. Capillary-size flow of human blood plasma: Revealing hidden elasticity and scale dependence. *Journal of Biomedical Materials Research Part A*, 110(2):298–303, 2022.

[36] Ruiyu Wang, Yunqian Zou, Richard C Remsing, Naomi O Ross, Michael L Klein, Vincenzo Carnevale, and Eric Borguet. Superhydrophilicity of α-alumina surfaces results from tight binding of interfacial waters to specific aluminols. *Journal of colloid and interface science*, 628:943–954, 2022.

[37] Laurence Noirez, H Mendil-Jakani, and P Baroni. Identification of finite shear-elasticity in the liquid state of molecular and polymeric glass-formers. *Philosophical Magazine*, 91(13-15):1977–1986, 2011.

[38] Laurence Noirez and P Baroni. Identification of thermal shear bands in a low molecular weight polymer melt under oscillatory strain field. *Colloid and Polymer Science*, 296(4):713–720, 2018.

[39] Ali Eltareb, Gustavo E Lopez, and Nicolas Giovambattista. Isotope-substitution effects on the thermodynamic, dynamic, and structural properties of water: H2o, hdo, d2o, and t2o. *The Journal of Physical Chemistry B*, 2025.

[40] Giancarlo Ruocco and F Sette. The history of the" fast sound" in liquid water. *Condensed Matter Physics*, 2008.

[41] J Teixeira, MC Bellissent-Funel, SH Chen, and B Dorner. Observation of new short-wavelength collective excitations in heavy water by coherent inelastic neutron scattering. *Physical review letters*, 54(25):2681, 1985.

[42] John G Landels. Water-clocks and time measurement in classical antiquity. *Endeavour*, 3(1):32–37, 1979.

[43] The indus river alley civilisations. https://historyguild.org/the-indus-river-valley-civilizations/?srsltid=AfmBOorpaRJ6TmSX_VTrcz-2yoheJN8cluhhsFDM11Jb5gp19_lRnU1O. Accessed: 06th August 2025.

[44] I Newton. *Philosophiæ Naturalis Principia Mathematica*. Apud G. & J. Innys, 1726.

[45] Matthias Rauter. The compressible granular collapse in a fluid as a continuum: validity of a navier–stokes model with-rheology. *Journal of Fluid Mechanics*, 915:A87, 2021.

[46] S Richardson. On the no-slip boundary condition. *Journal of Fluid Mechanics*, 59(4):707–719, 1973.

[47] Laurent Joly, Christophe Ybert, Emmanuel Trizac, and Lydéric Bocquet. Liquid friction on charged surfaces: From hydrodynamic slippage to electrokinetics. *The Journal of chemical physics*, 125(20), 2006.

[48] Yanbo Xie, Li Fu, Thomas Niehaus, and Laurent Joly. Liquid-solid slip on charged walls: The dramatic impact of charge distribution. *Physical review letters*, 125(1):014501, 2020.

[49] Abdul Aziz Shuvo, Luis E Paniagua-Guerra, Juseok Choi, Seong H Kim, and Bladimir Ramos-Alvarado. Hydrodynamic slip in nanoconfined flows: a review of experimental, computational, and theoretical progress. *Nanoscale*, 17(2):635–660, 2025.

[50] Jacob N Israelachvili and GE Adams. Direct measurement of long range forces between two mica surfaces in aqueous kno3 solutions. *Nature*, 262(5571):774–776, 1976.

[51] Jacob N Israelachvili. Measurement of the viscosity of liquids in very thin films. *Journal of Colloid and Interface Science*, 110(1):263–271, 1986.

[52] David Roylance. Engineering viscoelasticity (department of material science and engineering, 2001.

[53] Woldemar Voigt. Ueber die innere reibung der festen körper, insbesondere der krystalle. *Abhandlungen der Koeniglichen Gesellschaft der Wissenschaften in Goettingen*, 36:3–48, 1890.

[54] James G Oldroyd. On the formulation of rheological equations of state. *Proceedings of the Royal Society of London. Series A. Mathematical and Physical Sciences*, 200(1063):523–541, 1950.

[55] Prince E Rouse Jr. A theory of the linear viscoelastic properties of dilute solutions of coiling polymers. *The Journal of Chemical Physics*, 21(7):1272–1280, 1953.

[56] P. G. De Gennes. Dynamics of Entangled Polymer Solutions. II. Inclusion of Hydrodynamic Interactions. *Macromolecules*, 9(4):594–598, July 1976.

[57] Max Born and Herbert S Green. A general kinetic theory of liquids i. the molecular distribution functions. *Proceedings of the Royal Society of London. Series A. Mathematical and Physical Sciences*, 188(1012):10–18, 1946.

[58] Kim Sharp and Franz Matschinsky. Translation of ludwig boltzmann's paper "on the relationship between the second fundamental theorem of the mechanical theory of heat and probability calculations regarding the conditions for thermal equilibrium" sitzungberichte der kaiserlichen akademie der wissenschaften. mathematisch-naturwissen classe. abt. ii, lxxvi 1877, pp 373-435 (wien. ber. 1877, 76: 373-435). reprinted in wiss. abhandlungen, vol. ii, reprint 42, p. 164-223, barth, leipzig, 1909. *Entropy*, 17(4):1971–2009, 2015.

[59] Albert Einstein. Planck's theory of radiation and the theory of specific heat. *Ann. Phys*, 22:180–190, 1907.

[60] P. Debye. Zur theorie der spezifischen wärmen. *Annalen der Physik*, 344(14):789–839, 1912.

[61] Jaeyun Moon. *Heat Carriers in Liquids: An Introduction*. Springer, 2024.

[62] Lev Davidovich Landau, Evgenii Mikhailovich Lifshitz, and Lev P. Pitaevskii. *Statistical Physics: Theory of the Condensed State*, volume 9. Butterworth-Heinemann, 1980.

[63] Robert Piccirelli and TA Litovitz. Ultrasonic shear and compressional relaxation in liquid glycerol. *The Journal of the Acoustical Society of America*, 29(9):1009–1020, 1957.

[64] Robert Zwanzig and Raymond D Mountain. High-frequency elastic moduli of simple fluids. *The Journal of Chemical Physics*, 43(12):4464–4471, 1965.

[65] Thomas Pezeril. Laser generation and detection of ultrafast shear acoustic waves in solids and liquids. *Optics & Laser Technology*, 83:177–188, 2016.

[66] Tullio Scopigno, Giancarlo Ruocco, and Francesco Sette. Microscopic dynamics in liquid metals: The experimental point of view. *Reviews of Modern Physics*, 77(3):881–933, 2005.

[67] Hsuan-Wei Hu, George A Carson, and Steve Granick. Relaxation time of confined liquids under shear. *Physical review letters*, 66(21):2758, 1991.

[68] A Levent Demirel and Steve Granick. Glasslike transition of a confined simple fluid. *Physical review letters*, 77(11):2261, 1996.

[69] Yuanxi Yu, Sha Jin, Xue Fan, Mona Sarter, Dehong Yu, Liang Hong, and Matteo Baggioli. Emergence of debye scaling in the density of states of liquids under nanoconfinement. *ACS nano*, 18(36):24829–24841, 2024.

[70] BB Badmaev, BB Damdinov, and TS Dembelova. Viscoelastic relaxation in fluids. *Bulletin of the Russian Academy of Sciences: Physics*, 79(10):1301–1305, 2015.

[71] Badma Badmaev, Tuyana Dembelova, Bair Damdinov, Dagzama Makarova, and Ochir Budaev. Influence of surface wettability on the accuracy of measurement of fluid shear modulus. *Colloids and Surfaces A: Physicochemical and Engineering Aspects*, 383(1):90–94, 2011. A collection of papers presented at the14th International Conference on Surface Forces.

[72] H Mendil, P Baroni, and Laurence Noirez. Solid-like rheological response of non-entangled polymers in the molten state. *The European Physical Journal E*, 19(1):77–85, 2006.

[73] Laurence Noirez, Hakima Mendil-Jakani, Patrick Baroni, and Joachim H Wendorff. Richness of side-chain liquid-crystal polymers: From isotropic phase towards the identification of neglected solid-like properties in liquids. *Polymers*, 4(2):1109–1124, 2012.

[74] Meghanad Kayanattil, Zhipeng Huang, Djordje Gitaric, and Sascha W Epp. Rubber-like elasticity in laser-driven free surface flow of a newtonian fluid. *Proceedings of the National Academy of Sciences*, 120(27):e2301956120, 2023.

[75] M. A. Biot. Thermoelasticity and Irreversible Thermodynamics. *Journal of Applied Physics*, 27(3):240–253, March 1956.

[76] Eni Kume, Patrick Baroni, and Laurence Noirez. Highlighting thermo-elastic effects in confined fluids. *Polymers*, 13(14), 2021.

[77] Alessio Zaccone and Kostya Trachenko. Explaining the low-frequency shear elasticity of confined liquids. *Proceedings of the National Academy of Sciences*, 117(33):19653–19655, 2020.

[78] Anaël Lemaître and Craig Maloney. Sum rules for the quasi-static and visco-elastic response of disordered solids at zero temperature. *Journal of statistical physics*, 123(2):415–453, 2006.

[79] Vladimir V Palyulin, Christopher Ness, Rico Milkus, Robert M Elder, Timothy W Sirk, and Alessio Zaccone. Parameter-free predictions of the viscoelastic response of glassy polymers from non-affine lattice dynamics. *Soft Matter*, 14(42):8475–8482, 2018.

[80] Matteo Baggioli, Michael Landry, and Alessio Zaccone. Deformations, relaxation, and broken symmetries in liquids, solids, and glasses: A unified topological field theory. *Physical Review E*, 105(2):024602, 2022.

[81] Jeffrey Goldstone, Abdus Salam, and Steven Weinberg. Broken symmetries. *Physical Review*, 127(3):965, 1962.

[82] Fabio Peluso. Isochoric specific heat in the dual model of liquids. *Liquids*, 1(1):77–95, 2021.

[83] Fabio Peluso. Mesoscopic collective dynamics in liquids and the dual model. *Journal of Heat Transfer*, 144(11):112501, 2022.

[84] Fabio Peluso. The viscosity of liquids in the dual model. *Thermo*, 4(4), 2024.

[85] Fabio Peluso. How Does Heat Propagate in Liquids? *Liquids*, 3(1):92–117, March 2023. Number: 1 Publisher: Multidisciplinary Digital Publishing Institute.

[86] Fabio Peluso. Thermo-mechanical and mechano-thermal effects in liquids explained by means of the dual model of liquids. *Thermo*, 3(4):625–656, 2023.

[87] F Volino. Théorie visco-élastique non-extensive i. théorie simplifiée à modes rotationnels. In *Annales de Physique*, volume 22, pages 7–41. EDP Sciences, 1997.

[88] F Volino, H Gérard, and S Miachon. Théorie visco-élastique non-extensive ii. premiers tests expérimentaux de la théorie simplifiée à modes rotationnels. *Ann. Phys. Fr*, 22(1-2):43–82, 1997.

[89] F Volino. Théorie visco-élastique non-extensive iii. théorie simplifiée à modes translationnels. In *Annales de Physique*, volume 22, pages 83–120. EDP Sciences, 1997.

[90] F Volino. Théorie visco-élastique non-extensive v. équations de diffusion, fonctions de distribution, viscosités et coefficients de diffusion, fonctions de corrélation. In *Annales de Physique*, volume 22, pages 159–180. EDP Sciences, 1997.

[91] Frédéric Aitken and Ferdinand Volino. A new single equation of state to describe the dynamic viscosity and self-diffusion coefficient for all fluid phases of water from 200 to 1800 k based on a new original microscopic model. *Physics of Fluids*, 33(11), 2021.

[92] Frances Westall and André Brack. The importance of water for life. *Space Science Reviews*, 214(2):50, 2018.

[93] WRM Rocha, MG Rachid, MK McClure, J He, and H Linnartz. Water ice: Temperature-dependent refractive indexes and their astrophysical implications. *Astronomy & Astrophysics*, 681:A9, 2024.

[94] Maria Rescigno, Alberto Toffano, Umbertoluca Ranieri, Leon Andriambariarijaona, Richard Gaal, Stefan Klotz, Michael Marek Koza, Jacques Ollivier, Fausto Martelli, John Russo, et al. Observation of plastic ice vii by quasi-elastic neutron scattering. *Nature*, 640(8059):662–667, 2025.

[95] Katrin Amann-Winkel, Marie-Claire Bellissent-Funel, Livia E Bove, Thomas Loerting, Anders Nilsson, Alessandro Paciaroni, Daniel Schlesinger, and Lawrie Skinner. X-ray and neutron scattering of water. *Chemical reviews*, 116(13):7570–7589, 2016.

[96] Paola Gallo, Katrin Amann-Winkel, Charles Austen Angell, Mikhail Alexeevich Anisimov, Frédéric Caupin, Charusita Chakravarty, Erik Lascaris, Thomas Loerting, Athanassios Zois Panagiotopoulos, John Russo, et al. Water: A tale of two liquids. *Chemical reviews*, 116(13):7463–7500, 2016.

[97] John D Bernal, Ralph H Fowler, et al. A theory of water and ionic solution, with particular reference to hydrogen and hydroxyl ions. *J. chem. Phys*, 1(8):515–548, 1933.

[98] Felix Franks. *The physics and physical chemistry of water*, volume 1. Springer Science & Business Media, 2012.

[99] Peter H Poole, Francesco Sciortino, Ulrich Essmann, and H Eugene Stanley. Phase behaviour of metastable water. *Nature*, 360(6402):324–328, 1992.

[100] Osamu Mishima and H Eugene Stanley. The relationship between liquid, supercooled and glassy water. *Nature*, 396(6709):329–335, 1998.

[101] GP Johari and J Teixeira. Thermodynamic analysis of the two-liquid model for anomalies of water, hdl–ldl fluctuations, and liquid–liquid transition. *The Journal of Physical Chemistry B*, 119(44):14210–14220, 2015.

[102] Paola Gallo and H Eugene Stanley. Supercooled water reveals its secrets. *Science*, 358(6370):1543–1544, 2017.

[103] Anders Nilsson, Congcong Huang, and Lars GM Pettersson. Fluctuations in ambient water. *Journal of Molecular Liquids*, 176:2–16, 2012.

[104] Alan K Soper and Maria Antonietta Ricci. Structures of high-density and low-density water. *Physical review letters*, 84(13):2881, 2000.

[105] S Klotz, G Hamel, JS Loveday, RJ Nelmes, M Guthrie, and AK Soper. Structure of high-density amorphous ice under pressure. *Physical review letters*, 89(28):285502, 2002.

[106] S Klotz, Th Strässle, RJ Nelmes, JS Loveday, G Hamel, G Rousse, B Canny, <? format?> JC Chervin, and AM Saitta. Nature of the polyamorphic transition in ice under pressure. *Physical review letters*, 94(2):025506, 2005.

[107] Lars GM Pettersson and Anders Nilsson. The structure of water; from ambient to deeply supercooled. *Journal of Non-Crystalline Solids*, 407:399–417, 2015.

[108] K. T. Wikfeldt, A. Nilsson, and L. G. M. Pettersson. Spatially inhomogeneous bimodal inherent structure of simulated liquid water. *Phys. Chem. Chem. Phys.*, 13:19918–19924, 2011.

[109] Anders Nilsson and Lars GM Pettersson. The structural origin of anomalous properties of liquid water. *Nature communications*, 6(1):8998, 2015.

[110] Huib J Bakker and James L Skinner. Vibrational spectroscopy as a probe of structure and dynamics in liquid water. *Chemical reviews*, 110(3):1498–1517, 2010.

[111] Sow-Hsin Chen, Khaled Toukan, Chung-Keung Loong, David L Price, and José Teixeira. Hydrogen-bond spectroscopy of water by neutron scattering. *Physical review letters*, 53(14):1360, 1984.

[112] Maksim Grechko, Taisuke Hasegawa, Francesco D'Angelo, Hironobu Ito, Dmitry Turchinovich, Yuki Nagata, and Mischa Bonn. Coupling between intra-and intermolecular motions in liquid water revealed by two-dimensional terahertz-infrared-visible spectroscopy. *Nature communications*, 9(1):885, 2018.

[113] M-C Bellissent-Funel and J Teixeira. Dynamics of water studied by coherent and incoherent inelastic neutron scattering. *Journal of molecular structure*, 250(2-4):213–230, 1991.

[114] Matthias Heyden, Jian Sun, Stefan Funkner, Gerald Mathias, Harald Forbert, Martina Havenith, and Dominik Marx. Dissecting the thz spectrum of liquid water from first principles via correlations in time and space. *Proceedings of the National Academy of Sciences*, 107(27):12068–12073, 2010.

[115] Deepika Sharma, Banshi Das, and Amalendu Chandra. Terahertz spectrum of water at varying temperatures from 260 to 340 k: Contributions from permanent and induced dipole correlations at different length scales. *The Journal of Physical Chemistry B*, 127(30):6714–6725, 2023.

[116] Daniel C. Elton and Marivi Fernández-Serra. The hydrogen-bond network of water supports propagating optical phonon-like modes. *Nature Communications*, 7(1):10193, January 2016.

[117] F Sette, G Ruocco, M Krisch, U Bergmann, C Masciovecchio, V Mazzacurati, G Signorelli, and R Verbeni. Collective dynamics in water by high energy resolution inelastic x-ray scattering. *Physical review letters*, 75(5):850, 1995.

[118] M. Sampoli, G. Ruocco, and F. Sette. Mixing of Longitudinal and Transverse Dynamics in Liquid Water. *Physical Review Letters*, 79(9):1678–1681, September 1997.

[119] M Plazanet, I Morfin, V Honkimäki, T Buslaps, C Petrillo, and F Sacchetti. Hydrogen-bond network distortion of water in the soft confinement of nafion membrane. *The Journal of Chemical Physics*, 154(24), 2021.

[120] Benbing Shi, Xiao Pang, Shunning Li, Hong Wu, Jianliang Shen, Xiaoyao Wang, Chunyang Fan, Li Cao, Tianhao Zhu, Ming Qiu, et al. Short hydrogen-bond network confined on cof surfaces enables ultrahigh proton conductivity. *Nature Communications*, 13(1):6666, 2022.

[121] Gerry Lander Albert-José Dianoux. *Neutron Data Booklet*. OCP Science, 2003.

[122] Giulia Giubertoni, Mischa Bonn, and Sander Woutersen. D2o as an imperfect replacement for h2o: Problem or opportunity for protein research? *The Journal of Physical Chemistry B*, 127(38):8086–8094, 2023.

[123] Michele Ceriotti, Wei Fang, Peter G Kusalik, Ross H McKenzie, Angelos Michaelides, Miguel A Morales, and Thomas E Markland. Nuclear quantum effects in water and aqueous systems: Experiment, theory, and current challenges. *Chemical reviews*, 116(13):7529–7550, 2016.

[124] AK Soper and CJ Benmore. Quantum differences between heavy and light water. *Physical review letters*, 101(6):065502, 2008.

[125] Chenxing Liang, Archith Rayabharam, and NR Aluru. Structural and dynamical properties of h2o and d2o under confinement. *The Journal of Physical Chemistry B*, 127(29):6532–6542, 2023.

[126] Luigi De Marco, William Carpenter, Hanchao Liu, Rajib Biswas, Joel M Bowman, and Andrei Tokmakoff. Differences in the vibrational dynamics of h2o and d2o: observation of symmetric and antisymmetric stretching vibrations in heavy water. *The Journal of Physical Chemistry Letters*, 7(10):1769–1774, 2016.

[127] Janne Savolainen, Saima Ahmed, and Peter Hamm. Two-dimensional raman-terahertz spectroscopy of water. *Proceedings of the National Academy of Sciences*, 110(51):20402–20407, 2013.

[128] Wayne D Wilson. Speed of sound in heavy water as a function of temperature and pressure. *The Journal of the Acoustical Society of America*, 33(3):314–316, 1961.

[129] Elena R Dobrovinskaya, Leonid A Lytvynov, and Valerian Pishchik. *Sapphire: material, manufacturing, applications*. Springer Science & Business Media, 2009.

[130] Daniel C Harris. A century of sapphire crystal growth: origin of the efg method. In *Optical Materials and Structures Technologies IV*, volume 7425, pages 215–226. SPIE, 2009.

[131] Bahman Fartash and Kristina Arvidson. Long-term evaluation of single crystal sapphire implants as abutments in fixed prosthodontics. *Clinical oral implants research*, 8(1):58–67, 1997.

[132] Single crystal substrates. https://www.neyco.fr/uploads/media/product/0001/08/Materials_J_Substrats%20Monocristallins_1649325676.pdf. Accessed: 1st September 2025.

[133] S Kyropoulos. Ein verfahren zur herstellung großer kristalle. *Zeitschrift für anorganische und allgemeine Chemie*, 154(1):308–313, 1926.

[134] Kurt Nassau. Dr. avl verneuil: The man and the method. *Journal of Crystal Growth*, 13:12–18, 1972.

[135] Jan Czochralski. Ein neues verfahren zur messung der kristallisationsgeschwindigkeit der metalle. *Zeitschrift für physikalische Chemie*, 92(1):219–221, 1918.

[136] David F Bliss. Evolution and application of the kyropoulos crystal growth method. *50 years Progress in Crystal Growth*, page 29, 2004.

[137] Materials project allumina. https://legacy.materialsproject.org/materials/mp-1143/. Accessed: 20th August 2025.

[138] Mois I Aroyo. *International Tables for Crystallography: Crystallographic Symmetry*. John Wiley & Sons, 2021.

[139] E. Wigner and F. Seitz. On the constitution of metallic sodium. *Phys. Rev.*, 43:804–810, May 1933.

[140] Léon Brillouin. Les électrons dans les métaux et le classement des ondes de de broglie correspondantes. *Comptes Rendus Hebdomadaires des Séances de l'Académie des Sciences*, 191:292, 1930.

[141] https://www.globalsino.com/em/page2591.html. https://legacy.materialsproject.org/materials/mp-1143/. Accessed: 20th August 2025.

[142] H. Bialas. Contours of constant phonon energies in thebc-plane of sapphire (Al2O3) by means of inelastic neutron scattering. *Zeitschrift für Physik B Condensed Matter*, 27(2):121–123, June 1977.

[143] N. W. Ashcroft, N. D. Mermin, and R. Smoluchowski. Solid State Physics. *Physics Today*, 30(1):61–65, January 1977.

[144] Svetlana Kilina, Dmitri Kilin, and Sergei Tretiak. Light-driven and phonon-assisted dynamics in organic and semiconductor nanostructures. *Chemical reviews*, 115(12):5929–5978, 2015.

[145] H. Bialas, O. Weis, and H. Wendel. Dispersion of acoustic phonons in sapphire. *Physics Letters A*, 43(2):97–98, February 1973.

[146] H Bialas and H J Stolz. Lattice dynamics of sapphire (corundum). 1975.

[147] Guido Petretto, Shyam Dwaraknath, Henrique PC Miranda, Donald Winston, Matteo Giantomassi, Michiel J Van Setten, Xavier Gonze, Kristin A Persson, Geoffroy Hautier, and Gian-Marco Rignanese. High-throughput density-functional perturbation theory phonons for inorganic materials. *Scientific data*, 5(1):1–12, 2018.

[148] Dimitrios Argyris, Tuan Ho, David R Cole, and Alberto Striolo. Molecular dynamics studies of interfacial water at the alumina surface. *The Journal of Physical Chemistry C*, 115(5):2038–2046, 2011.

[149] Peter J. Eng, Thomas P. Trainor, Gordon E. Brown Jr., Glenn A. Waychunas, Matthew Newville, Stephen R. Sutton, and Mark L. Rivers. Structure of the Hydrated -Al2O3 (0001) Surface. *Science*, 288(5468):1029–1033, May 2000. Publisher: American Association for the Advancement of Science.

[150] P Guenard, G Renaud, A Barbier, and M Gautier-Soyer. Determination of the α-ai2o3 (0001) surface relaxation and termination by measurements of crystal truncation rods. *Surface Review and Letters*, 5(01):321–324, 1998.

[151] J Toofan and PR Watson. The termination of the α-al2o3 (0001) surface: a leed crystallography determination. *Surface Science*, 401(2):162–172, 1998.

[152] O Kurnosikov, L Pham Van, and J Cousty. High-temperature transformation of vicinal (0001) al2o3-α surfaces: an afm study. *Surface and Interface Analysis: An International Journal devoted to the development and application of techniques for the analysis of surfaces, interfaces and thin films*, 29(9):608–613, 2000.

[153] Z. Łodziana, J. K. Nørskov, and P. Stoltze. The stability of the hydroxylated (0001) surface of -Al2O3. *The Journal of Chemical Physics*, 118(24):11179–11188, June 2003.

[154] Yanhua Yue, Giacomo Melani, Harald Kirsch, Alexander Paarmann, Peter Saalfrank, R Kramer Campen, and Yujin Tong. Structure and reactivity of α-al2o3 (0001) surfaces: how do al–i and gibbsite-like terminations interconvert? *The Journal of Physical Chemistry C*, 126(31):13467–13476, 2022.

[155] Tianhao Tang, Wenhui Ding, Wanyi Fu, Shengyin Tang, and Xihui Zhang. Scale-dependent anomalous behavior of confined water between al2o3 layers. *Nano Res.*, 18:94907417, 2025.

[156] Giacomo Melani, Yuki Nagata, R Kramer Campen, and Peter Saalfrank. Vibrational spectra of dissociatively adsorbed d2o on al-terminated α-al2o3 (0001) surfaces from ab initio molecular dynamics. *The Journal of Chemical Physics*, 150(24), 2019.

[157] Manuel R Uhlig, Simone Benaglia, Ravindra Thakkar, Jeffrey Comer, and Ricardo Garcia. Atomically resolved interfacial water structures on crystalline hydrophilic and hydrophobic surfaces. *Nanoscale*, 13(10):5275–5283, 2021.

[158] Olle Björneholm, Martin H Hansen, Andrew Hodgson, Li-Min Liu, David T Limmer, Angelos Michaelides, Philipp Pedevilla, Jan Rossmeisl, Huaze Shen, Gabriele Tocci, et al. Water at interfaces. *Chemical reviews*, 116(13):7698–7726, 2016.

[159] Tong-Yi Zhang and Wei-Hua Xu. Surface effects on nanoindentation. *Journal of Materials research*, 17(7):1715–1720, 2002.

[160] J. Chadwick. The existence of a neutron. *Procedings of the royal society of London*, 136(830):692–708, 1932.

[161] H Von Halban. Preuve expérimentale de la diffraction des neutrons. *Acad. Sci. Paris*, 203:73–75, 1936.

[162] Paul Adrien Maurice Dirac. The quantum theory of the emission and absorption of radiation. *Proceedings of the Royal Society of London. Series A, Containing Papers of a Mathematical and Physical Character*, 114(767):243–265, 1927.

[163] Stephen W Lovesey. *Theory of neutron scattering from condensed matter. Vol. 1. Nuclear scattering*. Oxford Science Publications, 1984.

[164] Alfred Q R Baron. Introduction to High-Resolution Inelastic X-Ray Scattering.

[165] Michael Krisch and Francesco Sette. Inelastic X-Ray Scattering from Phonons.

[166] J. J. Thomson. Xl. cathode rays. *The London, Edinburgh, and Dublin Philosophical Magazine and Journal of Science*, 44(269):293–316, 1897.

[167] Léon Van Hove. Time-dependent correlations between spins and neutron scattering in ferromagnetic crystals. *Physical Review*, 95(6):1374, 1954.

[168] Alfred Q R Baron. Phonons in Crystals using Inelastic X-Ray Scattering.

[169] William Henry Bragg. The reflection of x-rays by crystals.(ii.). *Proceedings of the Royal Society of London. Series A, Containing Papers of a Mathematical and Physical Character*, 89(610):246–248, 1913.

[170] Bin Wei, Qiyang Sun, Chen Li, and Jiawang Hong. Phonon anharmonicity: a pertinent review of recent progress and perspective. *Science China Physics, Mechanics & Astronomy*, 64(11):117001, 2021.

[171] Jens Als-Nielsen • Des McMorrow. *Sources*. John Wiley & Sons, Ltd, 2011.

[172] F Sette and M. Krisch. Inelastic X-rays Scattering from Collective Dynamics.

[173] Alexeï Bosak and Daniel A. Chaney. High pressure phonon spectroscopy at esrf: Id28 beamline. *High Pressure Research*, 44(3):361–371, 2024.

[174] A Girard, T Nguyen-Thanh, SM Souliou, M Stekiel, W Morgenroth, L Paolasini, A Minelli, D Gambetti, B Winkler, and A Bosak. A new diffractometer for diffuse scattering studies on the id28 beamline at the esrf. *Synchrotron Radiation*, 26(1):272–279, 2019.

[175] Alessandro Longo, Stavros Alexandros Theofanidis, Chiara Cavallari, Nadadur Veeraraghavan Srinath, Jiawei Hu, Hilde Poelman, Maarten K Sabbe, Christoph J Sahle, Guy B Marin, and Vladimir V Galvita. What makes fe-modified mgal2o4 an active catalyst support? insight from x-ray raman scattering. *ACS Catalysis*, 10(12):6613–6622, 2020.

[176] S. Huotari, Ch. J. Sahle, Ch. Henriquet, A. Al-Zein, K. Martel, L. Simonelli, R. Verbeni, H. Gonzalez, M.-C. Lagier, C. Ponchut, M. Moretti Sala, M. Krisch, and G. Monaco. A large-solid-angle X-ray Raman scattering spectrometer at ID20 of the European Synchrotron Radiation Facility. *Journal of Synchrotron Radiation*, 24(2):521–530, Mar 2017.

[177] Luigi Paolasini. X-rays and their interaction with matter. In *Hercules Summer School*, 2023.

[178] Winfried Schülke. *Electron dynamics by inelastic X-ray scattering*, volume 7. OUP Oxford, 2007.

[179] Ch. J. Sahle, A. Mirone, J. Niskanen, J. Inkinen, M. Krisch, and S. Huotari. Planning, performing and analyzing x-ray raman scattering experiments. *Journal of Synchrotron Radiation*, 22(2):400–409, 2015.

[180] Esrf: Lighting the way. https://www.esrf.fr/files/live/sites/www/files/about/information-material/ESRF%20BRANDBook.pdf. Accessed: 30th July 2025.

[181] In8: Thermal neutron three-axis spectrometer. https://www.globalsino.com/EM/page2591.html. Accessed: 20th August 2025.

[182] MJ t Cooper and R Nathans. The resolution function in neutron diffractometry. i. the resolution function of a neutron diffractometer and its application to phonon measurements. *Acta Crystallographica*, 23(3):357–367, 1967.

[183] Gen Shirane, Stephen M. Shapiro, and John M. Tranquada. *Neutron Scattering with a Triple-Axis Spectrometer: Basic Techniques*. Cambridge University Press, 2002.

[184] B Hennion. La diffusion inélastique des neutrons sur monocristal. le spectromètre 3-axes. *Ecole thématique de la Société Française de la Neutronique*, 10:357–378, 2010.

[185] Matteo d'Astuto and Michael Krisch. High resolution inelastic x-ray scattering from thermal collective excitations. *Ecole thématique de la Société Française de la Neutronique*, 10:487–503, 2010.

[186] X-ray attenuation length calculator. https://henke.lbl.gov/optical_constants/atten2.html. Accessed: 09th Septembre 2025.

[187] BV Derjaguin and NV Churaev. Structural component of disjoining pressure. *Journal of Colloid and Interface Science*, 49(2):249–255, 1974.

[188] Hans-Jürgen Butt, Brunero Cappella, and Michael Kappl. Force measurements with the atomic force microscope: Technique, interpretation and applications. *Surface science reports*, 59(1-6):1–152, 2005.

[189] M Warburton, JM Ablett, J-P Rueff, P Baroni, L Paolasini, and Laurence Noirez. Identification by inelastic x-ray scattering of bulk alteration of solid dynamics due to liquid wetting. *Journal of Molecular Liquids*, 391:123342, 2023.

[190] Cecilie Rønne, Per-Olof Åstrand, and Søren R Keiding. Thz spectroscopy of liquid h 2 o and d 2 o. *Physical review letters*, 82(14):2888, 1999.

[191] Wenhui Duan, Bijaya B Karki, and Renata M Wentzcovitch. High-pressure elasticity of alumina studied by first principles. *American mineralogist*, 84(11-12):1961–1966, 1999.

[192] Ian K Robinson. Crystal truncation rods and surface roughness. *Physical Review B*, 33(6):3830, 1986.

[193] Aiyasami Jayaraman. Diamond anvil cell and high-pressure physical investigations. *Reviews of Modern Physics*, 55(1):65, 1983.

[194] Bernard A Weinstein and GJ Piermarini. Raman scattering and phonon dispersion in si and gap at very high pressure. *Physical Review B*, 12(4):1172, 1975.

[195] R Tarumi, H Ledbetter, H Ogi, and M Hirao. Low-temperature elastic constants of monocrystal corundum (α-al2o3). *Philosophical Magazine*, 93(36):4532–4543, 2013.

[196] Shun-Li Shang, Hui Zhang, Yi Wang, and Zi-Kui Liu. Temperature-dependent elastic stiffness constants ofα-andθ-al2o3 from first-principles calculations. *Journal of Physics: Condensed Matter*, 22(37):375403, 2010.

[197] Anubhav Jain, Shyue Ping Ong, Geoffroy Hautier, Wei Chen, William Davidson Richards, Stephen Dacek, Shreyas Cholia, Dan Gunter, David Skinner, Gerbrand Ceder, and Kristin a. Persson. Commentary: The Materials Project: A materials genome approach to accelerating materials innovation. *APL Materials*, 1(1):011002, 2013.

[198] Simo Huotari, Tuomas Pylkkänen, J Aleksi Soininen, Joshua J Kas, Keijo Hämäläinen, and Giulio Monaco. X-ray-raman-scattering-based exafs beyond the dipole limit. *Synchrotron Radiation*, 19(1):106–113, 2012.

[199] Nikita Kavokine, Marie-Laure Bocquet, and Lydéric Bocquet. Fluctuation-induced quantum friction in nanoscale water flows. *Nature*, 602(7895):84–90, 2022.

[200] Baptiste Coquinot, Lydéric Bocquet, and Nikita Kavokine. Quantum Feedback at the Solid-Liquid Interface: Flow-Induced Electronic Current and Its Negative Contribution to Friction. *Physical Review X*, 13(1):011019, February 2023. Publisher: American Physical Society.

[201] Yu G Gurevich and OL Mashkevich. The electron-phonon drag and transport phenomena in semiconductors. *Physics Reports*, 181(6):327–394, 1989.

[202] Gabriele Tocci, Laurent Joly, and Angelos Michaelides. Friction of water on graphene and hexagonal boron nitride from ab initio methods: very different slippage despite very similar interface structures. *Nano letters*, 14(12):6872–6877, 2014.

[203] Hui Li and Xiao Cheng Zeng. Wetting and interfacial properties of water nanodroplets in contact with graphene and monolayer boron–nitride sheets. *ACS nano*, 6(3):2401–2409, 2012.

[204] Sha Jin, Xue Fan, Caleb Stamper, Richard A Mole, Yuanxi Yu, Liang Hong, Dehong Yu, and Matteo Baggioli. Dissecting the experimental vibrational density of states of liquids using instantaneous normal mode theory. *arXiv preprint arXiv:2304.14609*, 2023.

[205] Yan-Feng Wang, Shu-Yan Zhang, Yue-Sheng Wang, and Vincent Laude. Hybridization of resonant modes and bloch waves in acoustoelastic phononic crystals. *Physical Review B*, 102(14):144303, 2020.

[206] Brian K Ridley. *Hybrid phonons in nanostructures*, volume 20. Oxford University Press, 2017.

[207] Tommaso Antonelli, Warda Rahim, Matthew D Watson, Akhil Rajan, Oliver J Clark, Alisa Danilenko, Kaycee Underwood, Igor Marković, Edgar Abarca-Morales, Seán R Kavanagh, et al. Orbital-selective band hybridisation at the charge density wave transition in monolayer tite2. *npj Quantum Materials*, 7(1):98, 2022.

[208] J Ruvalds and A Zawadowski. Two-phonon resonances and hybridization of the resonance with single-phonon states. *Physical Review B*, 2(4):1172, 1970.

[209] PG Klemens. Anharmonic decay of optical phonons. *Physical Review*, 148(2):845, 1966.

[210] Antonio Caretta, Michiel C Donker, Diederik W Perdok, Davood Abbaszadeh, Alexey O Polyakov, Remco WA Havenith, Thomas TM Palstra, and Paul HM van Loosdrecht. Measurement of the acoustic-to-optical phonon coupling in multicomponent systems. *Physical Review B*, 91(5):054111, 2015.

[211] AW Overhauser. Observability of charge-density waves by neutron diffraction. *Physical Review B*, 3(10):3173, 1971.

[212] I Mušsevič, R Blinc, B Žekš, C Filipič, M Čopič, A Seppen, P Wyder, and A Levanyuk. Observation of phason dispersion in a ferroelectric liquid crystal by light scattering. *Physical review letters*, 60(15):1530, 1988.

[213] Marc de Boissieu. Phonons, phasons and atomic dynamics in quasicrystals. *Chemical Society Reviews*, 41(20):6778–6786, 2012.

[214] D Moses, A Denenstein, AJ Heeger, PJ Nigrey, and AG MacDiarmid. One-to three-dimensional crossover in the lattice dynamics of hg 3- δ as f 6: Low-temperature specific heat. *Physical Review Letters*, 43(5):369, 1979.

[215] EM McIntosh, PR Kole, M El-Batanouny, DM Chisnall, J Ellis, and W Allison. Measurement of the phason dispersion of misfit dislocations on the au (111) surface. *Physical review letters*, 110(8):086103, 2013.

[216] M De Boissieu, M Boudard, B Hennion, R Bellissent, S Kycia, A Goldman, C Janot, and M Audier. Diffuse scattering and phason elasticity in the alpdmn icosahedral phase. *Physical review letters*, 75(1):89, 1995.

[217] Tsunetomo Yamada, Hiroyuki Takakura, Holger Euchner, Cesar Pay Gómez, Alexei Bosak, Pierre Fertey, and Marc De Boissieu. Atomic structure and phason modes of the sc–zn icosahedral quasicrystal. *IUCrJ*, 3(4):247–258, 2016.

[218] Michael Landry et al. Effective field theory for quasicrystals and phasons dynamics. *SciPost Physics*, 9(5):062, 2020.

[219] Matteo Baggioli. Homogeneous holographic viscoelastic models and quasicrystals. *Physical Review Research*, 2(2):022022, 2020.

[220] TC Lubensky, Sriram Ramaswamy, and John Toner. Hydrodynamics of icosahedral quasicrystals. *Physical Review B*, 32(11):7444, 1985.

Appendix A

Résumé substantiel en Français

La mécanique des fluides s'est construite à partir de l'hypothèse de continuité de la matière [1], donnant lieu à la célèbre équation de Navier-Stokes [2, 3]. Celle-ci décrit, avec succès, une grande gamme d'écoulements macroscopiques [4, 5]. Dans ce cadre, l'interface entre un solide et un liquide est comprise sur les principes de tension de surface et de mouillabilité [6], formalisés par la loi de Young [7], qui permet de faire une distinction claire entre surface hydrophile et hydrophobe en fonction principalement de l'énergie de surface du solide [8, 9]. Cette interaction entre solide et liquide est d'une importance cruciale, car elle dicte les conditions limites lors des mesures où la contrainte est transmise via une surface (rhéologie) [10]. Pour l'étude des liquides, le modèle dominant est celui de Maxwell [11, 12], qui postule une condition de non-glissement à l'interface solide-liquide [13]. Il introduit un temps de relaxation critique, τ_m, qui sépare les réponses de type liquide et de type solide d'un matériau à une contrainte mécanique. Une explication pour cette échelle de temps caractérisitique dans les liquides simples a été proposée par Frenkel [14], qui l'a identifiée comme le temps entre deux positions d'équilibre temporaires d'une molécule — une échelle de temps de l'ordre de la picoseconde pour l'eau [15]. Ce modèle établi prédit donc que les liquides sont principalement visqueux, et que tout comportement élastique de cisaillement est confiné au régime des très hautes fréquences (THz), bien au-delà des sollicitations mécaniques typiques.

Cependant, au cours des dernières décennies, un nombre croissant de résultats expérimentaux a directement remis en question cette vision classique [16, 17]. Des preuves se sont accumulées démontrant qu'une large gamme de liquides, allant des polymères fondus [18, 19] aux liquides moléculaires simples comme l'eau [20], peut présenter une élasticité de cisaillement finie à basse fréquence, de l'échelle nanométrique jusqu'à l'échelle mésoscopique sur plusieurs centaines de micromètres [21]. Ces résultats révèlent une réponse de type solide de faible module, dans un domaine de fréquence où les liquides étaient supposés être purement visqueux. Deux conditions expérimentales ont été identifiées comme requises pour que ce nouveau comportement soit observé : le liquide confiné doit être soumis à une faible déformation de cisaillement [22]. De manière critique,la mesure doit se faire dans des conditions de non-glissement, qui peut-être réalisé par un contact avec une surface hautement mouillante (notamment à haute énergie) [23]. Cette forte interaction solide-liquide semble être une condition nécessaire pour permettre au liquide confiné de maintenir une réponse élastique collective, indicative de modes vibrationnels à longue portée. De plus, au-delà d'une réponse purement élastique, des bandes thermiques inattendues associées ont été

identifiées [24]. L'observation de bandes thermiques au sein de multiples liquides sous cisaillement suggère l'existence de modes vibrationnels corrélés à longue portée, ignoré de la dynamique des fluides classique [25, 26, 27]. Ces multiples observations nouvelles ont convergé avec le développement indépendant de nouvelles initiatives théoriques [28], telles que la théorie du k-gap et la Dynamique des Réseaux Non-Affines (Non-Affine Lattice Dynamics) [29, 30, 31, 32], qui ont commencé à fournir des cadres capables de prédire certains de ces résultats expérimentaux [33].

Bien que l'interface solide-liquide ait été soulignée comme cruciale pour l'observation de ces phénomènes, l'une des perspectives manquantes dans la littérature actuelle est le couplage détaillé entre le solide et le liquide dans le régime THz puisse se faire. L'impact du liquide sur le volume (bulk) du solide a été ignoré, celui-ci étant traité principalement comme une frontière passive qui a permis de révéler la dynamique collective de cisaillement au sein du liquide [21, 20, 35]. Le solide est-il lui-même dynamiquement affecté par cette interaction ? Puisqu'il est démontré que les liquides présentent des dynamiques collectives de type phonon à longue portée lorsqu'ils sont fortement liés à une surface hydrophile, on peut se demander comment ces interactions influencent la dynamique du solide lui-même. C'est le sujet d'étude central de cette thèse. Le présent travail examine si ces états vibrationnels à longue portée au sein du liquide peuvent interagir avec les modes de phonons intrinsèques du solide et les modifier, loin de la couche interfaciale immédiate. Pour répondre à cette question, nous étudions un système modèle composé d'eau légère (H_2O) ou d'eau lourde (D_2O) en contact avec la surface (0001) hautement mouillante d'un substrat monocristallin d'α-Al_2O_3 (saphir). Le choix de l'α-Al_2O_3 est motivé par son statut de surface à haute énergie bien caractérisée [36], un matériau chimiquement inerte favorisant l'ancrage des liaisons H (liaisons hydrogène) et transmettant ainsi plus efficacement la contrainte mécanique à l'échantillon [37, 38], tandis que l'utilisation de la substitution isotopique (H_2O vs D_2O) permet de sonder directement comment la masse moléculaire du liquide et ses modes vibrationnels spécifiques modulent l'interaction. L'objectif est d'utiliser de multiples outils capables de sonder au volume (bulk) pour voir si une trace des modes vibrationnels complexes de l'eau [39, 40, 41] impact la structure ou le comportement phononique du solide.

Les expériences suivantes ont été menées:

- Les premières expériences ont été menées sur la ligne ID28 de l'ESRF, spécialisée dans la diffusion inélastique des rayons X à haute résolution énergétique ($\sim 3meV$). Un monocristal d'α-Al_2O_3 de 22 mm de diamètre et 2 mm d'épaisseur, a été monté dans un porte-échantillon permettant le mouillage *in situ* par H_2O ou D_2O de la surface orientée (0001). Les mesures ont été effectuées en géométrie de réflectométrie à température et pression ambiante, où l'angle d'incidence du faisceau X ($17.792keV$) détermine la profondeur de pénétration ($\sim 150\mu m$ à $\sim 300\mu m$ selon la zone de Brillouin étudiée). L'environnement de l'échantillon était contrôlé par un flux continu d'azote (0, 3 ou 6 L/min) pour minimiser la contamination et appliquer une contrainte mécanique via la circulation d'air induite à la surface du liquide. Les phonons acoustiques (transverses et longitudinaux) ont été sondés le long de la direction Γ-Z dans différentes zones de Brillouin, notamment $(\bar{1}014)$ et (0012).

- Pour compléter les mesures IXS, étudier une zone de Brillouin différente et s'affranchir

de l'évaporation et de la dépendance en profondeur liée à la réflectométrie, des expériences de diffusion inélastique des neutrons ont été réalisées sur le spectromètre 3-axes IN8 de l'ILL. Une cellule à flux continu a été conçue pour faire circuler H_2O ou D_2O(flux $F = 0.35$mL/s) sur quatre cristaux minces d'α-Al_2O_3 ($250\mu m$ épaisseur) co-alignés et espacés de $750\mu m$, montés en géométrie de transmission. Le faisceau de neutrons thermiques (monochromateur Cu(200), $k_f = 2.662\mathring{A}^{-1}$, résolution ~ 1.5 meV) traversait l'ensemble. L'environnement était protogé avec du Cadmium. Les phonons acoustiques transverses (TA) ont été mesurés le long de la direction Γ-Z dans la zone de Brillouin (300) pour les échantillons secs, sous flux liquide (H_2O ou D_2O), et après arrêt du flux.

- Pour examiner d'éventuels changements structuraux dans le volume du cristal induits par le mouillage sous contrainte, des expériences de diffraction X ont été réalisées sur la station secondaire (diffractomètre) de la ligne ID28 de l'ESRF. Un cristal d'α-Al_2O_3 plus fin ($150\mu m$ d'épaisseur, 4 mm de diamètre) a été utilisé et monté sur une tête goniométrique. Un faisceau X de $17.792keV$ (taille $20 \times 20\mu m^2$) traversait l'échantillon pendant qu'il effectuait une rotation de 170°. Un détecteur 2D (PILATUS3 X CdTE 1M) collectait les figures de diffraction. Un flux d'azote (~ 0.1 m/s à la surface) était appliqué sur l'échantillon mouillé avec H_2O. Des scans complets ont été enregistrés sur le cristal sec, puis à intervalles réguliers après mouillage pour détecter d'éventuelles modifications des pics de Bragg.

- Afin d'observer des changements potentiels dans l'environnement chimique et électronique local au sein du volume du cristal, des mesures de spectroscopie Raman X ont été effectuées sur la ligne ID20 de l'ESRF. Un cristal d'α-Al_2O_3 (22 mm diamètre, 2 mm épaisseur) a été exposé à un faisceau X incident de 9.69 keV sous un angle rasant (5°), résultant en une profondeur de pénétration d'environ $15\mu m$. Des modules de détection placés à différents angles ont permis de collecter le signal inélastique à différents transferts de moment **Q** (~ 3.2, 6.2 et 9.2 $\mathring{A}^{-1}$). Le seuil K de l'oxygène et les seuils $L_{2,3}$ de l'aluminium ont été mesurés sur l'échantillon sec puis après mouillage par H_2O, sous un flux d'azote constant (~ 0.3 m/s) pour maintenir la contrainte mécanique.

Nous avons ainsi mis en évidence une nouvelle interaction à longue portée entre un liquide sous contrainte mécanique (eau légère et eau lourde) et une surface hydrophile d'un cristal connu (α-Al_2O_3), impactant les phonons acoustiques du solide dans le volume (bulk). Les principaux résultats sont les suivants :

- **Une interaction anharmonique sélective en zone de Brillouin (BZ)**. En utilisant la diffusion inélastique des rayons X, nous avons observé une interaction phononique dans le volume du solide entraînant un durcissement des phonons acoustiques dans la BZ $(\bar{1}014)$ dans la direction Γ-Z (voir Fig.A.1d), accompagnée d'un élargissement (augmentation de la FWHM) des phonons LA (voir 5), mais sans effet de durcissement sur le phonon LA (0012) (voir 4.18), bien qu'un élargissement de ce phonon ait été noté. En utilisant la diffusion inélastique de neutrons, nous avons observé un élargissement du phonon TA dans la BZ (300) dans la direction Γ-Z, visible sur la Fig.A.1e), mais aucun durcissement. Ces résultats démontrent qu'une forme de couplage anharmonique est toujours induite dans l'ensemble du cristal, mais se manifeste différemment selon la BZ, suggérant une règle de sélection pour ce couplage qui reste à élucider.

- **Un fort impact de l'isotope du liquide sur l'anharmonicité**. L'effet anharmonique observé est fortement dépendant de l'isotope de l'eau. Il est significativement plus fort avec H_2O que D_2O. L'élargissement du phonon TA dans la BZ (300) est fortement isotopiquement dépendant, avec un élargissement plus prononcé avec le mouillage par H_2O que par D_2O, ce qui peut être vu sur la Fig.A.1e). De même, l'amplitude du durcissement observé dans la BZ $(\bar{1}014)$ des branches TA et LA est plus forte pour H_2O que pour D_2O, comme on le voit sur la Fig.A.1b), avec un rapport de décalage en énergie $\Delta\hbar\omega_{D_2O}/\Delta\hbar\omega_{H_2O}$ de ~ 0.7, similaire au rapport des masses balistiques des isotopes $\sqrt{m_H/m_D} \approx 0.707$. La combinaison de ces résultats suggère fortement que l'interaction anharmonique est pilotée par le réseau de liaisons Hydrogène (ou Deutérium) au sein du liquide. L'énergie vibrationnelle du liquide est probablement transférée plus efficacement via le réseau de liaisons H que par le réseau de liaisons D.

- **Un phénomène d'origine dynamique**. Les effets anharmoniques observés ne sont pas une conséquence du mouillage en tant que tel, mais nécessitent une contrainte mécanique externe. Celle-ci a été fournie par un flux d'azote externe dans les chapitres 3.4 et 6, et un écoulement d'eau imposé (cellule à écoulement) pour le chapitre 5. Ceci indique un phénomène hors équilibre induit par l'écoulement, mis en évidence sur la Fig.A.1. Une relaxation vers l'état du cristal sec est constatée, observée comme l'élargissement réduit lorsque l'écoulement est arrêté, voir Fig.5.9. L'interaction phononique anharmonique solide-liquide est induite et "alimentée" par une contrainte mécanique externe.

- **Confirmation de l'absence de changements structurels dans le solide**. Finalement, nous avons confirmé, par diffraction des rayons X à haute résolution, que le liquide sous contrainte mécanique n'a pas d'effet sur la structure du volume (bulk), et, par diffusion Raman des rayons X, qu'il n'en a pas non plus sur l'environnement chimique/électronique. Il n'y a pas de changements dans les états d'oxydation, la coordinence ou l'environnement chimique local, voir Fig.A.1c). Alors qu'au niveau de la première couche, à la surface, la littérature nous informe de la création d'une formation de type Gibbsite, montrée sur la Fig.A.1a), un phénomène équivalent ne se propage pas dans l'ensemble du solide.

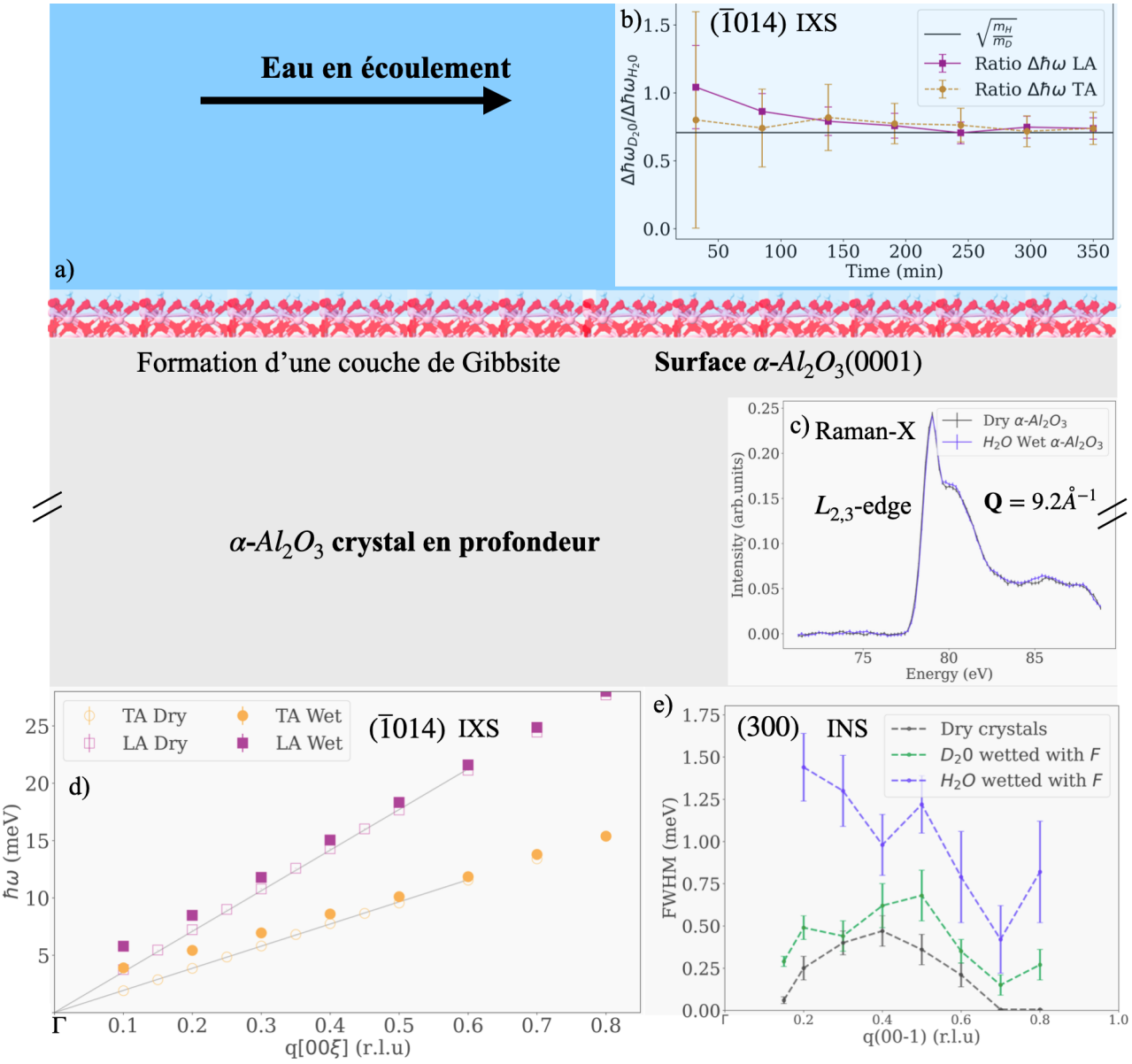

Figure A.1: Cette figure regroupe les résultats clefs de l'impact d'un liquide en écoulement sur l'inélastique du solide α-Al_2O_3 à température et pression ambiante. a) couche de Gibbsite à la surface lors du mouillage total de α-$Al_2O_3(0001)$ avec de l'eau [154]. Les atomes d'H sont en rouge et ceux d'Al en gris. b) Evolution temporelle du ratio de durcissement des TA (cercles oranges) et LA (carrés violets) ($\Delta\hbar\omega_{D_2O}/\Delta\hbar\omega_{H_2O}$) entre mouillage par eau légère et eau lourde de l'α-Al_2O_3 soumis à un écoulement d'azote de 6L.min^{-1} à la position $\mathbf{Q} = (\bar{1}013.5)$. Données obtenues par diffusion inélastique des rayons-X, voir Fig.4.17. c) α-Al_2O_3 Al $L_{2,3}$-edge obtenu en diffusion Raman-X d'un crystal sec (noir) comparé à un crystal mouillé avec de l'eau simple sous contrainte mécanique (bleu), voir Fig.6.8. d) Courbe de dispersion obtenue par diffusion inélastique aux rayons-X dans la zone de Brillouin $(\bar{1}014)$ avec la branche LA en violet et la branche TA en orange en comparant le crystal sec (symboles ouverts) et mouillés (symboles pleins) sous écoulement d'azote de 6L.min^{-1}, voir Fig.4.20. e) Largeurs à mi-hauteur dans la zone de Brillouin (300) mesurées par diffusion inélastique des neutrons comparant des cristaux secs (noirs) et sous écoulement d'eau lourde (vert) et eau légère (bleu), voir Fig.5.11.